Canarias avanza con Europa
Gobierno de Canarias
Consejería de Economía, Industria, Comercio y Conocimiento
Agencia Canaria de Investigación, Innovación y Sociedad de la Información
Unión Europea
FONDO SOCIAL EUROPEO
IUMA

UNIVERSIDAD DE LAS PALMAS DE GRAN CANARIA
Instituto Universitario de Microelectrónica Aplicada

AUTOMATIC CLASSIFICATION OF HISTOLOGICAL HYPERSPECTRAL IMAGES: ALGORITHMS AND INSTRUMENTATION

DOCTORADO EN TECNOLOGÍAS DE TELECOMUNICACIÓN E INGENIERÍA COMPUTACIONAL

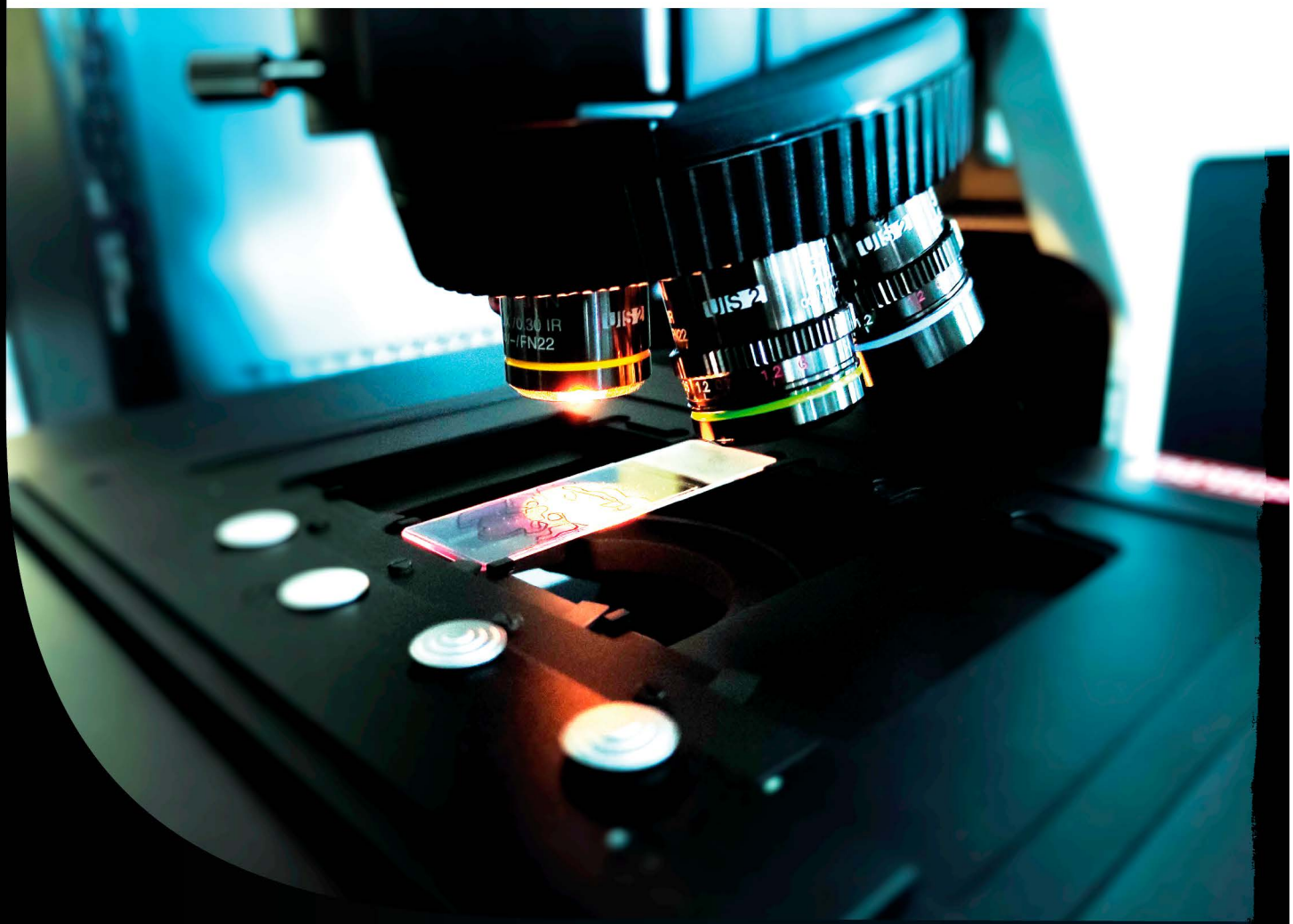

PhD Dissertation

Samuel Ortega Sarmiento

Las Palmas de Gran Canaria, **February 2021**

UNIVERSIDAD DE LAS PALMAS
DE GRAN CANARIA

D. GUSTAVO MARRERO CALLICÓ, COORDINADOR DEL PROGRAMA DE DOCTORADO EN TECNOLOGÍAS DE TELECOMUNICACIÓN E INGENIERÍA COMPUTACIONAL DE LA UNIVERSIDAD DE LAS PALMAS DE GRAN CANARIA,

INFORMA,

Que la Comisión Académica del Programa de Doctorado, en su sesión de fecha 23 de febrero de 2021 tomó el acuerdo de dar el consentimiento para su tramitación, a la tesis doctoral titulada "*Automatic classification of histological hyperspectral images: algorithms and instrumentation*" presentada por el doctorando D. Samuel Ortega Sarmiento y dirigida por el Doctor D. Gustavo Iván Marrero Callicó y el Doctor D. Fred Godtliebsen. Esta Tesis cuenta además con Mención Internacional.

Y para que así conste, y a efectos de lo previsto en el Artº 11 del Reglamento de Estudios de Doctorado (BOULPGC 7/10/2016) de la Universidad de Las Palmas de Gran Canaria, firmo la presente en Las Palmas de Gran Canaria, a 23 de febrero de dos mil veintiuno.

UNIVERSIDAD DE LAS PALMAS DE GRAN CANARIA
Escuela de Doctorado

tecnologías de telecomunicación
e ingeniería computacional

UNIVERSIDAD DE LAS PALMAS DE GRAN CANARIA

Programa de doctorado en tecnologías de telecomunicación e ingeniería computacional

Titulo de la tesis:

Automatic classification of histological hyperspectral images: algorithms and instrumentation

Tesis doctoral presentada por Samuel Ortega Sarmiento

Dirigida por el Dr. D. Gustavo Iván Marrero Callicó
Codirigida por el Dr. D. Fred Godtliebsen

El Director, (firma)	El Codirector, (firma)	El Doctorando, (firma)

Las Palmas de Gran Canaria, 15 de Febrero de 2021

UNIVERSIDAD DE LAS PALMAS DE GRAN CANARIA
Instituto Universitario de Microelectrónica Aplicada

DIVISIÓN DE DISEÑO DE SISTEMAS INTEGRADOS

TESIS DOCTORAL

AUTOMATIC CLASSIFICATION OF HISTOLOGICAL HYPERSPECTRAL IMAGES: ALGORITHMS AND INSTRUMENTATION

Samuel Ortega Sarmiento

Abstract

Hyperspectral imaging (HSI), also known as imaging spectroscopy, is a technology capable of sampling hundreds of narrow spectral bands across the electromagnetic spectrum through the use of optical elements that disperse the incoming radiation into discrete wavelengths. This technology combines the main features of two existing technologies: imaging and spectroscopy, making it possible to exploit both the morphological features and the chemical composition of objects captured by a camera. The interaction between electromagnetic radiation and matter is distinctive for each material, therefore by using this technology it is possible to discriminate among different materials.

Although historically HSI has been applied to remote sensing, in recent years this technology has become a trending topic in different research fields such as food quality analysis, military and security applications or precision agriculture, among many others. HSI is also an emerging imaging modality in the medical field. The study of light propagation through biological tissues is useful to identify several diseases. These properties of the interaction between light and biological tissue motivate the use of technologies that exploit the information of light propagation through tissues to develop tools for diagnosis support. As an alternative diagnostic tool, one of the strengths offered by HSI is being completely non-invasive and label-free.

Traditional computational pathology, also known as digital pathology, is an emerging technology that promises quantitative diagnosis of pathological samples, reduction of inter-observer variability among pathologists, and saving time in the manual examination of histological samples. Traditional computational pathology relies on RGB digitized histology images. Within computational pathology, several research groups have begun to explore whether hyperspectral/multispectral (HS/MS) imaging are technologies able to provide further advantages to this end.

In this Ph.D. thesis, we evaluate the potential of HSI as a diagnostic tool for the analysis of histological samples. First, we perform a literature systematic review, where we analyze the use of both HSI and MSI for pathological diagnosis, digital staining and other similar applications. Such systematic review adheres to the guidelines of the preferred reporting items for systematic reviews and meta-analyses (PRISMA). Additionally, we survey the most common processing methods which are used to extract useful information for disease detection and diagnosis using HSI.

Second, we characterize the instrumentation used to capture microscopic HS images, and we propose a methodology where we propose some recommendations to correctly set up the instrumentation in order to acquire high quality microscopic HS images. Next, different databases composed by histological HS data from both brain and breast tumors have been generated. The specimens consist of pathological slides where the Pathologists have indicated the areas corresponding to a concrete diagnosis, i.e., tumor or not tumor areas. The pathological slides used in this thesis were processed and analyzed by the Pathological Anatomy Department of the University Hospital Doctor Negrín at Las Palmas of Gran Canaria (Las Palmas de Gran Canaria, Spain), and by the Department of Pathology from the Tortosa Verge de la Cinta Hospital (Tortosa, Spain)

Due to the nature of the problem, HS images are processed using both Machine Learning and Deep Learning algorithms in order to evaluate the performance of automatic diagnosis using HS images. In this dissertation, we demonstrate that the combination of hyperspectral microscopic imaging and image processing techniques is a promising tool for future computational pathologies.

Resumen

La tecnología de imágenes hiperespectrales (HSI), también conocida como espectroscopia de imagen, es una tecnología capaz de muestrear cientos de bandas espectrales a lo largo del espectro electromagnético mediante el uso de elementos ópticos que dividen la radiación lumínica a su entrada en longitudes de onda discretas. Esta tecnología combina las principales características de dos tecnologías ya existentes: la imagen digital y la espectroscopia. Esto permite explorar tanto las características morfológicas como la composición química de los objetos capturados por una cámara hiperespectral. La interacción entre la radiación electromagnética y la materia es característica de cada material, y a través del empleo de esta tecnología es posible discriminar entre diferentes materiales.

Aunque históricamente este tipo de imágenes se ha aplicado en el campo de la teledetección, en los últimos años esta tecnología se ha convertido en un tema candente en diferentes campos de la investigación, como puede ser el análisis de la calidad de los alimentos, aplicaciones militares y de seguridad o la agricultura de precisión, entre otros. Las imágenes hiperespectrales son también una modalidad de imágenes emergente en el campo de la medicina. Esto está motivado porque el estudio de la propagación de la luz a través de los tejidos biológicos se ha demostrado útil para identificar varias enfermedades y patologías. Estas propiedades de la interacción entre la radiación lumínica y los tejidos biológicos motivan el uso de esta tecnología para desarrollar herramientas de ayuda al diagnóstico. Como herramienta alternativa de diagnóstico, una de las principales características que ofrece la imagen hiperespectral es ser completamente no invasiva y sin necesidad de etiquetado.

La patología computacional, también conocida como patología digital, es una tecnología emergente con la que se busca el diagnóstico cuantitativo de las muestras patológicas, proporcionando la reducción de la subjetividad de diagnóstico entre los patólogos, así como el ahorro de tiempo en el análisis manual de las muestras histológicas. La patología computacional convencional se basa en imágenes histológicas digitalizadas en RGB. En el marco de la patología computacional, varios grupos de investigación han comenzado a estudiar si las imágenes hiperespectrales son capaces de proporcionar ventajas sobre las tecnologías de imagen convencionales.

En esta tesis, se evalúa el potencial de la imagen hiperespectral como herramienta de diagnóstico para el análisis de muestras histológicas. En primer lugar, se ha realizado una revisión sistemática de la literatura, donde se analiza el uso de esta tecnología para el diagnóstico patológico, la tinción digital y otras aplicaciones similares. Dicha revisión sistemática se ha regido por las directrices de las *preferred reporting items for systematic reviews and meta-analyses* (PRISMA). Además, también se ha realizado un análisis sobre los métodos de procesamiento más comunes que se utilizan para extraer información útil para la detección y el diagnóstico de enfermedades utilizando HSI.

En segundo lugar, se ha caracterizado la instrumentación utilizada para capturar imágenes hiperespectrales microscópicas, y se ha propuesto una metodología en la que se proponen una serie de recomendaciones para configurar correctamente la instrumentación con el fin de adquirir imágenes microscópicas de alta calidad. A

continuación, se han generado diferentes bases de datos de imágenes hiperespectrales de muestras histológicas, tanto de tumores cerebrales como de mama. Los especímenes consisten en muestras histológicas en las que el patólogo ha indicado las áreas correspondientes a un diagnóstico específico, es decir, la localización de las áreas tumorales y no tumorales. Las muestras patológicas utilizadas en esta tesis fueron procesadas y analizadas por el Departamento de Anatomía Patológica del Hospital Universitario Doctor Negrín de Las Palmas de Gran Canaria (Las Palmas de Gran Canaria, España), y por el Departamento de Patología del Hospital Tortosa Verge de la Cinta (Tortosa, España).

Dada la naturaleza del problema, las imágenes se han procesado utilizando algoritmos de *Machine Learning* y *Deep Learning* para evaluar la capacidad del diagnóstico automático utilizando las imágenes hiperespectrales. En esta tesis, se demuestra que el uso de imágenes microscópicas hiperespectrales en combinación con técnicas de procesamiento de imágenes es una herramienta prometedora para el futuro de la patología computacional.

Acknowledgements

In the following lines, I would like to provide acknowledgements to the main contributors who made possible the development of this PhD. There is a wide variety of people who have been responsible for part of this PhD, and I hope not to forget any important names. Just in case, sorry if I forgot any names.

First, I would like to thank my whole family for their invaluable support during both the bachelor, the master, and the PhD. I would like to specially thank my parents, Matias and Myriam; my brother Matias; and my grandparents Cándida, Matías and Dolores; for their encouraging support during my whole life. I owe them all the success in my life.

I would like also to thank all my friends for their support during all this years. They have provided me plenty of good moments, which have positively affected to how I face my routine work. Specially, I would like to thank Richard Santana for the design of this PhD cover.

Second, I would like to thank my PhD directors, Gustavo Marrero and Fred Godtliebsen, for their advice and support during this period. Additionally, I would like to thank my main research colleague, Himar Fabelo, for his enthusiasm and hard work during the development of this PhD. We started with medical hyperspectral image processing as a small research group with a very limited budget, and since then we have tried to improve our research every day. I would really thank Gustavo and Himar for their leadership, their proactive attitude for networking and their continuous critical point of view. I really appreciate them to let me be part of such research, and I really would like to thank them for their unconditional support in my professional and personal life. I found in them the best colleges one can imagine (neither me could believe how lucky I was some years ago).

This PhD has been developed in the Integrated System Design division (DSI) of the Research Institute for Applied Microelectronics (IUMA). I would like to first thank Gustavo Marrero for giving me the opportunity to join the research group in early 2014. I also would like to thank the senior DSI members (Roberto Sarmiento, José Lopez, Gustavo Marrero, Sebastián López, Ernestina Martel and Eduardo Quevedo) for their active research aptitudes and continuous efforts, devoted to increase the productivity and resources of the group. When I joined DSI, the group had no hyperspectral cameras, and only a few researchers hired. Currently, it is difficult to have in mind all the DSI cameras in the laboratory, and also the number of researchers has significantly increased. I am really happy to have had the opportunity to witness how this research group has exponentially grown during the last years. Such grown could not be possible without the outstanding work of the other members of the group, namely Lucana Santos, Abelardo Baez, Raúl Guerra, Himar Fabelo, Ana Gómez, Noé Afonso, María Díaz, Antonio Sánchez, Pablo Hostrand, Yubal Barrios, Raquel León, Beatriz Martinez, Alejandro Morales, José Melián, Abián Hernández, Laura Quintana, Romén Neris and Diego Ventura. I would like to thank all of them for all the great moments we have shared, both in the lab and in our personal lives. Especially, I would like to thank Himar Fabelo and Raúl Guerra for their intensive work in the development of the main IUMA

laboratory for hyperspectral image acquisition. I will never forget the hard work we put there, and everything we learned and enjoyed. I am really proud of that.

This work is a consequence of a multidisciplinary collaboration between medical doctors and engineers. Since the contents of this PhD are related to the analysis of histological samples, the close collaboration with the pathologists was crucial to succeed. I would like to thank Maria de la Luz Plaza and Rafael Camacho (University Hospital Dr. Negrín at Las Palmas de Gran Canaria); and Carlos López and Marylene Lejaune (Verge de La Cinta Hospital) for their outstanding support during the development of this PhD thesis. This research definitely could not have been developed without their help. I really appreciate the hard work they put on our collaboration, with a meticulous sample preparation and illustrative feedback.

Additionally, an important part of this collaboration has been carried out during the collaboration with the Quantitative Bioimaging Laboratory at University of Texas at Dallas (UTD). I would like to thank Prof. Baowei Fei for his invaluable guidance and support during our research collaboration. Additionally, I would like to thank all the lab members who were involved in some way in my research stay at UTD, namely Martin Halicek, James Dorner, Maysam Shahedi, Ling Ma, Ximing Zhou, Patric Bettati and Fiaz Islam. I would like to make a special mention to Martin Halicek for his outstanding support for the development of really relevant parts of this PhD. I will always remember the good times we had, both inside and outside the lab.

This PhD dissertation is the consequence of the development of several research projects and research collaborations regarding the use of hyperspectral imaging in medicine. Specifically, my research in this field started with the European project HELICoiD. Similarly to this PhD, the HELICoiD project consisted of a multidisciplinary collaboration between medical doctors and engineers. I would like to firstly thank all neurosurgeons from the Neurosurgery Department from the University Hospital Dr. Negrín at Las Palmas de Gran Canaria for their proactive research aptitude during and beyond the HELICoiD project. Thanks to their work and effort, we were all able to search for the limits of hyperspectral imaging during brain tumor surgeries, namely Jesús Morera, Adam Szolna, Juan Piñeiro, Coralia Sosa, Aruma O'shanahan, Carlos Espino, Sarah Bishop, María Hernández, Mariano Marquez, and David Carrera. Additionally, I would like to thank the staff from the Electronic and Microelectronic Design Group (GDEM) at the Universidad Politécnica de Madrid (UPM) for our joint efforts to address all the technical problems that arose during the HELICoiD project. I would like to thank Eduardo Juarez, Ruben Salvador, Raquel Lazcano and Daniel Madroñal for their dedication and hard work. More than colleagues, I found in them good friends for the rest of my life. Furthermore, I would like to thank Daniele Ravi (The Hamlyn Centre, Imperial College London) and Ravi Kiran (Ecole Nationale Supérieure des Mines de Paris, MINES ParisTech) for our collaboration in the HELICoiD project, from which I learned a lot.

I also would like to thank other collaborators during this PhD for their proactive attitude, which made this research possible. Such collaborators are Bernardino Clavo (Research Unit, University Hospital Dr. Negrín at Las Palmas de Gran Canaria); Aday García and Ana Wagner (Complejo Hospitalario Universitario Insular Materno Infantil); Francesco Leporati, Emanuele Torti and Giordana Florimbi (Department of Electrical, Computer and Biomedical Engineering, University of Pavia, Italy); Alfonso Rodríguez, Jorge Portilla Rodrigo Mariño Cristian Wilsultschew, Cesar Sanz, Teresa Riesgo and

Eduardo de la Torre (Universidad Politécnica de Madrid); Alicia Martinez (Universidad de Castilla la Mancha); Fred Godtliebsen, Thomas Johansen, Miguel Tejedor and Kajsa Møllersen (Department of Mathematics and Statistics, UiT The Arctic University of Norway); Dimitris K. Iakovidis (Dept. of Computer Science and Biomedical Informatics, University of Thessaly, Greece); Anastasios Koulaouzidis (Endoscopy Unit, The Royal Infirmary of Edinburgh, UK); Daniel Campos-Delgado, Aldo Mejia-Rodriguez ,and Ines A. Cruz-Guerrero (Faculty of Sciences, Universidad Autónoma de San Luis Potosi, Mexico); Jan Broz (Department of Internal Medicine, Second Faculty of Medicine, Charles University, Czech Republic); Bradley Brimhall, Edward Medina and Marisa Whitted (Department of Pathology and Laboratory Medicine, UT Health San Antonio, Texas, USA).

This PhD thesis is also a consequence of what I learned at the Telecommunications and Engineering School at ULPGC. In such period of my life, I learned a lot from both the lecturers and colleagues. I would like to specially thank the work of some professors where I found inspiration, and a guidance to become a good engineer, namely Javier Miranda, Valentín de Armas, Félix Tobajas, Iván Pérez, Eugenio Jiménez, Pedro P. Carballo, Antonio Nuñez, Roberto Sarmiento, Rafael Pérez, Pablo Dorta, Roberto Esper-Chaín, and Francisco Cabrera. I would also thank my student colleagues for their support during college. I really think I could not become an engineer without them: Carlos Pérez, Pablo Mena, Marta Sánchez, Nerea Socorro, Javier Navarro, Alejandro Rodríguez, Cristo Santana, Marco Íñigo, Julia Batista, Adrián Rodríguez, Cristo Rodríguez, Miguel Ángel Tejedor, Patricia Rivera, Zeneida Perdomo, Guillermo Viera and Ángel Hernández.

During this PhD, I had the opportunity to lecture some laboratory lessons at ULPGC. I really like lecturing; therefore, I really appreciate the opportunity Gustavo Marrero gave me, and I really thank him for that. I would also like to thank all my senior colleagues during this period (Gustavo Marrero, Roberto Sarmiento, Tomás Bautista, Jorge Monagas, José López, Sebastián López and Javier Sosa), from who I learned a lot about how to become a good lecturer. I would also like to thank the staff from the Department of Electronic and Automatic Engineering, namely Ramón Macías and Marcos Martín, for their help and highly professional support. Besides, I would like to thank Margarita Marrero, head of the department, for her support in guiding us across all the paperwork required to lecture. Furthermore, during this PhD I have collaborated as co supervisor in several BSc and MSc theses. I would like to thank my students (Borja Alemán, Noé Afonso, Abián Benítez, Nauzet Rodríguez, Beatriz Martinez, Patricia Beltrán, Josua Hernández, Noemí Falcón, Laura Quintana and Cristian Rodríguez) for their hard work and implication. Additionally, I would like to thank Eduardo Quevedo and José Cabrera for inviting me to join interesting educational research projects.

Finally, I would like to thank staff members from IUMA and ULPGC for their invaluable daily work, which makes our lives easier. They really facilitate our work, and I would like to thank Enrique Montesdeoca, Agustín Quintana, Alfonso Canella, Juan Monzón, Cruci Melián and Fátima Melián, among others.

Contents

List of Figures

List of Tables

List of Acronyms

Acronym	Meaning
ACC	Overall Accuracy
ACIISI	Agencia Canaria de Investigación, Innovación y Sociedad de la Información
AF	Autoflorescence
ALL	Acute Lymphoblastic Leukemia
ANN	Artificial Neural Networks
ANOVA	Analysis of Variance
AOTF	Acousto-Optic Tunable Filter
API	Application Programming Interface
AUC	Area Under the Curve
BA	Balanced accuracy
BG	Benign Goiter
CAD	Computer-Aided Detection
CCD	Charge-Coupled Device
CEIC/CEI	*Comité Ético de Investigación Clínica-Comité de Ética en la Investigación*
cGAN	Conditional Generative Adversarial Network
CITSEM	Centre of Software Technologies and Multimedia Systems
CNN	Convolutional Neural Network
CNS	Central Nervous System
CS	Case Study
DCIS	Ductal Carcinoma In Situ
DL	Deep Learning
DR	Dimensionality Reduction
DT	Decision trees
EM	Electromagnetic
EMS	Electromagnetic Spectrum
ENSMP	Ecole Nationale Supérieure des Mines de Paris
EVG	Verhoef's Van Gieson
FAD	Flavin Adenine Dinucleotide
FCM	Fuzzy C-Means
FE	Feature Extraction
FL	Feature Learning
FLDA	Fisher Linear Discriminant Analysis
FM	Fontana Masson
FN	False Negative
FNA	Fine Needle Aspiration
FOV	Field of View
FP	False Positive
FTIR	Fourier Transform Infrared
GA	Genetic Algorithm
GAN	Generative Adversarial Network
GB	Glioblastoma
GFP	Green Fluorescent Protein
GMM	Gaussian Mixture Model
H&E	Hematoxylin and Eosin
H&N	Head and Neck
HELICoiD	HypErspectraL Imaging Cancer Detection
HG	High Grade
HS	Hyperspectral
HSI	Hyperspectral Imaging
ICL	Imperial College London
IF	Immunofluorescence
IFOV	Instantaneous Field of View
IHC	Inmunohistochemistry
InGaAs	Indium Gallium Arsenide
IR	InfraRed
ISH	In-Situ Hybridization
ITHACA	Hyperspectral Identification of Brain Tumors
IUMA	Institute for Applied Microelectronics
JCR	Journal Citation Reports
KNN	K-Nearest Neighbors
LBP	Local Binary Pattern
LCTF	Liquid Crystal Tunable Filter
LDA	Linear Discriminant Analysis
LED	Light-Emitting Diode
LG	Low Grade

Acronym	Meaning
LMMs	Linear Mixture Models
LR	Logistic Regression
LSTM	Long-Short-Term-Memory
MCT	Mercury Cadmium Telluride
ML	Machine Learning
MLi	Maximum Likelihood
MED	Minimum Euclidean Distance
MLP	Multilayer Perceptron
MLR	Multinomial Logistic Regression
mRMR	Maximum Relevance Minimum Redundancy
MT	Masson's trichrome
MS	Multispectral
MSI	Multispectral Imaging
NADH	Nicotinamide Adenine Dinucleotide
NCBI	National Center for Biotechnology Information
NIH	National Institutes of Health
NDI	Normalized Difference Index
NDVI	Normalized Difference Vegetation Index
NIH	National Institutes of Health
NIR	Near-InfraRed
PCA	Principal Component Analysis
PICOS	Participants, Interventions, Comparisons, Outcomes and Study Design
PLATINO	Plataforma Hw/Sw Distribuida Para El Procesamiento Inteligente De Informacion Sensorial Heterogenea En Aplicaciones De Supervision De Grandes Espacios Naturales
PLS	Partial Least Squares
PPV	Precision
PRISMA	Preferred Reporting Items for Systematic Reviews and Meta-Analyses
PSO	Particle Swarm Optimization
PTC	Papillary Thyroid Carcinoma
RBC	Red Blood Cell
RF	Random Forest
RGB	Red, Green and Blue
RNN	Recurrent Neural Networks
ROC	Receiver Operating Characteristic
ROI	Region of Interest
RS	Raman Spectroscopy
SAM	Spectral Angle Mapper
SCC	Squamous Cell Carcinoma
SFDI	Spatial Frequency Domain Imaging
SID	Spectral Information Divergence
SLIC	Simple Linear Iterative Clustering
Std	Standard Deviation
SURF	Speeded-Up Robust Features
SVMs	Support Vector Machines
SWIR	Short-Wavelength InfraRed
TN	True Negative
TP	True Positive
t-SNE	t-Distributed Stochastic Neighbors Embedding
UHDRN	University Hospital Doctor Negrin
UHS	University Hospital of Southampton
ULPGC	University of Las Palmas de Gran Canaria
UPM	Universidad Politécnica de Madrid
UTD	University of Texas at Dallas
UV	Ultraviolet
VNIR	Visible and Near-InfraRed
WBC	White Blood Cell
WHO	World Organization Health
WL	White Light
WSI	Whole-Slide Imaging

* Throughout the dissertation, some acronyms have been intentionally defined twice to improve the readability.

In memory of Agustín Ortega Arencibia and
María del Pino Báez Arencibia

Chapter 1: Introduction

1.1 Motivations

In the last decades, hyperspectral/multispectral (HS/MS) imaging (HSI/MSI) have become very popular techniques employed in numerous areas and applications. This type of images collects information along the electromagnetic (EM) spectrum, covering a wide range of wavelengths that generally span the visible, near-infrared and mid-infrared portions of the spectrum. HS/MS images can be seen as a three-dimensional (3D) data structure where two dimensions correspond to spatial information while the third dimension stands for the spectral information. This technology combines the main features of two existing technologies: imaging and spectroscopy, making it possible to exploit both the morphological features and the chemical composition of objects captured by a camera. Since all materials reflect, absorb or emit EM energy at specific wavelengths, this characteristic of the HS images permits to reconstruct the radiance spectrum of every image pixel and consequently, to identify different materials on the basis of their spectral shape. This property makes HS data beneficial for a wide variety of applications. Although historically HSI has been applied to remote sensing [1], in recent years this technology has become a trending topic in different research fields such as food quality analysis [2], [3], military and security applications [4] or agriculture [5], [6], among many others [7]. HSI is also an emerging imaging modality in the medical field. It has been proven that the interaction between the EM radiation and matter carries useful information for diagnostic proposes [8].

The use of HSI for microscopic examination of samples has recently attracted the attention of many researchers from different fields [9]. In mineralogy, Pirad et al used HS microscopic images for the quantitative analysis of minerals [10], finding strong correlation between the collected spectral signatures and previously collected spectrographic data. Jaap van der Weerd et al. applied this methodology to identify and classify different pigments in paint cross sections obtained from paintings, exploiting the potential of the visible spectra in the detection process [11]. Furthermore, this technology was used to evaluate the plant disease resistance against different pathogens in smart farming applications [12], [13]. However, it is in the medical field where HS microscopic imaging has emerged as a potential tool for non-invasive disease diagnosis.

Many clinical diagnoses of different diseases are usually carried out by HS microscopic examination of histological samples. Traditional diagnosis of histological samples is based on the manual examination of the morphological features of samples by skilled pathologists. In recent years, the use of computer-aided technologies for

improving these procedures has been an emerging trend to reduce the intra and inter-observer variability [14]. Such technologies are intended to improve the diagnosis, make it reproducible and quantitatively measurable, and save time in the examination of samples [15], [16].

Computational pathology, also known as digital pathology, is an emerging technology that promises quantitative diagnosis of pathological samples, reduction of inter-observer variability among pathologists, and the saving of time in the manual examination of histological samples [17], [18]. Traditional computational pathology relies on RGB (Red, Green and Blue) digitized histology images. Within computational pathology, several research groups have begun to explore whether HSI/MSI are technologies able to provide further advantages to this end.

HSI and MSI technologies have the potential to transform the fields of digital and computational pathology. Traditional digitized histopathological slides are sampled using RGB imaging. Utilizing HSI/MSI, spectral information across wavelengths within and beyond the visual range can complement the spatial information for the creation of computer-aided diagnostic tools for both stained and unstained histological specimens.

Motivated by the aforementioned context, in this PhD thesis we evaluate the potential of HSI as a diagnostic tool for the analysis of histological samples. The outline of this thesis can be summarized as follows. First, we present a detailed analysis of the usage of the HSI technology for histological applications. Then, we review the most important concepts regarding the HS instrumentation. Taking advantage of such concepts, the instrumentation used during this PhD thesis is described. Such instrumentation consists on a microscope and a HS camera. Afterwards, different datasets of HS images from histological samples were created. In this PhD thesis, histological samples corresponding to two different types of tumors were analyzed. The creation of such dataset involved a multidisciplinary collaboration between engineers and pathologists. Finally, the images were processed with the goal of evaluating the potential of the HS technology together with machine learning as an automatic diagnostic tool for computational pathology applications.

Concretely, the work presented in this thesis describes the main outcomes achieved during the collaboration between the Institute for Applied Microelectronics (IUMA) of the University of Las Palmas de Gran Canaria (ULPGC) with several relevant research institutions, such as the Centre of Software Technologies and Multimedia Systems (CITSEM) of the *Universidad Politécnica de Madrid* (UPM), the Hamlyn Centre of the Imperial College London (ICL), the *Ecole Nationale Supérieure des Mines de Paris* (ENSMP), the Wessex Neurological Centre of the University Hospital of Southampton (UHS), the Department of Anatomy Pathology of the University Hospital Doctor Negrin (UHDRN) of Las Palmas de Gran Canaria, and the Departament of Neurosurgery from the later hospital. These collaborations were framed within the European project HELICoiD (*HypErspectraL Imaging Cancer Detection*), funded by the Research Executive Agency, under Grant Agreement 618080, through the Future and Emerging Technologies (FET-Open) Programme, under the 7th Framework Programme of the European Union. HELICoiD was a collaborative project between four universities, three industrial partners and two hospitals, whose main goal was to use HSI to generalize a methodology to discriminate between normal and malignant tissues in real-time during neurosurgical procedures. Besides main goal of this project, biological specimens consisting of histological samples extracted during the neurosurgical interventions were

analyzed by pathologist and subsequently captured using a HS microscopic acquisition system. Finally, the images were processed in order to extract information about the samples' diagnosis using image processing techniques.

Besides this collaboration, in the context of the project PLATINO (*Plataforma Hw/Sw Distribuida Para El Procesamiento Inteligente De Informacion Sensorial Heterogenea En Aplicaciones De Supervision De Grandes Espacios Naturales*, reference TEC2017-86722-C4-4-R) founded by the Spanish Government, a microscope optimized for the capture of microscopic HS images was acquired by the research group. In the context of this thesis, such microscope was optimized for the acquisition of high-quality images, and several microscopic HS databases of histological samples were acquired.

In addition, thanks a collaboration carried out between the IUMA and the Department of Bioengineering of the University of Texas at Dallas (UTD), different algorithms were studied and applied to the automatic diagnosis of histological samples. This research was framed in the ITHaCA (*Hyperspectral Identification of Brain Tumors*) project, funded by the Canary Islands Government under Grant Agreement ProID2017010164. Besides, under the collaboration with the Department of Pathology of the Hospital de Tortosa Verge de la Cinta, in Tortosa, it was possible to include in this dissertation the analysis of breast cancer specimens.

Finally, this thesis was developed while Samuel Ortega was beneficiary of a pre-doctoral grant given by the "Agencia Canaria de Investigacion, Innovacion y Sociedad de la Información (ACIISI)" of the "Conserjería de Economía, Industria, Comercio y Conocimiento" of the "Gobierno de Canarias", which is part-financed by the European Social Fund (FSE) (POC 2014-2020, Eje 3 Tema Prioritario 74 (85%)).

1.2 Objectives

The main objective of this dissertation is to evaluate the combination of HSI with image processing techniques for the analysis of histological samples. The final goal of this study is to establish a relationship between the outcomes of the HS image processing and the diagnosis provided by the pathologists. To achieve this main goal, several specific objectives were proposed at the beginning of this thesis:

- **To acquire the required knowledge about the usage of HSI for computational pathology**, analyzing the current advantages and disadvantages of the technology, the instrumentation requirements, and the commonly used image processing methods for such type of data.
- **To design and develop a microscopic HS acquisition system** adequate for pathological slides, and to propose a methodology to **acquire high-quality images** by using such acquisition system. Using such instrumentation, different **HS image databases** will be generated and used as input for image processing algorithms devoted to extract useful clinical information about the samples.
- **To design and develop HS classification algorithms** capable of discriminate between tumor and normal tissues using different HS histological image databases.

1.3 Thesis organization

This thesis has been structured in 6 chapters that are interrelated as presented in Figure 1-1. A brief explanation of each chapter is presented next.

Chapter 1: **Introduction.** In the present chapter, the main motivations and objectives that have led to the development of the thesis are described. In addition, the structure of the document is presented.

Chapter 2: **State-of-the-art in computational pathology using hyperspectral imaging.** In this chapter, the main concepts regarding MSI/HSI are introduced. First, we present the main concepts regarding the MSI/HSI technology, including the basic knowledge about the instrumentation used to acquire HS data and the most common techniques for the information extraction from HS data. Second, we show the context on the usage of MSI/HSI for biomedical applications, especially in computational pathology.

Chapter 3: **Microscopic instrumentation and acquisition of hyperspectral data.** In this chapter, we present the details about the HS instrumentation that has been used during this research project. First, the key concepts related with HS acquisition systems are reviewed, highlighting how each element of the instrumentation influences the overall system response. Second, we describe the instrumentation used in this PhD thesis. Such instrumentation consists of a microscope and a push-broom HS camera. Finally, we propose a methodology to correctly set up a push-broom microscope to capture high-quality HS images.

Chapter 4: **Spectral-based classification of histological HS images.** In this chapter, we describe the use of HSI for the detection of brain tumor in pathological slides. We present two different supervised learning approaches for the processing of the same biological samples. These two approaches are different since the acquisition system, the data partition and the processing framework are different. First, the biological samples available for this study are presented. Second, an approach to process the HS data with data belonging to low magnifications is presented. Finally, an improved acquisition and processing system of high magnification HS images is performed.

Chapter 5: **Deep Learning for the spatial-spectral classification of histological HS data.** Deep Learning approaches are able to exploit simultaneously both the spatial and the spectral features of HSI. In this chapter, we explore the use of deep learning techniques for the classification of two types of specimens. First, we apply deep learning techniques to the HS human brain dataset which has been described in Chapter 4. Then, we create a novel dataset for discriminating between normal and tumor breast cancer cells using deep learning.

Chapter 6: **Conclusions & future lines.** In this chapter we summarize the main contributions of this PhD thesis, as well as we outline the main conclusions depicted from this research work. Then, we present the potential research lines which have arisen from the development of this

PhD thesis. Finally, the academic production developed in the context of this PhD is presented, i.e. the scientific communications performed during the development of the work described in this thesis and the different collaborations performed with other institutions and research groups are detailed. Specifically, 33 articles published in several journals indexed in the JCR (Journal Citation Reports), 24 peer-reviewed conference papers, a book chapter, and 1 patent have been achieved during the course of this thesis. In total, 59 scientific contributions have been accomplished.

Annex A: **Sinopsis en español.** In this annex, a brief summary of the thesis is presented in Spanish.

Bibliography: This thesis manuscript concludes with the list of references employed during the elaboration of this document.

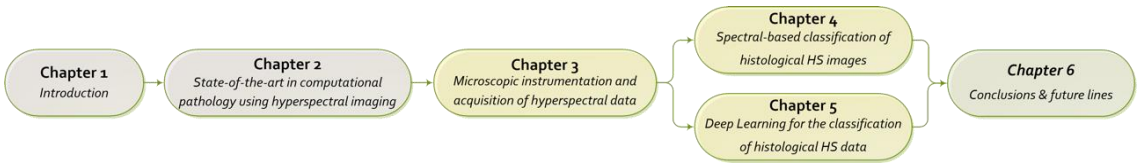

Figure 1-1: Thesis organization and interrelation between chapters.

Chapter 2: State-of-the-art in computational pathology using hyperspectral imaging

In this chapter, we provide a brief survey about the main concepts regarding HSI. First, we present the main concepts regarding the MSI/HSI technology, including the basic knowledge about the instrumentation used to acquire HS images and the most common techniques for the information extraction from HS data. Second, we show the context on the usage of MSI/HSI for biomedical applications, especially in computational pathology. Finally, we provide some discussion about the current status of this field, and the upcoming challenges for the future.

The contents depicted in this chapter have been published in two literature review articles and in a book chapter. The book chapter is entitled "*Information E*xtraction Techniques in Hyperspectral Imaging Biomedical Applications", published in the book "*In Multimedia Information Retrieval*" (2020, IntechOpen); and the literature review articles are the following ones: "*Use of Hyperspectral/Multispectral Imaging in Gastroenterology. Shedding Some–Different–Light into the Dark*" (2019, Journal of Clinical Medicine, MDPI), and "*Hyperspectral and multispectral imaging in digital and computational pathology: a systematic review [Invited]*" (2020, Biomedical Optics Express, OSA Publishing).

2.1 Hyperspectral imaging

HSI and MSI, also known as Imaging Spectroscopy, is a technology capable of overcoming the imaging limitations of the human vision based in white light (WL). In fact, HSI combines the features provided by two technologies that have been, for decades now, used separately i.e. digital imaging and spectroscopy. Digital imaging allows recording of the morphological features of a given scene, extracting information of different objects regarding shape and textures. Spectroscopy deals with the interaction between the EM radiation and matter. While the capabilities of the human vision are restricted to a certain region of the EM spectrum (EMS), the visible spectrum that spans from 400 to 700 nm, most common HS commercial systems expand this spectral range from 400 to 2500 nm. Although there are HS cameras able to cover the EM up to 12 microns, such systems are restricted to certain applications that are out of the scope of

this dissertation. HSI provides information in regions of the EMS that the human eye cannot see, revealing therefore substance properties that are normally unavailable to human beings. Furthermore, while the human eye is only capable of distinguishing three different wavelengths associated with the opsins of the retina (Cianopsin sensitive to 430 nm -*blue light*-; Cloropsin sensitive to 530 nm -*green light*-; and, Eritropsin sensitive to 650 nm -*red light*-), HS cameras can capture the EMS in hundreds of different narrow wavelengths, largely increasing the resolution over to what the humans can see. On the other hand, MSI is based on the same principle of HSI with the main difference that MSI is generally characterized by a lower number of spectral channels [19].

An HS image is recorded in a data structure called HS cube, which contains both spatial and spectral information from a given image. The information inside the HS cube can be visualized in several different ways. If a single pixel from an HS image is selected, the spectrum related to this pixel can be examined. Likewise, it is possible to visualize the entire spatial information for a given wavelength. The observed information at various wavelengths represents different properties of the matter. Figure 2-1 shows an HS cube, where both types of representations can be observed.

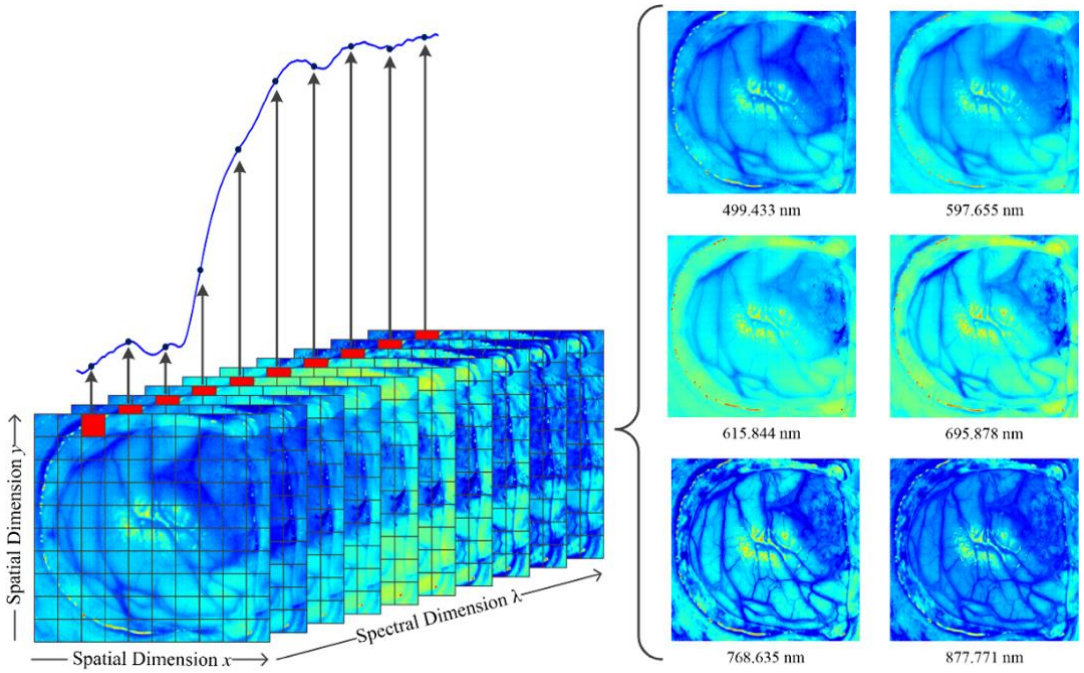

Figure 2-1: Example of an HS cube from in-vivo human brain surface and spectrum from the pixel in red (left). Several images at different wavelengths obtained from the HS datacube (right).

The spectral signature (also called spectral fingerprint) is the curve that links the EM radiation with a certain material. The key point of this concept is that each material has its own interaction with the EMS, hence the spectral signature of any given material is unique. By analyzing the spectral signatures contained in an HS image, it is possible to distinguish between the different substances that are present in the captured image. Nevertheless, to properly differentiate materials by using the spectral signature information, some issues have to be addressed. First, the measured spectral signature from the same material can present subtle variations, i.e. inter-sample variability. Second, there are materials that present spectral similarities among them, being extremely challenging to perform an automatic differentiation of such materials based only on their spectral signatures.

Many researchers have employed HSI technology for different applications such as non-invasive food quality inspection [1], [2], improving recycling processes [22], or examining paintings for accurate identification of the pigments used in order to refine their restoration [4], [5]. Geologists use HSI to identify the location of different minerals [25]. Furthermore, in agriculture this technology has been used to quantitatively characterize the soil [26] or to identify the stress levels of plants [27].

2.1.1 Hyperspectral systems

HS acquisition systems present a challenge to engineers, who have to handle sophisticated optical and electronic systems to generate an HS cube. Although a HS cube is a 3D data structure (Figure 2-1), most image sensors are 2D. For this reason, HS instrumentation can be classified in three main types, depending on how the HS cube is generated: spatial-scanning systems, spectral-scanning systems and snapshot cameras.

Prior to present the different types of HS cameras, some background about the HS instrumentation should be presented. The most important concepts to describe a hyperspectral acquisition system are the spectral range, the spectral resolution and the spatial resolution. The spectral range is the portion of the EMS sampled by a HS camera. There are several standard values for the spectral range from 400nm to 2500nm. The spectral resolution refers to the maximum number of spectral bands that can be resolved by a hyperspectral camera, and the spatial resolution is defined as the size of the smallest object that can be recorded by a camera. These definitions allow to establish a comparison between hyperspectral systems.

Here we provide a brief explanation of these technologies, intended to provide readers context about the HS instrumentation. Further readings about this topic can be found in [28].

2.1.1.1 Spatial scanning systems

Spatial scanning systems are usually compound by an optical element which performs the diffraction of the incoming light into fixed locations of a sensor, where the spectral channels are sampled. There are two types of spatial scanning HS systems. Whiskbroom systems are able to collect a 1-D data array containing the spectrum of the object that is being focused by the system. To capture an HS cube in this manner, it is necessary to perform a spatial scanning, where either the camera or the captured object(s) shift their position while the camera is capturing frames. The scanning can be also performed by using a mirror in front of the fore optic and moving the mirror to image the whole object. Although the use of mirrors allows developing more compact instrumentation (hence more appealing in clinical circumstances), it is necessary to take care about the geometric distortion that mirrors can produce in the captured image. In opposition to Whiskbroom HS systems, Pushbroom HS systems make use of optical gratings able to capture the spatial response of objects across a complete spatial dimension. In other words, pushbroom acquisition systems are capable of acquiring simultaneously a single spatial dimension (a narrow line of an image) and the whole spectral information for a given scene. In pushbroom systems, a spatial scan of the remaining spatial dimension is required to obtain a HS cube.

The core of these cameras is an optical element that splits the incoming radiation into specific wavelengths values [29]. These optical systems are able to provide very

competitive spectral resolution and are sensitive to a wider spectral range (from 300 nm to 2500 nm). The drawback of spatial scanning systems is the spatial resolution, which is limited both by the sensors and by the spatial scanning itself. Additionally, the requirement of a spatial scanning makes impossible for spatial scanning systems to acquire objects that are moving. In counterpart, these systems fit well in linear movement environments, such as a production line chain (e.g. in food industry), or in satellites for Remote Sensing applications. For this reason, in the medical field these types of cameras are used in open surgical procedures, for *in-vivo* surface inspection or for *ex-vivo* tissue analysis. It is not possible to directly attach this type of cameras to medical apparatus, like laparoscopes or intraoperative microscopes, due to their inability to perform spatial scanning. Some examples of HS acquisition systems, based on push-broom cameras, can be found in Figure 2-2.A and B, while the intraoperative use of these systems are presented in [30] and [31]. Furthermore, it is possible to use this kind of cameras for registering pathological slides [32], as can be observed in Figure 2-2.C.

Regarding the acquisition time, it is constrained by a tradeoff between the speed of the scanning system and the camera frame rate. However, the spatial scanning imposes longer acquisition times compared to other HS systems.

2.1.1.2 Spectral scanning systems

Another approach to create a HS cube is performing a spectral scanning where both spectral dimensions are captured each time for a single wavelength. This type of cameras employs an optical element that filters the incoming radiation, registering the entire spatial information of a single wavelength at each and every moment. Spectral scanning systems are also called staring array in the literature. There are several types of staring array cameras. The simplest one consists of a wheel containing optical filters, and the switch between different filters is performed mechanically. Nevertheless, filter wheels are limited in the number of spectral channels, and the time required to capture a HS cube is long due to the mechanical switch of spectral channels. However, there are other technologies which allow the acquisition of higher spectral resolution images.

Liquid Crystal Tunable Filter (LCTF) or the Acousto-Optic Tunable Filter (AOTF) are devices where the spectral transmission can be electronically controlled [33]. The spectral resolution of these systems is limited by the spectral bandwidth of the filter. Although there are narrow spectral filters available in the market, the spectral resolution is not as accurate as the achieved using a light-diffraction approach. Another drawback of AOTFs and LCTFs is that they are limited in the spectral range that can be covered. Despite this limitation, the use of spectral scanning technologies allows the use of conventional monochromatic cameras as sensors. For this reason, the spatial resolution can be high, depending on the selection of the sensors. It makes possible to obtain the highest spatial resolution among HS systems. The acquisition time in staring array systems is proportional to the number of spectral channels to be captured, and the switching time between different wavelengths. Common values of the switching time in AOTF and LCTFs are tens of milliseconds. Other advantages of LCTFs and AOTFs is that it would be possible to decrease the acquisition time of a HS cube by selecting only the most relevant spectral channels for a given application. Spectral scanning systems are not suitable for applications where the captured object is moving, because the spatial information may vary for different wavelengths. However, these cameras can be easily attached to medical instruments and can offer high spatial resolutions. An example of

HS acquisition system for medical applications using these cameras is shown in Figure 2-2.D [34].

Other less common spectral scanning technique make use of a spectrally-tunable light source to perform the spectral scanning.

2.1.1.3 Snapshot systems

The remaining type of HS cameras is called *snapshot* [35]. Snapshot technology is intended to deal with the main limitation imposed by the previously described HS technologies: real-time acquisition. It is not possible to collect HS or MS data in real-time using the above-mentioned HS technologies for the requirement of performing a scan (either spatial or spectral). These technologies are restricted to static situations, or scenarios where the object that is moving has a slightly lower speed compared to the scan speed. For these reasons, where necessary to obtain HS data of non-static scenes (e.g. living cell imaging) a snapshot camera must be employed. Furthermore, snapshot cameras can be directly attached to clinical instrumentation, such as endoscopes or laparoscopes. Nevertheless, both the spectral and the spatial resolution of the snapshot cameras are lower compared to the other HS technologies. To the best of our knowledge, there is no current research in GI using snapshot cameras, mainly because all preliminary exploration of HS technology in GI is focused to prove the capabilities of the technology for diagnosis, and hence it is necessary to evaluate each scenario using high performance spectral and spatial instrumentation.

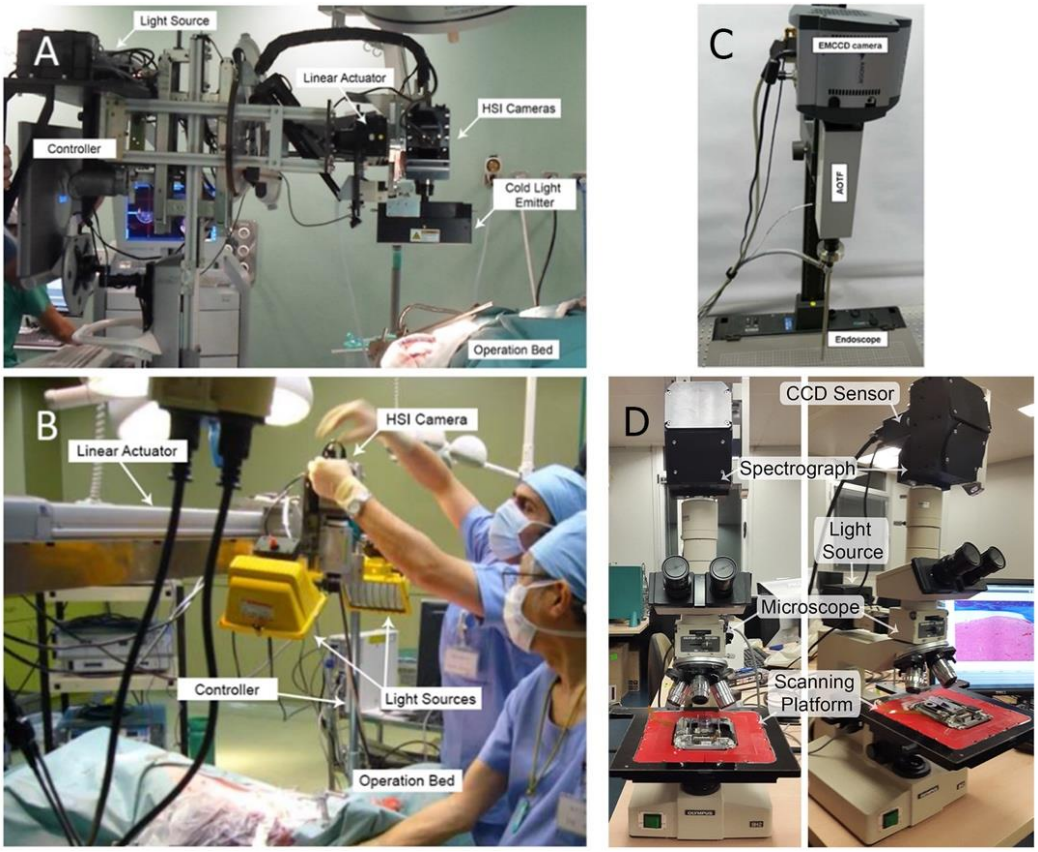

Figure 2-2: HS acquisition system used in medical applications. (a) and (b) HSI acquisition systems based on push-broom cameras for *in-vivo* human brain tumor detection [31] and *in-vivo* pig abdominal surgery [30]. (c) Liquid crystal tunable filter camera attached to an endoscope for cancerous tissue detection [34]. (d) Microscope coupled to an HSI push-broom camera for pathological slides registration [36].

2.1.2 Hyperspectral image processing

As mentioned in the previous sections, HSI data facilitates the identification of different materials. However, to successfully retrieve useful information from HS images, the application of appropriate image analysis techniques is necessary. In this section, a brief overview of such techniques is provided. They include pre-processing algorithms, e.g., for noise removal (HS images carry noise that may affect information extraction) [37], [38], HSI system calibration (with respect to the camera spectral range and resolution) [39], feature extraction [40], dimensionality reduction [41], classification [42], spectral unmixing [43], and Normalized Difference Index (NDI) estimation [44], [45].

Data acquired using HS instrumentation is highly biased by both the instrumentation and the environmental conditions. In order to remove the influence of instrumentation (mostly the wavelength dependencies of the sensor and grating efficiency and transmission of the lens), is common to perform a calibration. The typical calibration procedure in HS and MS imagery consists of capturing a reference image using a material that has a flat spectral response (e.g. Spectralon). This reference image captures the spectral dependencies of the instrumentation and is used to remove the influence of the instrumentation in the captured HS images.

There are two main types of medical HSI processing: optical inverse modeling and machine learning approaches. Next, both methods will be presented in detail, showing their main characteristics, as well as their advantages and disadvantages.

2.1.2.1 Optical inverse modeling

In optical inverse modeling techniques, a mathematical equation which models the interaction between the light and tissue is proposed, and the collected HS data is used to extract optical properties, such as the absorption or scattering of tissue. First, a physics-based model is proposed for the light propagation in tissues. Second, the HS data are used to extract optical properties from the proposed light propagation model. Although the number of studies which make use of this type of approach is limited, some researchers have used HS and light transport models in tissue to extract useful information for the detection of different diseases or conditions. Milanic *et. al* used Monte Carlo simulations of a light transport model in skin to extract information about the contents of melanin and blood saturation, with the goal of measuring cholesterol levels in human skin [46]. The same authors performed a similar processing analysis to skin HS data, but with the goal of detecting arthritis [47]. Claridge *et. al* demonstrated the utility of optical inverse modeling techniques for the estimation of the blood volume fraction of ex-vivo colon samples, showing statistically significant differences between the blood volume fraction of tumor and healthy conditions [48].

The use of optical inverse modeling for information extraction in medical HSI presents some advantages and challenges. The main advantage is to count with an established physical-based model for correlating measured data, which are theoretically strong and contain tissue optical parameters that can be used for diagnostics. The main disadvantage of this approach is the possibility of bias in the model development and over-simplification of complex physical processes, which could result in suboptimal performance for information extraction.

2.1.2.2 Machine learning methods

Machine Learning (ML) methods are algorithms able to learn from data. ML algorithms enable solutions to difficult tasks which usually cannot be performed by a traditionally designed computer program [49]. There are different ML algorithms depending on the task they perform. In regression problems, a numerical variable is estimated from the data. In the context of medical HSI, Arimoto *et al.* used regression techniques to estimate the oxygen saturation map from human retina [50]. In classification problems, the objective is to assign a data sample to a fixed category. For example, Fabelo. *et al.* used classification to identify normal tissue, tumor tissue, hypervascularized tissue and background in HS images from in-vivo human brain tissue [51]. The results of the classification of a medical HS image are usually represented as a classification map or heat map, where different colors for each class are used (Figure 2-3).

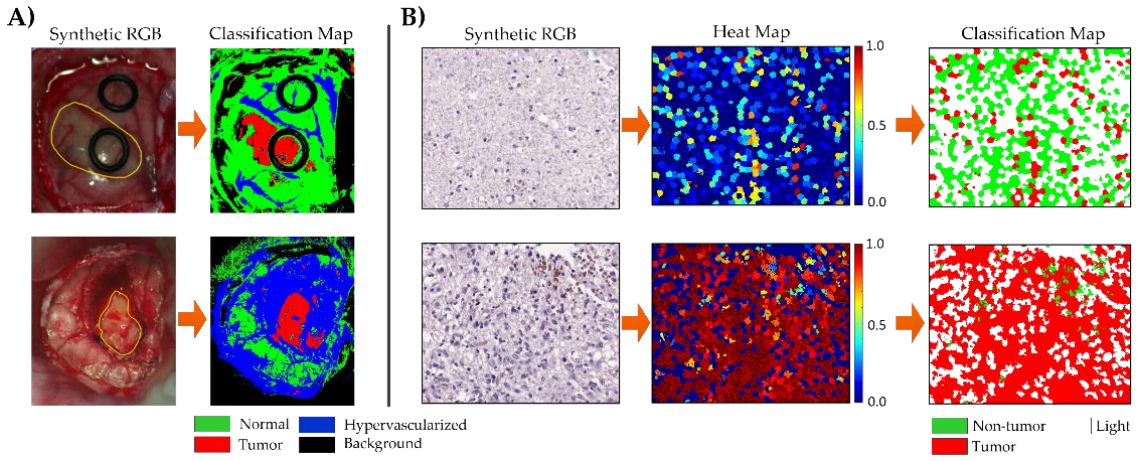

Figure 2-3. Example of classification and heat maps obtained through ML classification from (a) in-vivo brain tissue HS images [51] and (b) histological brain tissue HS images [52].

ML algorithms can be classified as supervised and unsupervised. In unsupervised algorithms, the goal is to cluster similar data samples in groups, extracting the information from data features. In supervised algorithms, the data is comprised of the data features and associated labels [53]. For example, in the example of Figure 2-3.A, the data features are the spectra of each pixel of the HS image, and the labels are the different categories into which each pixel can be categorized, i.e. normal tissue, tumor tissue, hypervascularized tissue and background. The main goal of supervised algorithms is to use data and their labels to train a model which can be used to perform predictions about new data. ML techniques can be categorized as Feature Learning (FL) or Deep Learning (DL) methods. In FL approaches, the inputs of a supervised classifier are given by features extracted from the data. For example, in an image processing framework, such features may be related to shape, texture or color. On the contrary, DL approaches are devoted to use all the data as input to a supervised classifier, and the important features to perform the classification task are learned by the supervised classifier.

There are challenges related with both types of ML approaches. On the one hand, in FL methods, the classification may be biased by which features are selected from the data for the classification, while the identification of features is performed automatically by the algorithm. On the other hand, DL methods usually require large amounts of data to succeed in the feature extraction and classification, while FL approaches may provide

good performance with a limited dataset. Next, we provide a survey about the different ML approaches which are commonly used for HSI processing in medical applications.

2.1.2.2.1 Feature Learning

In this section, we describe the most common FL approaches which have been employed for processing medical HS data. This section is categorized in three main categories, namely pixel-wise classification, feature extraction and selection methods, and the usage of both the spatial and spectral information.

a) Pixel-wise classifiers

In the HS literature, the concept of pixel-wise processing refers to the exclusive usage of the spectral information within an HS cube for extracting information from HS data. Recently, Ghamisi *et. al* performed a survey between the most commonly used classifiers in pixel-wise classification of HS images [54]. The most common classifiers used for the classification of HS images from a feature learning perspective are Support Vector Machines (SVMs), Random Forest (RF) and Multinomial Logistic Regression (MLR) based approaches.

SVM is a binary classification algorithm proposed by Vapnik [55]. The algorithm finds the optimal hyperplane that maximizes the margin between samples belonging to different classes. Although it was originally designed for linear classification, an SVM classifier can be used for nonlinear classification problems by using different kernels to map the data into a higher dimensional space. SVM has been shown to provide good classification performance even with a limited training sample [56].

RF was firstly proposed by Breiman [57]. This algorithm consists of an ensemble of decision trees, where, in each decision tree, the training data are hierarchically partitioned into smaller homogeneous groups. In RF, different decision trees are generated from the training data, and the different classification results are combined by a voting process. The main advantage of RF is a reduced training time. RF has been successfully used for the classification of HS images [58].

Finally, MLR [59] approaches exploit the posterior class distributions of the training data for making predictions, and these methods have been successfully applied for the classification of HS images. The main advantages of MLR are fast computation for training and customizability, which allows modifications to the original algorithm to provide better generalization, e.g. sparsity constraints or multiple feature learning.

In the context of medical HS classification, several authors have utilized spectral information for the diagnosis of different diseases in a pixel-wise manner. The most commonly used pixel-wise classifier in medical HSI is SVM. In the context of surgical guidance, Akbari *et. al* processed HS images from the abdomen to detect intestinal ischemia [60]. For cancer detection, SVM and HSI have been used for the identification of gastric cancer [61], prostate cancer [62], tongue cancer [63], and skin cancer [64]. Although RF and MLR have been widely used for HS information extraction, their usage in medical HSI is limited. RF has been used for the detection of in-vivo oral cancer [65], while MLR has been considered for identification of ulcerative colitis in histological slides [66]. The main challenge in this field is to determine which pixel-wise classifier is more suitable for the classification of certain HS data. In this sense, some authors have performed comparisons of performance of different pixel-wise classifiers for the detection of brain cancer in histological slides [36], or the detection of the tumor margins

in head and neck ex-vivo tissue [67]. Although SVM has been shown to outperform other classifiers, a deeper comparison between different classifiers should be urgently performed to definitively demonstrate which pixel-wise classifier performs better with HSI across multiple applications.

b) Feature extraction and feature selection

HS data are characterized by having a high dimensionality. For this reason, instead of exploiting the complete spectral signature for image analysis, one trend in HSI processing is the use of Dimensionality Reduction (DR) methods. These methods reduce the dimensionality of the original data while preserving the most relevant information [68]. DR methods have been extensively used for HS image processing. There are two main types of DR approaches: feature extraction and feature selection methods.

On the one hand, in feature extraction methods, a transformation is applied to the data to generate a new representation with lower dimensionality but similar information content. The most studied DR algorithm for HSI is Principal Component Analysis (PCA). The goal of PCA [69] is searching for a linear transformation of the data by using orthogonal projections which minimize the covariance matrix of the original data. On the other hand, several data transformation approaches have been proposed for dimensionality reduction, such as wavelet transformations [70], different orthogonal projection approaches, or the exploitation of manifold embeddings [71].

Nevertheless, in feature extraction methods the data are transformed, and thus the physical information about specific wavelengths is lost, which means that the provided interaction between light and tissue cannot be analyzed, which may affect certain applications. For this reason, feature selection methods are devoted to find the most relevant features from the original data by keeping the most relevant information. In the context of HSI, feature selection methods are also known as band selection methods, which also seek to identify the most relevant spectral features for a certain application. There are several types of band selection methods. In this chapter, we only describe the most prominent methods used in medical HSI. In a large-dissimilarity criteria approach, the goal is to select the most dissimilar spectral bands. Conversely, in a low-correlation criterion, the spectral bands showing low correlation between each other are selected. An example of this kind of algorithm is Maximum Relevance Minimum Redundancy (mRMR). In search-based methods, the band selection is performed by solving an optimization problem driven by a given optimization function. These algorithms search for the best bands to solve such optimization problem. Some search-based methods used in HSI are Genetic Algorithm (GA) [72] or Particle Swarm Optimization (PSO) [73]. Further details about more sophisticated band selection techniques can be found in [74].

In the context of medical HSI, feature extraction methods are used both as standalone methods and as a preprocessing stage before further data analysis. The former approach is to enhance the visualization of data, while the latter reduces the complexity of the data for being processed by other machine learning approaches. As an example of the direct application of PCA for tissue visualization enhancement, Zuzak *et. al* applied PCA to abdominal HS images in order to enhance the visualization of biliary trees using in-vivo samples [75]. Also, Wilson *et al.* demonstrated the ability of HSI for melanin detection in histological unstained specimens of melanocytic lesions in the skin and the eye using PCA and false-color representations of data [76]. PCA has been used for extracting the most important features of HS data prior to classification in different applications, such

as the detection of in-vivo oral cancer [77], prostate cancer in histological slides [78], the identification of white blood cells in blood smear slides [79] or the intraoperative delineation of brain tumors [80]. Another example of the utility of feature extraction methods was demonstrated by Hadoux *et. al*, where relevant differences between the retinal spectral data from patients with Alzheimer and healthy patients were found after applying an orthogonal projection of data [81]. Such differences in the spectral signature from different disease states were not possible using the raw spectral signature of tissue. Beyond PCA and orthogonal projection methods, Ravi *et. al* proposed a modification of the t-Distributed Stochastic Neighbor Embedding (t-SNE) feature extraction algorithm, a non-linear dimensionality reduction technique, prior to the identification of tumor tissue within in-vivo brain samples [82]. Other feature extraction methods used in medical HSI prior to classification are the use of Wavelet transformation for the detection of prostate cancer in mice models [83], or the use of Fourier Series coefficients for breast cancer detection [84].

The use of band selection methods for medical HSI applications is not as prominent as in other fields, such as remote sensing. However, some researchers have successfully exploited different band selection methods in HSI. Goto *et. al* used the Mahalanobis distance to determine the optimal wavelengths for gastric cancer identification between normal and tumor mucosa [85]. Additionally, mRMR has been used for the identification of the most relevant bands for ex-vivo breast cancer detection [84], and for in-vivo head and neck cancer [86]. Finally, Martinez-Vega *et. al* proposed a search-based method based on different optimization algorithms for the identification of the most relevant wavelengths for brain tumor detection within in-vivo HS images [87]. The optimization function was the pixel-wise classification performance metrics obtained by an SVM classifier. The results demonstrated that a GA optimization slightly improves tumor identification compared to the full-spectra counterpart.

Both feature selection and feature extraction methods aim to reduce the dimensionality of HS data while retaining the most important information. Successful application of these techniques leads to reduced computational time, which is required in applications such as surgical guidance. Nevertheless, for biomedical HS applications, there are some relevant advantages of using band selection methods instead of feature extraction methods. The first advantage is that the information about the concrete wavelengths that are used is retained. This fact allows further analysis about the physical response of different tissues to specific wavelengths. The second advantage of band selection methods is the possibility of developing custom HS cameras which only captures the most relevant spectral channels for a given application. Such reduced-band cameras would be able to acquire HS video, which would be also convenient for some surgical guidance applications.

c) Spatial-spectral information

Although the aforementioned data processing methods rely on the spectral information, a HS cube is a 3D data structure containing both the spatial and the spectral information of a scene. In a recent review manuscript, He *et. al* provided a survey about different spatial-spectral techniques which have been used for the classification of HSI [88]. The inclusion of both spectral and spatial information is motivated by limitations found in the spectral data. First, the high dimensionality of spectral data together with a limited dataset can lead to the *curse of dimensionality*. This phenomenon offers more detailed information about the captured scene, but it also contains redundant

information and increases the computational time required to process the data [4]. Second, the high variability shown in the spectral data due to different lighting conditions, instrumentation noise, or other phenomena, makes the classification based only on the spectral information a challenge. In addition, high intra-class and low inter-class variability of the spectral signatures produces difficulties in the differentiation between classes. This problem is particularly challenging in biomedical data, where data originate from multiple patients. For these reasons, researchers within the HSI processing community have successfully improved the classification of pixel-wise approaches by the utilization of spatial and spectral features from HS images.

In [88], the authors proposed a classification of spatial-spectral approaches in three main types, depending on how the spatial information is integrated in the processing framework. In pre-processing approaches, spatial and spectral features are extracted from the HS cube, and then such features are used for the classification. In integrated classification, both spatial and spectral features are used to train the classifier. Finally, in post-processing approaches, the spatial information is employed to refine the results of a pixel-wise processing of the HS cube.

In the context of medical HSI processing, most of the spatial-spectral approaches have been focused in pre-processing and post-processing schemes. Some pre-processing approaches are the following. In leukemia detection in blood smear slides, Wang *et al.* evaluated the usage of three types of inputs for a supervised classifier: spatial features, spectral features, and spatial-spectral features. The results of this study suggest that the exploitation of both the spatial and the spectral features significantly improves the quality of the classification [89]. Similarly, Li *et al.* evaluated the feasibility of utilizing HSI for Red Blood Cell (RBC) counting. After conducting the RBC counting using uniquely spatial or spectral features of blood cells, the authors found an improvement in the under-counting and over-counting rates when they performed the image analysis using both types of features together [90]. Ortega *et. al* make use of the spatial information of the HS data by performing superpixel segmentation [91]. In post-processing approaches, Fabelo *et. al* proposed the incorporation of the spatial information to the SVM pixel-wise classification by using a K-Nearest Neighbors (KNN) spatial filter which make use of a one-dimensional representation of the HS cube extracted using PCA for the identification of in-vivo brain tumor [80].

2.1.2.2.2 Deep Learning methods

Deep Learning is a family of machine learning algorithms that learn abstract features to best represent and make predictions about new data that is presented. More specifically, artificial neural networks (ANNs) consist of consecutive layers of neurons that have non-linear activations that connect the input data, extract features, and connect to logical outputs representing the classes of labels to provide prediction probabilities. Neural networks can have various dimensionalities, which largely depends on the size and dimensions of the input data. For example, utilizing only spectral signature information, a 1-D NN can extract features with fully-connected layers or 1-D convolutions. However, HS cameras acquire spatial information and spectral signatures simultaneously. Therefore, to exploit both sets of features, pseudo 3-D HS data can be input directly into a 2D-CNN (Convolutional Neural Network) and extract spatial features with learned convolutional kernels in the spatial domain, and these filters are connected across the entire spectral domain of the HS data. Lastly, 3D-CNN can utilize

the full pseudo 3D HS data as input and extract spatial-spectral features with 3D convolutional kernels. There are numerous approaches, but these methods require more computational processing as more features and dimensions are involved.

The most widely used approach is 2D-CNNs. Aggressive brain tumors, such as glioblastoma, often require surgical resection for treatment, and surgeons often implement multiple imaging modalities, including fluorescence, to aid in this very challenging task. In a pilot study to aid brain surgeons with label-free HSI, Fabelo *et al.* compared both 2D-CNN and 1D-DNN, considering spectral-only and spectral-spatial classification using DL [92]. In HSI digital histology, Ortega *et al.* detected glioblastoma brain cancer in digital slides using a patch-based 2D-CNN approach [93]. Additionally, Halicek *et al.* has employed very deep 2D-CNNs for classification, specifically the widely-used Inception v4 model (Figure 2-4) implemented in a sliding patch-based approach for head and neck squamous cancer [94] and thyroid and salivary gland cancers [95]. For comparing 2D-CNN and 3D-CNNs, in [96] Halicek *et al.* explored spatial-spectral convolutions in 3D CNNs with 3D convolutional kernels to 2D approaches. Although data were limited to only 12 patients, the preliminary results suggest 3D convolutions outperformed 2D convolutions for CNN design at the cost of computational power and speed.

Another desired application of DL for HSI is semantic segmentation, which allows the entire scene to be classified altogether from spectral-spatial features in the entire scene. Semantic segmentation does not require image reconstruction like patch-based 2D-CNN approaches. The most commonly used method is the U-Net, as first used in HSI by Trajanovski *et al.* for tongue cancer detection with a 2D input data using all HS channels for semantic segmentation of ex-vivo specimens [97]. Additionally, Kho et al. used ex-vivo specimens from patients with breast cancer and applied a standard U-net with 2D input HS data using all spectral channels for semantic segmentation [98].

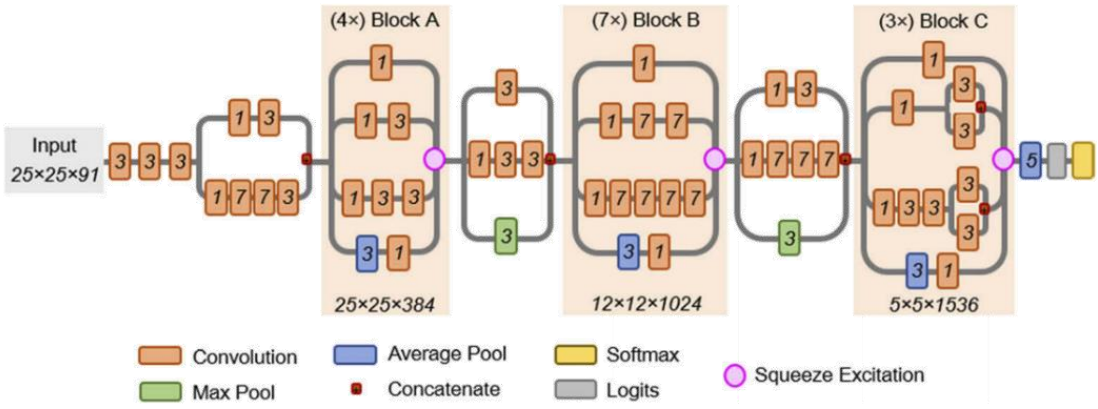

Figure 2-4. Schematic diagram of the modified inception v4 CNN architecture. The CNN was customized to operate on the 25×25×91 patch-size selected. The receptive field size and number of convolutional filters is shown at bottom of each inception block. The convolutional kernel size used for convolutions is shown in italics inside each convolution box. Squeeze-and-excitation modules were added to the CNN to increase performance [95].

More recently, several modern DL approaches with origins in computer-vision have been applied to medical HSI experimentally. In [99], a generative adversarial network (GAN) was applied to use DL to learn the association of RGB images and HS images to learn the ability to generate HS digital histology images from standard RGB digital histology images of breast cancer. Another modern approach is long-short-term-memory

(LSTM) and recurrent neural networks (RNN) which can utilize spatial-spectral and time-based inputs to operate in real-time video approaches. In [100], RNNs are compared to and outperform 2D- and 3D-CNN methods for in-vivo cancer detection with the goal of real-time video endoscopy.

The use of DL for HS processing is currently a hot topic in the research community in different fields. The main advantage of DL approaches in HSI is their capability to exploit jointly the spatial and the spectral information for image processing tasks. Currently, researchers are experimenting with different DL architectures in order to find the most appropriate DL model for HSI [101]. In the context of medical HSI, the use of DL in medical HS have shown good performance in different applications, but its usage is still limited compared to other ML approaches. The main reason is the limited number of data due to the novelty of the technology. More publicly available datasets with a large number of patients are required in order to definitively establish an adequate comparative of DL and traditional ML techniques.

2.1.2.3 Other HS processing approaches

In this section, we provide a survey about the most common processing frameworks for information extraction in medical HSI. However, there are other commonly used image processing techniques applied to HS image analysis, such as spectral unmixing or NDI estimation. On the one hand, spectral unmixing techniques, such as those based on Linear Mixture Models (LMMs), make the assumption that each pixel of an HS image can be modeled as the weighted sum of pure spectra elements (called endmembers). This technique tries to overcome the limited spatial resolution that generally characterizes MS and HS imaging compared to the traditional RGB imaging. Unmixing algorithms first find the endmembers and then estimate the abundance (proportion) of each endmember in a single pixel [43]. On the other hand, NDI-based approaches try to establish a combination of spectral channels that reveal some characteristics of the subject under study. For example, the Normalized Difference Vegetation Index (NDVI) aims to assess the presence of live vegetation in HS satellite images [44]. In the context of medical applications, a Melanoma Identification Index has been proposed in [45] for identification of skin lesions in dermoscopic HS images.

2.2 HSI for medical applications

The study of light propagation through biological tissues is useful to identify several diseases. Light propagation in biological tissues involves three different photophysical processes: refraction, scattering and absorption [102]. Refraction and reflection of light within biological tissues, which are usually non-homogeneous media, is related to the changes in speed and direction of light. The absorption of light involves the extraction of energy from light by molecules. Thus, absorption peaks are related to transitions between two energy levels in a molecule at a specific wavelength. These absorption peaks are used as a fingerprint of the molecules' response to light, providing information that can be used for diagnostic purposes. Scattering of light occurs when there is a spatial variation of the reflective index within tissues. The scattering of some biological components shows variations under certain disease conditions, becoming useful for diagnosis purposes [103]. Finally, some tissues show fluorescence when are excited by an external light source. For example, the emission of proteins and nucleic acids can be

observed after exciting tissue with ultraviolet light. Traditionally, these properties of tissue are measured in the spectral range known as therapeutic window, from 600 to 1300 nm [104], where tissues present weak absorption, and light is more likely to penetrate tissues.

These properties of the interaction between light and biological tissue motivate the use of technologies that exploit the information of light propagation through tissues to develop tools for diagnosis support. Raman Spectroscopy (RS) and Fourier Transform Infrared (FTIR) Spectroscopy make use of the information of the vibrating molecules produced by photons for diagnostics [105]–[107]. RS and FTIR spectroscopy are useful for identifying types of molecules, leading to their usage in biomedical applications. Both techniques are based on the vibrational state of the molecules, but while FTIR spectroscopy is more appropriate for absorption measurements, RS is more sensitive to scattering changes. This makes both technologies complementary. Additionally, Spatial Frequency Domain Imaging (SFDI) make use of modulated light sources and light transport models to extract information about absorption and scattering about different tissues, which can be subsequently used for diagnosis [108]. Finally, after the application of specific fluorescent agents to the sample, fluorescence spectroscopy techniques are able to measure the fluorescence spectra of the specimen after light excitation. Such fluorescence spectra can be associated with different disease states, leading in applications for biomedical diagnosis [109].

In opposition to these spectral technologies, HSI/MSI are optical spectroscopy imaging modalities, which directly measure the incoming radiance spectra of light. There are two major detection modes, depending on the incidence of light within the tissue: light reflection or light transmission. The spectral information measured by these technologies is usually related to the information about both scattering and absorption of light within the sample but can also be used for fluorescence measurements. In this sense, HSI/MSI are imaging techniques (also called imaging spectroscopy) able to obtain both spatial and spectral information within and beyond the human visual sensitivity, which is restricted to the spectral range from 380 to 740 nm. HSI/MSI can obtain additional information within the electromagnetic EMS by capturing the information regarding different wavelengths (also called spectral bands or spectral channels) up to 2500 nm. Similarly to the human eye capabilities, RGB imaging can be conceived as a multispectral image with only three spectral bands, related with the opsins of the retina (blue light – 430 nm – cianopsin; green light – 530 nm – cloropsin; red light – 650 nm – eritropsin)) [110]. Each pixel of an HS/MS image represent the light measured by the camera at each specific wavelength, creating a set of light measurements which comprise the spectral signature. This spectral signature can be understood as a fingerprint of each material that can allow differentiation of elements in a captured scene by using HS/MS processing algorithms [111].

In the medical field, several studies implement HSI/MSI for automated disease diagnosis and image-guided surgery [8], for example, both in-vivo and ex-vivo cancer detection [112], or gastroenterology applications [113], and many others.

2.3 HSI for computational histology

In this section, we analyze the use of both HSI and MSI for pathological diagnosis, digital staining and other applications. This literature review adheres to the guidelines of the preferred reporting items for systematic reviews and meta-analyses (PRISMA), and the objectives of this review can be summarized by using the PICOS (participants, interventions, comparisons, outcomes and study design) criteria [114]. The subjects of studies found in this review are limited to specimens from healthy and diseased humans and mammals. Prior to conducting the search and systematic review, it was unknown if other studies would compare outcomes of HSI to other image analysis techniques using conventional RGB images. Therefore, the nature of this review is non-interventional and studies the applications of HSI/MSI only for microscopic examination. Papers that provide comparisons of imaging modalities are reported, but this systematic review is not restricted to them. The outcome is to summarize the current status of HSI/MSI in histological analysis and methodology, including details about the population of each study, sample preparation, instrumentation and data analysis methods. Lastly, regarding study design, all primary research publications that make use of HSI/MSI for analysis of all types of histological specimens (including both journal papers and conference proceedings) are considered for inclusion in this review. A detailed technological analysis and summary is provided for clinical applications, methodology, instrumentation, data analysis techniques, limitations, and quality of outcomes compared to conventional imagery.

There are existing reviews related to the use of HSI/MSI for microscopy and digital histology available in the literature. Some of these reviews aim to present the basics on technology and the common processing approaches [115]–[117], but those manuscripts are limited in the number of applications covered and are not up to date. Other reviews are focused on technology aspects. Gao et al. performed a review describing the instrumentation used in HSI/MSI for microscopy applications [118], while Hermes et al. performed an overview of the different infrared sensing techniques [119]. Finally, Mansfield et al. presented a review about the application of only MSI for histopathological analysis more focused in the technical aspects [120].

2.3.1 Systematic review methodology

The methodology carried out for this systematic review adheres to the previously established PRISMA guidelines. The PRISMA guidelines consist of a four-phase flow chart and item checklist. The PRISMA statement [114] aims to improve the reporting of systematic reviews and meta-analyses. While the original focus of PRISMA is on randomized trials and interventions, it can also be used as the foundation for reporting systematic reviews of any type of research. Additionally, we used the PRISMA explanation and elaboration document [121] as a guideline, which is intended to enhance the use, understanding and dissemination of the PRISMA statement. The PRISMA statement establishes a methodology to perform a systematic review that includes a description of information sources to be used, the search strategy, the eligibility criteria of manuscripts, a report on how the study selection was carried out, and the protocol that researchers should follow when reviewing the manuscripts selected for the systematic review.

2.3.1.1 Eligibility criteria

The eligibility criteria of the manuscripts are highly related with the aforementioned objectives, which follow the PICOS guideline. To this end, the manuscripts eligible to be included in this systematic review consist of applications of MSI, HSI, or near-infrared (NIR) imaging. The former is included just in case that some studies exploit the use of only a few wavelengths, but not the standard RGB for histopathological analysis. Moreover, this review will only cover optical microscopy, which excludes point-wise and non-imaging spectroscopy, RS, SFDI, or FTIR from the scope of this review. Furthermore, the specimens used by the studies covered in this dissertation are restricted to be acquired from human or mammals. Regarding the data analysis methods, all data analysis techniques will be included in this dissertation. Articles considered must be published between 2004 and 2019 and written in English.

2.3.1.2 Information sources

The search for manuscripts to be included in this systematic review was performed in the Scopus and PubMed databases. The Scopus database [122] is the largest abstract and citation database of peer-reviewed literature. Scopus comprises a comprehensive collection of research outputs in the fields of science, technology, medicine, social sciences, and arts and humanities. On the other hand, the PubMed database [123] is a free resource developed by the National Center for Biotechnology Information (NCBI) and the National Institutes of Health (NIH) of United States of America. PubMed comprises over 30 million citations and abstracts from the fields of biomedicine and health, including life sciences, behavioral sciences, chemical sciences, and bioengineering. As an additional source of information, after performing the study selection, we considered all references cited by the selected manuscripts for the clinical diagnostic research category for potential inclusion if they adhere to the previous eligibility criteria.

2.3.1.3 Search

The database search for manuscripts was performed on August 13th 2019. The search was limited to manuscripts published between 2004 and 2019 and written in English. Two different researchers performed the search, one in PubMed and the other one in Scopus. The keywords used in both searches were:

(Hyperspectral OR Multispectral) AND (histology OR pathology OR histopathology)

The primary searches produced 2,213 citations and abstracts in total: 1,115 from PubMed and 1,098 from Scopus.

2.3.1.4 Study selection

The screening was performed by two researchers by reading the titles and abstracts of the manuscript citations found in the search. If the suitability of a manuscript was not clear from the abstract, the full manuscript was obtained and scrutinized to decide if the document should be included in the systematic review. The studies that adhere to the above eligibility criteria were selected.

2.3.1.5 Protocol and registration

As stated in the PRISMA guidelines, prior to the search and analysis of the manuscripts for this systematic review, we developed a protocol to be followed for reviewing manuscripts. This protocol is mainly focused in covering the objectives, i.e. questions to be addressed, of this systematic review, and it defines the data items to be sought during the evaluation of each manuscript. Our protocol is based on four major questions to be answered: the analysis of clinical data, the methodology used to carry out the experiments, the description of instrumentation employed, and the analysis of the data processing methods. For the analysis of clinical data, the authors should identify the types of tissues to be imaged, the number of patients, the types of patients, the histological preparation, e.g. staining, embedding, sectioning, etc., and the outcomes from a medical perspective. In the instrumentation, we searched for the type of HS/MS system employed and its characteristics, such as the spectral resolution, the spatial resolution, the number of bands, and the magnification. Lastly, regarding the data analysis methods, we sought for information regarding the calibration of data and the goal of the data analysis method, e.g. classification or segmentation. The information extracted from each manuscript is summarized in a table that contains all the data items previously mentioned.

2.3.1.6 Risk of bias

It is worth noting that the studies herein presented may suffer from publication bias or selection bias because these studies demonstrate positive results on the utility of HS/MS histological analysis. It is possible that only promising results are published and that comparison to other technologies, such as conventional imaging, could be intentionally omitted from experimental design or the final manuscript preparation.

2.3.1.7 Search results

In this section, we describe the study selection performed after the search. We make use of the PRISMA four-phase flow diagram (Figure 2-5). We also used Mendeley reference manager (Elsevier B.V., Amsterdam, Netherlands) as a computer-aid tool for the study selection. The primary search provided 1,115 manuscripts from PubMed and 1,098 manuscripts from Scopus, having a total of 2,213 manuscripts. After removing duplicates, we analyzed abstracts from 1,648 manuscripts. From these records, we selected 311 for full-text review, and we rejected 1,337 records. We excluded 497 records, which were not related to HSI/MSI, and 840 records, which were not associated to histology. After reviewing the full-text articles, 118 were excluded because they were not in the scope of this systematic review. Finally, additional 20 manuscripts were included from the references of the selected articles.

In total, we have included 193 research articles for this systematic review. The papers were categorized into five different sections: system development, color and staining, inmunohistochemistry (IHC), autoflorescence (AF) and diagnostic research for clinical routine practice. In addition to the systematic review of the selected papers, we have included some critical remarks on the current limitations and challenges of HSI/MSI at the end of each section.

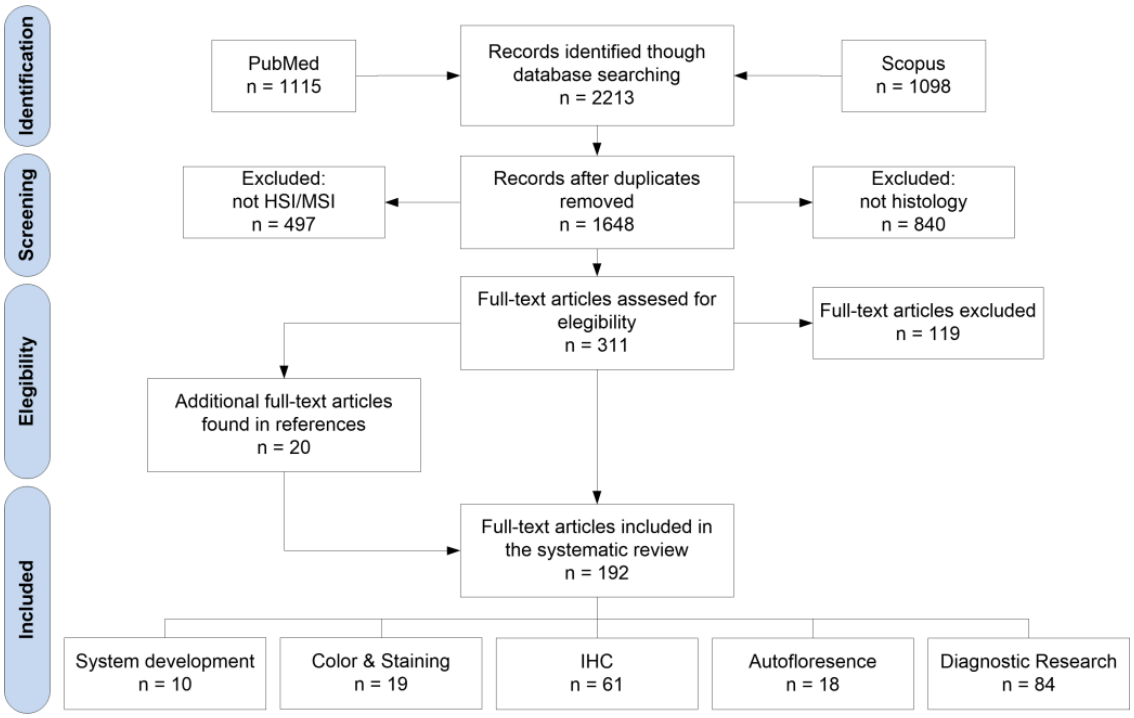

Figure 2-5: PRISMA flowchart for the search of literatures and studies.

2.3.2 Hyperspectral/multispectral system development

In this section, we provide readers with a basic background about the instrumentation used for HSI/MSI in histology applications, and we briefly summarize the main research carried out in the context of HS/MS instrumentation development and optimization.

There are three main characteristics of any HS/MS acquisition system: spectral range, spectral resolution, and spatial resolution. The spectral range is related to the range of EM wavelengths covered by the spectral camera. For biomedical applications, several light-tissue interactions can be observed in the diagnostic window, i.e. from 600 to 1300 nm. There are several types of commercial HS/MS acquisition systems which cover different spectral ranges: visible and near-infrared (VNIR) spectrum (400 – 1,000 nm), NIR spectrum (900 – 1,700 nm) or short-wavelength infrared (SWIR) spectrum (1,000 – 2,500 nm). The spectral resolution is defined as the resolution the EM is sampled, i.e. the difference between two consecutive spectral channels. A narrow spectral resolution may enable the identification of subtle absorption peaks, which is not possible to differentiate at lower spectral resolutions. Finally, the spatial resolution is related to the actual pixel size. Depending on the application, higher spatial resolutions are required to image small objects. In spectral imaging, the use of low spatial resolution can ultimately lead to spectrally-mixed measurements, i.e. finding the combined spectral signatures of several materials which are present in the current pixel. Low spatial resolution, and therefore high spectral-mixing, is admissible only when the application deals with homogenous materials, or at least materials that are homogenous enough for such spatial granularity.

In addition to the basic features of HS/MS instrumentation, there are several types of acquisition systems that can be found in the literature depending on the way of capturing the spectral and spatial information. Spatial-scanning techniques collect all the spectral information from a single point (point-scanning or whisk-broom sensors) or from a

single spatial line (push-broom or line-scanning sensors) [124]. In order to collect the spatial information, spatial-scanning techniques require relative movement between the camera and the sample. In opposition, spectral-scanning methods aim to collect progressively all the spatial information for different wavelengths. In spectral-scanning methods, a single wavelength is captured each time, and the scan is performed by changing the central wavelength of the spectral channel to be imaged. Examples of spatial-scanning systems are filter wheels, LCTFs, and AOTFs [33]. Finally, snapshot sensors are designed to simultaneously collect both the spatial and the spectral information of the sample in a single shot [33]. Further comparisons between HS/MS acquisition technologies in terms of spatial resolution, spectral resolution, spectral range and acquisition time requirements can be found in [125].

Most of the researchers who use HS/MS technologies for histopathological analysis use equipment based on a conventional microscope attached to a commercial HS/MS camera. Nevertheless, several research groups have focused their efforts in instrumentation development of HS/MS image acquisition systems for histological analysis of samples. These approaches include systems based on the following technology and sensors: AOTFs [126], [127], tunable light sources [128], imaging scanning spectrometers [129], [130], thin-film tunable filters [131], MS filter arrays [132], and push-broom scanning [133], [134]. Most of the acquisition systems in HSI/MSI are in the proof-of-concept stage and they are not ready to effectively perform whole-slide spectral imaging over the samples. However, Jiang et al. proposed a whole-slide imaging (WSI) system for HSI based on slit-array projections [135]. The aforementioned studies contain valuable information about development of HS/MS microscopic systems, but the contents are too technical for the previously established scope of this review. For completeness, the references are provided for interested readers to explore in more detail.

In this section, we defined the most important parameters of HS/MS acquisition systems. HS/MS technology is shown as a promising technology for biomedical applications, since the spectral interaction between light and tissue has been proven to provide information about diagnosis. However, the instrumentation is still quite expensive, large amounts of data storage are needed, and computational requirements are extremely high. These storage requirements are more evident for histopathological applications, where histopathological laboratories are able to digitize hundreds of slides per day.

However, it is possible to reduce the cost of the HS/MS instrumentation. If a reduced subset of spectral bands, which are useful for a certain application (e.g. certain tissue diagnosis) are identified, it would be possible to develop a low-cost MS system with similar storage requirements compared to conventional RGB imagery. In this situation, different low-cost MS systems can be used for different applications, where different spectral bands are required. Nevertheless, to reach this situation, more research should be performed with high resolution and wide spectral range HS instrumentation to determine which bands are relevant for each application. Furthermore, the storage capacity requirements can be also alleviated by making use of HS/MS data compression algorithms. The impact of using lossless or lossy compression in the data analysis should be determined in the close future. More investigation is required for histological applications where HS/MS analysis may increase the diagnosis ability of disease compared to conventional RGB imagery.

2.3.3 Color enhancement and digital staining

The examination of pathological slides provides the final diagnosis for most diseases, and color plays an important role. In this context, Cukierski et al. made use of the concept of metamers for analyzing the advantages of MSI for histopathological imaging. If a color has a higher probability of being metameric, then MSI will likely improve the task of distinguishing two structures, which have similar color but different absorption spectra. Using the concept of metamers and linear algebra transformations, the authors concluded that the maximum spectral difference between two metamers is beyond the capabilities of the human eye, where MSI could boost the diagnostic capabilities of conventional RGB imagery [136], [137]. Uneven color conditions among different samples can complicate the examination of samples and may be caused by different staining conditions (staining time, temperature or pH of the solution) and instrumentation (camera and microscope characteristics). To handle this problem, Abe et al. proposed a method where the amount of dye is estimated by using MS images in combination with the Beer Lambert law, and then the original image is weighted to obtain a color-corrected image. The method was proven to perform the color correction under different conditions of H&E (hematoxylin and eosin) stained slides of human liver, namely over-staining, under-staining, and excess of either hematoxylin or eosin [138], [139]. Yagi et al. proposed a method for color standardization based on MSI and the use of a standardized color chart [140], [141]. This procedure was proven to deal with the variations in appearance of H&E stained slide from different laboratories, which is one of the biggest challenges in whole slide imaging of histological slides. Additionally, the capabilities of HSI/MSI to measure colors accurately make it attractive to be employed as benchmark for measuring the color performance. Motivated by the lack of conventional color performance techniques, such as colorimetry or spectroradiometry, to measure microscopic biological tissues, Salehen et al. evaluated the color performance of two different whole-slide imaging systems using HSI and three different H&E stained histological samples as color targets [142], [143].

Another interesting application of HSI/MSI in histopathology is digital staining. The main goal of this approach is to highlight molecular components in digitized slides without performing a physical stain of the samples. For example, Masson's trichrome (MT) stain is used to emphasize fibrosis structures, which can aid in the diagnosis of chronic liver diseases. In this sense, Bautista et al. proposed several techniques to digitally stain H&E MS images and virtually transform into MT stained samples [144]–[150]. Apart from the digital stain to simulate MT, the same group also applied digital staining to visualize the color differences between tissue structures that displayed similar H&E staining patterns. This approach promises to be useful to visualize tissue structures that are not emphasized by the original stain, without the requirement of additional physical staining [151], [152]. An example of this application can be observed in Figure 2-6. Beyond digital staining of previously H&E stained samples, some researchers have focused their work in performing digital staining of unstained samples. In this field, Bautista et al. also performed digital generation of an H&E image from an unstained kidney slide using supervised classification of nucleus, cytoplasm and RBCs, and then applied a linear transformation to stain those components into a H&E like image [153]. Additionally, Bayramoglu et al. digitally stained an unstained lung specimen, producing the appearance of H&E staining, using a conditional generative adversarial network (cGAN) [154].

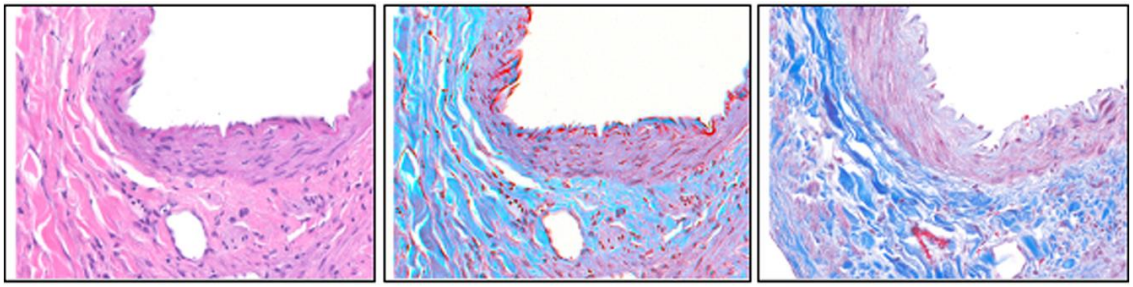

(a) (b) (c)

Figure 2-6: Example of digital staining of H&E images to provide them with the appearance of MT stain. (a) Original H&E image (b) Digitally stained image (c) MT stained image. Reproduced from [62]; Creative Commons BY 4.0; published by SPIE (2012).

In summary, the current state-of-art uses of HSI/MSI in the field of digital staining and color optimization are mostly focused on color optimization, standardization of digitized slides, and digital staining of samples.

In the context of color enhancement and standardization, the research carried out by the HSI/MSI community has been limited to proof-of-concept research, where the color reproducibility and the inter-laboratory variations of digitized slides are improved by means of HS/MS image processing. Nevertheless, such studies have not demonstrated a significant difference between conventional WSI digitized slides and HSI/MSI. For this reason, HSI/MSI solutions have been proven as a realistic alternative to conventional RGB imagery for clinical environments despite increased instrumentation costs, data storage, and computational requirements for color enhancement and standardization. Furthermore, recently, Campanella et al. found a performance drop in a supervised classification for histological diagnosis when data used for training belong to different institutions, even when the number of training samples was high [155]. For this reason, and regardless of the cost associated with image acquisition in the preliminary stages, HSI/MSI technology should be further analyzed as an alternative to compensate the differences in color between data from different institutions or acquisition systems. Once such research is performed, there could be a well-founded argument discussion about the enhancements of using expensive HSI/MSI to alleviate inter-laboratory differences, and hence, compensating the problems in automatic machine learning approaches, which could benefit histopathological laboratories in the long-term.

In the context of digital staining, some of these works have the goal of generating trichromatic images from H&E stained images by processing MS/HS images. Some researchers have recently proposed new approaches to reach the same goal using conventional imaging techniques. Fereidouni et al. demonstrated the feasibility of HSI/MSI for the generation of trichrome images exploiting the combination of a fluorescence image and a brightfield image [156]; while Rivenson et al. suggested the use of deep learning to generate trichrome images from standard RGB data from H&E slides [157]. In fact, both approaches were presented as cost-effective alternatives to the use of HSI/MSI. However, these are only examples of the generation of one specific type of digital stain. Further research should be performed in order to investigate if HSI/MSI is able to outperform RGB or fluorescence technologies for this and other digital stain applications. For this reason, the research in the field of digital staining by using HSI/MSI should be focused on the exploration of unstained samples. The dyes used to stain tissues for subsequent examination of histological samples modify the spectral signature of the sample itself, restricting the spectral information only to the visible

spectral range of light. Therefore, it should be investigated if the spectral information within unstained histological samples could provide advantages compared to conventional stained samples. The main opportunity of HSI/MSI technologies is to use unstained samples for digitally synthesized multiple-dye digital staining. According to the literature, this information can be found in the diagnostic window of the EMS from 600 to 1300 nm [104]. In addition, Sordillo et al. have recently proposed the spectral window from 1600 to 1800 nm to be also useful for diagnosis [158]. The investigation of histological samples at these wavelengths should be performed with unstained samples and with HS/MS cameras in the NIR spectral range. In summary, to explore the possibilities of this promising technology, more research should be performed in order to determine the potential clinical usage of HSI/MSI for such applications.

2.3.4 Immunohistochemistry and immunofluorescence

Our extensive literature review located 59 research articles that present two commercially available MS microscope systems that are predominantly applied in the literature for immunohistochemistry and immunofluorescence (IF). These MS microscopes are clinically useful because they allow quantitative analysis of multiple molecular biomarkers in multi-label tissue specimens, both in bright-field and fluorescence modes. The Nuance CRi Multispectral Imaging System (Cambridge Research and Instrumentation, Woburn, MA; PerkinElmer, Inc., Hopkinton, MA) is available in three versions (VX, FX, and EX), which capture MS images in the wavelength ranges of 420 to 720 nm (VX and FX) and 450 to 950 nm (EX). A LCTF acquisition system is used for spectral imaging with spectral bandwidths of 20 or 40 nm for the EX/FX versions and 7, 10, or 20 nm for the VX version. The more recent Vectra Quantitative Pathology Imaging System (PerkinElmer, Inc., Hopkinton, MA) performs MS imaging and automated whole-slide scanning, available in 6 slides and 200 slides versions, using both the same camera. The Vectra captures MS images from 440 to 720 nm and uses a LCTF to capture MS images with a 10 or 20 nm spectral bandwidth. As summarized in Table 2-1, the MS microscopy has been used to study both IHC and IF in a variety of diseases, but it has been predominantly used to identify and quantify cancer biomarkers in human patients using the Nuance MS system, [159], [160], [169]–[178], [161], [179]–[184], [162]–[168] and the Vectra MS system [185], [186], [195]–[204], [187], [205]–[213], [188]–[194]. The IHC and IF studies reported below cover both human and animal subjects across all organ systems [159], [160], [169]–[178], [161], [179]–[188], [162], [189]–[198], [163], [199]–[208], [164], [209]–[218], [165]–[168]. The detection of IHC biomarkers using MS microscopy is usually carried out by performing spectral unmixing of the samples, identifying the spectra of biomarkers that are similar to the spectra previously recorded in spectral libraries. An example of MSI for spectral unmixing of IHC stains for detecting biomarkers of follicular lymphoma is shown in Figure 2-7.

Table 2-1. HS histopathological dataset summary

IHC/IF Study Feature	No. (%)	Relevant Research Article References
MS Microscope		
Nuance MS System	27 (46%)	[159], [160], [169]–[178], [161], [179]–[184], [162]–[168]
Vectra MS System	28 (47%)	[185], [186], [195]–[204], [187], [205]–[213], [188]–[194]
Other/ Unspecified	2 (5%)	[214]–[218]
Molecular Markers		
IHC		[159], [160], [169]–[178], [161], [179]–[181], [183]–[189], [162], [190]–[199], [163], [200]–[209], [164], [210]–[212], [214], [215], [217], [165]–[168]
IF		[182], [213], [216]
IHC and IF		[159], [160], [192]–[198], [200], [201], [206], [168], [209]–[212], [214], [215], [218], [169], [170], [174], [176], [183], [188], [189]

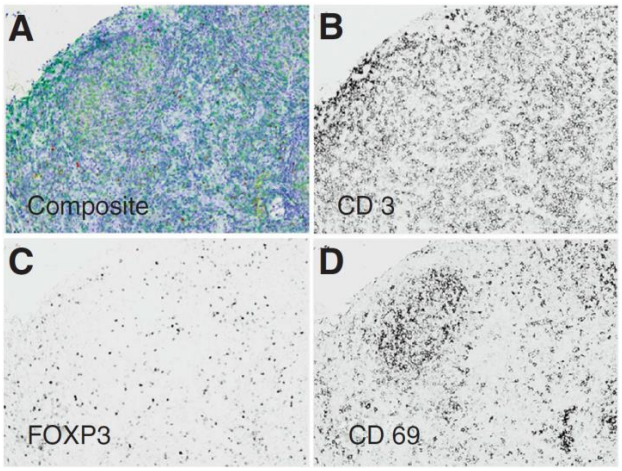

Figure 2-7: Multiple IHC markers in one tissue specimen of follicular lymphoma. MS images acquired using the Vectra system and software for spectrally unmix each IHC stain component. (a) Triplex IHC composite image. (b-d) Spectral-unmixed grayscale images of IHC for CD3, FOXP3, and CD69, respectively. Reproduced from [107]; Creative Commons BY 4.0; published by Nature (2015).

The advantages of MSI are arguably most prominent for IHC, specifically regarding clinical translation. Firstly, with respect to the equipment needed, relatively small bands with ability for high-throughput slide scanning has been somewhat standardized and is commercially available in Vectra and Nuance. This is important because in much of HSI/MSI research, the technology is still research-grade, meaning that it is customized, developmental, and potentially cumbersome to deploy. Secondly, there is a clearly defined clinical need: the interpretation of IHC staining can be variable, user dependent, and often with an ill-defined threshold of immunopositivity [219]. Next, the data analysis techniques needed to solve the problem are quite rudimentary, with spectral-unmixing as straightforward and effective algorithms for identifying immunopositivity in the literature. Finally, there is the added ability of detection and quantification of multiple IHC stains and antigens in single specimens with some preliminary success.

On the contrary, however, pathology and laboratory medicine departments have not yet widely adopted standard RGB digital pathology. Therefore, it is unlikely that even more advanced digitization equipment, whose prohibitive cost has been already described above, would be widely adopted without convincing merit. The approach would have to be tested in multiple institutions with all types of stains, imaging

parameters, and acquisition systems before it would ever be able to be clinically utilized and relied upon for routine diagnosis of immunopositivity in specimens. Therefore, though it is promising, there are numerous and substantial hurdles to the clinical translation of even this most plausible application of MSI technology.

2.3.5 Fluorescence and autofluorescence spectral imaging

Histological specimens can be excited by a specific, narrow band of light, and longer wavelengths can be imaged with MS or HS microscopy to observe the characteristic emission from the tissue. AF uses label-free specimens, allowing only endogenous fluorophores to create the measured signal, but both AF and dye-based fluorescence, such as green fluorescent protein (GFP), can be used for detecting pathologies. In the work performed by Pantalone et al., lymph node sections (5 microns thick) from unstained, frozen-section specimens were imaged with 365 nm excitation light and 375 to 750 nm emission. Lymph nodes with metastatic gastric or colon cancer showed differences from normal lymph nodes, which was reproducibly validated with multiple observers [220]. On the other hand, Constantinou et al. implemented a fluorescent slide scanner to image sections of a human colonic adenocarcinoma xenograft with excitation light of 488 nm that had detectable AF from elastin and flavin adenine dinucleotide (FAD) despite staining with a relevant antibody [221]–[223]. Similarly, Duong et al. developed a MS light-emitting diode (LED) array used to photo-irradiate tissue specimens, reducing artifactual AF. The appearance of artificial AF from formalin fixation degrades the ability to detect fluorescent signatures of interest. Therefore, fixed slices of mammalian brains were treated with the LED array with emissions from ultraviolet (UV) to infrared (IR), and successful and reproducible removal of artifact AF was observed. Treated IHC-stained slides were imaged using excitation/emission of 495 nm and 520 to 700 nm, and visible reduction of artificial AF were observed [224]. Ellingsen et al. demonstrated that using laser excitation of 800 nm, which produces 2-photon absorption at 400 nm, and capturing AF HS images with confocal microscopy allow the detection of amyloid plaque in cryo-sections of mouse brain [225], [226].

Another study performed by Leavesley et al. employed HS imaging to capture data from cryo-sections of lung tissue for resolving the fluorescence of GFP [227], [228]. Additionally, Dolloff et al. explored the application of spectral signatures of GFP in tissues for measuring autophagy [229]. The Leavesley et al. group also developed an excitation-scanning AF HS microscope imaging system for acquiring microscopic images of thin ex-vivo tissues (<1 mm), applied to rat organs [230] and human colon cancer [231], [232]. Moreover, as shown in Figure 2-8, this group applied the same technique to calculate the properties of FAD, nicotinamide adenine dinucleotide (NADH), elastin, and collagen from human colonic cancer tissues [233], [234]. In ocular diseases, Dey et al. implemented a tensor decomposition approach to detect age-related macular generation using AF with a range of excitation and emission wavelengths [235], [236]. Additionally, Habibalahi et al. used MS AF imaging to detect ocular squamous neoplasia in unstained, cover-slipped slides with multiple excitation and emission wavelengths [237].

In summary, there are various advantages and disadvantages of autofluorescence and fluorescence spectral imaging methods. The main advantage is that spectral autofluorescence can sense the concentrations of endogenous molecules in specimens using precise excitation and emission [233], [234]. For example, it can be used to assess

the concentration of NAD, FAD, collagen, and keratin, which have well-known excitation and emission signatures. One major attraction of this technique is that it works with unstained tissue specimens, so no time is lost by applying different histochemical stains, which supposes a loss of information. However, there are certain drawbacks of fluorescent spectral imaging for histopathology. Mainly, the equipment is not standardized, and most experiments are conducted with research-grade, custom-fitted microscopes that can be complex and expensive. As most tissues are comprised of numerous endogenous fluorophores, it is still unknown what wavelengths are best for excitation/emission for certain applications. Additionally, the fluorescence signals can be difficult to discern, especially if a stain or label is also used [238]. Therefore, while spectral autofluorescence imaging may seem promising, there are many challenges which currently hinder its widespread adoption.

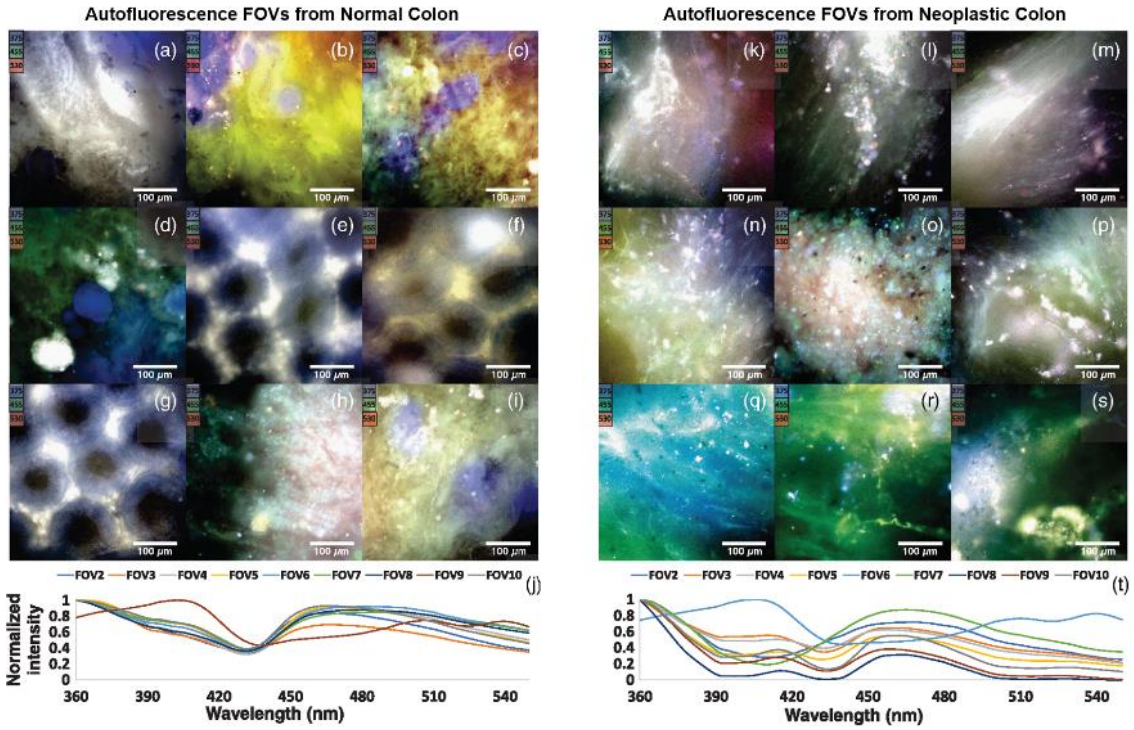

Figure 2-8: Autofluorescence from excitation-scanning hyperspectral imaging of colon. (a)–(i) Psuedocolor RGB images of FOVs from normal healthy colon. (j) Normalized intensity of autofluorescence spectral signatures from normal colon. (k)–(s) Psuedocolor RGB images of FOVs from neoplastic colon. (t) Normalized intensity of autofluorescence spectral signatures from neoplastic colon. Reproduced from [233]; Creative Commons BY 4.0; published by SPIE (2018).

2.3.6 Trends in diagnostic research for clinical routine practice

In this section, we summarize the research performed for clinical diagnosis of histological samples using HSI/MSI. A total of 84 research articles have been analyzed, and the systematic review of these manuscripts has been sorted according to the different fields within medical diagnosis, namely hematology, breast, central nervous system, gastrointestinal, genitourinary, head and neck, and skin. To conclude, we provide a summary table where the main characteristics of these research are synthesized.

2.3.6.1 Central Nervous System

HSI and MSI have been applied for aiding central nervous system (CNS) diagnosis and characterization, where these technologies have been investigated for the study of brain, nerves, and some indicators of different diseases. To investigate the normal histology of brain specimens, Bouzid *et al.* developed a customized MS microscopic system based on tunable light sources [239]. Cell nuclei segmentation was performed on a stained rat brain sample, and the results obtained were compared across 3 to 10 band MS images within the visual range. Ortega et al. investigated the use of HSI for detection of high-grade brain tumors in H&E stained slides using a customized push-broom VNIR microscopic system. Their results suggest that the differences in the spectral signatures of normal and tumor areas within the slides are sufficient to automatically provide a prediction of the diagnosis using supervised classifiers, such as SVM or ANNs [32], [36].

Nerves are also a significant constituent of the CNS. The automatic identification and quantitative morphometry of nerve fibers can complement the clinical and histopathological evaluations of injured nerves in humans. Li et al. proposed an automatic segmentation of unstained nerve fiber specimens using HSI, and relying on RGB images of stained samples as ground truth. They found HSI successfully provided morphological parameters in unstained nerves, such as myelin thickness and area [240]. Additionally, the fiber diameter, perimeter, area, and myelin thickness and area were extracted in a later study, showing agreement with the manually labeled ground truth [241]. The conclusions of these studies suggest that HSI may be a promising analysis tool for unstained nerve sections, making possible a rapid characterization of nerve fibers compared to traditional techniques. On the other hand, to investigate pathological nerve samples, spinal cord tissue samples from mice were microscopically analyzed by Vazgiouraki et al. using MSI to develop a tool for diagnosis of spinal cord myelin loss associated with multiple sclerosis. The MS microscopic system used a custom-made rotating filter wheel, and the authors concluded that the maximum difference observable between normal and demyelinated lesion areas was at 500 nm [242]. Additionally, Kopriva et al. demonstrated the contrast enhancement within an unstained sample of sciatic nerve fibers from a mouse using nonlinear unsupervised segmentation [243].

The study of samples from CNS constituents can reveal the presence or progression of different diseases. In such context, More et al. studied the use of HSI as a potential tool for early detection of amyloidopathy in Alzheimer's disease through statistical analysis of the spectral signatures from histological mouse retina and brain samples obtained with a push-broom VNIR microscopic system [244]. Diabetes can cause degeneration of the blood vessels in the eye, specifically in the retina, which can lead to blindness. To investigate this, Li et al. performed studies with control group, untreated, and treated diabetic rats to study HS analysis techniques of retina sections. The spectral signatures showed relevant differences in the range of 636 to 722 nm between the three groups, which motivates the quantitative study of the spectral differences for the evaluation of the therapeutic efficacy of drugs [245]–[248]. Finally, to investigate the detection of the Newcastle disease virus infection, which produces a neurological condition known as spongiosis, Abeysekera et al. obtained infected specimens from poultry [249]. In this work, a processing framework combined a customized feature extraction technique based on statistical indicators obtained from the MS data and supervised classifiers, SVM and LDA (Linear Discriminant Analysis), and the results demonstrated that MS data outperformed RGB data.

2.3.6.2 Head and Neck

Cancer of the head and neck (H&N) can be diverse due to the anatomical diversity of this region. In the oral cavity and upperaerodigestive tract, approximately 90% of cancers are squamous cell carcinoma (SCC) [250]. Ou-Yang et al. combined transmission and fluorescence based HSI using a push-broom system with hundreds of VNIR spectral bands for detection of oral SCC in 34 patient samples. The cell nuclei were identified in the basal-cell layer manually and a five-fold method combined spectral and morphological features to yield good performance on the testing patients [251]. In order to investigate the detection of SCC after metastasizes, Akbari et al. used SVM supervised classification for identifying human oropharyngeal SCC cancer cell line xenograft that metastasized into lung and lymph node tissues in mice [252]. The SCC detection was performed macroscopically within H&E slides without a microscope.

The thyroid gland rests in front of the trachea in the neck, and masses can often be visually observed by the patient. To assess if a thyroid mass is benign or malignant, a fine needle aspiration (FNA) biopsy is performed and microscopically investigated, and HSI/MSI may be able to increase diagnostic ability. Mansoor et al. used MS histology for detecting non-cancerous thyroid and parathyroid adenomas in FNA, using 8 cases of follicular adenoma and 7 cases of parathyroid adenoma. Papanicolaou-stained cells were manually annotated, and cell-based classification was performed with a basic neural network [253]. Thyroid cancer biopsies were also studied by Hahn et al. using 100 cases of papillary thyroid carcinoma (PTC) and benign goiter (BG), developing a classifier to segment MS images and classify each region as background, PTC, or BG with successful results [254], as shown in Figure 2-9. Additionally, the experiments were performed with different number of training cases, from 10 to 40 cases, without observing significant improvements in the classification results. However, the authors concluded that nuclear features offer improvement over nuclear and cytoplasmic regions when developing a classifier [254]. Finally, He et al. incorporated Muller matrix polarization HSI to distinguish papillary thyroid carcinoma tissues in unstained histological sections [255].

Regarding the detection of thyroid nodules in FNA smears, several works performed by Shah et al. investigated MSI analysis techniques. After manually labeling the target cells to be detected, the authors performed a watershed image segmentation of the cells [256], finding that MSI yielded significantly fewer false positives compared to conventional image analysis. Furthermore, Wu et al. performed a minimally supervised band selection and reduction method of thyroid FNA to increase contrast of RBCs using histogram-based local descriptors evaluated by three distinct metrics [257]. On the other hand, Gabriel et al. used unsupervised k-means clustering for classification of cells in FNA thyroid lesion smears suspicious for cancer [258]. Lastly, Wu et al. also presented a conditional random field model segmentation scheme for classification of different thyroid nodules. Hyperplastic nodules, PTC, and follicular neoplasm were segmented successfully, and it was concluded that MS features offered increased accuracy compared to conventional image analysis [259]–[262].

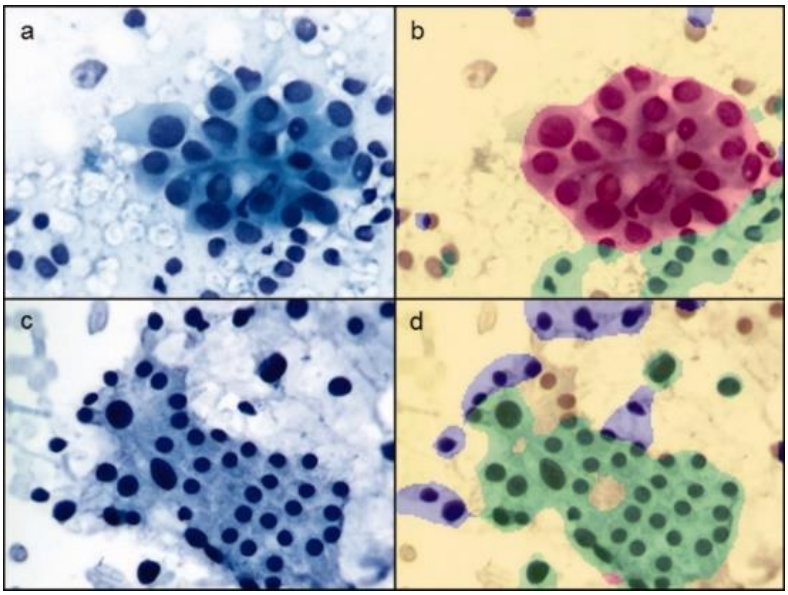

Figure 2-9: Thyroid FNA biopsies with Papanicolaou stain in RGB (left) and classification results with MSI spectral unmixing (right). (a,b) case of PTC. (c,d) case of benign goiter. Background (yellow), PTC (red), benign goiter (green), out-of-focus or crowded areas (blue). Reproduced from [254]; Creative Commons BY 4.0; published by ACS (2012).

2.3.6.3 Breast

Several approaches have been proposed in the literature for breast cancer identification in histological slides using HSI/MSI. Boucheron et al. performed a benign versus malignant nuclei classification using MSI, and compared the results with the ones obtained using 3 different synthetic RGB images generated from the MS images [263]. The authors did not find a significant boost on the classification using MSI compared to conventional RGB image processing. Nevertheless, Qi et al. also explored the utility of MSI for histological breast cancer diagnosis, finding an improvement in MSI data exploitation compared to RGB [264], [265]. Although the instrumentation of both approaches was similar, there were some differences in the experimental procedures, especially in the type of staining, the magnification and the image analysis approaches. While Boucheron et al. used H&E stained samples acquired with 40× magnifications, Qi et al. employed hematoxylin-only specimens acquired with 10× magnification. Even if the contradictory conclusions can be caused by the differences in magnification or stain, the image analysis frameworks present several differences. Both studies used supervised classifier approaches, but while Boucheron et al. used the raw spectral bands of the MS image as features for classification, Qi et al. used the features, extracted from the MS image, that were supposed to maximize the underlying differences between normal and tumor tissue samples. More experimentation should be performed in this research line to provide a more relevant discussion about the importance of the staining, magnification, and the processing framework for these applications.

Beyond the discrimination between normal and tumor tissue, more specific approaches have been recently proposed to identify ductal carcinoma in situ (DCIS) or mitotic cells within breast histological slides. In one approach, Khouj et al. proposed the detection of DCIS with HSI using two types of specimen preparations of breast biopsies: unstained and H&E-stained [266]. Using as inputs some pixels manually annotated by pathologists, a semi-supervised k-means approach was applied to both types of images, suggesting a good discrimination between normal and tumor regions even in unstained

samples. In Figure 2-10, the spectral signatures of DCIS and normal tissue samples are depicted. Additionally, mitotic cells counting is an important indicator in breast cancer grading. Roux et al. proposed a contest for detecting mitotic cells within H&E stained breast cancer specimens. In this contest, three types of datasets were released: two of them composed of conventional RGB images, and a single dataset composed of MS images. In this challenge, the detection of mitotic cells was suggested to be superior to conventional imaging approaches [267]. Nevertheless, some authors have kept working in this dataset. Malon et al. proposed a CNN framework for mitotic cell detection, but the authors claimed that more images were necessary to successfully train deep learning models [268]. Furthermore, by using different band selection methods and different supervised classifiers, such as SVM, MLP (Multilayer Perceptron), LDA, Irshad et al. [269], [270] and Lu et al. [271] were able to outperform the classification performance on this dataset stated by previous groups. Irshad et al. also found improvements in performance when exploiting the MS information compared to only the RGB information.

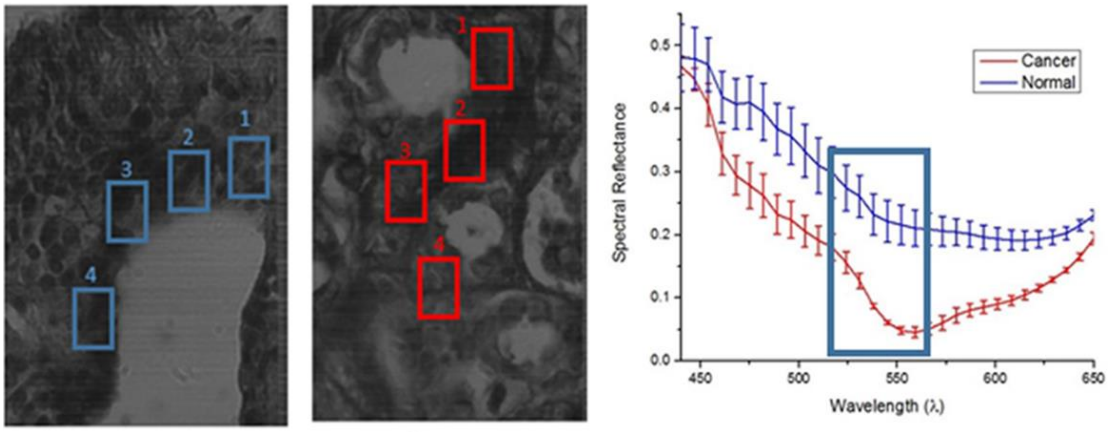

Figure 2-10: Spectral signatures of normal breast tissue (blue) and DCIS (red). Reproduced from [266]; Creative Commons BY 4.0; published by Frontiers (2018).

2.3.6.4 Gastrointestinal

The use of HSI/MSI has been also employed for gastrointestinal disease detection, where colorectal cancer is the most prominent application. In colorectal cancer diagnosis, an appropriate identification of different tissue constituents within pathological slides can help in tracking disease progression and improve the selection of an optimal treatment.

The preliminary studies for colorectal cancer detection using HSI/MSI were limited to discrimination between benign adenoma and malignant carcinoma tissues within H&E stained colon histological slides. To this end, Masood et al. employed spatial features extracted with local binary patterns, and then colonic specimens were classified using a SVM classifier [272]. Another approach, proposed by Maggioni et al., consisted of an initial segmentation of the MS images into nuclei, cytoplasm and background, and subsequently, nuclei were later classified into benign or malignant using a partial least squares (PLS) classifier based on morphological features [273]. A similar processing framework was followed by Rajpoot et al. and Masood et al., consisting of an initial segmentation of colon cell images into nuclei, cytoplasm, lumina propria and lumen, followed by the extraction of multiscale morphological features and supervised

classification. Using this common framework, Rajpoot et al. employed a SVM classifier [274], while Masood et al. employed PCA and LDA algorithms [275].

Beyond binary classification between benign and malignant colon tissues, a more detailed tissue identification scheme was followed by several authors, aiming to detect different types of cancer cells within colon samples: carcinoma, intraepithelial neoplasia, and benign hyperplasia. The results from Chaddad et al. suggested the utility of texture features of MS images for classification [276]–[278]. An example of this technique is demonstrated in Figure 2-11. Using the same dataset, Peyret et al. demonstrated that exploiting morphological features in MSI improves the performance of panchromatic images in colon tissue classification [279], [280]. Using a hybrid method which combines unsupervised clustering and supervised method using PCA and logistic regression, Nakaya et al. detected four stages of colon cancer progression from patients with ulcerative colitis, namely cancer, non-cancer, low grade dysplasia and high grade dysplasia [66]. In addition, Lao et al. used MS histology to directly quantify the optical signal obtained from in-situ hybridization (ISH) of colorectal adenocarcinoma tissues and counter-stained nuclei with methyl green. For the ISH, a small segment of microRNA was used to target cancer differentially, compared to low-grade and high-grade neoplasia and normal tissues [281]. In a later work, Chaddad et al. also revealed that the quantification of the spatial heterogeneity of the pathological tissues can help to detect the progression from benign cell proliferation to malignant lesions [282]. Also, Haj-Hassan et al. performed comparative research that demonstrated the boost in classification performance when using CNNs instead of feature-based approaches [283].

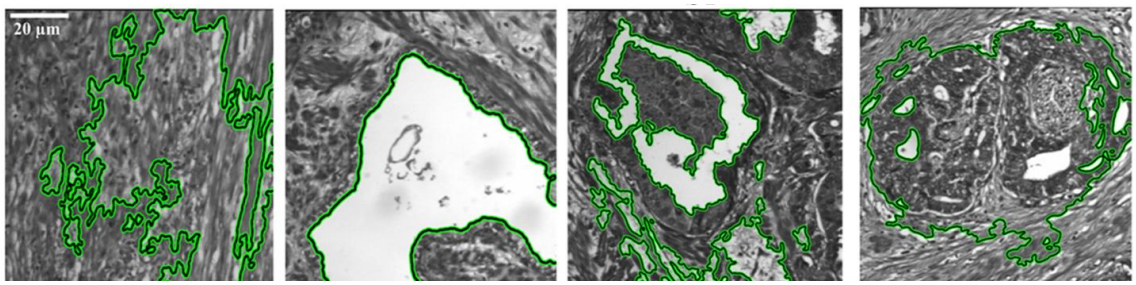

(a) (b) (c) (d)

Figure 2-11: Segmentation of four types of tissue within colon pathological slides. (a) Stroma (b) Benign hyperplasia, (c) Intraepithelial neoplasia, (d) carcinoma. Reproduced from [278]; Creative Commons BY 4.0; published by Frontiers (2018).

Recently, Awan et al. improved the research in colorectal cancer detection within H&E pathological slides with two relevant innovations: a large patient dataset ($n = 151$) and the exploitation of information within near-infrared spectral bands (beyond 1,000 nm). The authors performed the classification in two different schemes: a two-class classification (normal versus tumor) and a four-class classification (normal, tumor, hyperplastic polyp, and tubular adenoma with low-grade dysplasia). Using different types of feature extraction, band selection methods and SVM classification, the authors found that the use of a greater number of spectral bands significantly improves the discrimination of the different classes. Furthermore, they found that the use of near-infrared spectral bands improved the classification [284].

Extending beyond detection of primary colon cancers, Kopriva et al. applied MS histology for the detection of colorectal adenocarcinoma metastasis in the liver. Although the application is quite novel and the classification result was assessed with IHC staining

as ground truth, the study was limited to a single patient, thus the results cannot be considered conclusive [285].

In addition to colorectal cancer detection, only pancreas, liver, spleen, and esophagus have been explored by means of HS/MS histological analysis. The first computer-aided tool for pancreas diagnosis was motivated by the drawbacks of conventional techniques for the identification of elastic and collagen fibers within pathological slides, which usually requires the use of Verhoef's Van Gieson (EVG) staining, which is a more complex and expensive procedure compared to standard H&E staining. To deal with such limitations, Septiana et al. successfully exploited the spectral information within pancreatic ductal carcinoma H&E stained slides, showing a good capability of this technology to identify collagen and elastic fibers samples [286]. Similarly, motivated by the difficulty of distinguishing fibers and cytoplasm in H&E slides, Hashimoto et al. used a pixel-wise bag of features classification method over H&E stained liver samples by employing simultaneously spatial and spectral features for detecting five liver tissue components: nucleus, sinusoid, lymphocytes, fibers and cytoplasm. In this context, HSI was shown to outperform conventional RGB imagery [287]. Beyond the segmentation of tissue constituents, Wang et al. evaluated the ability of microscopic HSI to early detect bile duct carcinoma within H&E stained rat liver samples [288]. In this research, the authors were able to quantitatively measure the tumor areas in the biopsies at different time points through the analysis of the HS data with a feature extraction method based on the morphological watershed algorithm followed by SVM classification. On the other hand, Kopriva et al. applied a contrast enhancement technique, previously mentioned with application on sciatic nerves, for the evaluation of unstained spleen specimens [243]. Finally, Bautista et al. implemented MSI of an H&E stained slide from esophagus tissue to enhance the visualization of eosinophilic esophagitis [289]. The nuclei of eosinophils were automatically detected using spectral transmission PCA and a thresholding method. The authors concluded that this approach allowed tissue classification despite the nearby staining attributes, which facilitates a better specimen analysis compared to conventional RGB imagery.

2.3.6.5 Genitourinary

The genitourinary section comprises the organs of the urinary system, such as kidney and bladder, and both male and female reproductive organ systems. Prostate cancer is the second leading cause of cancer deaths for men [290]. It has been proposed in recent literature that histology using MS spectral analysis may improve the diagnosis of genitourinary cancers, such as cervical, prostate, ovarian, and bladder cancers.

Distinguishing between normal and cancerous cervical cells under Papanicolau stain requires the examination of texture, size, shape and contextual information of cells. For this reason, Zhang et al. proposed a method for the automatic segmentation of cervical cell nuclei that can automate the identification of the relevant cells to be examined carefully among other types of cells that are present in the specimens [291]. Another approach for identifying abnormal cervical cells that may be malignant in Papanicolau smears was implemented using cosine correlation analysis to exploit the differences of spectral signatures [292]. For the detection of cervical cancer cells in Pap smears, a segmentation method was applied to MSI based on a Gaussian mixture model (GMM) for unsupervised nuclear segmentation, and a similarity distance measurement was developed to quantity the similarity between the segmentation results and the original

data, which were able to reveal intra-spectrum information achieving high nuclear segmentation accuracy despite wavelength reduction [293]. Another cervical cancer study that employed HSI for the discrimination of normal, precancerous, and cancerous cells demonstrated that it is possible to correctly classify high-grade precancerous cells, as shown in Figure 2-12, but low-grade precancerous cells are more difficult to automatically distinguish from normal cervical cells [294]. The Mueller matrix provides a comprehensive characterization of the polarization properties of specimens, and contains information regarding optical properties of biological tissues that can be used for diagnosis. Using this principle, He et al. successfully analyzed the Muller matrix to distinguish cervical carcinoma tissues within unstained histological sections [255].

There is only a single research study in the literature that deals with HSI applied to ovarian cancer. After the extraction of a dataset carefully annotated by pathologist attending to cell morphology, Nakaya et al. suggested HSI as a suitable technology to differentiate between normal and cancer cells by using both supervised and unsupervised techniques [66].

For prostate cancer detection, several groups have implemented MSI for H&E stained prostate cancer pathological samples. Tahir et al. successfully performed a round-robin Tabu search algorithm along with a nearest neighbor classification method for classifying prostate cancer, benign prostatic hyperplasia, prostatic intraepithelial neoplasia, and normal stroma in MS histological images of H&E stained prostate specimens from nearly 600 cases [280], [295]–[297]. Additionally, Khelifi et al. worked in the same task for performing a spatial-spectral feature extraction approach and SVM classification for the same four types of prostate H&E MS images [298]. Akbari et al. used spectral feature based SVM for detection of human prostate cancer in H&E slides imaged macroscopically [62]. On the other hand, for automated detection of glandular structures and nuclei in prostate cancer H&E slides using MSI, Zarei et al. proposed a method combining the PCA algorithm, to generate an artificial RGB image, and the k-means unsupervised segmentation [78].

With the goal of early detection of bladder cancers, MS examination of urine samples could lead to improved diagnosis and follow-up. Angeletti et al. proposed a genetic algorithm combining spatial features and MS spectral analysis of Papanicolau-stained cells in urine specimens with promising sensitivity and specificity values for detecting bladder cancer cells in urine specimens [299].

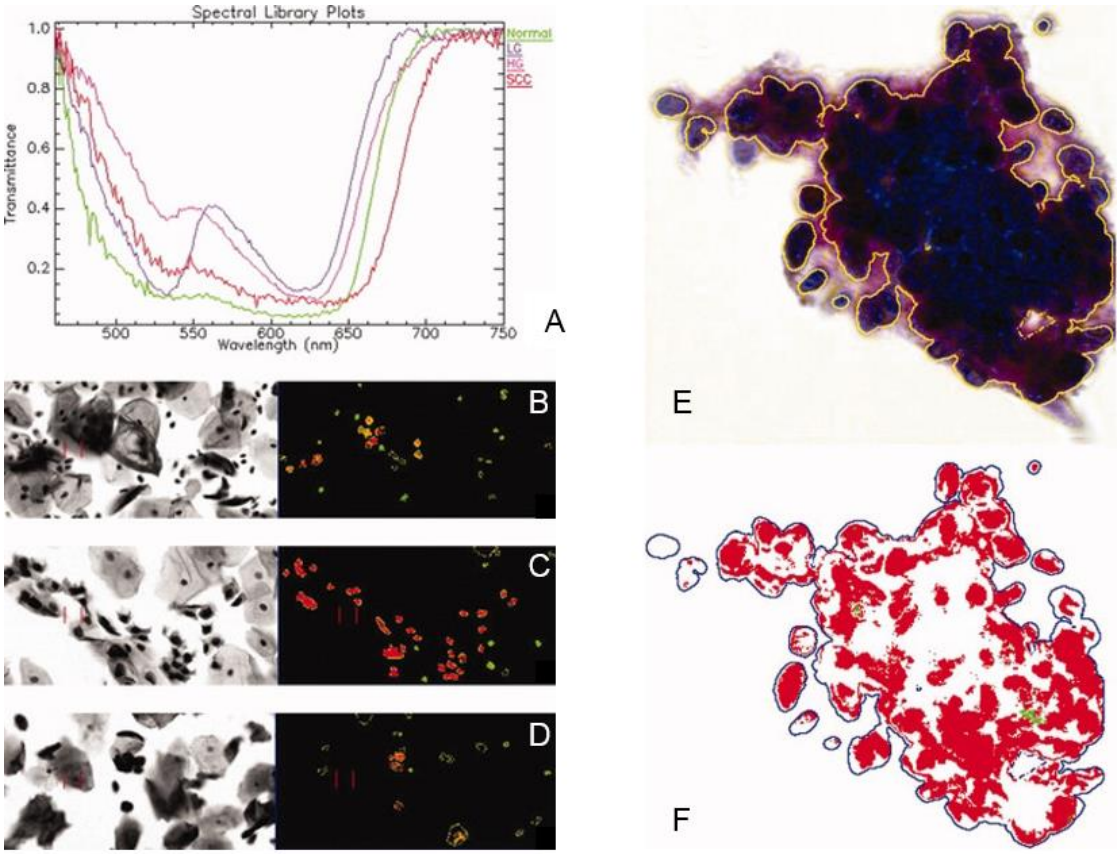

Figure 2-12: (a) Spectral plots of Papanicolaou-stained cells from cervical Pap smear: normal, low-grade (LG), high-grade (HG) and squamous cell carcinoma (SCC). (b-d) Classified HS images of normal (green), LG (yellow), and HG/SCC (red) cells. (e-f) RGB image with annotation of cervical SCC (e) and HS results of the automatically extracted and classified HG/SCC nuclei (f). Reproduced from [294]; Creative Commons BY 4.0; published by ACS (2008).

2.3.6.6 Hematology

For the diagnosis of a wide variety of diseases, blood sample examinations are usually performed by skilled hematologists through microscopic analysis and evaluation of blood smears. Although automatic hematological analyzers are available to perform this task, pure optical technologies and imaging processing tools are shown as cost-effective alternatives to this end. Furthermore, hematological analyzers are not able to consider information about cell morphology. To aid researchers and physicians in the analysis of blood samples, HS/MS technologies are proposed as an alternative to conventional RGB imagery, whose main limitations are the low capabilities to handle both the uneven staining of samples and the differences in the instrumentation used to digitize the samples [141].

In the field of RBC analysis, Li et al. evaluated the feasibility of exploiting HSI for RBC counting. After conducting the RBC counting using uniquely spatial or spectral features of blood cells, the authors found an improvement in the under-counting and over-counting rates when they performed the image analysis using both types of features together [90], [300]. Some authors have also proposed HSI as a promising technology for white blood cells (WBCs) segmentation. After the careful annotation of nucleus, cytoplasm, erythrocytes and background within blood smears specimens by pathologists, different authors have demonstrated a successful differentiation between the

aforementioned cell parts based only in their spectral profiles. While Guo et al. employed the SVM classifier [301], Guan et al. performed the same task with SID (Spectral Information Divergence), k-means and SAM (Spectral Angle Mapper) algorithms [302]. Besides the identification of blood cells, morphological characterization is further important for diagnosis, especially in WBCs, which present a complex taxonomy with more than 20 subtypes. For this reason, Li et al. proposed a method to automatically extract morphological features of leukocytes from blood smear samples by using HSI. After leukocyte segmentation, morphological parameters such as cytoplasm area, nuclear area, perimeter, nuclear ratio, form factor, and solidity were extracted from the segmented images [79]. Additionally, due to the complexity of contents of bone marrow smears, the identification of WBCs is even more challenging in such type of samples. Wu et al. presented an approach to identify WBCs within bone marrow samples, showing the capabilities of this technology to identify WBCs in both high and low magnifications (100× and 10×) [303]. Finally, another interesting approach in the context of blood cell detection was proposed by Verebes et al., who proposed an approach to analyze blood samples without prior sample preparation, i.e. with no requirement of stains. The authors suggest the capability of darkfield HS microscopy to identify different types of red blood cells (ordinary RBCs, stacked erythrocytes), WBCs, and neutrophils within unstained samples [304], which can lead in a reduction in the cost and time required for blood sample preparations.

In addition to identification and examination of RBCs and WBCs, HS/MS analysis of blood samples has been also used for the identification of diseases. In leukemia analysis, Li et al. were able to identify leukemic cells in blood smears based only on their spectral differences from RBCs [305]. Additionally, Wang et al. proposed a method to differentiate between lymphoblasts and lymphocytes, which is an important task in diagnosis of acute lymphoblastic leukemia (ALL) [89]. Due to the high similarity between lymphoblasts and lymphocytes, the examination of these samples is challenging by both visual examination and RGB analysis. The authors employed a neural network for classification, using three types of inputs: spatial features, spectral features and spatial-spectral features. The results of this study suggest that the exploitation of both the spatial and the spectral features significantly improves the quality of the classification. Figure 2-13 shows some RGB images of lymphoblasts and lymphocytes, and the classification maps extracted from this study.

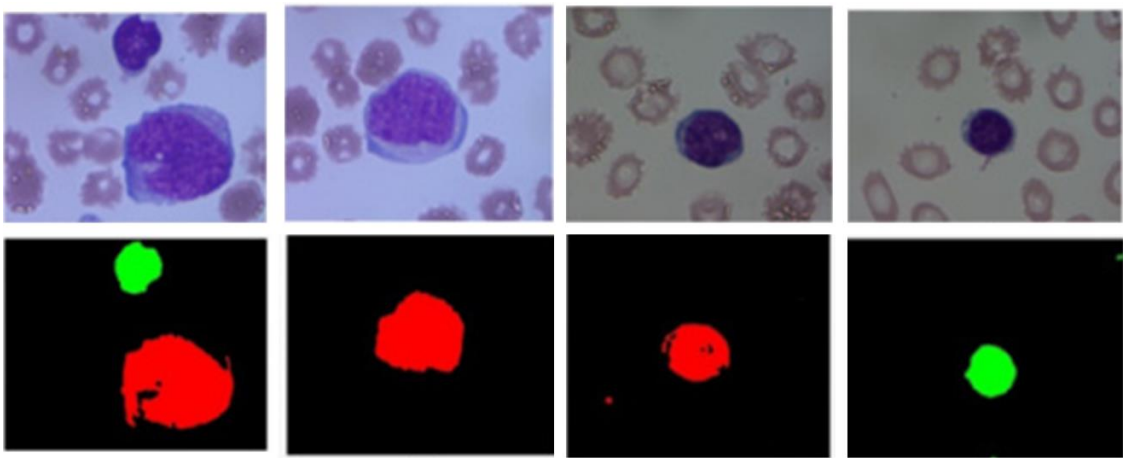

Figure 2-13: Differentiation between lymphoblast and lymphocytes. Top: conventional microscope images. Bottom: Identification of lymphoblast (red) and lymphocytes (green). Reproduced from [89]; Creative Commons BY 4.0; published by OSA (2017).

In another application, some authors proposed the use of MSI to identify malaria in blood smear samples by using a multi-mode LED illuminated microscope. These authors performed a PCA transformation of normal blood smears and their counterpart infected by malaria. Their findings indicate that the parasite presents differences in spectra compared to normal blood samples in the spectral range from 590 to 700 nm, making the identification of malaria possible using such information. The use of MSI can save time in malaria detection compared to traditional methods [306]–[309].

Finally, the use of HS/MS analysis of blood samples is not limited to cell examination. Qian et al. presented a proof-of-concept system for the visualization enhancement of vessels within histological slides, which consisted in the application of a spectral correction technique to the MS image [310]. This pre-processing algorithm showed a reduction in the variance of the spectral signatures of the specimen, and it was shown as a promising method to be applied prior to subsequent segmentation and classification of the cells within histological samples.

2.3.6.7 Skin

Mammalian skin is comprised of epithelial cells forming a stratified squamous epithelium above an inner layer that contains connective tissue, glands, and vessels. Normal histological skin samples from rats were studied by Li et al. to enhance the visualization of different microanatomical skin structures. Different combinations of wavelengths were used to generate false color images for visual inspection, and 3D surface views of skin sections were generated by combining spectral and textural information from HS data [311]. Normal skin also contains melanin to protect from UV exposure, and its quantification can be of clinical utility. Melanin identification was performed in H&E sections directly using MSI by Kalleberg et al., comparing the results obtained with the traditional gold standard Fontana Masson (FM) silver-staining, which directly targets melanin [312]. It was discovered that spectral unmixing of MSI can identify melanin in H&E sections directly and more accurately, without the need of an additional FM staining. Additionally, spectrally separated MSI of FM stains allowed even more sensitive identification of melanin, which led the authors to conclude that FM staining was not required and that MSI would yield faster and more accurate results [312]. The ability of HSI for melanin detection was further illustrated by Wilson et al. in unstained specimens of melanocytic lesions in the skin (cutaneous) and the eye (conjunctival) using PCA and false-color representations [76].

Melanoma is a malignant form of skin cancer arising in melanin-producing melanocytes. In this field, Gaudi et al. used a HS push-broom microscope to evaluate over 100 H&E sections from different patients with melanocytic lesions. A clustering method using spectral Euclidean distance classified the data into 12 clinically-relevant spectral classes that were correlated with benign and malignant melanocytic lesions [313]. Melanocytic skin cancer has been studied using HSI microscopic systems to capture H&E pathological samples for the detection of normal skin, benign nevus, and malignant melanoma samples, taking into account the minimum correlation coefficient between their spectra [314]. This study also found that the use of higher magnifications can reveal more spectral differences between the diverse samples than lower magnifications, due to the ability to observe intracellular and extracellular components. On a cellular level, Wang et al. proposed a custom spatial-spectral SVM classification

method for the analysis of H&E skin samples to detect malignant melanoma cells from normal melanocytes with high specificity and sensitivity [315].

2.3.6.8 Summary table

In Table 2-2, we show a summary of the main applications of HSI/MSI for diagnostic research targeting clinical histological practice, which is intended to provide readers with a quick overview of the current usage of HSI/MSI in histopathological diagnosis assessment. The table is organized by different fields, following the same structure previously presented for this section. The information of the table is related to the number of patients involved in the study, the magnification used for specimen's acquisition, the type of staining and the details on the instrumentation, and the image processing techniques used for the analysis of data. Specifically, the instrumentation details consist of the type of technology of the HS/MS camera, the spectral range, the spatial resolution, and the number of bands. As can be observed, not every field in the table was available for every article. For this reason, and following the PRISMA recommendations, we emailed every author whose information was missing. In the cases that we got a reply with the information, the table was updated.

2.3.6.9 Concluding remarks

In this section, we summarize the current status of the usage of HSI/MSI technologies for histopathological analysis and diagnosis. According to the results depicted in the analyzed research articles, it can be concluded that HSI/MSI technologies are able to succeed in histological disease detection. The range of applications which make use of HSI/MSI diagnosis research within pathological slides is wide, and mostly focused on the detection of cancer. There are some positive outcomes on the use of HSI/MSI technologies for histological analysis. First, researchers have found differences in spectral information between diseased and normal tissue to be discriminant enough to detect some illnesses (e.g. [32], [36], [244] or [301], among others). These results suggest that the spectral signatures of tissues can be a complementary source of information for disease detection in histopathology, where the disease identification is commonly based on the morphological analysis of tissue components. Second, the advantages of HSI/MSI compared to conventional RGB digitized slides have been reported in various clinical research applications [249], [264], [265], [271], [287], [289]. Nevertheless, in the computational pathology community, there is a need to further quantify such improvements in disease detection compared to conventional RGB digitized slides. Additionally, most investigations on the use of HSI/MSI technologies were performed in applications where conventional RGB digital pathology has been proven to be successful. In order to really prove the utility of HSI/MSI, future investigations should be highly focused in diseases in which current diagnostic procedures are not effective, thus allowing the benefit of HSI/MSI to be demonstrated. Third, some researchers suggest the utility of the analysis of unstained samples [76], [243], [255], [266], [306]–[309]. In most current state-of-art research using HSI/MSI, histological dyes are used for the observation of samples. Such dyes modify the spectral response of tissue to light, and thus transform the spectral information of the tissue. For this reason, the future HSI/MSI analysis should also be focused on the exploitation of the spectral information of tissues with no external dyes. Finally, the real capabilities of HSI/MSI in diagnostic detection are likely hidden by the broad options for image processing information

retrieval techniques. In most of the research carried out at this moment, different processing techniques are used with successful results.

There may be some challenges to the adoption of MSI/HSI for digital pathology in a clinical setting. Firstly, the spectral acquisition equipment is unstandardized, complex, research-grade, and expensive. The imaging technology is inconsistent between research groups. It is impossible at the moment to know which imaging parameters, wavelengths, or spectral resolution are best for each application. The experimental results reported in the literature are difficult to compare since each of them are usually performed using a single HS camera with data from a single institution. Additionally, the CAD (computer-aided diagnosis) and analysis algorithms are often different. Most CAD methods also use custom software, which is not suitable for easy clinical deployment. It is difficult to determine if experiments are performed objectively or contain bias. Additionally, publication bias may be present in the literature, which yields only positive results, and the negative results remain unpublished. Moreover, it is extremely difficult to extrapolate the results obtained in one particular diagnostic application in one specific organ system to another application/organ, mainly due to the heterogeneity of the spectral properties of the different tissues. In this sense, to generalize and standardize a methodology capable of achieving accurate results for several different frameworks, more research is required, exploring several organ systems and applications, performed in large experiments, employing a wide spectral range HS system. Finally, one major challenge that cannot be ignored is that storage size of data is greater than RGB digital pathology, which is already a challenge with no straightforward solution. The use of HSI/MSI for digital and computational pathology is promising and is still in its infancy, requiring more investigation and creative solutions to the problems listed above for clinical translation.

Table 2-2. Summary table of applications of HSI/MSI for diagnostic research targeting clinical histological practice.

Application	#Pat.	Stain	Mag.	HSI Technique	Spectral Range (nm)	#B	Spatial Resolution	Objective	Method	Ref. (s)
Central Nervous System										
Normal Brain*	1*	H&E†	10×†	TLS	400-780	3-10	500×500†	Segmentation	Expectation-maximization/Ellipse fitting	[239]
Brain Ca.	10	H&E	5×	Push-broom	419-768	159	1004×600	Classification	SVM/RF/MLP	[32], [36]
Nerve fiber	20*†	Unstained	20× 100×	AOTF	550-1000	80	1600×1200	Segmentation	Prewitt/Canny/ISAM/SAM/Custom spatial-spectral method	[240], [241]
Autoimmune Encephalomyelitis from Multiple Sclerosis*	20*	Myelin Basic Protein (MBP immunostaining)	5× 10×	Filter Wheel	400-1200	13 10	2560×1920	Visualization	SAM	[242]
Sciatic nerve*	N.A.*	Unstained	400×	Filter Wheel	465-620	4	N.A.	Visualization	rth-order rational variety mapping (RVM)	[243]
Early detection of amyloidopathy in Alzheimer's disease*	6*	DAPI	40×	Push-broom	400-1000	467	696×520†	Statistical analysis	SAM	[244]
Retina *	40* 34*	H	40×	Push-broom	400-800	240	640×300 460×300	Visualization	Normalized index/SAM	[245]–[248]
Spongiosis*	10*	H&E	20×	LCTF	400-720	33	1392×1040	Feature extraction/ Classification	Custom FE/SVM/SLDA	[249]
Head and Neck										
Oral Ca.	34	H&E	20×	Push-broom	400-1000	215	1000×1000	Classification	Spectral and nuclear morphology	[251]
Oropharynx Ca. Metastasis*	19 Mice	H&E	Macro	LCTF	450-950	101	1392×1040	Classification	Spectral SVM	[252]
Thyroid & Parathyroid	15	Pap	60×	LCTF	420-700	29	1392×1040	Classification	ANN	[253]
Thyroid Ca.	100	Pap	60×	LCTF	400-700	16	1392×1040	Unmixing	Cell spectra	[254]
Thyroid Ca.	N.A.	Unstained	N.A.	LCTF	500-680	7	1392×1040	Visualization	Muller matrix	[255]
Thyroid Ca.	24	Pap	40×	TLS	400-700	31	768×512	Segmentation	Conditional Random Field/Watershed/Band selection/k-Means	[256]–[262]
Breast										
Breast Ca.	N.A.†	H&E	40×	LCTF	420-700	29	768×896	Classification	MLi/MED/SAM/FLDA/SVM	[263]
Breast Ca.	N.A.	H	10×	LCTF	420-720	31	1392×1040	Classification	Adaboost/SVM	[264], [265]
Breast Ca.	10	H&E,Unstained	40×	Snapshot	461-641	31	443×313	Clustering	K-Means	[266]
Breast Ca., Cell Mitotis	5	H&E	40×	N.A.	410-750	10	1360×1360	Feature extraction/ Classification	Spectra differentiation/ mRMR/CNN/ MLP/SVM/DT/ LDA/Bayes/ SVM	[267]–[271]

Application	#Pat.	Stain	Mag.	HSI Technique	Spectral Range (nm)	#B	Spatial Resolution	Objective	Method	Ref. (s)
Gastrointestinal										
Colon Ca.	32 59	H&E	40×	TLS	440-700	128	491×652	Classification	LBP/ LDA/SVM/PLS	[272], [273]
Colon Ca.	N.A.	H&E	40×	TLS	450-640 450-850	20 28	1024×1024	Feature extraction/ Segmentation/ Classification	Multiscale morphological FE/ k-Means/SVM	[274], [275]
Colon Ca.	30	H&E	40×	LCTF	500-650	16	512×512	Feature extraction, Classification, Segmentation	Morphological Texture/FE/PCA/Wavelet/SVM/RF/ Active Contour	[276]–[280], [282], [283]
Ulcerative colitis	10	H&E	40×	Push-broom	350-1050	141	640×480	Clustering, Classification	Ward's method/LR	[66]
Colon Ca.	31	NBT/BCIP & Methyl Green	50×	LCTF	420-720	31	1392×1042	Visualization	ISH signal intensity	[281]
Colon Ca.	151	H&E	10×	LCTF	470-710 1150-1650	13 26	256×320	Feature extraction, Classification	SVM/Ensemble	[284]
Colon Ca. Metastasis	1	H&E	20×	Volume Bragg Tunable Filter	450-800	351	1392×1040	Classification	Unmixing/SAM	[285]
Pancreatic Ca.	3†	H&E	20×†	Push-broom	420- 720	61	752×480	Classification	LDA	[286]
Liver	N.A.	H&E	40×	Push-broom	420-720	61	752×480	Classification	Spatial-spectral Bag of Features	[287]
Liver Ca.	10*	H&E	4×†	AOTF	550-1000	60	1280×1024	Feature extraction/ Classification	Morphological/ Watershed/SVM	[288]
Normal Spleen*	N.A.*	Unstained	400×	Filter Wheel	465-620	4	N.A.	Visualization	rth-order rational variety mapping (RVM)	[243]
Esoinphilic esaphagitis	1	H&E	20×	LCTF	400-720	55	1034×1050	Segmentation	Eosophil segmentation/PCA/Thresholding	[289]
Genitourinary										
Cervical Ca.	300	Pap	20×	LCTF	400-720	33	1024×1024	Segmentation	Cosine correlation	[291], [292]
Cervical Ca.	100	Pap	40×	AOTF	460-750	30	512×640	Segmentation	GMM	[293]
Cervical Ca.	8	Pap H&E	40×	Push-broom	400-1000	600	400×800	Classification	Normalized index	[294]
Cervix Ca.	N.A.	Unstained	N.A.	LCTF	500-680	7	1392×1040	Visualization	Muller matrix	[255]
Ovarian Ca.	10	H&E	40×	Push-broom†	350-1050	141	640×480†	Clustering	PCA/Logistic regression	[66]
Prostate Ca.	592 624	H&E	40×	LCTF	400-720 500-650	65 16	128×128	Classification	Tabu search/ kNN/Spatial-spectral SVM	[280], [295]–[298]
Prostate Ca.	4	H&E	Macro	LCTF	450-950	101	1392×1040	Classification	Spectral SVM	[62]
Prostate Ca.	67†	H&E	20×	LCTF	420-720	16	2048×2048	Clustering	PCA/k-Means	[78]
Bladder Ca.	17	Pap	40×	LCTF	420-700	29	896×768	Classification	GA	[299]

Application	#Pat.	Stain	Mag.	HSI Technique	Spectral Range (nm)	#B	Spatial Resolution	Objective	Method	Ref. (s)
Hematology										
RBC	N.A.	Giemsa	100×	AOTF	550-1000	80	1024×1024	Segmentation	Custom spatial spectral	[90], [300]
WBC	N.A.	N.A.	100×	LCTF	400-720	33	640×480	Classification	SMO/SVM	[301]
WBC	N.A.	Wright	N.A.	AOTF	550-950	80	N.A.	Segmentation	SID/k-Means/SAM	[302]
WBC	N.A.	Giemsa	100×	AOTF	550-1000	80	1024×1024	Segmentation	Custom spatial-spectral/PCA/k-Means/FCM	[79]
WBC, bone marrow	N.A.	N.A.	10× 100×	LCTF	400-700	31	1024×1024	Classification	Hierarchical tree	[303]
RBC, WBC	27	Unstained	100×	Push-broom	400-1000	240	N.A.	Classification	Unmixing/SAM	[304]
Leukemia	56†	Giemsa†	100×†	Push-broom	400-800	240	460×300	Segmentation	SAM	[305]
Leukemia	16	Giemsa	100×	AOTF	550-1000	70	1280×1024	Classification	Custom spatial-spectral classifier	[89]
Malaria	1	Unstained	15×	TLS	375-940 375-1100	13 14	2592×1944 640×480	Segmentation	PCA/Cluster analysis/ Kriging	[306]–[309]
Blood vessels	30†	H&E†	40×	AOTF	400-700	80	1024×1024 †	Visualization	Continuum removal algorithm	[310]
Skin										
Normal Skin*	10 Rats	H&E	20× 40×	AOTF	550-1000	80	1024×1024	Visualization	False RGBs/Spectral clustering	[311]
Melanin	24†	H&E, FM	20×	LCTF	420-720	16	1392×1040	Visualization	Spectral Unmixing	[312]
Melanoma	15	Unstained	10×, 20×, 40×†	Push-broom	460-900	332†	700×700†	Visualization	PCA	[76]
Melanocytic Ca.	102	H&E	40×	Push-broom	385-880	496	240×N.A.	Clustering	ISODATA	[313]
Skin Ca.	N.A.	H&E	2.5× 10× 63×	Push-broom	410-750	640	240×N.A.	Classification	Spectral Cross-correlation	[314]
Melanoma	49	H&E	20×	AOTF	550-1000	60	1280×1024	Classification	Spectral-spatial SVM	[315]

N.A.: Information not available; Ca.: Cancer; Pat.: Patients; B: Bands; Mag.: Magnification.

†: Information provided by the authors, not available in the manuscript.

*: Animal study.

A list of acronyms is provided at the beginning of the dissertation.

2.4 Discussion and conclusions

In this chapter, we have provided a brief introduction about the most common concepts regarding HSI. First, we have presented the main characteristics of the HS technology, with particular emphasis on the most important concepts about the instrumentation. Besides, we have surveyed the most common approaches for HSI processing in the medical field. Second, we have provided an introduction on the main motivations of the usage of HSI for medical applications. Finally, the most relevant aspects of HSI/MSI for the analysis of histopathological specimens have been systematically reviewed. To this end, we employed the PRISMA guidelines for systematic reviews to provide a rationale about the motivations of performing this review and details about how the review process was performed. We have analyzed the manuscripts selected for this review in four major categories: digital staining and color correction, autofluorescence, IHC, and histology clinical diagnostic research. The main goal of this systematic review has been to provide readers with the current context of the applications of HSI/MSI in this field and to illustrate the main limitations and challenges for future research.

Finally, the main focus of this chapter details clinical diagnosis research applications of HSI/MSI in histopathology. Given the research works summarized, we conclude that HSI/MSI is useful for the identification of diverse diseases and tissues, where cancer detection is the most common application. The instrumentation strongly varies among different studies. It is not clear which instrumentation parameters are more appropriate for HSI/MSI histological analysis. The most important challenge is to determine which spectral range is more informative. Regarding the spectral range, most of the studies covered in this systematic review are restricted to wavelengths below 1,000 nm. The exception is the research performed by Awan et al., whose results suggest an improvement in performance of the classification of colon cancer tissues when information from NIR bands was also incorporated [284]. Thus, the exploration of the performance of the spectral range beyond 1,000 nm is a challenge in HSI/MSI. Additionally, for the full exploitation of the spectral range, it should be taken into account how different stains limit the spectral range of the sample [316]. Furthermore, there are substantial differences among data analysis methods across the different studies. Most approaches target automated classification of different types of tissues or diseases using machine learning techniques, and others deal with image visualization enhancement of different tissue constituents. In order to reach an agreement about an adequate common framework for HSI/MSI data processing for histopathological applications, there is a need for publicly available datasets, where a fair comparison across different methods could be performed. In this context, to allow a fair comparison between different studies, we strongly recommend future authors in this field to report in their manuscripts the details regarding the number of patients involved in the study, the type of staining, the magnification, and details of the instrumentation, namely spectral range, spectral resolution, and number of bands. Most importantly, the experimental design of the papers should minimize bias, especially in machine learning approaches, i.e. performing data partitions with independent patient data for testing.

Although promising results have been obtained using HSI/MSI technology for histopathological diagnosis, there are still challenges to be investigated. There are several

studies that point out that HSI/MSI are able to outperform standard RGB for disease detection [249], [264], [265], [271], [287], [289]. However, HSI/MSI technologies are associated with unique challenges, such as large data storage, expensive processing requirements, and whole-slide-imaging acquisition. These problems are already solved in conventional RGB digitize slides, where obstacles related to WSI and image processing are well-established. For this reason, to state if HSI/MSI has a future in computational pathology, more performance comparisons should be carried out to definitively demonstrate the suggested superiority of HSI/MSI for disease detection.

In conclusion, in this chapter we have analyzed the current status of HSI/MSI for histopathological analysis of biomedical samples. On the one hand, in the field of IHC research, the use of MSI is currently established as a technology demonstrated to be useful for evaluation of biomarkers. On the other hand, the results pointed out by researchers for autofluorescence and for histopathology diagnostic research were demonstrated to be promising, but these technologies still present several challenges. In the field of color correction, HSI/MSI is presented as a suitable technology for dealing with the inter-laboratory variability of digitized slides. Finally, digital staining of samples is presented as one of the most promising future trends for HSI/MSI in histological analysis, either for the analysis samples with no requirement of physical stain, or to digitally improve the visualization of tissue structures within stained slides that are difficult to identify with conventional stains. HSI/MSI should be further investigated to be proven as an effective and accurate alternative to conventional technologies for digital and computational pathology.

Chapter 3: Microscopic instrumentation and acquisition of hyperspectral data

Prior to capture the histological HS images which will be used in this PhD, the HS instrumentation should be properly characterized, and an adequate methodology to capture high quality images should be analyzed.

In this chapter, we present the details about the HS instrumentation that has been used during this PhD dissertation. The chapter is organized as follows. First, the key concepts related with HS acquisition systems are reviewed, highlighting how each element of the instrumentation influences the overall system response. Second, we describe the instrumentation used in this PhD dissertation. Such instrumentation consists of a microscope and a push-broom HS camera. Finally, we propose a methodology to correctly set up a push-broom microscope to capture high-quality images.

This work is presented as a solution to the limitations imposed by the push-broom scanners to be properly combined with HS microscope imaging system. Using push-broom cameras in microscopes imposes to perform an accurate spatial scanning of the sample to collect the full HS image. In this chapter, we discuss how the dynamic range maximization, the focusing, the alignment and the adequate speed determination affect the overall quality of the images. Finally, we present some examples of HS data showing the most common defects that usually appear when capturing HS images using a push-broom camera, and a set of images acquired from real microscopic samples.

3.1 Hyperspectral/multispectral instrumentation overview

In this section, we provide a brief description of HS systems and we discuss how each element of the instrumentation affects to the spectral response, the spatial resolution and the dynamic range of the acquisition system.

There are three key elements in every HS acquisition system: a lens, an electronic sensor and a light source. The lens is intended to focus the scene, while the sensor records the HS data. The light is devoted to illuminate the scene. Depending on the HS technology, a fourth element will perform the EMS sampling. On the one hand, spectral-scanning systems make use of an optical element that filters the incoming light at discrete wavelengths, being able to collect the whole spatial information for such wavelength. The

central wavelength of such optical filters can be tuned both mechanically (filter wheels) or electronically (AOTF and LCTF) to generate an HS cube. On the other hand, push-broom systems make use of optical grating elements able to perform the diffraction of light across a narrow line. In this sense, the complete spectral dimension and a single spatial dimension are captured simultaneously. In order to obtain an HS cube, push-broom systems require to perform a spatial scanning across the remaining spatial dimension. In this sense, the complete spectral dimension and a single spatial dimension are captured simultaneously. In order to obtain an HS cube, push-broom systems require to perform a spatial scanning across the remaining spatial dimension.

Each element of the acquisition system contributes to its overall **spectral response**. Firstly, the sensor that samples the information has an intrinsic spectral response due to its quantum efficiency, which is wavelength-dependent. In conventional greyscale or RGB high-performance imaging systems, Silicon-based sensors are widely employed. Nevertheless, Silicon shows poor sensitivity above 1100 nm. For this reason, other detectors have to be used for measurements beyond the IR range of the spectrum. In HS imagery, the most common semiconductors used to record data within the IR are Indium Gallium Arsenide (InGaAs) or Mercury Cadmium Telluride (MCT), which are sensitive up to 2500 nm approximately [124] . Although this type of sensors is used to record the IR spectrum, they present some drawbacks such as a limited number of pixels and higher shot noise than Silicon-based sensors. Due to this reason, cooling systems are typically coupled to HS sensors to alleviate such noise. Secondly, light transmission through the lens is also wavelength-dependent. For this reason, specific lens with fixed transmission spectra have to be used in order to avoid spectral losses [317]. Finally, the overall spectral response of the HS acquisition setup relies on spectral shape of the light source. Typically halogen or Xenon-based light sources are employed to this end [318].

In addition, the **spatial resolution** is influenced by both the lens and the sensor. On the one hand, the optical properties of the lens determine the Field of View (FOV) of the optical system, which is usually expressed as an angle. Furthermore, the size of the final image depends on the distance between the lens and the object to be captured. Besides the FOV, the optical properties of the lens also limit the size of the minimum object that can be captured, i.e. the resolving power of the lens. On the other hand, the number of pixels that the sensor is able to acquire will determine the spatial resolution of the overall acquisition system. While Silicon sensors are characterized by high pixel density, other sensor technologies (such as InGaAs or MCT) are restricted to a lower pixel density. This means that IR measurements (above 1000 nm) are restricted in the sensor size, worsening the spatial resolution in such spectral range. Besides, in push-broom systems the spatial resolution in the scanning direction is ultimately determined by the mechanical resolution of the linear movement mechanism that performs the scan.

Finally, the **dynamic range** is defined as the difference between the maximum and the minimum values that bounds the measurements capabilities of an instrument [319]. In this context, the dynamic range of an HS camera is determined by the radiometric resolution of the sensor, i.e. it is directly related to the number of bits used for the image digitalization. Nevertheless, in an HS acquisition system the maximization of the dynamic range does not exclusively depend on the bit depth of the sensor. The light measured by the sensor depends on two main factors: the power of the incoming light and the exposure time. The illumination power may be constrained by each application, existing situations where is not possible to just increase the light power to maximize the

effective dynamic range of a measurement, i.e. daylight condition measurements. The exposure time (also known as the integration period) is the fraction of time while the sensor is collecting light. For this reason, the quantity of light measured by the sensor is ultimately determined by the integration time.

For the previously mentioned reasons, HS images are highly biased by both the instrumentation and the environmental conditions. In order to remove the influence of the acquisition system in the measurements, a calibration procedure is usually followed. The calibration of HS images will be covered latter in this chapter.

3.1.1 Further notions about push-broom measurements

The HS cameras used in this PhD dissertation are push-broom cameras. For this reason, in this section we provide some insights about some concepts regarding this type of HS cameras. As mentioned before, push-broom cameras are able to acquire a 2-D frame containing both the spatial and the spectral information of a narrow line across the lens FOV.

In order to acquire a HS cube, a scanning procedure where a relative motion between the HS sensor and the targeted sample is required. An appropriate scanning procedure involves appropriate values for the exposure time, the scanning speed, and the pixel size. The pixel size, also known as Instantaneous FOV (IFOV) is the width of the push-broom frame. As already mentioned, this value depends on both the lens of the optical system and the sensor size. In order to capture an undistorted image from the scene, the optimal speed for the scanning platform should be configured as the quotient between the pixel size and the exposure time (Equation (1)). If the scanning speed is not properly configured, the resulting image will be affected by morphological deformations.

$$\text{Speed} = \frac{\text{Pixel Size}}{\text{Exposure Time}} \tag{1}$$

In Figure 3-1 we present a graphical representation of a push-broom scan. At each instant, a push-broom frame (namely Y-lambda image) is captured, and the scanning is performed in the X direction. In this chapter, we make an extensive use of Y-lambda images, so we provide some insights about such images.

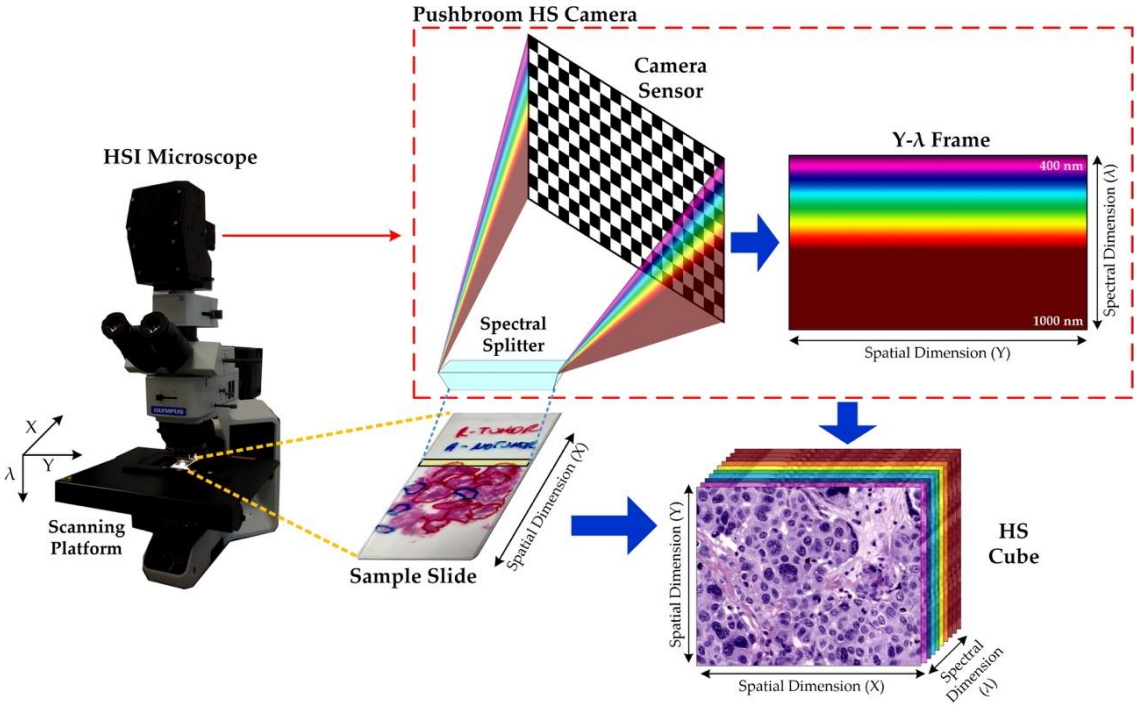

Figure 3-1: Graphical example of the generation of a push-broom HS cube.

A Y-lambda image is a conventional 2-D grayscale image, where the Y-axis represents the spectral dimension, the X-axis represents the spatial dimension, and the gray level indicates the luminance at a certain pixel. Usually, the first rows of the image are associated to the lowest wavelengths, and the latter ones to the highest wavelengths. For a certain pixel, its value represents the measured luminance at a certain wavelength in a certain position across the spatial dimension. If we extract a single column (fixed X position) from a Y-lambda image, it is possible to visualize the spectra of a certain pixel within the X-axis, while a single row represents the spatial distribution for a fixed wavelength (Figure 3-1, Y-lambda frame).

An appropriate visualization and interpretation of Y-lambda images are important for an intuitive usage and configuration of push-broom cameras. Y-lambda images are commonly used for focusing push-broom HS cameras. In addition, Y-lambda images can be used to set up the optimal illumination level for a given application. The visualization of Y-lambda images can reveal, among others, non-homogeneous distribution of light across the FOV or the spectral distribution of the light source.

In Figure 3-2 we present a toy example to visually clarify some concepts regarding Y-lambda images. To this end, we select a sample contained in a slide, where there is only a single black dot printed on its center. A graphical representation of the HS cube of this toy example is shown in Figure 3-2.a, while its spatial shape is shown in Figure 3-2.b. Within the sample, we represent three different push-broom lines, namely P_1, P_2, and P_3. P_3 is located in a blank part of the slide, while P_1 and P_2 are sections that cross different parts of the black dot.

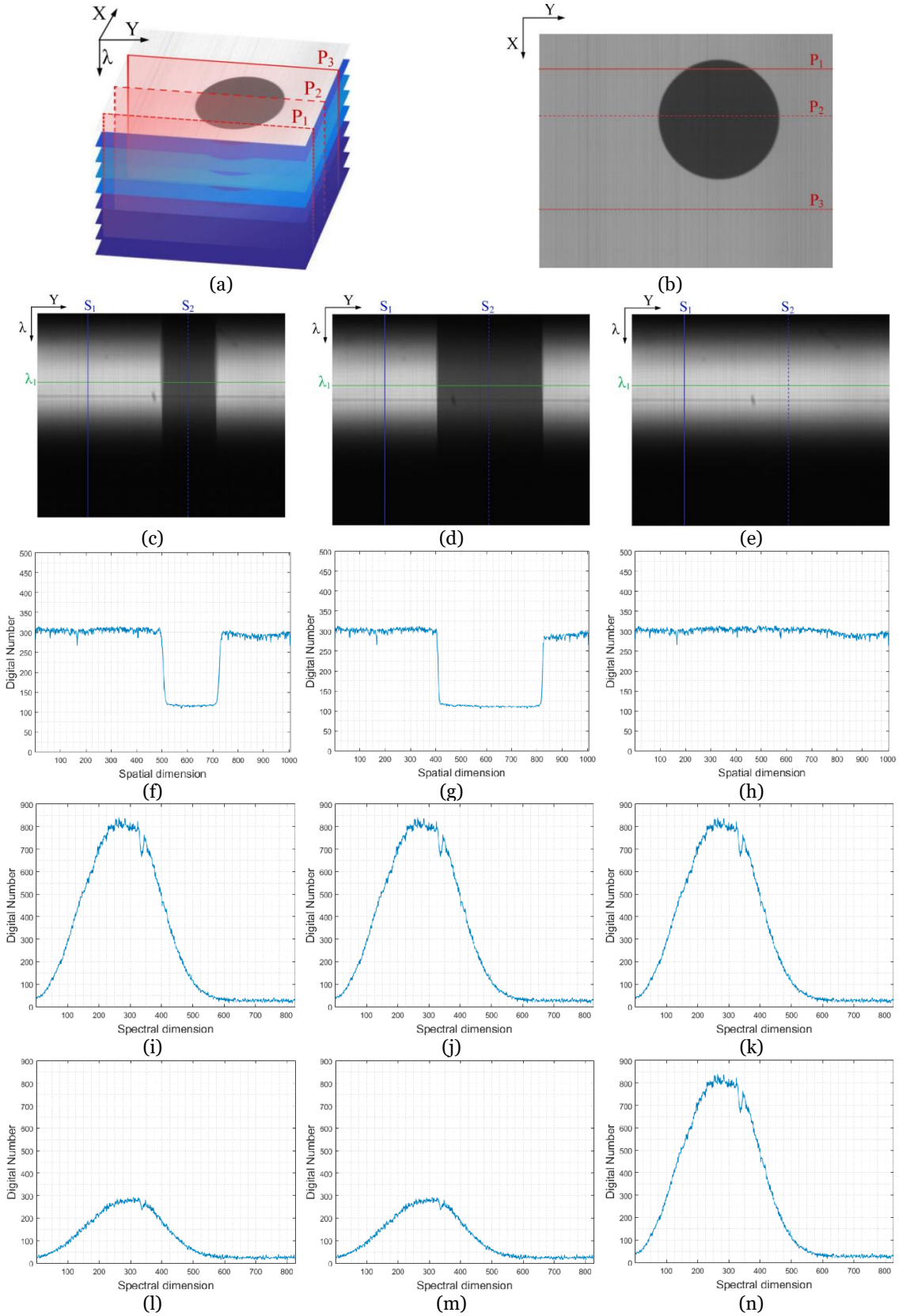

Figure 3-2: Y-lambda image a) HS cube b) Spatial distribution of the HC and spatial location of different P planes, c)-e) Y-lambda planes for P_1, P_2 and P_3, f)-h) Spatial profiles at λ_1, i)-k) Spectral profiles at S_1, l)-n) Spectral profiles at S_2.

In Figure 3-2.c-e we represent the Y-lambda images associated to P_1, P_2,and P_3. Some conclusions can be extracted directly from the Y-lambda image, such as the presence of objects within the FOV, or some intuitions about the illumination conditions. Nevertheless, to correctly exploit the information within a Y-lambda image, we can visualize the spatial and the spectral information separately. First, the visualization of the spatial information of a given scene within the Y-lambda image requires the selection of a fixed wavelength. This spatial information can be extracted from the Y-lambda image by selecting a discrete row ($\lambda_1$in Figure 3-2.c-e). The corresponding spatial profile for such spectral channel can be extracted as the pixel values of all the columns for such row. In Figure 3-2.f, Figure 3-2.g and Figure 3-2.h , we can visualize the spatial profile of P_1, P_2, and P_3 respectively. For P_3, where there is no sample, the spatial profile is flat, showing high luminance values for the entire FOV. On the contrary, the P_1 and P_2 counterpart show low luminance values in the center of the spatial profile, corresponding to the presence of the black dot within the FOV. The visualization of such spatial profiles is extensively used for focusing HS push-broom cameras. Secondly, to visualize the spectral information we have to select a spatial position. Within the Y-lambda images represented in Figure 3-2.c-e, we chosen two different spatial points, namely S_1 and S_2, located in a blank part of the scene and inside the black dot respectively (blue lines in the figure). If we represent the rows corresponding to such spatial locations, we retrieve their spectral shape (Figure 3-2.i-n). On the one hand, we can observe the spectral shape of the blank part of the scene in Figure 3-2.i-k and Figure 3-2.n, which represent the spectral shape of the light source used in the toy example. On the other hand, in Figure 3-2.l-m the spectral shape of the black dot is represented, showing low transmittance values in all wavelengths.

3.2 Instrumentation

The instrumentation employed in this study is composed by two main parts: an optical subsystem and a mechanical subsystem. The optical subsystem is composed by both a microscope optic path, and a push-broom HS camera. During this PhD dissertation, a single push-broom camera has been used, while two different microscopes have been employed. The mechanical subsystem is mainly devoted to perform the spatial scanning in the push-broom acquisition subsystem. For the mechanical subsystem, in this PhD dissertation we have employed three different scanning mechanisms. Two of them were custom, while the latter is a commercial one. In this section, we will describe the instrumentation used in this PhD.

3.2.1 Optical subsystem

The optical subsystem employed in our system consists of an HS camera coupled to a conventional light microscope. In this section, we present the main details of the optical subsystem.

3.2.1.1 Microscopes

3.2.1.1.1 Olympus BH2-MJLT

The first microscope used was an Olympus BH2-MJLT (Olympus, Tokyo, Japan). The main features of this microscope are the dual illumination mode, which allows the

observation both in transmittance and reflectance; the trinocular (BH2-TR3), permits the attachment of a camera with a selectable light path (i.e. is able to bring the light into the observation eyepieces, to the camera or to both of them); the objective lenses, that are from the Neo S Plan family (Olympus, Tokyio, Japan) with five different magnifications: 5x, 10x, 20x, 50x and 100x. The microscope also provides an in-house illumination system based on a 12 V - 50 W halogen lamp. This microscope is shown in Figure 3-3.A.

The HS camera is directly coupled to the microscope using the Olympus MTV-3 C-mount adapter. The MTV-3 adapter includes a 0.3x relay lens. In order to project the image from the trinocular to the MTV-3, a special lens for microphotography is used. In our setup, this lens is the NFK 3.3 LD (Olympus, Tokyo, Japan) and it is devoted to maximizing the area covered by the camera attached to the trinocular and hence, makes this area closer to the one observed through the trinocular eyepieces.

The FOV captured by the camera will depend on both the lens magnification M_i and the sensor size of the camera S_S , as shown in Equation (2). The sensor size can be calculated as the product of the pixel size of the sensor P_S by its number of pixels N. For this camera, the pixel size is 7.4 μm, while the overall magnification of the optical system is determined by the magnification of each lens, the 0.3× relay lens and the 3.3× from the microphotography lens. This means that the overall magnification of the system is about 0.99 the lens magnification. Using this information, we are able to calculate the FOV for the different magnifications.

$$\mathrm{FOV} = \frac{\mathrm{P_S} \cdot \mathrm{N}}{\mathrm{M_i}} = \frac{\mathrm{S_S}}{\mathrm{M_i}} \tag{2}$$

3.2.1.1.2 Olympus BX-53

The main limitation of the aforementioned microscope is a limited spectral bandwidth, since the microscope is a conventional one, and its parts are not optimized for infrared imaging. Using such microscope, the overall acquisition system is limited to wavelengths lower than 750 nm approximately. In order to improve the spectral range of the overall system, we decided to acquire a microscope optimized for a wide spectral range.

In order to guarantee an enhanced spectral range, we tested different microscopes from the main microscope manufacturers, i.e. Carl Zeiss, Leica, Nikon and Olympus. After several experimental testing, we selected the Olympus BX-53 (Olympus, Tokyo, Japan) microscope. The objective lenses are from the LMPLFLN family (Olympus, Tokyo, Japan), which are optimized for infra-red (IR) observations. Such microscope is shown in Figure 3-3.B.

Beyond the enhanced spectral range, the main features of this microscope are the dual observation modes (i.e. transmittance and reflectance); a tube lens (U-TLU-IR, Olympus, Tokyo, Japan) which allows the attachment of different imaging sensors; a motorized dual-axis mechanical stage (Scanning Stage SCAN 130×85, Märzhäuser), which provides accurate movement of the specimens; and an integrated light source consisting in a 12 V, 100 W halogen lamp.

(a) (b)

Figure 3-3: Microscopes. (a) Olympus BH2-MJLT; (b) Olympus BX-53.

3.2.1.2 HS camera

The push-broom HS camera is a Hyperspec® VNIR A-Series from HeadWall Photonics (Fitchburg, MA, USA), which is based on an imaging spectrometer coupled to a CCD (Charge-Coupled Device) sensor, the Adimec-1000m (Adimec, Eindhoven, Netherlands). This HS system works in the spectral range from 400 to 1000 nm (VNIR) with a spectral resolution of 2.8 nm, being able to sample 826 spectral channels and 1004 spatial pixels. As already mentioned, several factors affect the overall spectral response of an HS acquisition system, e.g. the quantum efficiency of the sensor, the spectral shape of the light source, or the light transmission of the lens. When the HS camera is attached to the microscope, the aforementioned elements affect the overall spectral response of the system. In Figure 3-4 we show a comparative of the effective spectral range of the acquisition system for the different microscopes. We can observe the spectral bandwidth of the Olympus BH2-MJLT microscope is limited to approximately 750 nm, while the system which includes the Olympus BX-53 microscope is sensitive to wavelengths up to 950 nm.

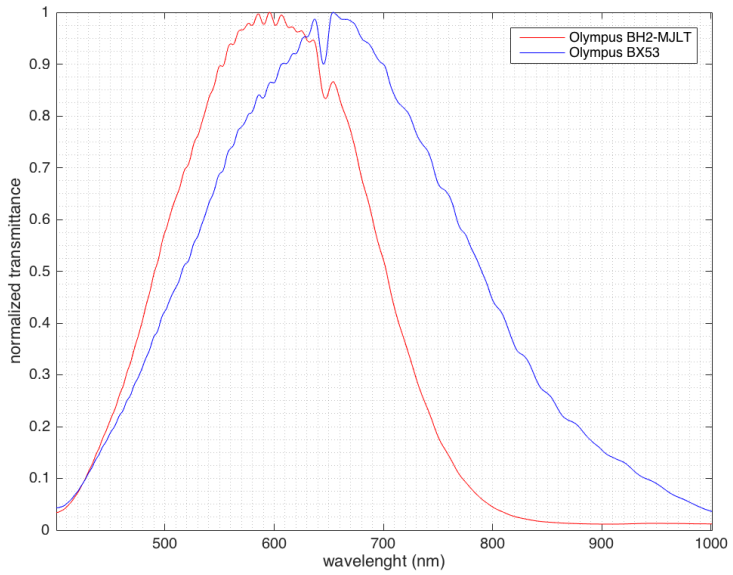

Figure 3-4: Comparative of the spectral range of both optical subsystems: Olympus BH2-MJLT (red) and Olympus BX53 (red).

3.2.2 Mechanical subsystems:

A relative motion between the HS sensor and the targeted sample is needed in order to acquire HS data cubes using a sensor based on a push-broom scanner. The quality and limitations of the acquired images are strongly related to the characteristics of this relative movement. In our particular acquisition system, the HS sensor remains motionless, placed over the microscope, while the sample to be scanned is moved taking advantage of the microscope moving system. In the acquisition process followed in this work, the HS push-broom sensor is continuously capturing frames while the sample to be scanned is moving in the X direction according to the motor steps. Two important mechanical restrictions must be fulfilled in order to acquire high quality images using this kind of acquisition process. First of all, the resolution of the mechanical movement system must be considerably higher than the optical resolution. That is, the smaller distance that the sample can be moved has to be considerably smaller than the pixel size. In this way, the mechanical movement of the sample is perceived as a continuous and uniform displacement by the scanning sensor. On the contrary, if the smaller distance that the sample can be moved is close to the pixel size, the scanning sensor perceives the movement as a sequence of jumps that correspond with the motor steps. Needless to say, that if the smaller distance that the sample can be moved is larger than the pixel size, there will be gaps between subsequent acquired frames. Secondly, the stepper motor rotation speed has to be not too high, nor too low, so it can efficiently work, avoiding vibrations and overheating. The required motor rotation speed depends on the mechanical resolution and the linear speed at which the sample has to be moved. This linear speed depends on the optical resolution and the frame rate at which the sensor is capturing the data, as previously explained in this chapter.

In this PhD. dissertation, three different mechanical subsystems have been employed. For the BH2-MJLT microscope, the mechanical subsystems were designed and developed. In this section, we describe all the custom mechanical systems used in this PhD dissertation. For the BX-53 microscope, a commercial dual-axis motorized stage (Scanning Stage SCAN 130 × 85) is used to perform the spatial scanning. The main features of this Scanning Stage are a movement resolution of 10 nm in both axis; and the possibility to be controlled both by software or by using a joystick.

3.2.2.1 Custom mechanical subsystems

3.2.2.1.1 Preliminary prototype

So as to obtain a HS cube from the pathological slides, a customized scanning platform based on a linear-movement mechanism with a resolution of 4.5 μm was developed. The scanning platform was attached to the microscope employing a customized 3D-printed flat base, which replaces the original plate of the microscope (Figure 3-5.b). For a 5x magnification, each pixel represents an area of 1.32×1.32 mm, while the movement resolution of the linear mechanism is limited to 4.5 μm. The lower resolution of the linear mechanism compared to the pixel resolution of the optical system imposes a limitation in the spatial information that can be collected to create a HS cube. This fact implies that a complete pathological slide cannot be captured in a single shot, because there is a spatial information gap between the contiguous lines that compose the HS cube.

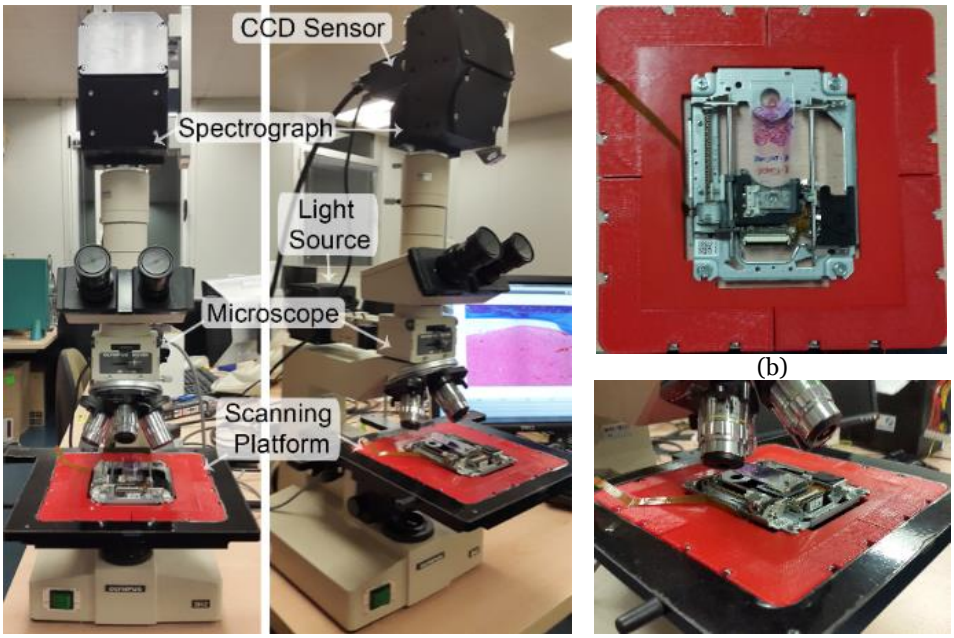

Figure 3-5: Microscopic HS acquisition system. (a) System overview modified for HSI acquisition. (b) Designed flat base of the scanning platform. (c) Scanning platform attached to the microscope.

3.2.2.1.2 Optimized prototype:

This mechanical subsystem is composed by a custom 3D printed transmission mechanism, a stepper motor and a controller. By default, the movement system of the microscope is manual, in which two knobs can be manually rotated for moving the sample in the X and Y directions using two rack and pinion gears mechanisms. A stepper motor has been set up for driving the handle corresponding to the X direction. By doing so, the movement in the X direction has been automated, which can be controlled from the computer in order to synchronize the sample movement with the sensor acquisition process. The stepper motor is controlled using a DRV8825 driver plugged into an Arduino UNO board, which communicates with the computer through the USB serial port. The stepper motor has been mechanically fixed using a custom designed 3D printed mechanism that includes a pulley transmission and a planetary reduction, as it can be seen in Figure 3-6. The main goal of this mechanism is to fulfill the mechanical requirements imposed by the application at hand, i.e. the resolution of the mechanical movement system must be considerably higher than the optical resolution.

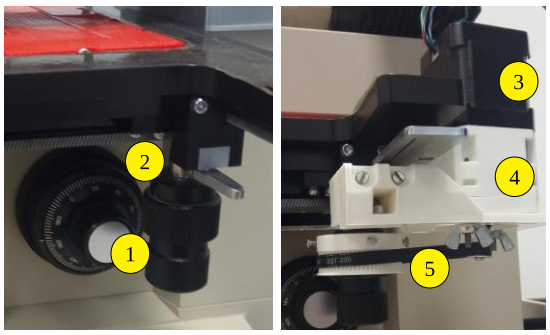

Figure 3-6: Mechanism made of custom designed 3D printed parts for automatically moving the samples in the X direction. 1: Microscope handles for manual movements. 2: Microscope rack and pinion gear mechanism. 3: Stepper motor. 4: Planetary reduction. 5: Pulley reduction.

Generally, the linear movement of the sample is proportional to the movement of the stepper motor, multiplied by the transmission ratio of the system (TR_{system}) as shown in Equations (3) and (4), where D_{linear} refers to the linear distance that the sample is moved for each motor step, and S_{linear} is the linear speed at which the sample is moved according to the rotation speed of the motor ($S_{rotation}$) measured in steps per second. $MSPR$ refers to the number of steps per motor revolution.

$$D_{linear} = TR_{system} \cdot \frac{1}{MSPR} \tag{3}$$

$$S_{linear} = TR_{system} \cdot \frac{1}{MSPR} \cdot S_{rotation} \tag{4}$$

Whereas we are targeting a microscopic application and the aforementioned mechanical requirements for acquisition systems based on push-broom sensors has to be fulfilled, the project at hand needs a mechanical system able to accurately move very short distances and at a very low but continuous and uniform speed. Hence, according to Equations (3) and (4), a small TR_{system} value is desired, as well as a high MSPR. In particular, the selected stepper motor has 400 steps per revolution. Additionally, the DRV8825 driver is able to increase the stepper motor steps per revolution by introducing micro-steps up to a maximum of 32 micro-steps per motor steps. Accordingly, the minimum MSPR for our motor is 400 steps per revolution and the maximum is 12800 steps per revolution ($400 \cdot 32$).

The TR_{system} can be depicted as shown in Equation (5), where $TR_{planetary}$ refers to the transmission ratio of the planetary reduction placed after the motor, TR_{pulley} refers to the transmission ratio of the pulley reduction placed between the planetary reduction and the microscope handle, and TR_{gear} refers to the transmission ratio of the microscope rack and pinion gear mechanism, measured in millimeters per revolution. The transmission values that correspond to the custom designed 3D printed parts are $TR_{planetary} = 1/5$ and $TR_{pulley} = 16/64$. The transmission ratio of the rack and pinion gear mechanism is 42 millimeters per revolution (28 teeth with a pitch of 1.5 millimeters). These results (Equation (6)) in a considerably small transmission ratio (TR_{system} = 2.1 mm per revolution (rv)). Additionally, more than one planetary reduction can be stacked together for obtaining extra 1/5 reductions. According to these values, the mechanical resolution of the system is 164.0625 nm per motor step. This means that the minimal distance that the sample can be moved is $D_{linear} = 0.1640625$ µm.

$$TR_{system} = TR_{planetary} \cdot TR_{pulley} \cdot TR_{gear} \tag{5}$$

$$TR_{system} = \frac{1}{5} \cdot \frac{16}{64} \cdot 42 = 2.1 \frac{mm}{rv} \tag{6}$$

3.2.3 Summary

In this section we have provided a brief overview of the previously described acquisitions systems. In Table 3-1 we showed a summary of the different features of the different acquisition systems, namely System-I, System-II and System-III. In such table we can observe the main features of both the optical and the mechanical subsystems, including the specifications of the FOV, the pixel size, and the mechanical resolution. As

can be observed from the table, there are some situations where the mechanical resolution of the system is higher than the pixel size for some magnifications. In those situations (marked as † in the table), the mechanical resolution is not enough to capture the complete spatial information in a push-broom scan, since the movement size is higher than the pixel size. We show a graphic representation of the three acquisition systems in Figure 3-7.

Table 3-1: Summary table of the acquisition systems. † indicates a pixel size lower to the mechanical resolution.

Configuration		System-I	System-II	System-III
Optical Subsystem				
Microscope		BH2-MJLT	BH2-MJLT	BX-53
Objective Lens		Neo S Plan family	Neo S Plan family	LMPLFLN family
Hyperspectral camera		HeadWall Hyperspec®VNIR A-Series		
FOV (μm)	5×	1471	1471	1485
	10×	735.53	735.53	742.96
	20×	367.76	367.76	371.48
	50×	147.10	147.10	148.59
Pixel Size (nm)	5×	1465 †	1465	1480
	10×	732.60 †	732.60	740
	20×	366.30 †	366.30	370
	50×	46.52†	146.52 †	148
Mechanical subsystem				
Scanning mechanism		Based on Blue-Ray linear actuator	Custom 3-D printed	XYZ stage
Mechanical resolution (nm)		4500	164	10

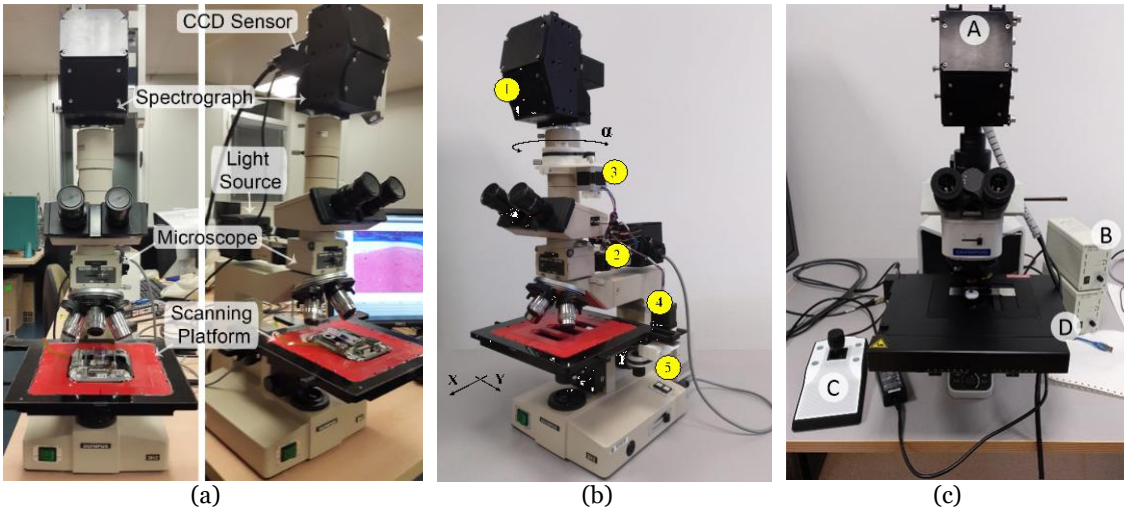

(a) (b) (c)

Figure 3-7: Acquisition systems used in this PhD. (a) System-I, (b) System-II, (c) System-III.

3.3 Methodology

In this section, we present a methodology to correctly set up an HS push-broom microscope to capture high quality HS images. This methodology involves the setup of the light conditions, the optical focusing of the system, the camera alignment, and the empirical measurement of both the FOV and the mechanical resolution of the scanning platform. Additionally, a methodology for quantitatively verifying the correct set up of the whole system is described. Finally, we show the most common defects that may appear when the system is not properly configured.

Although three different acquisition systems are available, this methodology has been developed by using the System-II (Figure 3-8). However, this methodology can be applied to any push-broom HS camera and microscope.

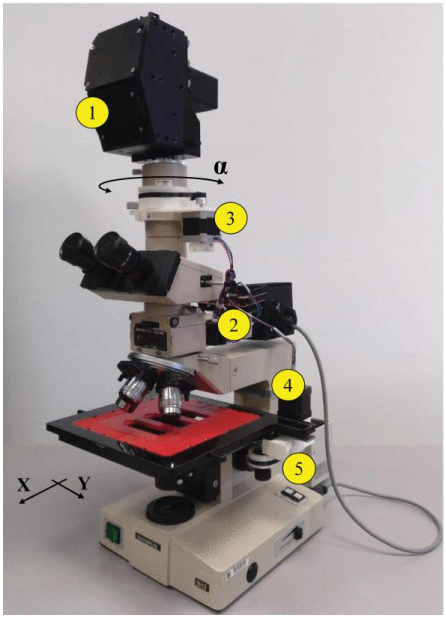

Figure 3-8: Acquisition System-II. 1) VNIR HS camera. 2) Controller of the mechanical system. 3) Camera alignment mechanism. 4) Stepper motor for controlling the sample movement. 5) Custom 3D printed transmission mechanism.

For this research, an additional custom 3D printed mechanism is included, which allows to perform an accurate positioning of the HS camera relative to the microscope, and thus facilitating a precise alignment between the HS camera and the microscope (Figure 3-8.3). The methodology described in this section has been published in a research paper entitled "*Hyperspectral Push-Broom Microscope Development and Characterization*" (2019, IEEE Access, IEEE) [134].

3.3.1 Calibration instrumentation

In the proposed methodology for setting up an HS push-broom microscope, we employ a microscope calibration slide (Figure 3-9) composed by four different parts: a single axis micrometer scale, a dual axis micrometer scale and two dots with different diameter. The single axis micrometer scale has a length of 10 mm with divisions of 0.1 mm, numbered from 10 to 1. The dual axis scale ranges in 0.01 mm each division, having also additional markers which facilitates measurements of 0.05 mm. Finally, the diameters of the target dots are 0.15 and 0.07 mm respectively.

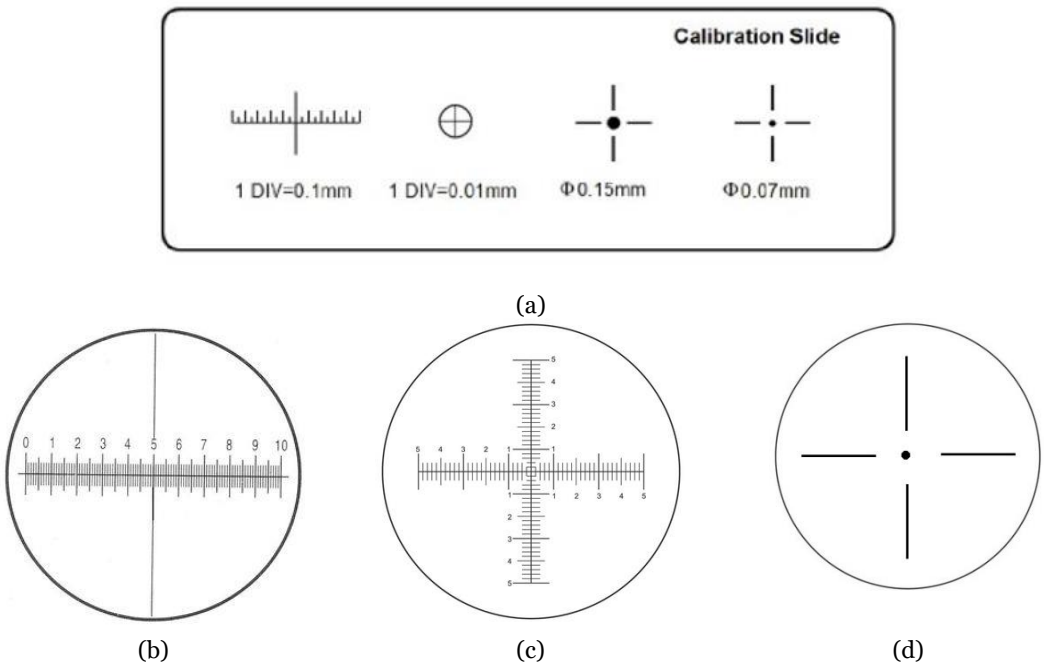

Figure 3-9: Calibration slide. (a) Complete calibration slide. (b) Micrometer scale, with 0.1 mm divisions. (c) Two-axis micrometer scale, with 0.01 mm divisions and (d) Black dot, 0.07 and 0.15 mm diameter.

3.3.2 Dynamic range characterization of the HSI system

The first step prior to capture an HS cube is the configuration of the illumination conditions. There are three main factors that should be taken into account for light adjustment of HS cameras: the spectral shape of the light source, the light intensity and the spatial distribution of light across the camera's FOV. First, an optimal light source for HSI should ideally present a flat spectral response along the spectral range of the camera. If there is no radiation of light in some regions of the spectral range of the camera, it will be impossible to acquire images in such spectral bands. The spectrum emitted by the light source depends on the type of illumination. Second, normally it is desirable to maximize the light intensity measured by the camera, i.e. maximizing the dynamic range. There are two ways to maximize the dynamic range in HS measurements: increasing either the exposure time or the illumination intensity. On the one hand, the exposure time adjustment can improve the dynamic range conditions, but at the expenses of increasing the time required to collect an HS cube. The exposure time can be also limited by the hardware itself, i.e. the maximum and minimum exposure time will strongly depend on sensor manufacturers. On the other hand, variations in the light source power can improve the dynamic range exploitation, but light illumination adjustment is not possible in some situations. Summarizing, there is a trade-off between acquisition time, dynamic range and the available illumination conditions.

For the reasons discussed above, to properly characterize the illumination conditions of an HS instrumentation, we should pay special attention to the spectral shape of the light source, the light intensity, and the spatial distribution of light across the FOV. In our acquisition system (System-II), the illumination is provided by the in-house 50 W halogen lamp of the microscope, and the maximum exposure time that can be configured in the camera is 40 ms. The first configuration of the system was just observing the

microscope light (with no sample) using the highest light power provided by the in-house lighting and also the highest exposure time supported by the camera. To fully characterize the illumination conditions, we analyzed an Y-lambda image. In order to observe both the measured spectral shape and the dynamic range exploitation, we analyzed the mean spectral profile of the Y-lambda image (Figure 3-10.a) using the 4 different magnifications available. By visual inspection, it is possible to notice that the spectral shape of the measured light is not flat. These spectra are mostly influenced by the spectra of the light source, the spectral transmission response of the microscope light path and the spectral response of the sensor. Attending to Figure 3-10.a, it is possible to notice that, although the spectral range of the HS camera covers from 400 to 1000 nm, the instrumentation limits the effective spectral range to approximately 400-800 nm.

To visualize the spatial distribution of light in our system, we analyze a spatial profile from the Y-lambda image. In Figure 3-10.b, we show the spatial illumination conditions of our system, where a flat response can be observed for each objective lens.

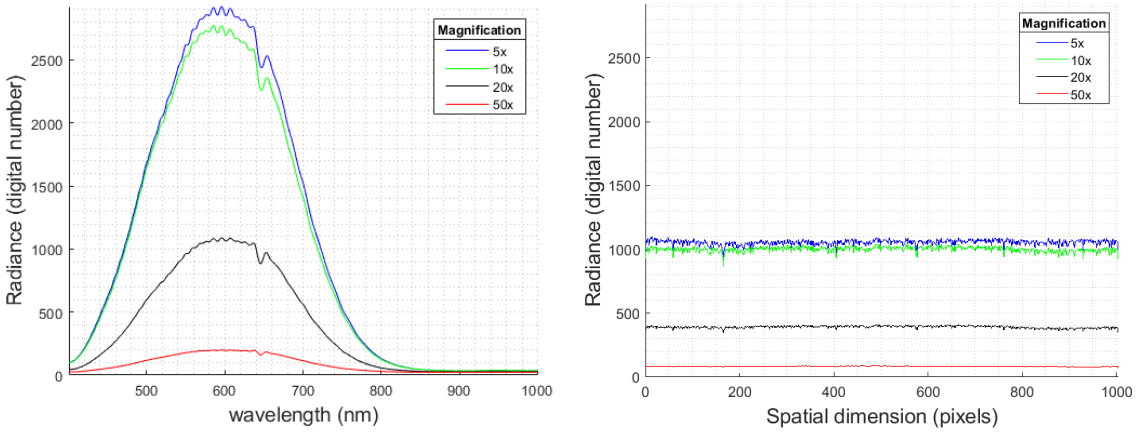

Figure 3-10: Light measurements. (a) Spectral and (b) spatial distribution of light varying the magnification.

Figure 3-10 also shows that the full dynamic range of the acquisition system is not maximized, even with the maximum light power and exposure time. Furthermore, it can be observed that each objective lens present different transmission losses, being the higher magnifications the ones which present higher attenuation of light. In the herein setup, the only way to improve the dynamic range usage of our system is by attaching an external high-power light source. The improvement of the dynamic range conditions is mandatory to acquire HS images with high magnification. Due to the poor light intensity captured when using the 50× objective lens, the experiments in this paper are limited to the 5×, 10× and 20× magnifications.

Finally, we performed an additional experiment to illustrate the effect of varying the exposure time. Figure 3-11 shows that the best dynamic range exploitation is achieved when the higher exposure time is selected.

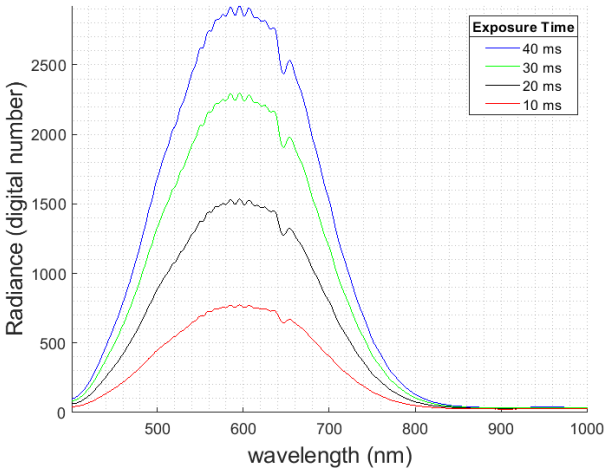

Figure 3-11: Spectral distribution of light varying the exposure time.

3.3.3 Focusing an HS image

Focusing targets are usually employed for focusing both conventional and HS cameras. Using an appropriate focusing target, the acquisition system is considered focused when the Y-lambda is sharp, showing high contrast between lines and gaps, otherwise the system is out of focus. The coarse focusing of an HS image can be performed through Y-lambda image inspection. An Y-lambda image from a micrometer contains both low luminance areas (corresponding to the micrometer marks) and the high luminance counterpart (related to the blank areas in the calibration slide). In this work, we used the micrometer scale from the calibration slide as a focusing target (Figure 3-9.b). Figure 3-12.a shows an example of a focused Y-lambda image, while Figure 3-12.a shows an Y-lambda image out of focus.

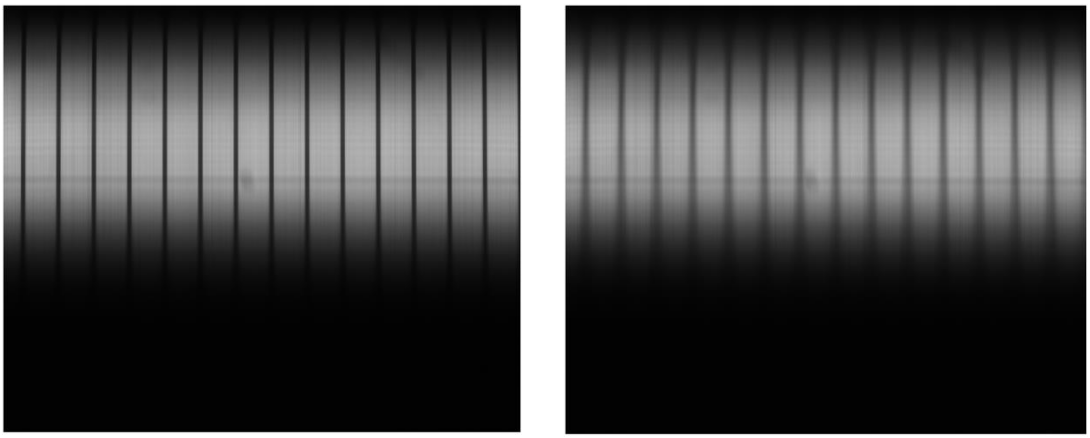

(a) (b)

Figure 3-12: Focused (a) and unfocused (b) push-broom frames from a focusing target.

For a precise focus adjustment, it is mandatory to make use of the spatial profile of the Y-lambda image. This spatial profile is a one-dimensional signal where low luminance values correspond to the micrometer marks, and high luminance values correspond to the blank spaces in the calibration slide. In a focused image, this profile looks like a square signal, showing high contrast between lines and gaps. In opposition, if the system is completely out of focus, the spatial profile will look like a sinusoidal signal. Partially focused images present a shape similar to a square signal but revealing soft edges. Figure 3-13 shows an example of different spatial profiles of a focusing target.

In such figure, the focused spectral profile is drawn using a blue line, a near-focused image is represented using a black line and finally an unfocused image is represented using a red line.

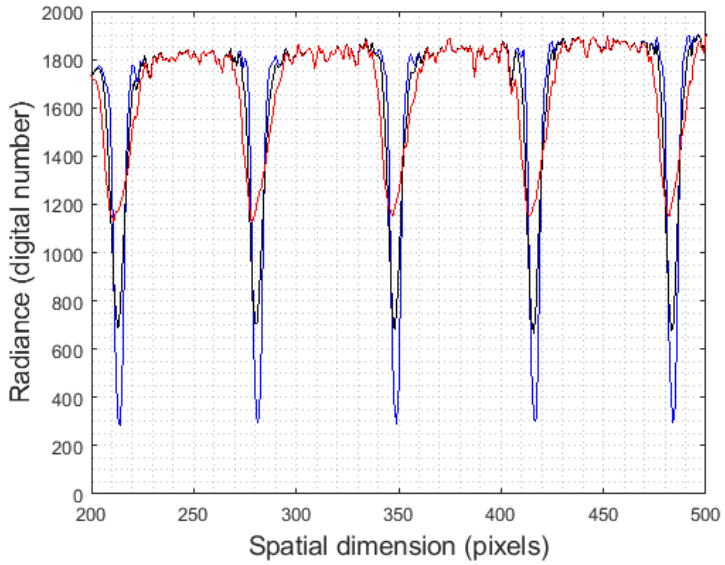

Figure 3-13: Examples of a focused (blue), unfocused (red) and near focused (black) push-broom frames using a spectral profile.

3.3.4 Microscope-HS camera alignment

In the following sections, we will extract some information about the precision of our acquisition system by measurements taken from a calibration slide. For some of these measurements, the calibration slide and the FOV of the push-broom camera are required to be correctly aligned. The calibration slide is fixed on the microscope stage, so the only manner to align the camera and the calibration slide is by rotating the camera position relative to the microscope mount. As a coarse alignment methodology, we propose to make use of the micrometer ruler. Figure 3-14 shows a representation of two different push-broom frames within a micrometer ruler. The solid line (p_2) represents a scenario where the camera and the microscope stage are aligned, being the FOV of the camera perpendicular to the ruler marks. By contrast, the dashed line (p_1) shows an example of a misaligned setup, where the FOV of the camera is not perpendicular to the sample.

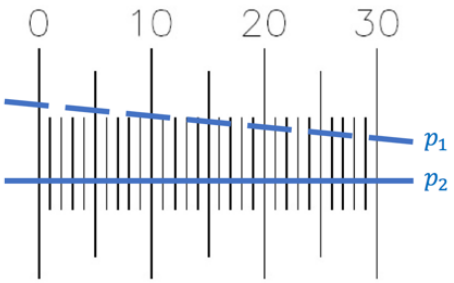

Figure 3-14: Example of the spatial location of different push-broom frames within a micrometer ruler. The blue solid line p_2 represents a correct alignment, while blue dashed line shows misalignment p_1.

In this example situation, the camera's FOV was placed exactly at the end of the micrometer marks to facilitate the misalignment detection. In this scenario, when the camera and the microscope stage are properly aligned (Figure 3-14, p_2), the Y-lambda

image present a similar shape to Figure 3-15.a. Furthermore, when the FOV and the sample are aligned, there is no variation in the observed Y-lambda image when manually varying the position of the push-broom frame relative to the sample. Conversely, when FOV position is not perpendicular to the sample (Figure 3-14, p_1) the Y-lambda image looks like Figure 3-15.a, where some of the micrometer marks are missing, revealing misalignment.

In order to perform the coarse alignment, we propose to iteratively rotate the HS camera position relative to the microscope stage while visualizing the Y-lambda image. A most reliable methodology to align the HS camera once it is coupled to the microscope will be covered later section.

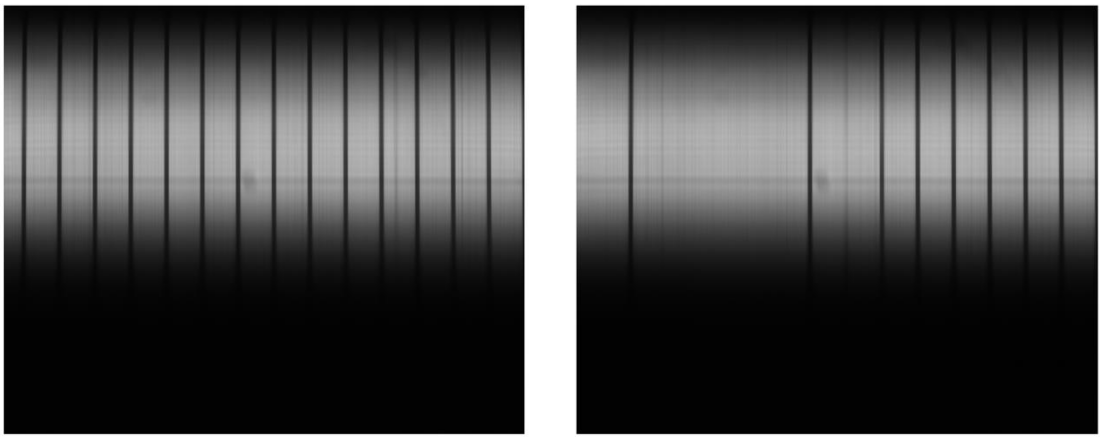

(a) (b)

Figure 3-15: Aligned (a) and not aligned (b) frame of the HS camera respect to the sample.

3.3.5 Spatial resolution measurement

In this section, we aim to determine the effective FOV measured by the HS camera, which also will reveal the width of the push-broom line. This measure allows to determine the proper scanning speed. As mentioned before, the camera should be correctly aligned prior to this step-in order to avoid undesired measurement errors. For the FOV measurement, both the micrometer ruler and the dual axis scale (Figure 3-9.b and Figure 3-9.c) from the calibration slide are used. Using both calibration targets, it is possible to record images where the distance between lines is known, and hence the effective FOV of the camera can be estimated by performing image analysis over such targets.

The setup of this experiment consists in positioning the FOV of the camera within the micrometer scale. For the measurements to be correct, the microscope and the HS camera should be correctly aligned, being the situation similar to the one shown in Figure 3-14, p_2. The associated Y-lambda image is exactly the same as shown in Figure 3-15.a.

Our image analysis approach is devoted to determine the distance (in pixels) between two consequent lines (as drawn in Figure 3-14, p_2) by finding the edges of the ruler lines, and counting the pixels between consecutive edges in order to estimate the FOV of the HS camera. To this end, we first extract the spatial ruler profile from the Y-lambda image. Then, we search for the edges of the Y-lambda image by calculating the first derivative of the ruler profile. The ruler profile and its derivative are shown in Figure 3-16. The

positive peaks from Figure 3-16.b corresponds to the rising edges, and the negative peaks to the falling edges of the ruler profile.

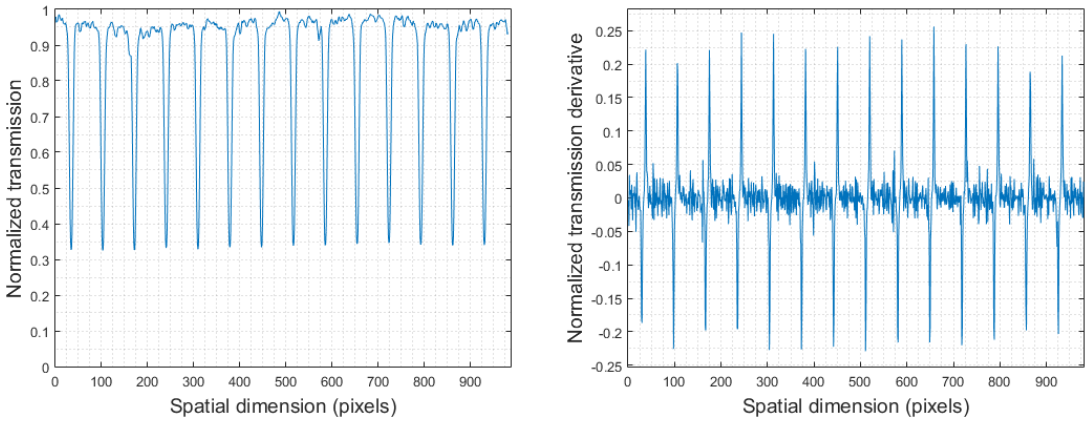

Figure 3-16: Information extracted from the micrometer ruler. (a) Ruler spatial profile. (b) Ruler profile derivative.

Prior to estimate the distance between lines, we have to find the peaks within the ruler first derivative. To this end, we set a threshold to identify the positive and negative peaks within the ruler derivative profile. Once the peaks are located, we estimate the mean distance (in pixels) between two consecutive peaks of the same sign (positive peaks and negative peaks respectively). The distances are calculated independently for the rising edges and for the falling edges of the ruler profile. In Figure 3-17 the peaks corresponding to rising edges are marked in red, while the falling edges counterpart are marked in blue. Once these peaks are identified, it is possible to calculate the distance between two consecutive lines as the mean of both distances (between positive and negative peaks). Using this distance, we are able to retrieve an estimation about the pixel size, and hence, about the FOV.

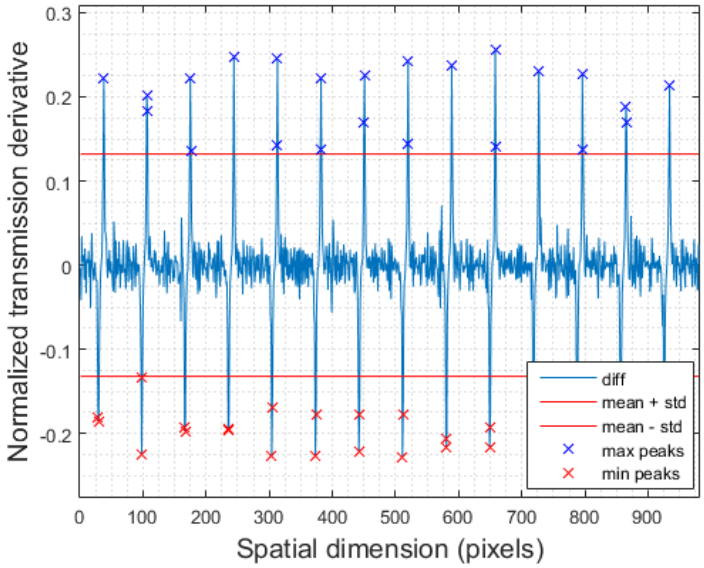

Figure 3-17: Distance calculation based on the ruler's profile derivative.

In this experiment, the estimation of the FOV was carried out for three different magnifications (5×, 10× and 20×), and the micrometer scale allows to measure three different distances (0.1 mm, 0.05 mm and 0.01 mm). Prior to show the experimental estimation of the FOV for each magnification, some considerations should be

highlighted. First, although the calibration slide allows measuring three different distances, the width of the line for 0.05 mm and 0.01 mm divisions keeps constant. For this reason, measures using the 0.01 mm ruler are highly biased by the line width. For an adequate FOV estimation using this methodology, the micrometer ruler should present a low line width compared to the distance between consequent lines.

Although the proposed methodology to measure the FOV is straightforward, the image analysis method will strongly depend on the threshold used to identify the ruler edges within the derivative. Threshold values will be related to the magnification and the distance of the ruler. Assuming that R_d is the first derivative of the ruler profile, we propose to detect the peaks within the ruler's derivative using the threshold defined in Equation (7). Nevertheless, the manual determination of the constant k to be general enough for the different scenarios (varying magnifications and line widths) is difficult. For this reason, to tackle with the manual determination of a threshold, and to fully automate the process, k was determined using a non-linear fitting of manually picked k values for the different magnifications and ruler distances. We found that a third-grade polynomial fit provides enough generalization over our process.

$$\text{threshold} = \text{mean}(R_d) + k \cdot R_d \tag{7}$$

Using this methodology, we found agreement between the estimated FOV using Equation (2), shown in Table 3-1, and the measured FOV using the ruler profile, as we can see from results collected in Table 3-2.

Table 3-2: Measured FOV (μm)

Distance	5x	10x	20x
0.1	1470.62	733.94	366.30
0.05	1492.58	738.01	368.32
0.01	1538.53	800.00	392.16
Theoretical	1471	735.53	367.76

3.3.6 Empirical assessment of the mechanical movement precision and repeatability

As described in Section 3.2.2.1, the mechanical resolution of the system is a critical characteristic for being able to acquire high-quality images. Due to this reason, a stepper motor has been set up in the microscope using a custom 3D printed mechanism for automatically controlling the sample movement and theoretically achieving a very high movement resolution (D_{linear} = 0.1640625 µm). In order to verify the precision of the developed mechanism as well as its repeatability and tolerance, the linear displacement of the microscope stage in the X direction when rotating the motor 200,000 steps has been measured using a digital caliper gauge. For doing so, the digital caliper gauge has been installed also using custom design 3D printed parts.

Using this set up, a set of 10 measurements have been taken. The average obtained distance was 32.941 mm with a standard deviation lower than the 0.3%. According to this value, the minimal distance that the sample could be moved (mechanical resolution) is 0.164705 µm. As it can be observed, this value is very closed to the theoretically calculated one (D_{linear} = 0.1640625 µm), being the difference lower than 0.5%.

3.3.7 System speed and alignment calibration improvement

At this stage of the calibration process, the camera has been aligned by visual inspection, as described in Section 3.3.4. The pixel size has also been calculated using the methodology described in Section 3.3.5. Additionally, the spatial resolution of the system is also known (calculated in Section 3.3.6). Using the pixel size, the mechanical resolution and the capturing frame rate of the HS camera, the required motor rotation speed can be calculated using Equation (4), as it was described in Section 3.2.2.1.2. Hence, relatively good HS images should be obtained using this set up. Nevertheless, one extra stage is carried out in this section in order to slightly improve and/or verify the correct execution of the previous calibration stages. In this calibration stage the entire acquisition system (microscope, camera, and movement mechanism) is considered as a whole. The goal is to take a picture of a circle of the calibration slide and evaluate its spatial appearance in order to determine possible camera misalignment's and/or not optimal movement speeds. Figure 3-18 graphically indicates the different scenarios that may be faced in this process.

As it can be seen in Figure 3-18, when the image of the circle of the calibration slide is taken at the correct speed, it shapes perfectly corresponds with a circle (Figure 3-18.a). However, when the speed is too high or too low, its shape seems like an ellipse (Figure 3-18.b and Figure 3-18.c, respectively). Additionally, when the camera is not correctly aligned, the circle seems to be slightly rotated. However, this effect can be better perceived when the speed is too low, and the circle seems outstretched (Figure 3-18.d). Accordingly, in order to verify the correct alignment of the camera, a low speed can be forced in this experiment.

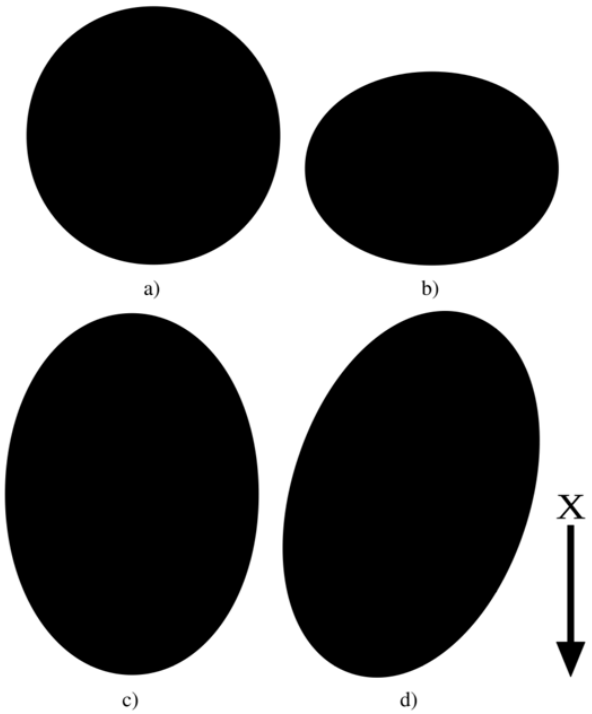

Figure 3-18: Possible scenarios when capturing a circle (Movement in the X direction). a) Correct motor speed. b) Motor speed is too high, camera is aligned. c) Motor speed is too low, camera is aligned. d) Motor speed is too low, camera is misaligned.

Despite a relatively good assessment of the correct system calibration can be done by visual inspection, an automatic methodology has been proposed in order to make it in a more precise and rigorous manner. For such purpose, the circle (or ellipse) eccentricity has been used together with a PCA method. The employed automatic methodology is described as follows:

- **Image binarization:** The image is firstly binarized generating a single 2D classification map where the pixels corresponding to the circle are labeled as 1, and the background pixels are labeled as 0. This is a relatively straightforward process considering that once that the image is calibrated, the HS pixels corresponding to the circle already have very low values and the background pixels have very high ones.

- **Principal components extraction:** A 2D principal component analysis is computed over the binarized classification map. This analysis provides two eigenvalues, corresponding to the directions of the longest and shortest axes of the ellipse (λ_{max} and λ_{min}), as well as their corresponding eigenvectors, which conform the rotation matrix, as shown in Figure 3-19.

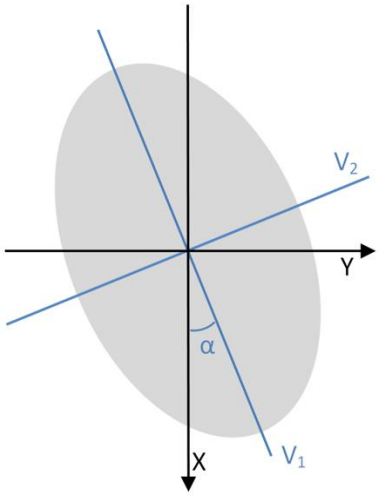

Figure 3-19: Principal component analysis of the pixels that conform the ellipse. X represents the sample moving direction. V_1 and V_2 represent the eigenvectors corresponding to the λ_{max} and λ_{min} eigenvalues, respectively. α represents the rotation angle.

- **Eccentricity calculation:** The eccentricity of the ellipse can be expressed in terms of its major and minor (ϕ_{max} and ϕ_{min}) axes as shown in Equation (8). In order to simplify the calculations, we are using the two eigenvalues extracted in the previous stage in order to calculate the eccentricity, as shown in Equation (8), taking advantage of the fact that ${\phi_{min}}^2/{\phi_{max}}^2 = \lambda_{min}/\lambda_{max}$. Using this methodology, when the speed at which the sample is moved is perfectly fixed according to the pixel size and the camera frame rate, the obtained eccentricity (e) should be ideally zero.

$$e = \sqrt{1 - \frac{{\phi_{min}}^2}{{\phi_{max}}^2}} = \sqrt{1 - \frac{\lambda_{min}}{\lambda_{max}}} \tag{8}$$

- **Rotation angle calculation:** Using the first eigenvector of the rotation matrix V_1, which corresponds to the first eigenvalue, the "counterclockwise" rotation

angle, with respect to the X axis, α, can be calculated as shown in Equation (9). For simplicity, we are always considering the first eigenvalue as the largest one, and hence, the rotation angle can be represented as shown in Figure 3-19. This angle is equivalent to the camera misalignment. If the obtained angle value is 0°or 90°, it means that the camera is perfectly aligned. Notice that for making this calculation is better to set a relatively low speed in order to obtain an outstretched appearance of the ellipse, being 0° the desirable angle value. If a relatively high speed were used, the desirable angle value would be 90°. It is also important to highlight that the axis are rotated 90°clockwise so that the X axis of the capture image corresponds with the sample moving direction (X).

$$\alpha = \tan^{-1}\left(\frac{V_{1_y}}{V_{1_x}}\right) \tag{9}$$

Figure 3-20 displays a set of example HS images collected by the described system, as well as the alignment and eccentricity values provided by the described method. On the one hand, Figure 3-20.a and Figure 3-20.b display a set of images collected with the HS camera misaligned and at a relatively low speed in relation to the optimal capturing speed for the specified frame period and pixel size. The low speed was established in order to highlight the misalignment in the dot circle sample, which cannot be appreciated in optimal scanning speed conditions. Such images are useful for obtaining the rotation angle that needs to be applied to the HS camera in each situation in order to correctly align it. On the other hand, Figure 3-20.c and Figure 3-20.d display a set of images collected with the camera already aligned but using different speeds. In these images we can observe that the measured rotation angle is close to either 0 or 90 degrees, while the rotation angle calculated from Figure 3-20.a and Figure 3-20.b indicate a misalignment between the camera and the microscope. Nevertheless, the eccentricity values calculated for Figure 3-20.c and Figure 3-20.d is not close to zero, which indicates that the circle dots were not captured using an appropriate scanning speed. Finally, Figure 3-20 show a HS cube captured in adequate conditions, i.e. the scanning speed is correctly configured and the microscope and the HS camera are aligned. In such example, the value of the eccentricity is close to zero, indicating that the image was acquired in adequate conditions.

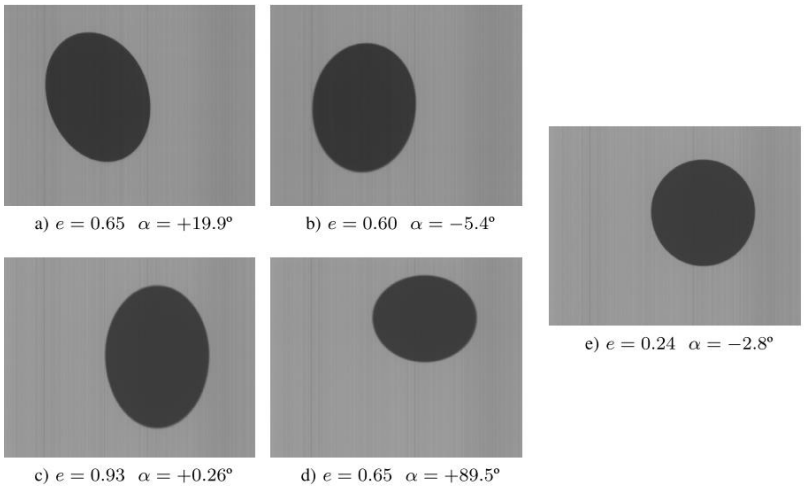

Figure 3-20: Real examples of the results provided by the described methodology. a-b) Examples of misaligned HS images. c-d) Examples of images acquired with a bad scanning speed configuration. e) Image acquired with correct alignment and speed conditions.

3.3.8 Calibration

The goal of HS acquisition systems is to provide a spectral signature per spatial pixel of the captured scene. These spectral signatures indicate the percentage of incident radiation at each spatial pixel that the scanned object transmits or reflects at each captured wavelength.

As already mentioned in Section 3.1, the spectral response of an HS acquisition system is affected by several factors, namely the intrinsic spectral response of sensor, the light transmission through the lenses and optical elements, and the spectral shape of the light source. Due to this reason, in order to obtain spectral signatures that really indicate the percentage of transmitted or reflected radiation at each of the different wavelengths, the data acquired by the HS system need to be radiometrically calibrated. This calibration consists in normalizing the captured HS pixels by linearly scaling their values considering the maximum and minimum values that the sensor could measure if the scanned object transmitted the 100% and 0% of the incident radiation. This calibration must be performed in the exact same capturing conditions that the HS image is taken.

The next process is followed in order to carry out this calibration process. First of all, once the adequate capturing conditions (exposure time, light intensity, etc.) have been set up, the sample slide is positioned at a blank area. Then, an HS frame is obtained at this position. This HS frame is typically referred as *White Reference*, (WR). Since there is not any sample material in such position of the slide, this HS frame contains the maximum values that the sensor is able to measure for each pixel and band in the specified capturing conditions (exposure time, light intensity, etc.). Afterwards, the light source is turned off and a new HS frame is collected. This HS frame is typically referred as *Dark Reference*, (DR), and contains the minimum values that system is able to provide for each pixel and band. Ideally, the DR values should be very close to zero, however higher values may be obtained, typically due to the intrinsic noise of the sensor. Once the WR and DR have been collected, the light source is turn on again and the HS image is captured. Each HS frame of the captured image is radiometrically calibrated using the WR and DR as shown in Equation (10), where Raw_i refers to the i^{th} HS frame of the acquired image while r_i refers to the same frame after the radiometric calibration. Additionally, in order to mitigate the noise influence, the WR and DR are collected 100 times each, thus calculating their average values.

$$\mathrm{r_i} = \frac{\mathrm{Raw_i} - \mathrm{DR}}{\mathrm{WR} - \mathrm{DR}} \tag{10}$$

Figure 3-21 shows an example of how the spectral signatures of different pixels are scaled to transmittance values using the aforementioned radiometric calibration process. This effect is shown for certain pixels within an example image (Figure 3-21.a). Concretely, Figure 3-21.b shows the uncalibrated raw spectral signatures, including the spectral signatures of the white and dark references (WR and DR), representing with the black color lines. Figure 3-21.c shows the same spectral signatures after applying the calibration procedure. The effect of scaling the spectral values to reflectance or transmittance values can also be observed in Figure 3-22.a and Figure 3-22.b where RGB images are obtained using the spectral bands centered at 709.0, 539.5 and 479.6 nm, respectively.

Additionally, the calibration process also helps to remove the stripping noise effect, which typically appears when acquiring HS images using push-broom scanners [320]. The stripping noise consists in spatially coherent lines that appear in the spatial scanning axis due to static artifacts produced in the sensors, that are repeated in each push-broom frame, as shown in Figure 3-22.a and Figure 3-22.c. In the calibrated images, the effect of the stripping noise disappear (Figure 3-22.b and Figure 3-22.d).The stripping noise is mainly due to the fact that different photo-receptors of the sensor have slightly different sensibility, producing slightly different values when measuring the exact same amount of incident radiation.

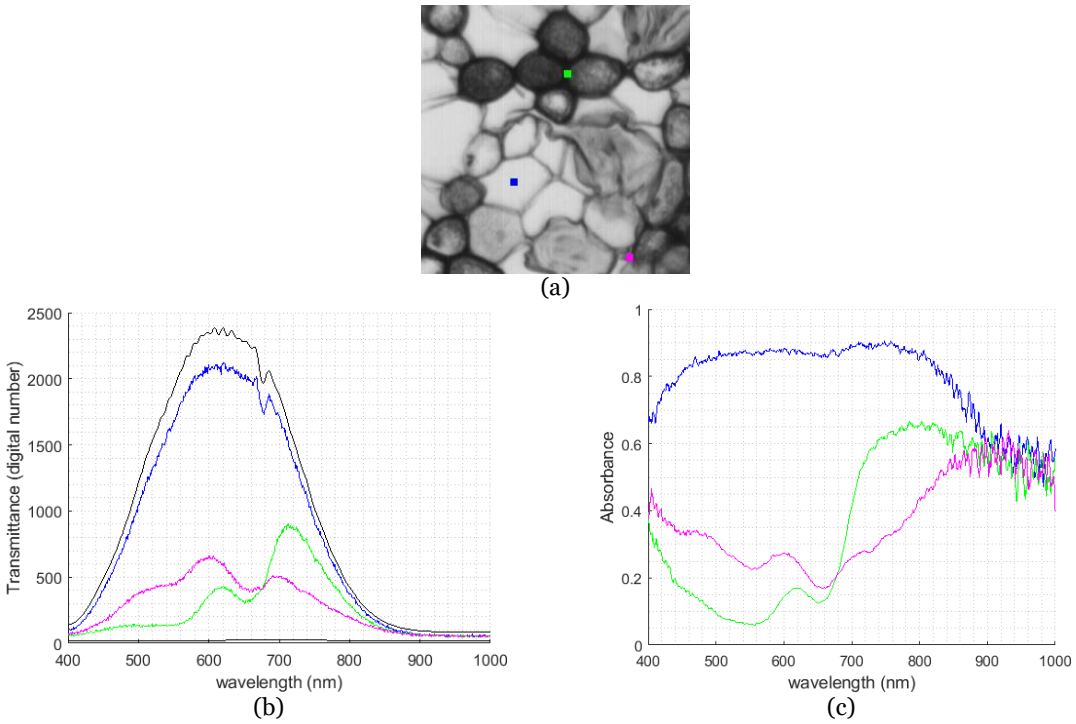

Figure 3-21: Effect of calibration in the spectral signatures. a) Selected pixel within an example image. b) Uncalibrated spectral signatures. c) Calibrated spectral signatures.

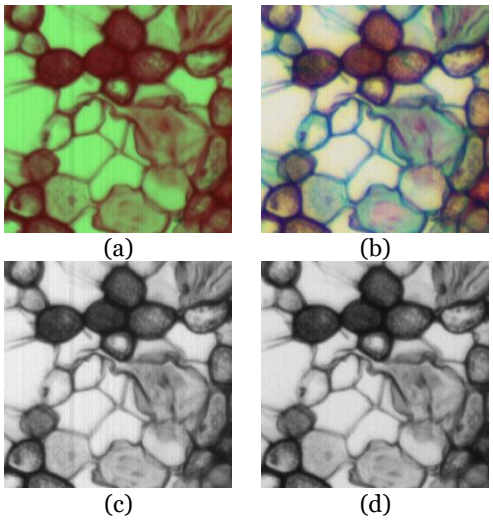

Figure 3-22: Real examples of the uncalibrated and calibrated spectral images. a) Uncalibrated RGB image (709.0, 539.5 and 479.6 nm). b) Calibrated RGB image (709.0, 539.5 and 479.6 nm). c) Uncalibrated single image band (539.5 nm). d) Calibrated single band image (539.5 nm).

3.3.9 Common defects in HS images

In this section, we show some examples of how the images look like when the setup of the HS acquisition system is not appropriate. To this end, we collected images from the micrometer ruler grid (Figure 3-9.b). Images were collected using the 20× magnification for this experiment. To perform the comparative between the different scenarios, we show the panchromatic images from the original HS cubes, i.e. we average all spectral channels and visualize the defects spatially. Figure 3-23 shows an HS image collected in adequate conditions, while Figure 3-24 illustrates some common defects in HS images.

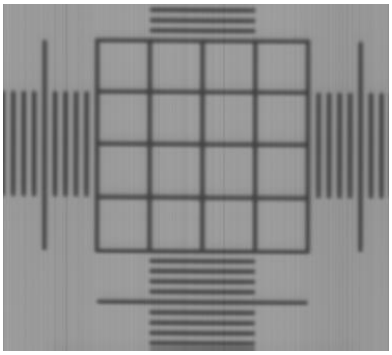

Figure 3-23: Correct HS image from a micrometer ruler.

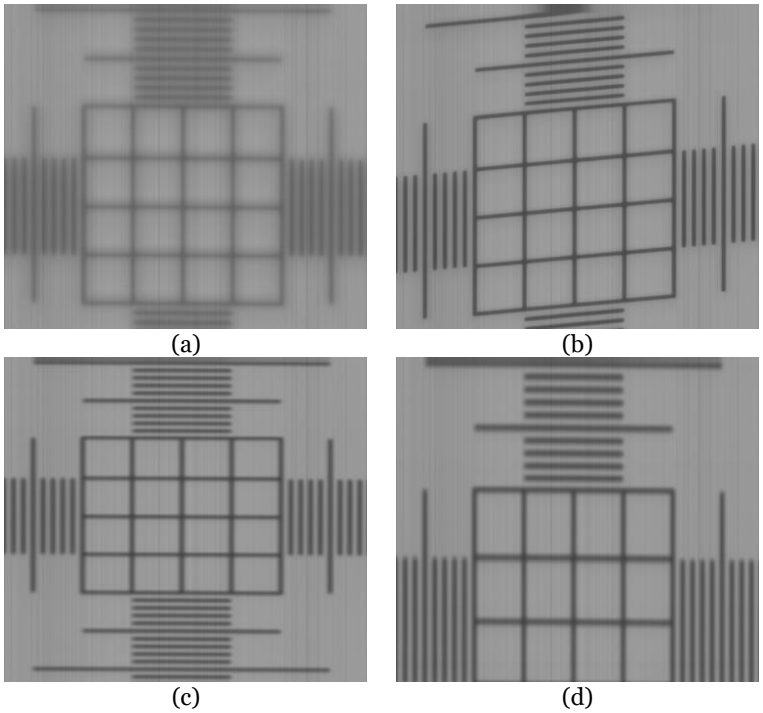

Figure 3-24: Common defects in HS images. a) Unfocused image. b) Misaligned image. d-e) Bad speed configuration (fast and low scanning speed respectively).

In Figure 3-24.a, we can observe an unfocused image. The image is not sharp, and hence small details are lost. Although it is desirable a proper focusing, there are several techniques to enhance the quality of badly focused images [321]. Besides, we can see the effect of an image captured when the camera and the microscope stage are not correctly aligned in Figure 3-24.b. As far as the spectral information is concerned, there will be no change in the spectral signature of different materials in a misaligned image. Nevertheless, this misalignment can cause morphological deformations over the sample,

which has to be avoided in applications where the morphological features of the samples are important.

Finally, we show the effect of a bad scanning speed configuration. On the one hand, if the scanning speed is fast compared to the sensor frame rate, some lines of the scene will be skipped, resulting in the loss of some information from the scene. The spatial appearance of a fast-scanning speed can be visualized in Figure 3-24.c, where the shape of the image seems to be flat compared with the original one. On the other hand, if the scanning speed is slow compared to the acquisition time, each line of the spatial scanning is re-sampled, resulting in an outstretched image of the original sample, Figure 3-24.d.

3.3.10 Capturing real samples

Finally, Figure 3-25 shows different representations of HS data collected from real samples using the described acquisition system at different magnifications. The specimens under evaluation are prepared slides from Brunel Microscopes (Brunel Microscopes, Wiltshire, U.K.), Specifically, we imaged a pine stem sample (BS17 Stem Structure) and a rat kidney histology sample (BS28 Rat Histology).

Figure 3-25 display a RGB representation of the data acquired using 5x, 10x and 20x magnifications from the BS28 Rat Histology and BS17 Stem Structure samples, respectively. As it happens in any microscope system, more spatial details can be observed for higher magnifications.

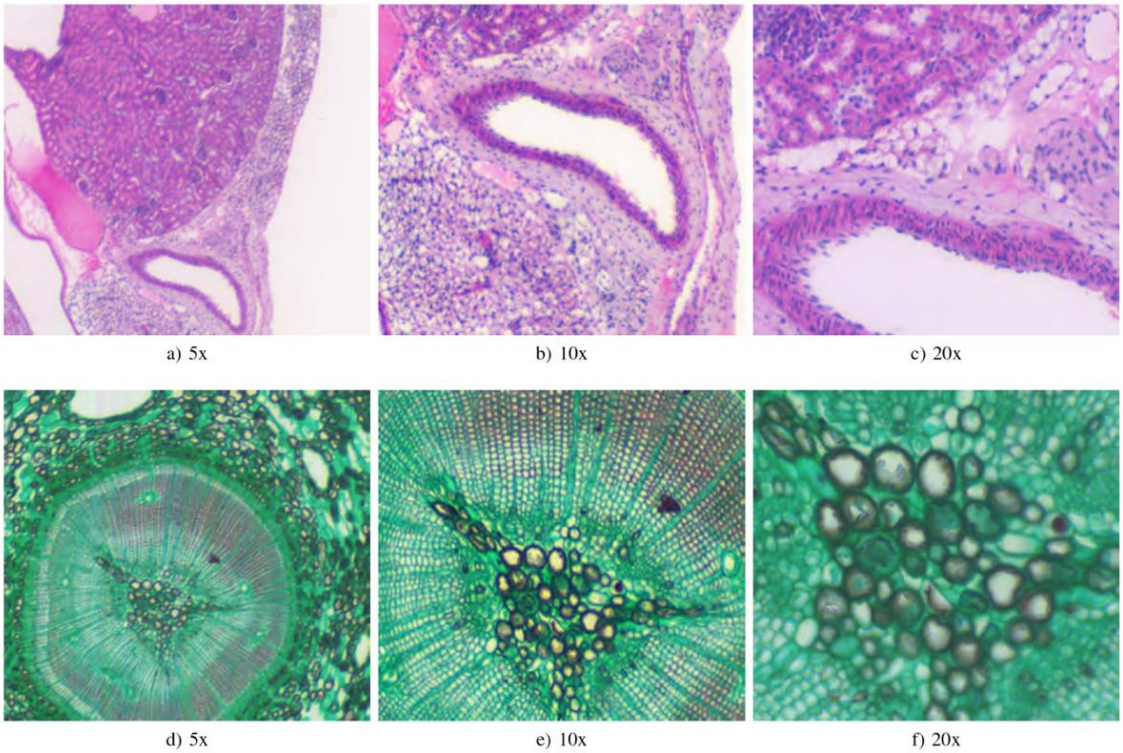

Figure 3-25: RGB representation of the HS data collected using different magnifications for the rat kidney histology sample (a-c) and for the pine stem sample (d-f).

Besides, Figure 3-26 shows some spectral signatures extracted from the HS data acquired using the 20x magnification. Each of these spectral signatures corresponds to one HS pixel of the image. As it can be observed, there are many differences in the spectral signatures displayed for both data sets. This suggests the presence of different

materials and provides the possibility of distinguishing them using their spectral characteristics, what justifies using microscope acquisition systems based on HS push-broom scanners for many different applications, such as the ones cited in Section 2.3. It can also be observed that the pixel size increases for lower magnifications, and targets that can be clearly distinguished using higher magnifications appear mixed in a single pixel. This results in mixed spectral signatures [43] making more challenging the detection of some specific targets, what justifies the use of high magnifications and resolutions for some applications where the targets to be analyzed are especially small.

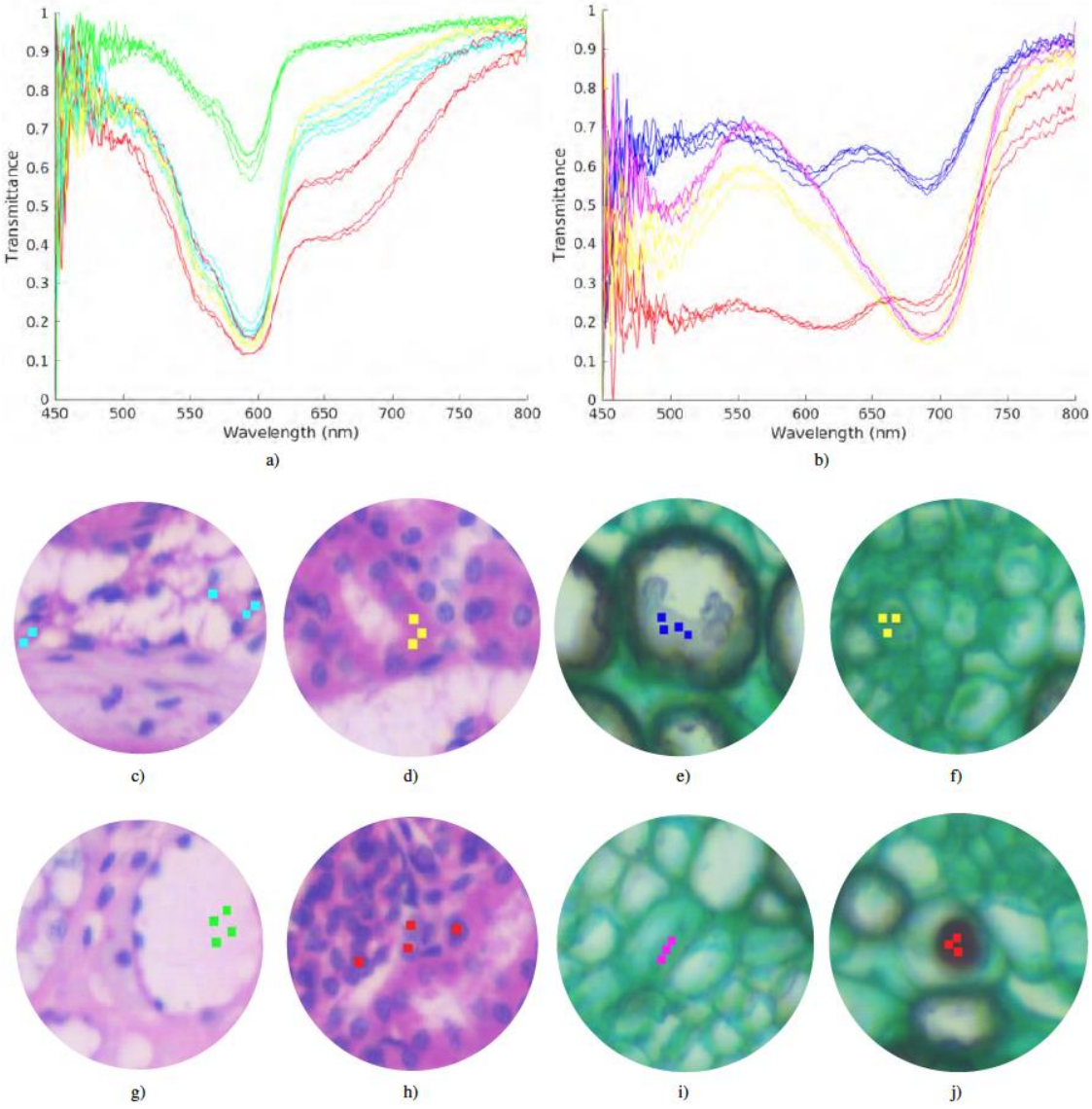

Figure 3-26: Spectral signatures present in the rat kidney histology sample (a) and the pine stem sample (b). Pixels corresponding to the rat histology sample are shown in subfigures (c), (d), (g) and (h). Pixels corresponding to the pin stem sample are displayed in subfigures (e), (f), (i) and (j).

3.4 Conclusions

In this chapter, we present the instrumentation that was used during this PhD. thesis, which is based on push-broom hyperspectral cameras. Among other HS technologies,

push-broom cameras present high spectral resolution, and are the ones able to capture HS images in the NIR or SWIR spectral ranges, making them a very interesting technology in this field.

First, we presented three different microscopic HS acquisition systems, and we discuss their main differences and drawbacks. Secondly, we presented a methodology to correctly set-up a push-broom HS microscope to acquire high-quality HS images. The main motivation of such methodology is to propose a sorted list of automatic and semi-automatic tasks that should be executed prior to acquire high-quality microscopic HS images using push-broom cameras. This methodology has been tested using a Hyperspec® VNIR A-Series from HeadWall Photonics coupled to an Olympus BH2-MJLT microscope, using a self-developed 3D printed mechanism for accomplishing the required mechanical movements, which provides a low-cost alternative to commercial motorized microscope stages. Nevertheless, the proposed methodology is intended to be general enough to be suitable for whatever microscope and whatever push-broom HS camera is used. This methodology involves the setup of the light conditions, the optical focusing of the system, the camera alignment and the setup of the optimal scanning speed. In addition, it allows the empirical measurement of both the FOV and the mechanical resolution of the scanning platform, as well as detecting and characterizing the limitations of the acquisition system under analysis.

Concretely, firstly a method for characterizing the HSI dynamic ranges and the latter optimization of the intensity of the light source and exposure time of the camera to achieve optimal illumination conditions has been proposed. Secondly, a method for correctly focusing the HS camera has been introduced using calibration slides and Y-lambda images. Thirdly, a method for calculating the adequate scanning speed has been introduced, which requires the previous knowledge of the pixel size and the mechanical resolution of the scanning platform. In case that these values are not known in advance, a methodology for empirically calculating them is also described. Finally, a semi-automatic method based on PCA has been introduced, which helps the user to precisely carry out the HS camera alignment as well as fine tuning the scanning speed. Additionally, this method for fine-tuning the scanning speed of a push-broom camera can be directly used even if the technical details of neither the optical system nor the mechanical system are known. However, the setup process may take considerably less time if an initial speed value closed to the optimal one is set.

The methodology presented in this dissertation is intended to provide a fast and accurate configuration of HS push-broom microscopes for researchers in this field. To be able to apply this methodology, a HS push-broom camera and a mechanism able to perform the linear movement of the sample are needed. Any push-broom camera is suitable to be used in the application of the proposed methodology, i.e. to perform the experiments regarding the dynamic range and the FOV measurements. As far as the mechanism is concerned, although in this dissertation we employed a custom 3D printed mechanism, commercial mechanisms are also compatible with the proposed methodology. To perform the steps of this methodology which involve a linear movement mechanism, the only requirement is to be able to control by software both the speed and the movement of the linear mechanism.

Although in this manuscript we have presented some quantitative outcomes (such as the relationship between the theoretical values of the FOV or the mechanical resolution and the experimental ones), we have not performed quantitative measurements of the

overall quality of the acquired HS images, both spatially and spectrally. In future works, we are planning to further investigate in this field in order to provide measurements of the quality of the HS images obtained by the acquisition system.

After applying this methodology to the acquisition system named System-II, some of its limitations have been described. Particularly, it has been observed that the illumination conditions are not optimal. The dynamic range cannot be maximized due to limitations in the light source power and also in the exposure time (which has an upper limit of 40 ms). To improve the dynamic range conditions in this scenario, an external light source could be used. Additionally, in the acquisition system under analysis, the focus is carried out manually by the user. Although we are able to acquire good quality images when focusing manually, a better focus plane configuration could be achieved if the Z-axis of the microscope were motorised.

Most of the aforementioned shortcomings of this acquisition system have been solved with the System-III. First, the Z-axis has been motorized, which facilitates the focusing procedure. Second, the spectral range of the microscope has been enhanced, enabling the exploitation of the spectral range beyond 1000 nm. Finally, there is possibility to use external light sources, which allows the improvement of the dynamic range, enabling the use of higher magnifications than 20×.

Chapter 4: Spectral-based classification of histological HS images

In this Chapter, we describe the use of HSI for the detection of brain tumor in pathological slides. In this research work, HS data from pathological slides belonging to human brain tissue suffering high-grade gliomas have been analyzed. The main goal of this study is to analyze if it is possible to discriminate between normal and tumor tissue in pathological slides by processing only the HS data.

Using the instrumentation described in the previous Chapter, several databases of histological slides diagnosed with high-grade gliomas have been generated, and then such images have been processed in order to retrieve from the HS data useful information for diagnosis. We present two different supervised learning approaches for the processing of the same biological samples. These two approaches are different since the acquisition system, the data partition and the processing framework are different.

This chapter is organized as follows. First, the biological samples available for this study are presented. Second, an approach to process the HS data with data belonging to low magnifications is presented. Finally, an improved acquisition and processing of high magnification HS images is presented.

4.1 Biological samples description

The specimens investigated in this research work consist of human biopsies extracted during brain tumor resection procedures (Figure 4-1). The pathological slides in this study were processed and analyzed by the Pathological Anatomy Department of the University Hospital Doctor Negrín at Las Palmas of Gran Canaria (Spain). The study protocol and consent procedures were approved by the *Comité Ético de Investigación Clínica-Comité de Ética en la Investigación* (CEIC/CEI) of the same hospital. After the resection, the samples were dehydrated and embedded in paraffin blocks. The blocks were then mounted in microtomes and sliced in 4 μm thick slices. Finally, the slices were rehydrated and stained with H&E. After routine examination of the samples, every sample was diagnosed by pathologists as glioblastoma (GB), according to the World Health Organization (WHO) classification of tumors of the nervous system [322].

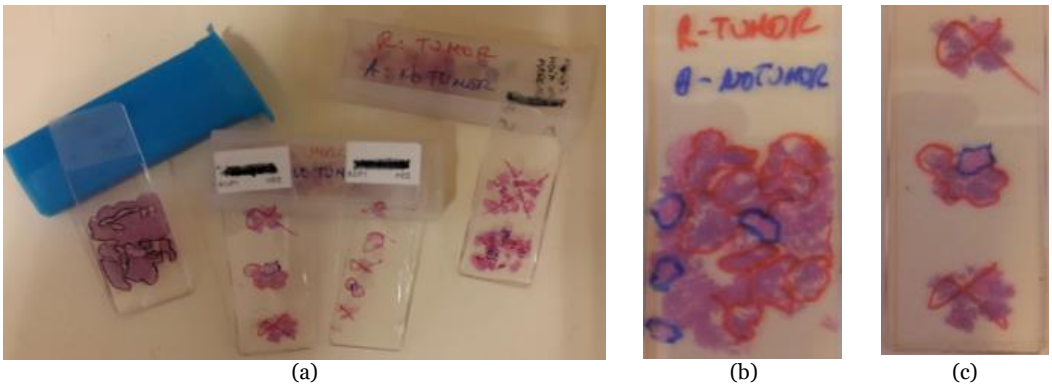

(a) (b) (c)

Figure 4-1: Biological samples. (a) Pathological slides overview. (b) and (c) Diagnosed pathological slides with the tumor and normal tissue surrounded by red and blue color respectively.

After the pathologist confirmed the GB diagnosis, macroscopic annotations of the GB locations were made on the physical glass slides using a marker-pen. Non-tumor areas are defined as areas in the pathological slide where there is no discrete presence of tumor cells. Within the areas annotated by a pathologist, we selected regions of interest (ROI) that were subsequently digitized using HS instrumentation. Within each ROI, different numbers of HS images were acquired for analysis. Figure 4-2 shows an example of the annotations within the pathological slide, and the selection of different ROIs (shown at 5×) and the HS images (imaged at 20×). In this case, red color annotations indicate areas diagnosed as GB, while non-tumor areas were annotated in blue marker.

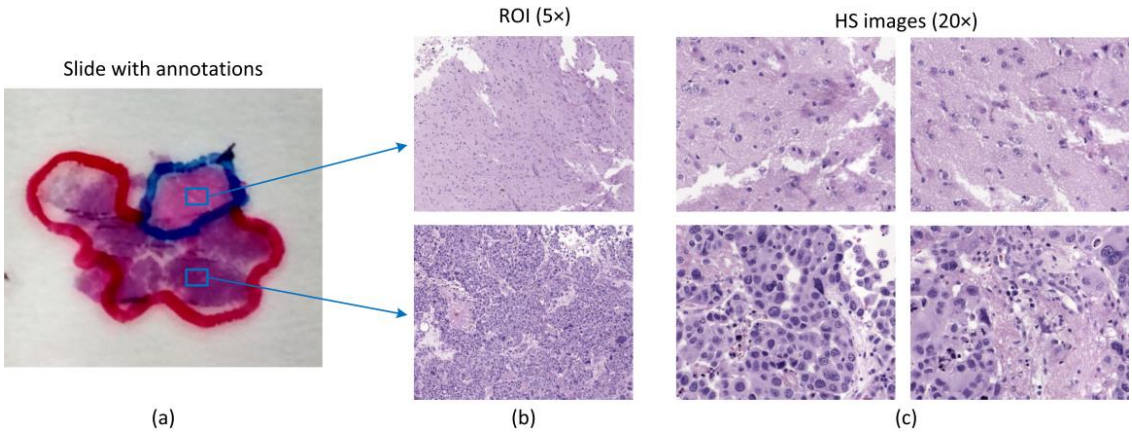

Figure 4-2: Pathological samples used in this study. (a) Macroscopic annotations performed in pathological slides after diagnosis. Blue squares denote ROIs within annotations. (b) ROIs from (a) shown at 5×. (c) Examples of HS images used in this study for classification (imaged at 20×).

4.2 Low magnification experiments

The experiments carried out in this research work were performed employing hyperspectral images obtained from human brain pathological slides, using a custom microscopic hyperspectral acquisition system. Then, data were processed with three different ML algorithms to classify and identify the tissue samples. Three different classifiers have been employed to automatically distinguish between tumor and normal tissue, using as features only the spectral information of the tissues. A qualitative description of this methodology has been recently published [323], and the work

described in this section has been published in a manuscript entitled "*Detecting brain tumor in pathological slides using hyperspectral imaging*" (2018, Biomedical Optics Express, OSA Publishing) [36].

4.2.1 Dataset description

In this research work we used the System-I described in Chapter 3. Such acquisition system is characterized by a low resolution of the mechanical system. As indicated in the description of the HS acquisition system, not all the spatial information can be captured by this HS camera. If the full spatial information would be available, the morphological characteristics of the tissue could be exploited, employing similar criteria of that used by pathologists for diagnosing (i.e. cell proliferation and nuclei morphology). Figure 4-3.c shows a typical histological image used by pathologist to diagnose brain tumor. Compared with Figure 4-3.a or b, it can be seen that the histological image allow distinguishing cells, what is not possible in the acquired HS images. This spectral information consists of a mixture of all tissues inside a certain area of a pathological slide. Nevertheless, in real applications, different regions of a tissue could have different spectrum. Although we would like to isolate the different elements in a pathological slide, i.e. cells, our scanning system constraints the spatial resolution of the images. For this reason, in this research study all the tissue inside an area is macroscopically extracted for the classification. Due to this fact, in this study only the spectral information obtained from the HS cubes has been taken into account. Furthermore, the objective of this research work is to analyze if solely the spectral signature analysis is a useful complementary tool for detecting brain tumor in pathological slides, as the morphological analysis has been already proven to be appropriate to this end.

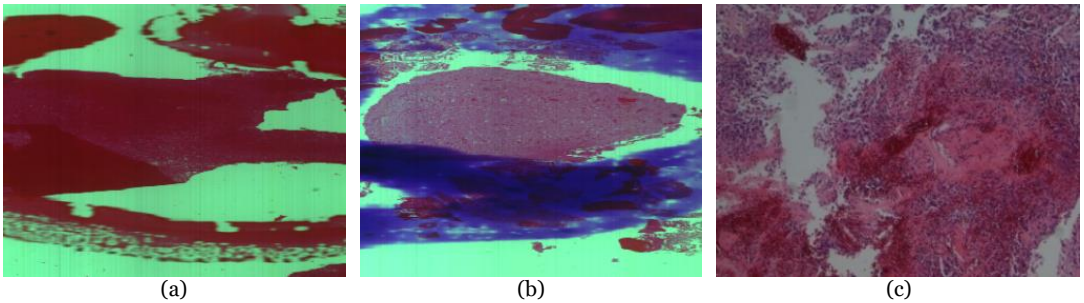

(a) (b) (c)

Figure 4-3: Synthetic RGB representations of a HS cube acquired from a pathological slide of (a) tumor tissue and (b) normal tissue. (c) Histological image of a brain tissue sample (10×).

Employing the microscopic HS acquisition system named System-I previously described in this document, the spectral database described in [32] was obtained. This database consists of 36 HS cubes collected using a 5× magnification. Each hyperspectral cube is composed by 826 spectral channels and 1004×600 pixels. Figure 4-3.a and b show the synthetic RGB representations of two different HS cubes captured from pathological slides presenting tumor and healthy tissue respectively. As previously mentioned, tissue inside red markers were diagnosed as tumor while tissue inside blue marker were diagnosed as normal tissue.

As it will be detailed next in the pre-processing chain description section, a ROI of each HS cube were defined to extract a spectral signature dataset. In this study, two different classes of tissue have been defined: tumor tissue and normal tissue. Table 4-1 summarizes the labelled dataset of spectral signatures available for each patient per

tissue class after defining the ROI and extracting the spectral data from each hypercube. The spectral signatures for both classes and all patients are shown on Figure 4-4. These spectral signatures have been calculated as the mean spectrum of each tissue type for each patient. The spectral signatures depicted in blue lines belong to normal tissue and the ones depicted in red lines belong to tumor tissue. After a visual inspection of these spectral signatures, it can be noticed that there are significant differences between the signatures of normal and tumor tissue, especially in the spectral range between 550 nm and 700 nm.

Table 4-1: Spectral signature labelled dataset summary

#Patient	#Total of spectral samples	
	Normal	Tumor
P1	36,648	36,685
P2	36,923	37,826
P3	35,159	35,181
P4	36,821	37,800
P5	37,321	35,230
P6	35,366	37,379
P7	36,605	37,718
P8	36,736	38,242
P9	-	38,325
P10	-	39,399

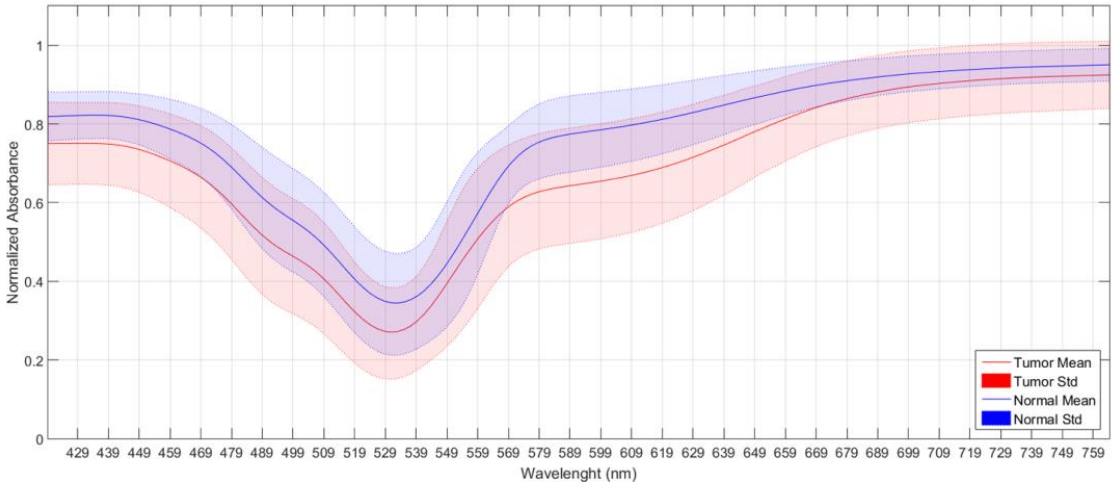

Figure 4-4: Average spectral signatures of tumor tissue (red) and normal tissue (blue) and their respective standard deviation.

4.2.2 Data partition strategy

In order to validate supervised classification algorithms for discriminating between normal and tumor tissue, three different case studies (CSs) have been proposed. This approach differs in which patients are included as subject of study. These scenarios are described below:

- **Case study 1 (CS1):** The goal of this CS is to check if the discrimination between normal and tumor tissue can be performed using the available labelled data, avoiding the inter-patient variability of data. The datasets explored in this CS include HS cubes from pathological slides where both type of tissue, normal and tumor, are present. In order to avoid the inter-patient variability of data, data

from each patient is used independently for training and testing the supervised classifiers. Patients #9 and #10 are not included in this CS because no normal samples are available from these two patients.

- **Case study 2 (CS2):** In CS2, all the available labelled data are merged into a unified dataset, taking into account the inter-patient variability in this scenario. All the samples for the ten patients have been included in this CS.
- **Case study 3 (CS3):** This case study is the most realistic one in a diagnosis context. In this scenario, each patient data are used independently as a test set for the classification algorithm. The classifier model is trained by using the information from the rest of the HS labelled data that belong to the remaining patients. This CS represents a real case where new samples arrive to the pathological laboratory and the classification must be performed using a classifier trained with data from previous patients.

In this research work, a 10-fold cross-validation (CV) was used as model validation scheme for CS1 and CS2, randomly partitioning the dataset in 10 folds and using only one fold for training the classifier (10% of data) and the remaining data are used to assess the classifier performance. The process is repeated until each fold has been used to train the classifier, and finally the classifier performance is calculated as the average of the performance obtained in each iteration. In CS3, it is not possible to apply cross-validation, so the model was evaluated using hold-out validation, where the test set corresponds to the spectral samples from one patient, and the classifier is trained using all the available spectral signatures from the remaining patients.

4.2.3 Processing framework

The proposed processing framework is based on a supervised classification scheme. Although it has been proven that combining both the spatial and spectral features of the hyperspectral images can improve the accuracy in the predictions [324], in this research work only the spectral characteristics of the data have been taken into account. The inputs of the classifiers are the measured spectral signatures from healthy and tumor pixels. Figure 4-5 shows an overview of the processing framework employed in this study. The first stage of the proposed framework consists of a pre-processing chain that aims to compensate the effects produced by the environmental conditions and the sensor response of the acquisition system during the capture procedure of the HS cubes. Then, a supervised classification is performed using three different classification methods. Finally, the performance of the classifiers is evaluated using standard metrics for assessing a classifier performance.

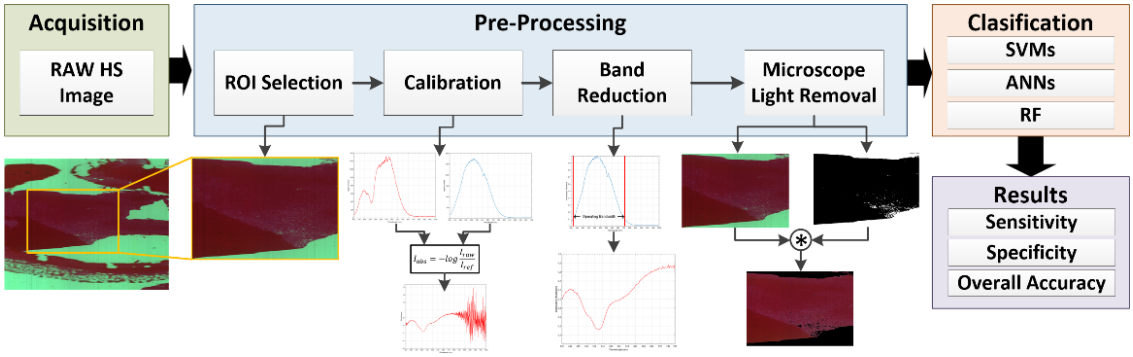

Figure 4-5: Processing framework block diagram.

4.2.3.1 Data preprocessing

The pre-processing chain proposed in this research work is based on four steps: 1) selection of the ROI; 2) image calibration; 3) spectral band reduction; and 4) removal of the microscope light inside the pathological slide where there is no tissue sample. Following, each step of the pre-processing chain is explained.

1) ROI selection: First, due to the high dimensionality of the HS cubes, which extremely slows down the processing of the data, a manual ROI selection is applied. In this procedure, the ROI selection is carefully performed taking a ROI that is a balanced solution between selecting a reduced area (that involves decreasing the computational cost) and choosing enough relevant data inside each area.

2) Calibration: The second stage of the preprocessing chain is related to the calibration of the image. Through the calibration, the acquired image is transformed from radiance observation to transmittance. The transmittance image (I_{trans}) is calculated by taking the ratio between the raw HS image (I_{raw}) with respect to a reference image (I_{ref}), as shown in Equation (11). This is a standard procedure for hyperspectral images [325]. The reference material provides a measure of the instrument response function from the resultant optical density image set [326]. Figure 4-6.a shows a single spectral signature extracted from the raw data acquired by the HS camera while Figure 4-6.b shows the reference spectrum of the microscope light, passing through an empty pathological slide, acquired by the HS camera. Finally, the calibrated spectrum in absorbance mode is shown in Figure 4-6.c.

$$\mathrm{I_{trans}} = -\log \frac{\mathrm{I_{raw}}}{\mathrm{I_{ref}}} \tag{11}$$

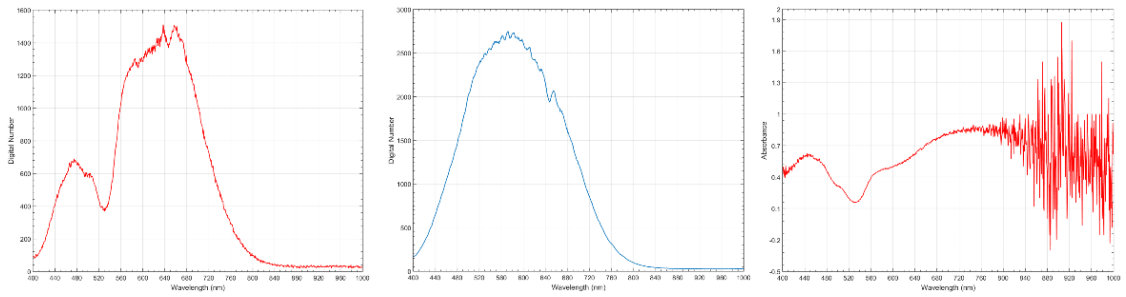

(a) (b) (c)

Figure 4-6: Spectral signatures of a single tumor pixel in each calibration step. (a) Raw spectrum. (b) Reference spectrum. (c) Calibrated spectrum.

3) Band reduction: The next stage in the pre-processing chain consists of a band reduction of the HS cube, since there are spectral channels which do not carry any relevant information. The band reduction is performed in two different ways. First, in the reference spectrum presented in Figure 4-6.b, it can be observed the measured intensity is almost zero for the extreme wavelengths (mainly produced because the microscope is not optimized to be employed beyond the limits of the visible spectral range). For this reason, such bands can be removed to avoid the inclusion of meaningless information in the machine learning scheme. The selected operating bandwidth covers the spectral range from 419 nm to 768 nm (Figure 4-7.a). Second, the measured spectral signatures present high redundancy between contiguous bands due to the high resolution of the HS camera sensor related with the diffraction capability of the optical

grating. The spectral resolution of the HS camera is 2.8 nm, obtaining 826 spectral bands, so each contiguous band is sampled at 0.6 nm approximately, thus producing redundant information. In order to avoid this redundancy and to reduce the dimensionality of the HS cubes (to accelerate the processing of the samples), the spectral bands were averaged in a similar way as proposed in [327]. The spectral signature generated after applying the band average can be observed in Figure 4-7.b. It can be observed that the overall shape of the spectral signature does not change compared with the full-spectra signature, with 826 spectral channels (Figure 4-6.c).

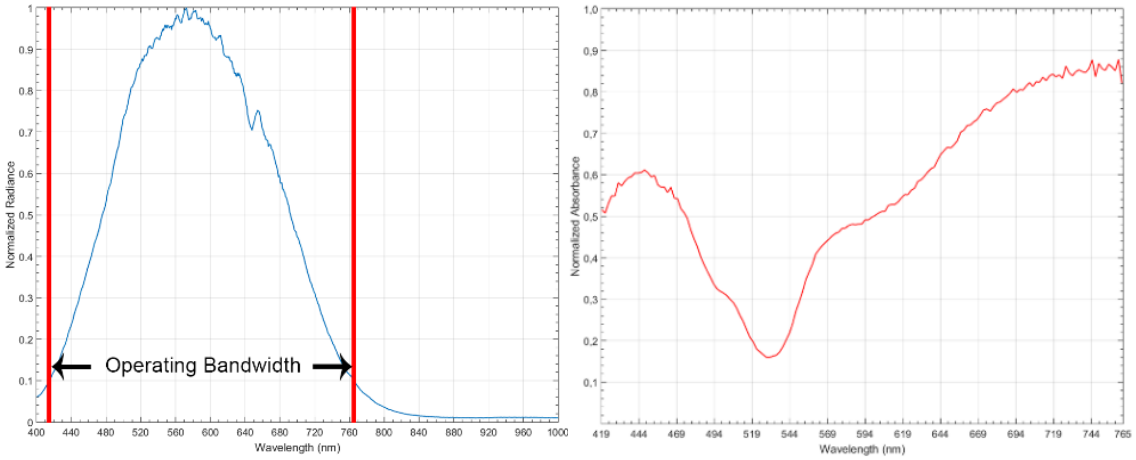

(a) (b)

Figure 4-7: Spectral signatures of a single pixel in the band reduction step. (a) Selected operating bandwidth in the reference spectrum. (b) Calibrated spectral signature after the spectral band reduction.

4) Microscope light removal: Finally, in order to process only the useful information of the HS cube, a method to discriminate between pixels that belong to the microscope light were developed. This method is based on a binarization process performed over the synthetic RGB image extracted from the HS cube, taking advantage of the white color of the measured light. After a manual selection of the suitable threshold for binarizing the image, it is possible to isolate the microscope light to avoid processing light pixels without relevant information. Figure 4-8.a shows the synthetic RGB representation of a HS cube acquired from a healthy pathological slide before the binarization process. Figure 4-8.b shows the binarized images and Figure 4-8.c the synthetic RGB representation after removing the pixels associated with the microscope light.

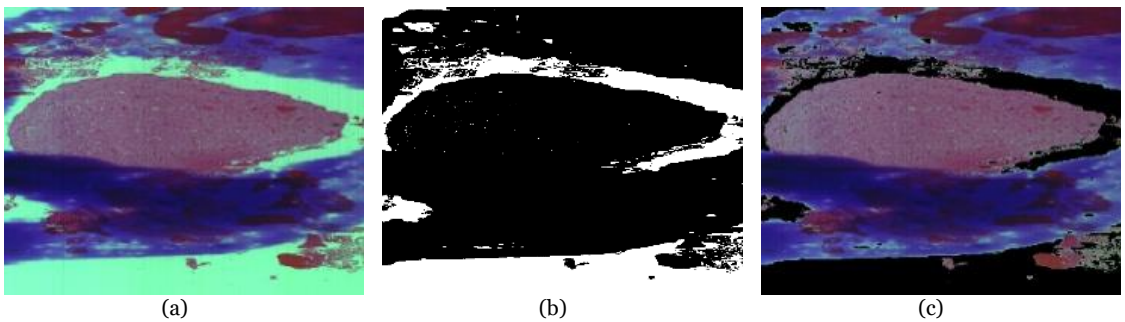

(a) (b) (c)

Figure 4-8: Synthetic RGB representations of a HS cube acquired from a healthy area of pathological slide. (a) Synthetic RGB image without light pixels removal. (b) Binarized image. (c) Synthetic RGB image after the binarization process application to remove light pixels.

4.2.3.2 Supervised classification

An extensive literature about pixel-wise classification of HS images is available in the current state-of-the-art. When using this technique, each pixel of a HS cube is assigned to a certain class based exclusively on its spectral signature analysis. For this purpose, approaches based on decision trees, neural networks and kernel-based methods have been widely used. These algorithms have to face two main problems: the high dimensionality of data and the limited size of sample data [328]. The supervised algorithms employed in this research work have been SVMs, ANNs and RF. In a recent review article [54], these classifiers have been highlighted among others, such as MLR or DL techniques, for the pixel-wise classification of hyperspectral images. Nevertheless, in this study we only analyses SVM, ANNs and RF as they have been shown to be more computationally efficient.

SVMs are kernel-based supervised classifiers that have been widely used in the classification of HS images. In the literature, it is shown that SVMs achieve good performance for classifying HS data, even when a limited number of training samples are available [329]. Due to its strong theoretical foundation, good generalization capabilities, low sensitivity to the curse of dimensionality, and ability to find global classification solutions, many researchers usually prefer SVMs instead of other classification algorithms for classifying HS images [125]. In this research work, the LIBLINEAR [330] integrated software for support vector classification has been used.

Recent remote sensing literature has shown that SVM methods generally outperform traditional statistical analysis based on ANN methods in classification problems involving HS images. Nevertheless, ANNs have been also successfully employed in the classification of HS images [329], [331]. Some studies have applied ANNs as classifiers over HS images in the medical field [332], [333]. The ANN used in this research work is a feed forward MLP network, trained using a backpropagation algorithm. The MATLAB® Neural Network Toolbox™ has been selected to test the quality of these algorithms in the classification of in-vitro hyperspectral brain tissue.

Finally, the third algorithm considered in this supervised classification approach is Random Forest. RF is an ensemble classification algorithm that builds a set of classifiers and classify new data by performing a voting of their predictions [334]. In order to test this supervised ensemble algorithm in the classification of HS pathological data, the MATLAB® Machine Learning Toolbox™ has been employed.

4.2.3.3 Evaluation metrics

The results obtained by the supervised classifiers were evaluated using the standard sensitivity, specificity, and overall accuracy (ACC) metrics. These are frequently employed as statistical measures of the performance of hyperspectral image classification[252], [335], [336]. Sensitivity is related to the tests ability to identify a condition correctly. It is obtained as the number of true positives (TP) divided by the total number of true positives and false negatives (FN) in a population (Equation (12)). Specificity is related to the tests ability to exclude a condition correctly. It is obtained as the number of true negatives (TN) divided by the total number of true negatives and false positives (FP) in a population (Equation (13)). Finally, overall accuracy is calculated by dividing the total number of successful results by the total population (Equation (14)).

$$\text{Sensitivity} = \frac{\text{TP}}{\text{TP} + \text{FN}} \tag{12}$$

$$\text{Specificity} = \frac{\text{TN}}{\text{TN} + \text{FP}} \tag{13}$$

$$\text{ACC} = \frac{\text{TotalSuccess}}{\text{TotalPopulation}} \tag{14}$$

4.2.4 Experimental results

This section presents the results achieved after applying the supervised classification framework described in section 2 to the histological human brain hyperspectral dataset. These results present the performance estimation of each classifier for each CS. In addition, the computational time of each classifier is shown as a measure of the time required to train and evaluate the performance of each classifier, employing a computer with Intel® Core™ i7-4770k at 3.5 GHz.

Three different supervised classifiers were evaluated: SVMs, ANNs and RF. A linear kernel has been tested in the SVM classifier. Several ANN topologies were tested, (varying the number of hidden layers, the number of neurons inside each layer and the activation function selected for each layer). The selected ANN topology consists of a multilayer neural network with two hidden layers composed by 36 and 16 neurons respectively (employing a logistic activation function for these layers) and using a hyperbolic tangent sigmoid activation function for the output layer. After simulating the classifier using different network topologies, it has been experimentally determined that this architecture is the most suitable for this application. Finally, an ensemble of 50 different classification trees composes the RF configuration. It has been detected that the use of an increased number of classification trees does not improve the classification accuracy.

4.2.4.1 Case Study 1

As described before, CS1 implies the classification of data that only belongs to a single patient. The main goal of this CS is the evaluation of the possibility of discriminating between the spectral signatures belonging to tumor or normal areas of the pathological slides when no inter-patient variability of data is considered. For this reason, due to the absence of normal tissue for patient #9 and #10, these patients were not included in this experiment. The estimation of the model performance was obtained using 10-fold cross-validation. Table 4-2 shows the classification results obtained for each classifier per patient in this CS.

It can be seen that the results achieved employing the SVM classifier offers a competitive discrimination between normal and tumor tissue with high sensitivity and specificity (higher than 90% in any case). On the other hand, the results obtained using ANNs outperform 93% of overall accuracy for every patient, being the most suitable classifier for this CS. In terms of specificity and sensitivity, these results show a good discrimination rate between the different classes, being the sensitivity and specificity values also higher than 93% in all the cases, achieving an average ACC of 97.88%. Regarding the computational cost, ANNs show a higher computational cost compared with the SVM classifiers for this CS. Finally, RF also offers accurate results to

differentiate between normal and tumor tissue, achieving results that outperform 89.5% of specificity and sensitivity.

Table 4-2: Supervised classification results in CS1.

Classifier Type	#Patient	ACC (%)	Sensitivity (%)	Specificity (%)	Time–1 Fold (s)	Time–10 Fold (s)
SVM Linear Kernel	P1	98.84	99.06	98.63	16.59	165.96
	P2	99.99	99.99	99.98	1.89	18.97
	P3	97.83	97.49	98.17	11.02	110.22
	P4	96.89	96.41	97.35	12.54	125.42
	P5	97.32	97.07	97.58	12.27	122.74
	P6	90.55	91.02	90.11	30.08	300.84
	P7	91.61	90.30	92.89	26.28	262.87
	P8	97.24	96.67	97.79	20.81	208.11
	Avg.	96.28	96.00	96.56	**16.44**	**164.39**
ANN	P1	98.79	99.00	98.58	84.35	843.57
	P2	99.99	99.99	99.99	30.05	300.56
	P3	98.94	98.93	98.95	74.71	707.19
	P4	99.05	98.71	99.38	70.66	706.62
	P5	98.23	98.33	98.12	83.07	830.75
	P6	93.75	93.11	94.37	84.41	844.17
	P7	94.37	94.49	94.26	86.04	860.47
	P8	99.91	99.89	99.93	66.64	666.43
	Avg.	**97.88**	**97.81**	**97.95**	72.49	719.97
RF	P1	97.76	98.20	97.32	27.76	277.62
	P2	99.93	99.92	99.93	16.01	160.12
	P3	96.91	96.04	97.78	27.00	270.08
	P4	98.54	98.03	99.03	23.40	234.07
	P5	95.88	95.47	96.31	28.79	287.98
	P6	91.73	91.67	91.79	38.29	382.98
	P7	90.48	89.50	91.43	39.86	398.61
	P8	99.76	99.68	99.84	20.87	208.79
	Avg.	96.37	96.06	96.68	27.75	277.53

The results achieved in the CS1 scenario shows that all the classification algorithms can reach significant classification results. The behavior measured for all the classifiers is very similar in this CS, having close averaged metrics around 96% of overall accuracy, specificity and sensitivity. It can be observed that the classification quality also depends on the subject of study, i.e. patients #6 and #7 show lower accuracy than the other patients whatever classifiers is employed. The worst results in terms of overall accuracy are higher than 90% of success, and the values of sensitivity and specificity outperform 89.5% in all the cases. As far as computational cost is concerned, it can be seen that SVM and RF can perform the training and classification tasks more efficiently.

4.2.4.2 Case Study 2

This CS aims to introduce some inter-patient variability in the classification task by merging all available data from all patients in a single dataset. The model evaluation was accomplished through 10-fold cross-validation. The results achieved by all the classifiers for this CS are shown in Table 4-3. Although the discrimination rate in all the supervised classifiers present good discrimination capabilities to distinguish normal and tumor tissue (higher than 80% in terms of overall accuracy, sensitivity and specificity), the results have worsened compared to CS1 results. In this CS, RF and ANNs show the most competitive classification results, with values of overall accuracy, sensitivity and specificity higher than 90%. It can be also observed that the results achieved using SVM

have the lowest accuracy, which metrics around 80%. The computational cost in this CS has extremely increased compared with CS1 time results due to the higher amount of data that compose the CS2 dataset (more than 665,000 spectral signatures). In this CS, the computational time required for ANNs is much higher than the one required for SVM or RF. The time consumed by ANNs is almost twice than RF or SVM for training the classifier and evaluating its performance. For these reasons, RF provides more competitive prediction results, having significantly lower computational cost. Although the SVM classifier performs the classification with a lower computational cost compared to ANNs, the classification performance is slightly worst.

Table 4-3: Supervised classification results in CS2.

Classifier Type	ACC (%)	Sensitivity (%)	Specificity (%)	Time−1 Fold (s)	Time−10 Fold (s)
SVM Linear Kernel	82.94	86.33	79.14	**418.53**	**4185.4**
ANN	91.71	92.45	90.78	795.16	7951.6
RF	**93.25**	**93.97**	**92.35**	467.95	4679.6

4.2.4.3 Case Study 3

This experimental setup emulates a realistic situation where a pathological slide, belonging to a new patient, arrives to the Pathological Anatomy department and the prediction of the disease is performed based only on the information from previous patients. In this CS, the model evaluation is performed following a hold-out method, where the samples from a certain patient are used as a test set to evaluate the performance of the classifier model generated employing the remaining patients of the database. Patients #9 and #10 only have tumor tissue samples, so the measurement of the specificity cannot be obtained due to the impossibility of getting neither false positives nor true negatives. Therefore, the overall accuracy and the sensitivity are the same for these two patients.

Table 4-4 shows the classification results of each classifier per patient in the CS3 as well as the computational time results for the hold-out process. It can be seen that the classification results of this CS are not as accurate as in the other two cases. Furthermore, as it can be observed, the sensitivity and specificity values are not balanced as occurs in the other CSs. Unlike the results obtained in CS1, the prediction accuracy strongly varies between the different patients. There are some success subjects in this study, such as patients #1, #2, #3, #9 and #10, where the classification results are higher than 80% of overall accuracy. Some patients even show a classification accuracy similar to the one obtained in CS1, for instance patient #2 using the SVM classifier. Nevertheless, the models cannot be generalized enough to produce quality prediction about tissues diagnosis in the rest of the patients.

The best classification results are obtained for patient #9 where the overall accuracy and sensitivity are higher than 98% whatever classifier is employed. According to Table 4-4, it is possible to see that there could be chance for cross-fertilization between the different classifiers. For instance, the results obtained using SVM for patient #1 are better than 90% of overall accuracy, whereas the results for the patient #3 using this same classifier are near to 80%. Analogously, the results obtained for patient #1 in ANN is about 80% of overall accuracy, while the results for patient #3 are better (90%). Moreover, ANN achieves the best average overall accuracy (78.02%), SVM achieves the best average sensitivity (75.69%) and RF achieves the best average specificity (79.33%), demonstrating that none of the analyzed classifiers is optimum for all the patients. This

fact can motivate an ensemble of supervised classifiers where the misclassifications from one classifier are compensated with the correct classification of another. Following the same trend as in the other CSs, ANNs are the classifier with the higher computational load.

Table 4-4: Classification results in CS3.

Classifier Type	#Patient	ACC (%)	Sensitivity (%)	Specificity (%)	Time (s)
SVM Linear Kernel	P1	90.65	92.19	89.12	468.73
	P2	96.75	99.97	93.62	492.41
	P3	80.37	63.26	97.46	457.00
	P4	66.62	66.93	65.54	426.61
	P5	57.18	62.27	51.78	381.72
	P6	38.75	21.81	54.77	349.74
	P7	81.10	74.62	87.40	428.12
	P8	58.82	90.80	28.11	413.94
	P9	99.48	99.48	-	410.59
	P10	85.58	85.58	-	474.33
	Avg.	75,53	**75.69**	70.97	**430.31**
ANN	P1	86.51	79.87	93.14	788.04
	P2	82.48	99.95	65.42	778.60
	P3	92.48	86.60	98.35	781.80
	P4	70.36	67.23	73.40	774.45
	P5	61.20	38.72	85.02	781.99
	P6	53.67	24.67	81.10	786.06
	P7	72.84	68.36	77.18	771.44
	P8	69.91	98.23	42.70	776.62
	P9	98.73	98.73	-	824.74
	P10	92.04	92.04	-	830.83
	Avg.	**78.02**	75.44	77.03	789.45
RF	P1	80.54	70.35	90.72	426.62
	P2	92.18	99.39	85.15	506.75
	P3	8i6.46	73.62	99.28	489.01
	P4	66.46	57.11	75.56	466.18
	P5	58.87	41.64	77.13	443.80
	P6	60.69	39.74	80.51	437.98
	P7	70.93	60.26	81.29	444.93
	P8	69.59	95.18	45.01	461.59
	P9	99.42	99.42	-	526.78
	P10	92.70	92.70	-	513.57
	Avg.	69.13	72.94	**79.33**	471.72

4.2.5 Discussion

In this section we have proposed and validate several supervised classification methods to obtain an automatic diagnostic tool based on HSI to assist pathologist in the task of distinguishing between tumor and non-tumor human brain tissue using pathological slides. For this purpose, customized microscopic HS instrumentation was used (System-I, described in the previous chapter).

One of the main challenges of this research was the creation of the first library of spectral signatures from different tissues, which have been collected according to the current diagnosis of the tissue, provided by a pathologist. The contents depicted in this section are just a step forward in the achievement of an automatic diagnosis tools.

The research shown in this section presents several drawbacks. First, the instrumentation used for this study is not suitable to capture the whole spatial information of a pathological slide, and thus the spatial information of the HS cube cannot be used in the image processing scheme. Additionally, this restriction in the spatial resolution imposes the use of a low magnification (5x) for this study. Second, in terms of the data partition, CS1 and CS2 represent a proof of concept to demonstrate the capabilities of HS data processing for the discrimination between tumor and normal areas in histological slides. However, such experimental design is not appropriate since data from the same patient are used for both train and test the supervised classifiers, which can lead in a data leakage problem. Finally, the optimization of the classifier hyperparameters have not been carried out exhaustively. In this sense, the classification performance can be also further improved.

In the next Section, we present an evolution of this research work where most of the aforementioned shortcomings are addressed.

4.3 High magnification experiments

In this section, we propose to further investigate the effectiveness of the exclusive exploitation of the spectral information within HS images. For this reason, we have created a new database of HS data from brain histological slides using a more sophisticated acquisition system (System-III). Such acquisition system allows to capture all the spatial information from the histological slides, and also allows the exploitation of the spectral range up to 1000 nm. Additionally, both the data partition scheme and the hyperparameter tuning of the supervised classifiers are improved.

The novel contributions of this work are as follows. First, we explore superpixels for region-based grouping of similar pixels using both spatial and spectral information in HS digital histology images from GB tumor patients. For superpixel generation, we utilized the original SLIC (Simple Linear Iterative Clustering) algorithm but modifying the distance metric to be more suitable for spectral data. Next, the objective of this work is to employ only the spectral information from superpixels for supervised classification for GB tumor detection.

The work described in this section has been published in a manuscript entitled "*Hyperspectral Superpixel-Wise Glioblastoma Tumor Detection in Histological Samples*" (2020, Applied Sciences, MDPI) [52].

4.3.1 Dataset description

The dataset for this study consisted of a set of HS images acquired from human brain histological slides, as described in Section 4.1. For this research work, we used the System-III (Figure 4-9.a) described in the previous chapter. Such acquisition system is characterized by a high spectral sensitivity in the spectral range from 400 to 1000 nm, and an accurate mechanical system, which allows the acquisition of the full spatial information of a sample. Using this system, we were able to address the aforementioned disadvantages of the previous acquisition system (System-I).

To ensure high quality acquisitions, the methodology proposed in the previous chapter to maximize the quality of HS images acquired with a push-broom microscope

[134] was followed. This methodology includes the optimal speed determination of the scanning, a dynamic range configuration, an appropriate alignment, and the correct focusing procedure. We developed custom software for synchronizing the scanning movement and the camera acquisition. Although we are not focused on collecting a whole-slide HS image of the specimens, the software was developed to allow the acquisition of consecutive HS cubes in a row to save time in the acquisition of the images, thus reducing the human intervention in the process. Due to the challenges imposed by the high dimensionality of the HS images, we decided to collect images with a spatial size of 800 lines, producing HS cubes of 800 × 1004 × 826, *i.e.* number of lines × number of rows × number of bands.

HS image acquisition was performed within the annotated areas of tumor and non-tumor in the slides (Figure 4-9.b). The spectral range of the images was from 400 to 1000 nm with a spectral resolution of 2.8 nm, sampling 826 spectral channels. The camera captures 1004 pixels per line, and the image width was fixed to 800 lines. The images were captured using 20× magnification, producing a HS image size of 375 × 299 µm (Figure 4-9.c). After pre-processing, the HS cubes were formed by 275 spectral channels. Further details about the acquisition system and the data acquisition procedure can be found in Chapter 3.

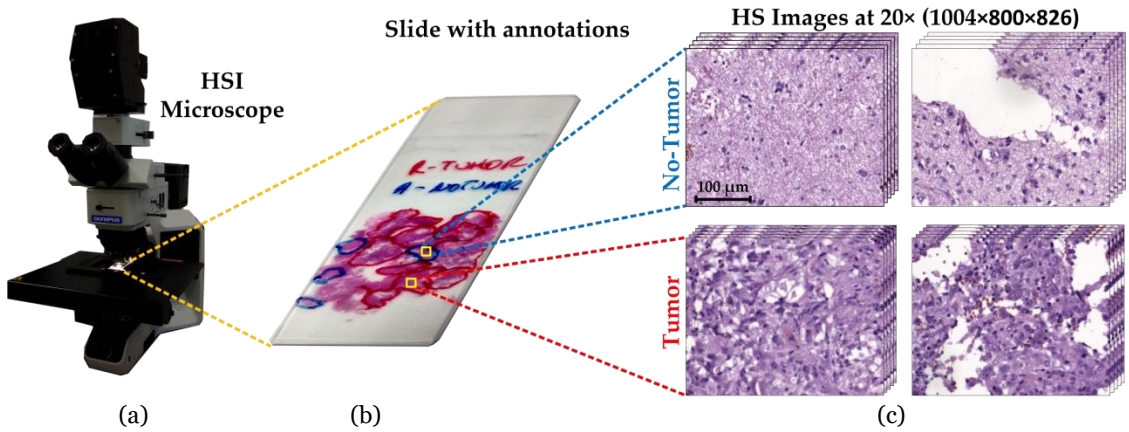

Figure 4-9: HS data acquisition procedure. (a) HS microscope-based acquisition system. (b) Pathological slide with macroscopic diagnosis annotations. Yellow squares represent an example of the captured areas for tumor and non-tumor HS images. (c) Examples of non-tumor and tumor HS images acquired at 20×.

Using the aforementioned instrumentation, some of the areas highlighted by pathologists from each slide were imaged. The positioning joystick of the microscope was used to select the initial position of the first HS image within a ROI to be captured. Then, we configured in the software the number of images to be captured consecutively. This number of images should keep relatively low to avoid the focus worsening of the images throughout the specimen. In this case, a maximum of 10 HS images were extracted consecutively from a ROI. We used a 20× magnification for image acquisition, producing a HS image size of 375 × 299 µm. This magnification was chosen because it allowed the visualization of the cell morphology, and hence the classifier was able to exploit both the spatial and the spectral features of data. In Figure 4-10, we show some examples of HS images used in this study, together with the spectral signatures of representative tissue components, i.e. cells and background for both tumor and non-tumor regions.

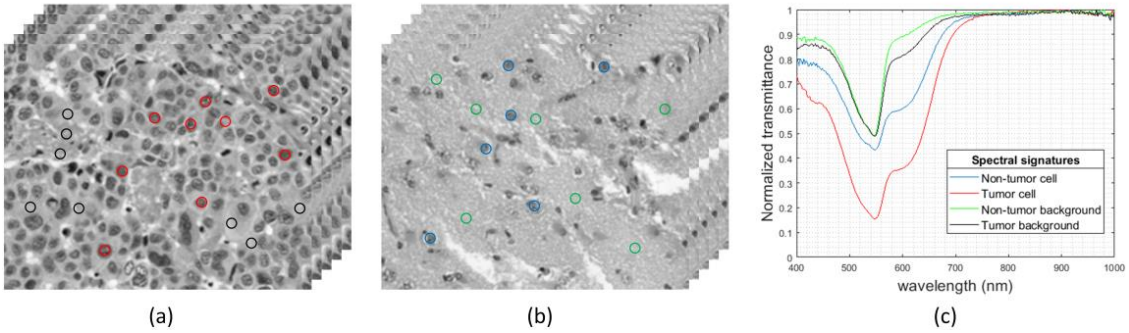

Figure 4-10: HS histopathological dataset. (**a**) and (**b**) are HS cubes from tumor and non-tumor samples, respectively. (**c**) Spectral signatures of different parts of the tissue: tumor cells (red), non-tumor cells (blue), tumor background tissue (black), and non-tumor background tissue (green).

A total of 494 HS images were acquired from 13 slides from 13 different patients with GB. A brief description of the dataset can be seen in Figure 4-11, which demonstrates that the dataset is not balanced, having more samples from non-tumor tissue than tumor tissue. Additionally, some of the slides only contained tumor tissue, as occurs in patients P9 to P13.

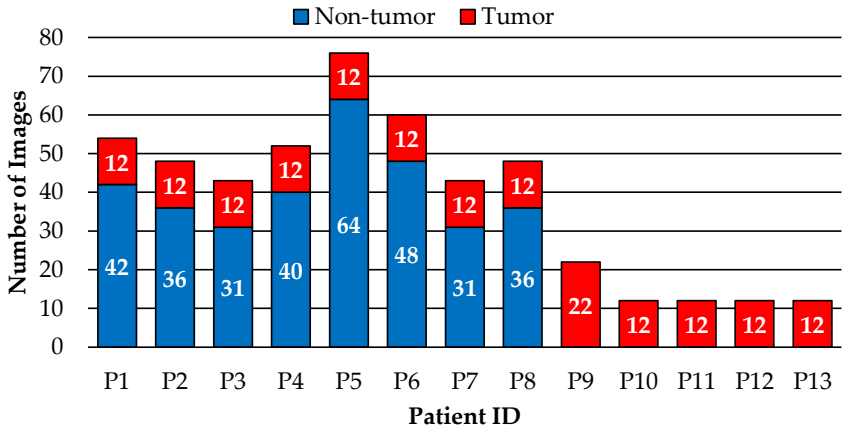

Figure 4-11: Number of non-tumor and tumor HS images per patient

4.3.2 Data partition strategy

In order to perform the machine learning analysis, an unbiased data partition should be performed. The dataset used for this study poses three problems. First, the dataset is limited in the number of patients. Second, samples containing both classes (non-tumor and tumor) are only available for 8 patients. Hence, the information about the non-tumor samples is limited in terms of patients. Third, the dataset is not balanced, having more images annotated as non-tumor.

In this work, we split data into training, validation and test sets. We are targeting a real clinical application. For this reason, the data partition scheme is intended to minimize bias, where the patients used for train, validation and test are independent. We are limited to 13 patients, where five of them only have samples belonging to tumor class. For this reason, we decided to perform the data partition in 4 different folds, where every patient should be part of the test set across all the folds. We propose the use of three folds with 9 training patients, a single validation patient, and 3 test patients. The remaining fold is composed by 8 training patients, a single validation patient, and 4 test patients.

Regarding the distribution of the classes in each fold, the patient selected for validation in each fold should have samples from both types of classes (non-tumor and tumor). The initial data partition scheme is shown in Table 4-5, where data from patients who only have tumor samples has been highlighted (‡).

Table 4-5: Data partition design (patients with only tumor samples are marked with ‡).

Fold ID	#Training Patients	#Validation Patients	#Test Patients
F1	9 (5 + 4‡)	1	3 (2 + 1‡)
F2	9 (5 + 4‡)	1	3 (2 + 1‡)
F3	9 (5 + 4‡)	1	3 (2 + 1‡)
F4	8 (5 + 3‡)	1	4 (2 + 2‡)

We decided to make the patient assignment randomly within the different folds. However, the distribution of patients in fold F4 was different from the others, and required some minor manual adjustments in data partitioning. Nonetheless, the rest of assignments were performed randomly. Fold F4 required assigning two tumor-only specimens for testing, so we decided to manually assign the tumor-only samples that have the least number of patches (i.e. P10 and P12). Furthermore, because fold F4 had fewer training patients compared to the other folds, we decided to assign the patient with the most patches (i.e. P5) to train this fold. The final data partition into the different folds is shown in Table 4-6.

In summary, the data partition used in this research consists of dividing the data in four different folds, each one built with patient-independent train, validation and test sets (Figure 4-12).

Table 4-6: Final data partition (patients with only tumor samples are marked with ‡).

Fold ID	Training Patients	Validation Patients	Test Patients
F1	P2, P3, P4, P5, P8 P9‡, P10‡, P12‡, P13‡	P6	P1, P7, P11‡
F2	P1, P2, P5, P7, P8 P9‡, P10‡, P11‡, P12‡	P3	P4, P6, P13‡
F3	P1, P3, P4, P6, P8 P10‡, P11‡, P12‡, P13‡	P7	P2, P5, P9‡
F4	P2, P4, P5, P6, P7 P9‡, P11‡, P13‡	P1	P3, P8, P10‡, P12‡

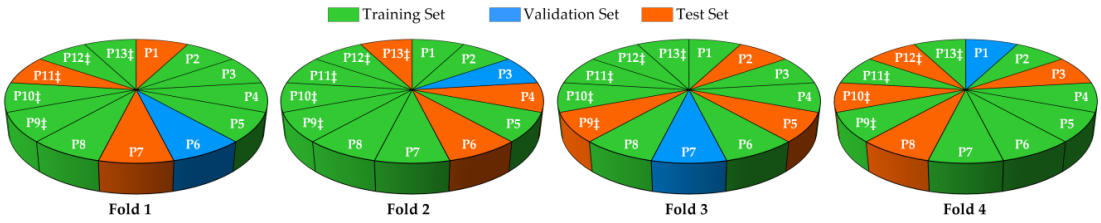

Figure 4-12: Data partition among the different folds (patients with only tumor samples are marked with ‡).

4.3.3 Processing framework

The proposed processing framework is divided into six steps (Figure 4-13). First, homogenous spectral areas of the input HS cube (Figure 4-13.a) are extracted by using a superpixel segmentation algorithm (Figure 4-13.b). The main motivation on the use of a superpixel segmentation approach prior to classification is to alleviate the amount of data to be processed, without losing relevant information from the HS image. After superpixel segmentation, superpixels belonging to the background light of the

microscope are removed, while superpixels corresponding to tissue are stored (Figure 4-13.c). Since the annotation of the images was performed at a macroscopic level, all the superpixels extracted from a single image are annotated as non-tumor or tumor depending on the annotation of the current image (Figure 4-13.d). Finally, the spectral data from all patients in a fold are used to train, validate and optimize, and test a supervised classifier (Figure 4-13.e). In the test stage, the prediction about the diagnosis of each superpixel (non-tumor or tumor) is performed using the classifier trained and optimized in the training/validation stage. Finally, the classification performance is quantitatively measured, and a representation of the classification is provided as heat and classification maps (Figure 4-13.f).

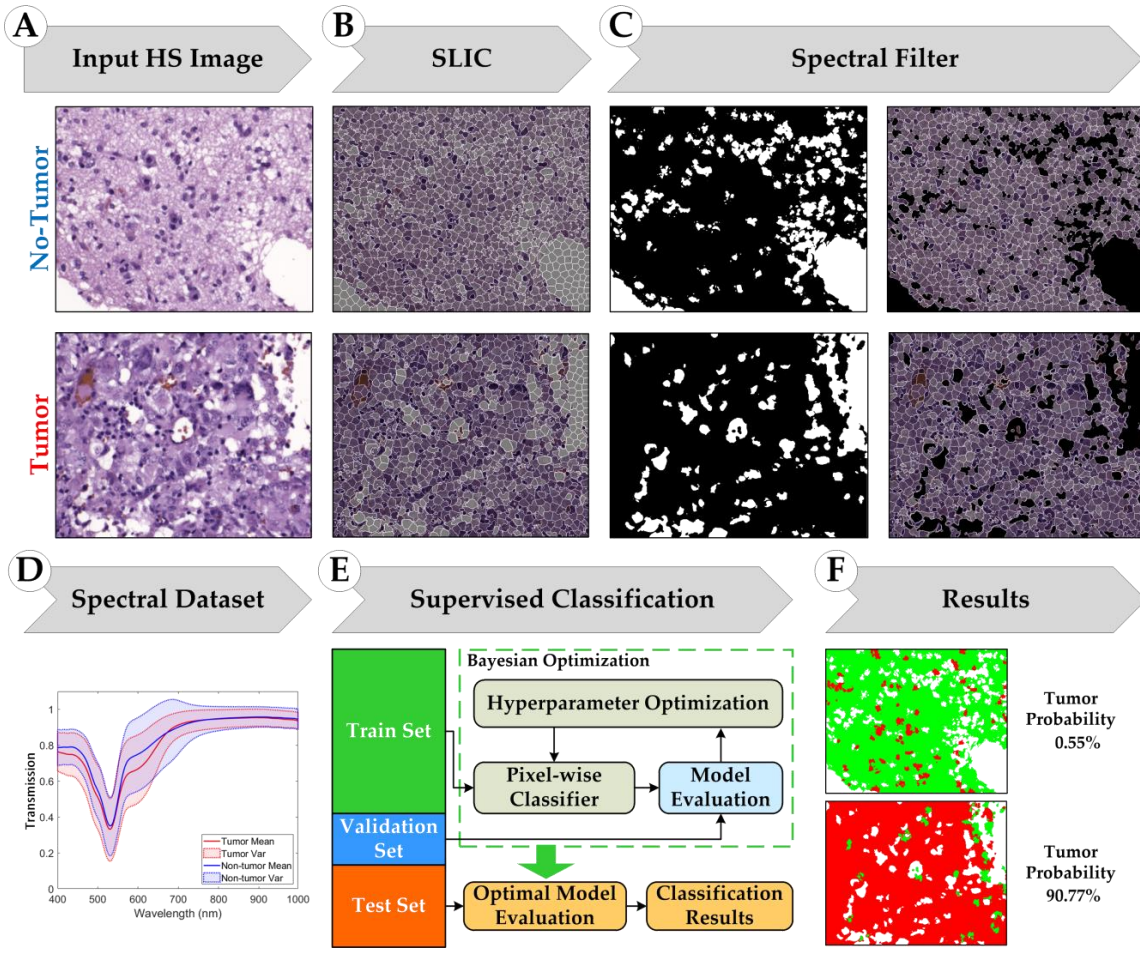

Figure 4-13: Proposed superpixel-based hyperspectral image processing framework.

4.3.3.1 Simple linear iterative clustering (SLIC) approach

In this research, we used the SLIC superpixel segmentation method proposed by Achanta *et al.* [337]. This algorithm is a modification of the k-means clustering algorithm to work with superpixels. Given a fixed number of target superpixels (K), the SLIC algorithm first initializes the superpixels by dividing the input image (Figure 4-14.a) in a regular grid (Figure 4-14.b). The initial area of the superpixel is S pixels. Next, the initial centroids of each superpixel are assigned to a randomly selected pixel within the superpixel area. Then, for each superpixel centroid, the distance between the superpixel centroid and the pixels in an area of $2 \cdot S$ pixels are computed (Figure 4-14.c). After computing this distance for all pixels in the images, each pixel is assigned to a superpixel.

Finally, the superpixel centroid is updated (Figure 4-14.d), and the process is repeated until the error in pixel assignment is minimized (Figure 4-14.e).

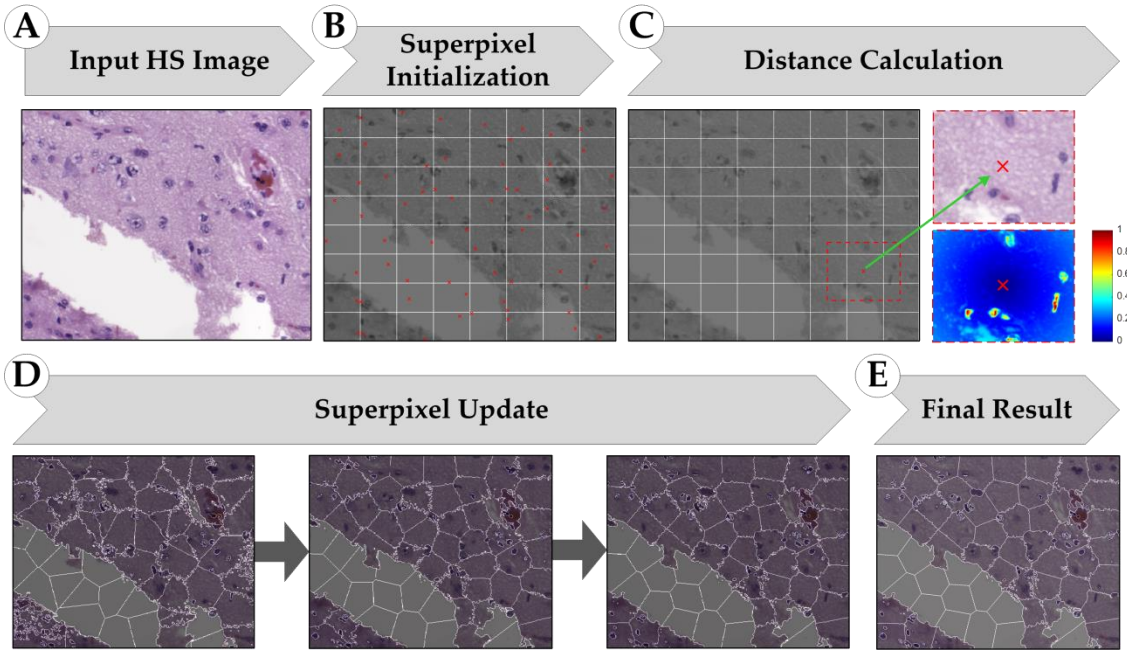

Figure 4-14: Block diagram of the different steps of the SLIC approach for superpixel classification.

In the original paper, the SLIC segmentation approach was developed for conventional RGB images. The distance between a superpixel and a pixel in its neighborhood is calculated as the root mean squared of the color distance and the spatial distance. For each pixel, the color distance (d_c) is defined as the Euclidian distance between two color components in the CIELAB color space (a color space defined by the *International Commission on Illumination* in 1976 [338]), and the spatial distance (d_S) is defined as the Euclidean distance between the spatial coordinates of the pixels. In order to compensate for the difference in range between d_c and d_S, a hyperparameter m is defined (Equation (15)). This hyperparameter weighs the importance of each type of distance in the overall distance computation. Small values of m make the distance more sensitive to the color distance component, while a large m provides more importance to the spatial component.

$$D_{SLIC} = \sqrt{{d_c}^2 + \left(\frac{d_S}{S}\right)^2 \cdot m^2} \tag{15}$$

In a first attempt, we utilized the original SLIC algorithm with the HS data. However, in our experiments we found the use of the Euclidian distance for the spectral similarity was not convenient for spectral data. The superpixels generated when using the Euclidian distance were not able to successfully group spectrally similar materials, showing high spectral variations between pixels belonging to the same superpixel. For this reason, we propose some modifications to such distance metrics for adapting the SLIC algorithm to HSI. First, we propose the use of the Spectral Angle (SA) as a distance metric for measuring the spectral similarity between two pixels p_1 and p_2 with N spectral bands (Equation (16)). The use of this type of distance is widely extended in the HSI research community [339]. For the spatial distance, we keep the Euclidian distance

between two pixels. The SA distance (d_{SA}) is in the range [0,1]. For this reason, in order to compute the total distance ($D_{proposed}$), we propose to simply weight the influence of the spatial distance by multiplying it for a factor m (Equation (17)). This hyperparameter is used to weigh the importance of the spatial and the spectral distance in the superpixel assignment.

$$d_{SA} = \frac{\sum_{i=1}^{N} p_{1_i} \cdot p_{2_i}}{\sqrt{\sum_{i=1}^{N} {p_{1_i}}^2} + \sqrt{\sum_{i=1}^{N} {p_{2_i}}^2}} \tag{16}$$

$$D_{proposed} = d_{SA} + \left(\frac{d_S}{S}\right) \cdot m \tag{17}$$

4.3.3.2 Supervised classification

The last stage of the super-pixel-based processing framework is composed by a supervised classifier employed to perform the classification of each superpixel centroid. SVMs were employed to perform the experiments since it has been demonstrated in the literature this algorithm performs well with imbalanced datasets [54]. The SVM classifier can be used for data which is not linearly separable by using different kernels to map the data in higher dimensional space. In this work, we selected the linear kernel for the SVM approach, employing two different evaluation metrics to optimize the hyperparameter cost (C). This hyperparameter is the constant of constraint violation, which is in charge of deciding if a data sample is classified on the wrong side of the decision limit [340]. MATLAB® was employed to perform the experiments and LIBSVM (Library for Support Vector Machines) was used for the classifier implementation [341].

4.3.3.3 Evaluation metrics

The evaluation metrics employed in this work to assess the performance of the data classification are accuracy (*ACC*), sensitivity, specificity, precision (*PPV*), F_1 score (*F1*) and balanced accuracy (*BA*). *BA* allows a measurement of the performance of the classifier by balancing the weights o sensitivity and specificity results (Equation (18)). As will be shown later in this work, this metric was necessary to improve the optimization of the hyperparameters of the supervised classifiers. Finally, *PPV* is the proportion of positive results correctly classified, as expressed in Equation (19), while *F1* is the harmonic mean of precision and sensitivity (Equation (20)).

$$BA = \frac{Sensitivity + Specificity}{2} \tag{18}$$

$$PPV = \frac{TP}{TP + FP} \tag{19}$$

$$F1 = \frac{2 \cdot TP}{2 \cdot TP + FP + FN} = 2 \cdot \frac{PPV \cdot Sensitivity}{PPV + Sensitivity} \tag{20}$$

4.3.4 Experimental results

4.3.4.1 SLIC hyperparameter selection

There are two hyperparameters to be configured on SLIC algorithm: the number of targeted superpixels (K) and the weight parameter (m), which balances the contribution

of the spectral and the spatial distance. The superpixels will be used as input to a supervised classifier. The main motivation for the use of a superpixel algorithm in the proposed processing framework is to extract the most salient spectral information from each HS image. Therefore, the subsequent superpixel-based classification can be affected if the spectral information within each superpixel does not belong to spectrally consistent areas, i.e. if some superpixels contain pixels with significant different spectral signatures. For this reason, we evaluated the effect of varying both K and m in the mean intra-cluster distance (Equation (21)), where c_j is the centroid of the superpixel j, and x_i represents a pixel on the image assigned to such superpixel. The lower D_{IC}, the most similar pixels within a superpixel.

$$D_{IC} = \frac{1}{K}\sum_{j=1}^{K}\frac{1}{N_i}\sum_{i=1}^{N_i} d_{SA}(c_j, x_i) + \left(\frac{d_S(c_j, x_i)}{S}\right)\cdot m \tag{21}$$

To select the optimal hyperparameters for the SLIC segmentation, we ran the SLIC segmentation with different K and m values and calculated the corresponding intra-cluster distance (D_{IC}). We analyzed values of K ranging from 64 to 1024, while the values for m varied from 0.005 to 0.1. In Figure 4-15, we present the results of these experiments, showing the mean D_{IC} for each hyperparameter.

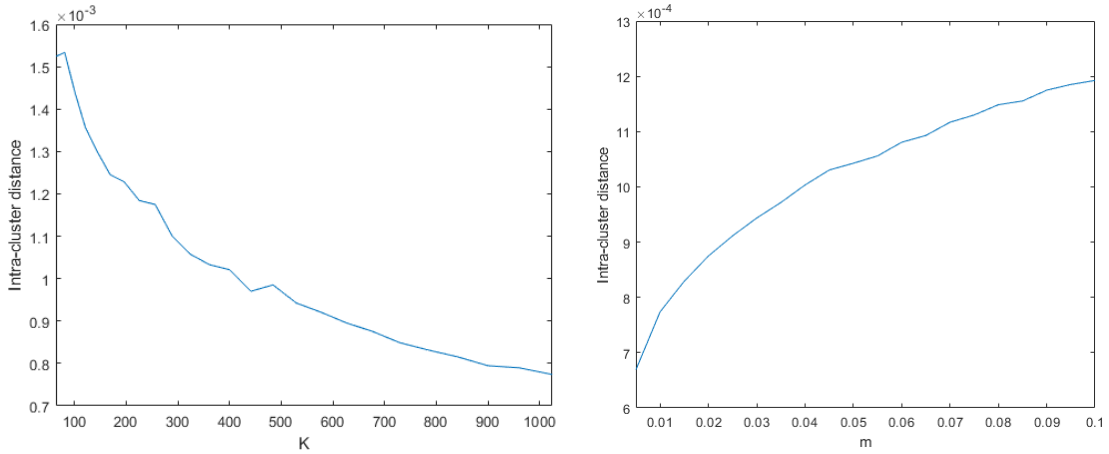

(a) (b)

Figure 4-15: Different SLIC Intra-cluster distance for different SLIC hyperparameters: (a) K and (b) m.

First, we can observe that with an increased number of superpixels, K, the lower inter-cluster distance is achieved. The rationale of this behavior is the following. If the number of superpixels is low, a pixel may be assigned to a superpixel for spatial similarity. On the contrary, if the number of superpixels is high, each superpixel is more likely to reject pixels which are not spectrally similar. For this reason, we selected the maximum value of K, 1024.

Second, the value of m equalizes the importance of both the spectral and the spatial distance during the superpixel assignment. Low values of m reduce the importance of the spatial proximity, while prioritizing the importance of the spectral similarity. As can be observed in Figure 4-15.B, the greater values of m result in greater intra-cluster distance. The rationale for this behavior is the following. Large values of m result in the spatial distance outweighing the spectral distance, and superpixels are likely to include pixels that are spatially closer, more than spectrally different. For this reason, we selected a

value of $m = 0.01$ to provide relevance to the spatial information, while keeping the inter-cluster distance low.

An example of the variation of the SLIC results depending on K is represented on Figure 4-16. If K is low, the area covered by a single superpixel is high, and could result in a mixture of different elements in a superpixel. As K increases, the area covered by each superpixel decreases, resulting in more compact superpixels. Figure 4-16 shows that low values of K (64 and 256) produce superpixels that are comprised of pixels from different materials. Additionally, for large values of K (512 and 1024), the superpixels are able to isolate pixels from single materials. In this application, we used the superpixels as a spectral summary of the current HS image. For this reason, the presence of superpixels with heterogenous spectra may lead to inaccurate predictions during supervised classification. In this research, we empirically selected $K = 1024$, which was shown to provide spectrally compact areas.

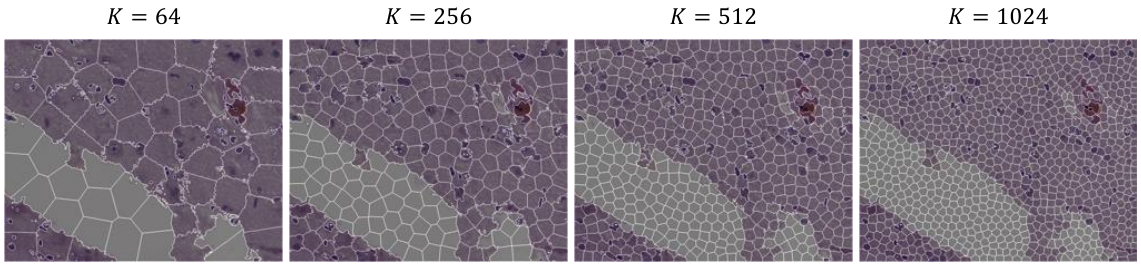

Figure 4-16: Different SLIC segmentation results depending on the number of target superpixels (K).

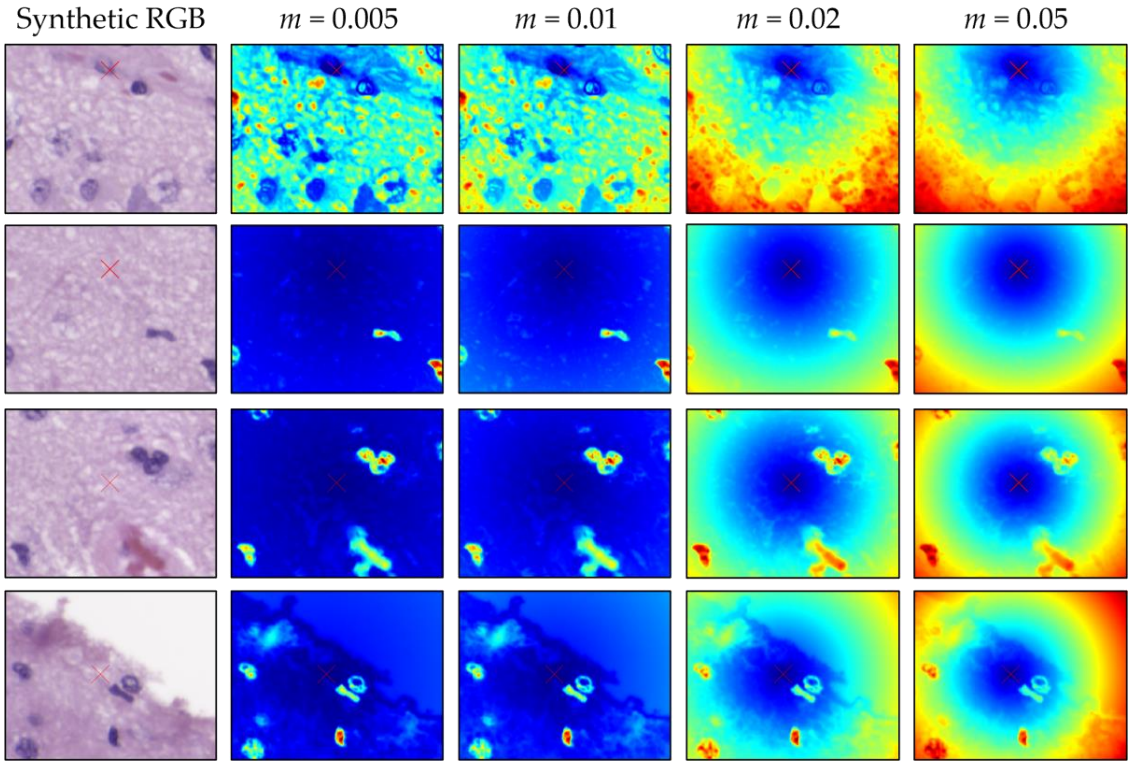

Figure 4-17: Different SLIC segmentation results depending on the distant hyperparameter (m). The rows present different image area example around a superpixel centroid (red cross). The first column shows the synthetic RGB image of the area and the remaining columns shows the distance between the superpixel centroid and the rest of pixels in the area with different values of m.

An example of this effect can be observed in Figure 4-17 for different regions of an image. In this application, we would expect the superpixels to be spectrally coherent. For this reason, we selected $m = 0.01$ for the generation of the superpixels.

4.3.4.2 Supervised classification results

After performing SLIC segmentation in all the images of the dataset, a superpixel dataset was constructed of both tumor and non-tumor annotations. In Figure 4-18.A, we show the distribution of superpixels among the different patients, while Figure 4-18.B represents the distribution of classes between the different folds. In this figure, the imbalanced nature between non-tumor and tumor samples is evident.

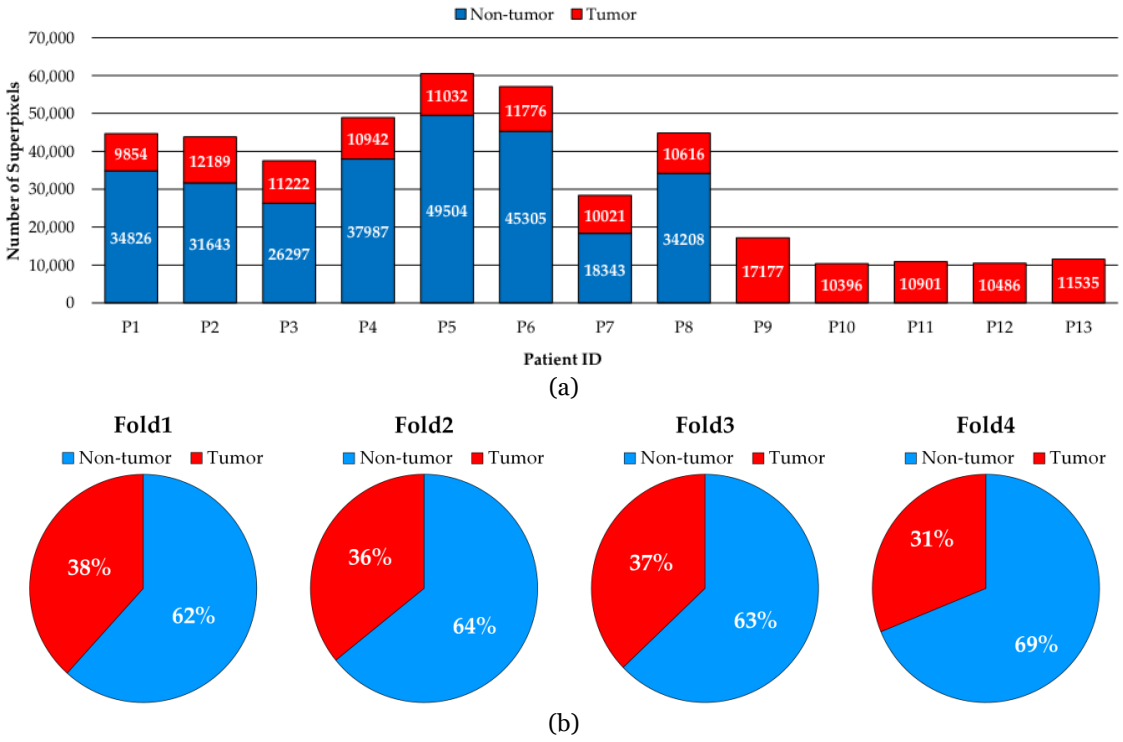

Figure 4-18: Number of non-tumor and tumor superpixels per patient (a) and percentage of the total per fold (b).

4.3.4.3 Validation results

Using the aforementioned superpixel dataset, we used the training data of each fold for training a supervised classifier, and we employed the validation data of each fold to optimize the hyperparameters to increase performance. In this section, we describe the results obtained by using SVMs with linear kernel as classifier. RF and 1-D CNNs were also evaluated, but the performance of those classifiers was not competitive. For RF we used the MATLAB Machine Learning Toolbox, while 1-D CNN experiments were carried out using the TensorFlow implementation of the Keras Deep Learning API [22-23]. Average validation sensitivity and specificity results of the 1-D CNN classifier were 66.0±31.4% and 60.8±44.2%, respectively. Regarding RF classification, the sensitivity and specificity results were 59.3±43% and 62.3±24%, respectively. Because of inadequate performance on the validation set, these classifiers were not further evaluated in the subsequent experiments.

In order to tune the hyperparameters of the supervised classifier, the model was trained using the training data, and the performance of the model was evaluated using

the validation set. This process was repeated several times by varying the hyperparameters' values to find the optimal hyperparameters which provided the best performance on the validation set. Finally, the performance of the tuned model was evaluated using the test set.

In this investigation, we performed the classification independently for each fold. Additionally, we proposed several optimization strategies for the hyperparameter optimization. Due to the large number of superpixels in each training fold, the time required to train a linear SVM classifier was about 21 hours. Although this computation time is not prohibitive, the required number of iterations to find the optimal hyperparameter in each fold drastically increased the execution time for finding the optimal classification models. In order to alleviate these training times for each fold, we decided to divide the training data into 10 different data partitions, and then train an ensemble of 10 different SVM classifiers. We first proved there was no performance drop when using the SVM ensemble compared to using all the training data at once. Then, we realize that using the SVM ensemble the execution time required to train a single fold decreased from 21 hours to 4 hours, which made hyperparameter optimization possible in a reasonable time.

For linear SVM, the cost value was the hyperparameter to be tuned. Instead of performing a grid search of the hyperparameters, we searched the optimal hyperparameters by using a Bayesian optimization algorithm [344]. Due to the imbalanced nature of our dataset, we proposed the use of BA and sensitivity metrics as optimization functions to be minimized. In this case, ACC is not a good metric to be optimized, since it would produce models that are more specialized in detecting the majority class of the dataset. In this optimization framework, the values of cost were bounded between 10^{-5} and 10^{5}.

Table 4-7 shows the final validation results for each fold using the linear kernel with the default cost value ($C = 1$) and with the optimal hyperparameters obtained using the BA and the sensitivity metrics. The most relevant outcomes of these results are the following. First, we can notice that hyperparameter optimization has a positive impact in the classification results, achieving an increase of 16% (ACC), 29% (sensitivity), 13% (specificity), 29% (PPV), and 28% (F1 metric). Second, the results obtained with optimized models show high accuracy, sensitivity and specificity for Fold 2 and Fold 4 (higher than 88%), while models for Fold 1 and Fold 3 suffer from low sensitivity (47-54%) and low specificity (35-41%), respectively. However, only Fold 1 shows remarkable PPV and F1 results. Finally, the results suggest the hyperparameter selection using BA as the optimization function provides subtly better performance, obtaining an improvement of 1% in the ACC, sensitivity, specificity and PPV metrics and an improvement of 2% in the F1 metric with a reduced standard deviation (std).

As mentioned in the dataset description, the usage of a single patient as validation patient may result in overfitting on the validation patient. We ensure there is no overfitting to the validation data by checking for similar performance between the classification of the training and validation samples within a fold.

Table 4-7: Superpixel classification results of the validation set in each fold using the SVM with Linear Kernel, with and without hyperparameter optimization.

	No Opt.					Opt. Metric (BA)					Opt. Metric (Sensitivity)				
Partition	**ACC**	**Sens.**	**Spec.**	**PPV**	**F1**	**ACC**	**Sens.**	**Spec.**	**PPV**	**F1**	**ACC**	**Sens.**	**Spec.**	**PPV**	**F1**
Fold 1	0.65	0.12	0.78	0.13	0.13	**0.88**	**0.54**	**0.97**	**0.84**	**0.66**	0.87	0.47	**0.97**	0.81	0.60
Fold 2	0.81	0.57	0.91	0.73	0.64	**0.95**	**0.89**	0.98	**0.96**	**0.92**	0.95	0.88	**0.99**	**0.96**	**0.92**
Fold 3	0.39	0.92	0.10	0.36	0.51	**0.61**	**0.99**	**0.41**	**0.48**	**0.64**	0.58	0.99	0.35	0.45	0.62
Fold 4	0.80	0.48	0.89	0.56	0.52	**0.89**	0.88	**0.89**	**0.69**	**0.78**	0.88	**0.89**	0.88	0.68	0.77
Avg.	0.66	0.52	0.67	0.44	0.45	**0.83**	**0.82**	**0.81**	**0.74**	**0.75**	0.82	0.81	0.80	0.73	0.73
Std.	0.20	0.33	0.39	0.26	0.22	**0.15**	**0.19**	**0.27**	**0.21**	**0.13**	0.17	0.23	0.30	0.22	0.15

Sens.: Sensitivity; **Spec.**: Specificity; **Avg.**: Average; **Std.**: Standard Deviation.

In this research work, the dataset annotation was performed at a macroscopic level. Because of this, the HS images annotated as tumor would contain some superpixels with spectral features which are not indicative of tumor, such as superpixels that are common in both tumor and non-tumor tissue. These wrong annotations could lead to false positives in the superpixel classification. For this reason, we considered an alternative approach to evaluate the results. Instead of performing the classification over all the superpixels of the validation patient, we also evaluated the image level. To this end, we used the trained SVM model to classify each image from the validation patient. Then, an image is flagged as tumor if more than 50% of the image superpixels are classified as tumor. On the contrary, if fewer than 50%, then the image is flagged as non-tumor. The threshold value of 50% to decide if an image should be flagged as tumor or not was experimentally determined using the validation data. Although it seems 50% is a high value since intuitively the presence of a few superpixels flagged as tumor may suggest the presence of tumor, this high threshold can be a consequence of the aforementioned incorrectly annotated superpixels. These inappropriate annotations would lead to false positives in the superpixel classification. A graphic representation of this approach is shown on Figure 4-19.

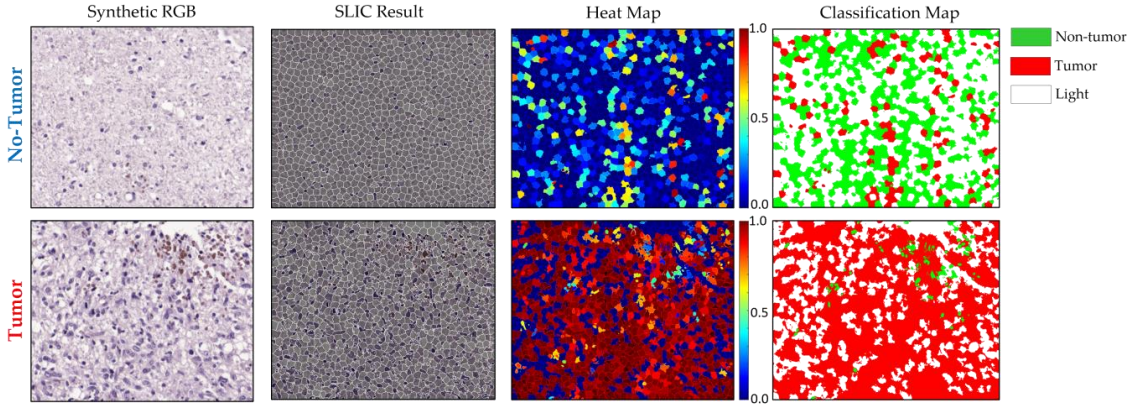

Figure 4-19: Classification results of the majority voting of superpixels classified by SVM. The top row shows a representative non-tumor image RGB composite and its corresponding SLIC result (left), the corresponding superpixel heat-map and the binarized form of tumor and non-tumor superpixels (right), where the white color represents the superpixels that correspond with light, green and red colors represent the non-tumor and tumor superpixels respectively. The result contains less than 50% tumor superpixels, so it is classified as non-tumor. The bottom row shows of a tumor image, where it is possible to observe that the result contains higher than 50% tumor superpixels, so this image is classified as tumor.

Results on the validation set using the image classification approach are shown in Figure 4-20. These results were obtained from the SVM model optimized using BA and sensitivity. On the one hand, similarly to the previous evaluation, Fold-2 and Fold-4

present the best performance. In Fold-2 all the images are correctly classified. For Fold-4, only a single non-tumor image and one tumor image are misclassified. For these folds, the performance of both types of SVM models work similarly. On the other hand, the classification performance for Fold 3 and Fold 4 is lower. In Fold 1, the sensitivity is low, and several images from tumor samples are not flagged as tumor, but all the images from non-tumor class are correctly classified. In opposition, in Fold 3 all tumor images are correctly classified, but one half of the non-tumor images are misclassified.

Regarding the comparison about the type of optimization for hyperparameter selection, the performance of the SVM optimized by BA is subtly higher compared to optimization driven by sensitivity.

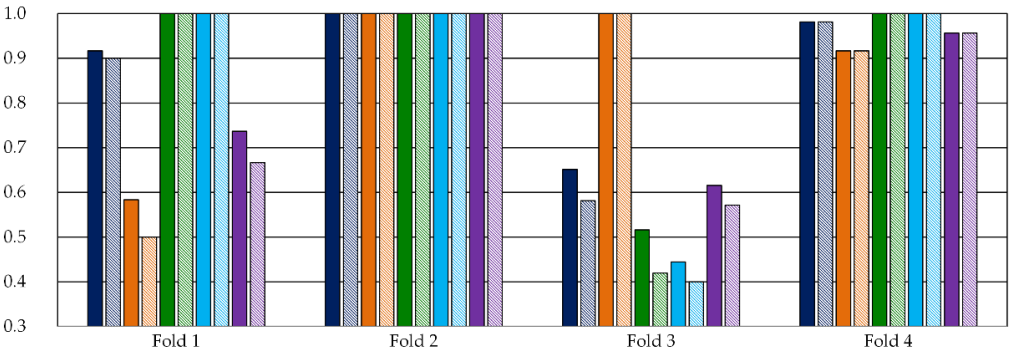

	Fold 1	Fold 2	Fold 3	Fold 4
ACC (Opt. BA)	0.92 (55/60)	1.00 (41/41)	0.65 (28/43)	0.98 (53/54)
ACC (Opt. Sens.)	0.90 (54/60)	1.00 (41/41)	0.58 (25/43)	0.98 (53/54)
Sens. (Opt. BA)	0.58 (7/12)	1.00 (12/12)	1.00 (12/12)	0.92 (11/12)
Sens. (Opt. Sens.)	0.50 (6/12)	1.00 (12/12)	1.00 (12/12)	0.92 (11/12)
Spec. (Opt. BA)	1.00 (48/48)	1.00 (29/29)	0.52 (16/31)	1.00 (42/42)
Spec. (Opt. Sens.)	1.00 (48/48)	1.00 (29/29)	0.42 (13/31)	1.00 (42/42)
PPV (Opt. BA)	1.00	1.00	0.44	1.00
PPV (Opt. Sens)	1.00	1.00	0.40	1.00
F1 (Opt. BA)	0.74	1.00	0.62	0.96
F1 (Opt. Sens)	0.67	1.00	0.57	0.96

Figure 4-20: Average image classification results of each fold in the validation set using both metrics (BA and Sensitivity) for the hyperparameter optimization of the SVM Linear kernel.

4.3.4.4 Quantitative test results

In this section, we show the classification results for the test set of each fold. The quantitative results obtained for the test set for the SVM Linear classifier optimized with the BA and the sensitivity metrics are shown in Figure 4-21. On average, the use of the BA metric for the hyperparameter optimization provided better *ACC* results (82.6±7.1%) than the Sensitivity metric (78.3±6.2%). Considering sensitivity and specificity results, the classifier optimized with the BA metric provided a result of 88.5±10.2% and 80.2±16.9%, respectively, representing an improvement in the sensitivity of 4.3% with respect to the classifier optimized with the sensitivity metric. Regarding to the differences between the use of BA metric and sensitivity metric in the PPV and F1 results, PPV practically were the same, achieving 73.4±19% and 73.1±17.6%, respectively, while F1 improved 1.6% using the BA metric (78.3±6.4%). For this reason, the BA metric was shown as a suitable evaluation metric to optimize the hyperparameters of a supervised classifier with imbalanced datasets for this specific application.

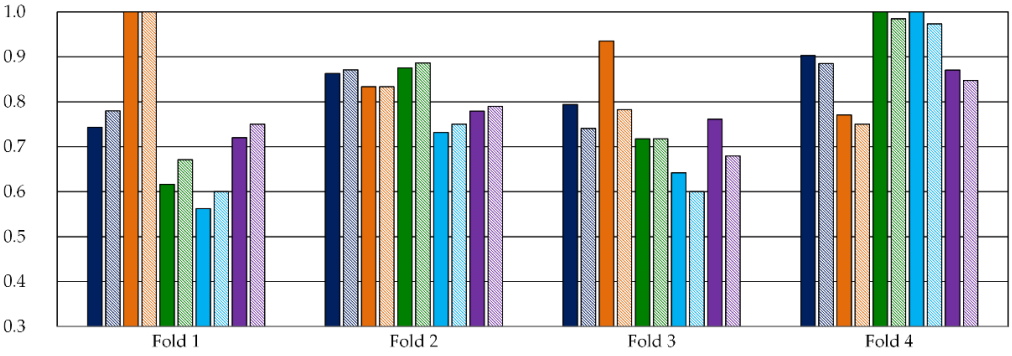

	Fold 1	Fold 2	Fold 3	Fold 4
ACC (Opt. BA)	0.74 (81/109)	0.86 (107/124)	0.79 (104/131)	0.90 (102/113)
ACC (Opt. Sens.)	0.78 (85/109)	0.87 (108/124)	0.74 (97/131)	0.89 (100/113)
Sens. (Opt. BA)	1.00 (36/36)	0.83 (30/36)	0.93 (43/46)	0.77 (37/48)
Sens. (Opt. Sens.)	1.00 (36/36)	0.83 (30/36)	0.78 (36/46)	0.75 (36/48)
Spec. (Opt. BA)	0.62 (45/73)	0.88 (77/88)	0.72 (61/85)	1.00 (65/65)
Spec. (Opt. Sens.)	0.67 (49/73)	0.89 (78/88)	0.72 (61/85)	0.98 (64/65)
PPV (Opt. BA)	0.56	0.73	0.64	1.00
PPV (Opt. Sens)	0.60	0.75	0.60	0.97
F1 (Opt. BA)	0.72	0.78	0.76	0.87
F1 (Opt. Sens)	0.75	0.79	0.68	0.85

Figure 4-21: Average image classification results of each fold in the test set using both metrics (BA and Sensitivity) for the hyperparameter optimization of the SVM Linear kernel.

Finally, in Figure 4-22, we show the results obtained for each patient individually. For every patient except for P2, P6, P8 and P10, the sensitivity is higher than 90%. For P2 and P8 the sensitivity is also high, beyond 80%. For P6 and P10, the sensitivity is low. These patients were classified using models from Fold 2 and Fold 4, respectively. However, models from those folds demonstrated good sensitivity for the remaining patients. This fact will be further investigated in future works. The specificity can only be measured for patients with both types of annotations (non-tumor and tumor), i.e. from P1 to P8. Five of these patients present a sensitivity of 100%, while the others present low specificity. The worst case is P7, where the specificity is 10%.

The high sensitivity of the proposed methodology suggests that it could serve as a clinical tool to detect images with suspicious tumor presence for a pathologist to examine. However, despite the fact that the overall amount of time spent in examination could be reduced, the low specificity would likely result in some false positives.

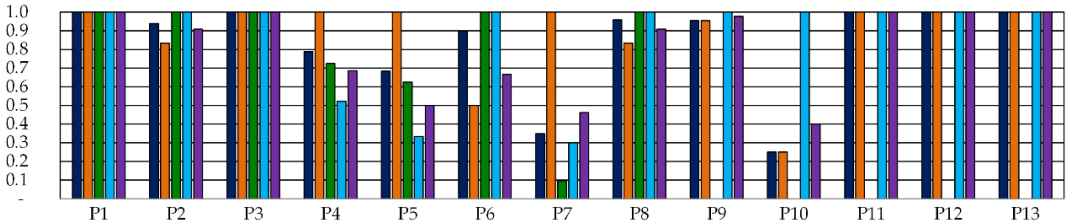

	P1	P2	P3	P4	P5	P6	P7	P8	P9	P10	P11	P12	P13
ACC	1.00	0.94	1.00	0.79	0.68	0.90	0.35	0.96	0.95	0.25	1.00	1.00	1.00
Sensitivity	1.00	0.83	1.00	1.00	1.00	0.50	1.00	0.83	0.95	0.25	1.00	1.00	1.00
Specificity	1.00	1.00	1.00	0.73	0.63	1.00	0.10	1.00	-	-	-	-	-
PPV	1.00	1.00	1.00	0.52	0.33	1.00	0.30	1.00	1.00	1.00	1.00	1.00	1.00
F1	1.00	0.91	1.00	0.69	0.50	0.67	0.46	0.91	0.98	0.40	1.00	1.00	1.00
	Fold 1	Fold 3	Fold 4	Fold 2	Fold 3	Fold 2	Fold 1	Fold 4	Fold 3	Fold 4	Fold 1	Fold 4	Fold 2

Figure 4-22: Average image classification results per patient in the test set using the SVM Linear kernel optimized with the BA metric. P9 to P13 only have samples from tumor class.

4.3.4.5 Qualitative test results

The results of the proposed approach can be visualized as a heat map, which shows the predicted tumor probability map of superpixels, or as a classification map, where the superpixels are assigned to a class using a probability threshold of 50%.

Figure 4-23 shows four examples of qualitative results obtained from four tumor images, belonging to P3, P4, P5, and P7, with their respective tumor presence probability. For P3, 61% of the superpixels were classified as tumor, thus the image-scale prediction is tumor. The heat maps for P4 and P7 suggest the presence of tumor with high probability. On the contrary, the heat map for P5 shows a misclassification, where about 46% of the superpixels were classified as tumor, so the image is misclassified, being a false negative prediction.

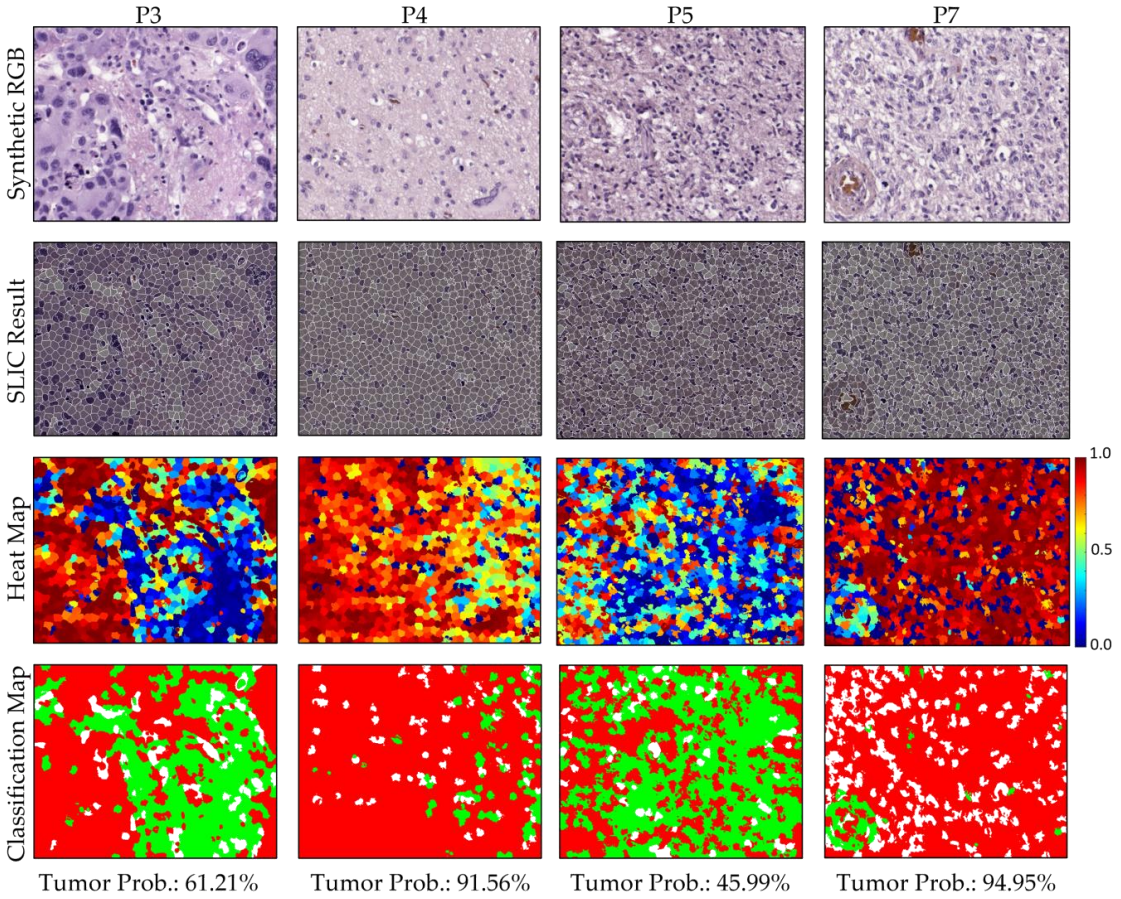

Figure 4-23: Heat and classification maps of four example tumor images. First row shows the synthetic RGB image of the HS cube, while second row represents the SLIC result. Third row represents the heat map, where red colors represent higher tumor probability. Fourth row shows the classification map, where red, green and white colors indicate tumor, non-tumor and light superpixels, respectively. In the last row, the tumor presence probability of the image is indicated. HS images with classification results with tumor probability >= 50% were considered tumor images, while results <50% were considered non-tumor images.

Figure 4-24 shows the results of four example non-tumor images that belong to P3, P4, P5, and P7 with their respective tumor probability results. As can be seen, the heat maps for P3, P4 and P5 show a successful classification of non-tumor samples. For P3 and P4, only a few superpixels were classified as tumor, less than 13% of the image in either case. In the case of P5, the image was flagged as non-tumor, but the number of superpixels classified as tumor is higher, about 36%. Finally, we show an example of a

false positive, where 68% of the superpixels were classified as tumor and thus the image was flagged as tumor.

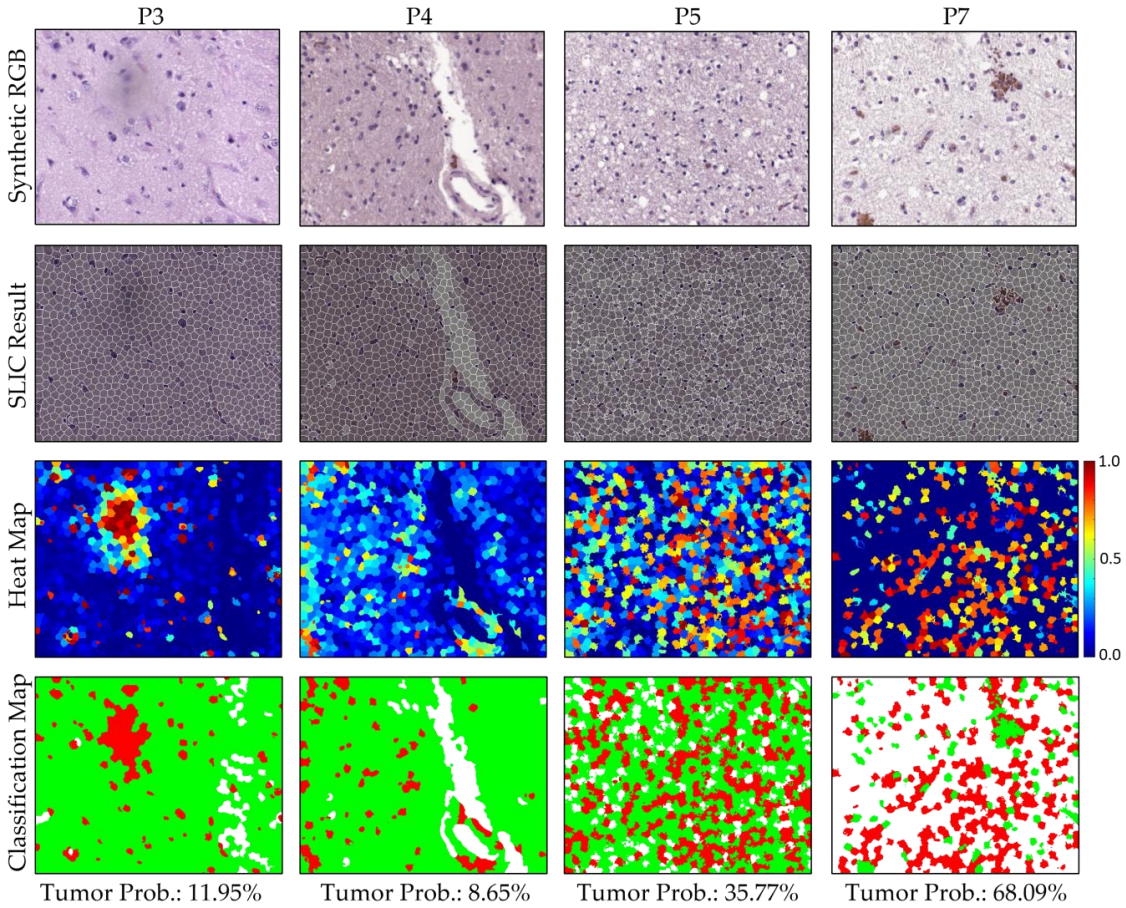

Figure 4-24: Heat and classification maps of four example non-tumor images. First row shows the synthetic RGB image of the HS cube, while second row represents the SLIC result. Third row represents the heat map, where red colors represent higher tumor probability. Fourth row shows the classification map, where red, green and white colors indicate tumor, non-tumor and light superpixels, respectively. In the last row, the tumor presence probability of the image is indicated. HS images with classification results with tumor probability >= 50% were considered tumor images, while results <50% were considered non-tumor images.

As mentioned previously, the presence of misannotated superpixels in the dataset could lead in misclassifications. For this reason, we selected the 50% tumor threshold. Although in most situations this strategy provides an accurate diagnosis, there are some limitations. For example, in Figure 4-23, we can observe how the image belonging to P5 was misclassified as a non-tumor image, while the number of superpixels classified as tumor was around 46%. On the contrary, the image from P7 in Figure 4-24 represents a false positive because around 68% of the superpixels were classified as tumor. However, this behavior is only found in a few examples of the dataset.

4.3.5 Discussion

In this section, we have proposed a combination of superpixel segmentation and supervised classification for the identification of GB tumor in HS images from brain histological slides. Regarding the HS images, the image quality and spectral range have been significantly improved, resulting in a more appropriate experimental design for realistic clinical applications. We modified and optimized the original SLIC

segmentation algorithm for HS images. These modifications included the use of a spectral distance based on the spectral angle, and the modification of the global distance, which is a tradeoff between the spectral and the spatial distances between pixels in a neighborhood. After optimizing the hyperparameters of the SLIC algorithm to generate compact pixels, the superpixels were used to build a dataset where superpixels were labeled as tumor or non-tumor according to pathologists' annotations. The data were then partitioned in patient independent training, validation, and test sets. Finally, superpixels were classified using a linear SVM classifier.

The results obtained with this methodology are promising, showing high sensitivity and specificity values for almost all the patients independently. On average, our proposed approach achieved 87% and 81% of sensitivity and specificity, respectively. Additionally, 8 out of the 13 patients obtained a sensitivity of 100%, and 3 out of the 13 had a sensitivity of 83-95%. Screening tests with high sensitivities could be useful clinically. The outcomes of this processing framework could potentially be used in a clinical application to flag which regions of the histological slide are of interest to be further analyzed by a pathologist, and then reduce whole-slide examination.

Regarding the supervised classification, after testing SVM, 1-D CNN, and RF algorithms, the only classifier that demonstrated accurate classification results in our data was SVM. For other applications, all of these classifiers have demonstrated high performance with spectral data in the literature [10]. However, the classification performance strongly depends on the data used to train the model. Although those classifiers did not perform well in our application, we cannot suggest that using a larger dataset would allow those classifiers to correctly classify the spectral data. Moreover, it is possible that the 1-D CNN underperformed because of the nature of the task. Specifically, the HS signatures were 1-D signals averaged from across a superpixel. The strengths of CNN methods are typically learning from highly variable data with spatial features.

In this work, we only explored the linear kernel of the SVM to demonstrate the feasibility of the superpixel-based approach exploiting only the spectral information. However, in future works, we will evaluate the performance of additional kernels for this task with the goal of trying to improve the classification results obtained in this work.

The main limitation of this study is the reduced number of patients and the imbalance of the dataset. Regarding the imbalanced dataset, in this dissertation we deal with this problem by using a hyperparameter optimization guided by metrics which may compensate the data imbalance, i.e. balanced accuracy and sensitivity. The use of sensitivity was motivated by the lower number of examples in the tumor class (~35% of tumor superpixels, compared to ~65% of non-tumor superpixels). Nevertheless, other metrics can be used to drive the hyperparameter optimization to alleviate the effect of the imbalanced dataset. For example, the F-1 score or a weight balance between precision and recall, where the weight will favor the class with lower number of samples.

Other limitations of this research are depicted herein. Although the spatial information of the HS is partially considered when the superpixels are extracted with SLIC, the supervised classification is only focused on the spectral information. In this study, we demonstrated the potential of the exclusive use of spectral information for the identification of tumor areas in HS digitized slides. Nevertheless, these results can be further improved if we also include additional spatial information into the classification

framework. For example, as shown in the work by Zhao *et al.* [345], it could be possible to develop a method which efficiently combines the spectral information from the proposed superpixel approach with the spatial information extracted from the HS data using a 2D-CNN. Another challenge to be addressed in future works is to improve the way the optimal number of superpixels is extracted. In this research, we selected the number of superpixels to minimize the intra-cluster distance, but more sophisticated methods can be used in the future to reduce the number of superpixels while retaining the most important information from each image [346]. In this research, we overestimated the number of superpixel centroids in order to ensure proper extraction of spectral features from the HS image. However, the computational time could be reduced by decreasing the number of superpixels per image, which is more competitive for screening histology slides.

4.4 Conclusions

In this Chapter, we have presented two different approaches for analyzing HS images from histological slides. The first approach (Section 4.2) presented some limitations. The total number of HS cubes used was limited to 40, only 4 HS cubes per patient. Secondly, the instrumentation used in this preliminary work presented limitations in both the spectral and spatial information. Regarding the spectral information, the spectral range was restricted to 419–768 nm due to limitations of the microscope optical path. The spatial information was limited due to the use of a scanning platform not able to image the complete scene, so the analysis of the HS images was restricted to a low magnification (5×), which was not sufficient to image the morphological features of the sample. Additionally, the main goal of such previous work was to develop a preliminary proof-of-concept on the use of HSI for the differentiation of tumor and non-tumor samples, showing promising results.

With the research presented in Section 4.3, we addressed the main limitations found in Section 4.2. An improved acquisition system capable of capturing high-quality images in a higher magnification (20×), and with a higher spectral range (400–1000 nm) has been used to capture a high number of HS cubes. The use of 20× magnification allows the classifier to exploit both the spectral and the spatial differences of the samples to make a decision.

The main limitation of this study is the reduced number of patients and the imbalance of the dataset. Additionally, only 8 out of the 13 patients have annotated data available from the two classes, i.e. tumor and non-tumor. This fact, together with the known histological heterogeneity of GB tumors, makes this task very challenging. Therefore, more patients are needed in future analysis to obtain more robust conclusions about the ability of HSI and ML for the automatic detection of GB in histological slides. More concretely, to obtain statistically significant results, we hypothesize that at least 10 patients are needed with both types of annotations for both validation and test. This would require at least 40 patients with both types of annotations to train the classifiers. The main challenges for the acquisition of such a dataset are the large amounts of data generated during image acquisition and the time-consuming manual annotation for the ground-truth definition. Further data acquisition campaigns will be deployed to increase our dataset, reinforcing the conclusions achieved in this work about the potential use of HSI to detect GB in histological slides.

Additionally, as previously mentioned, due to the macroscopic annotations, some regions of the tumor HS images are in fact not characteristic of GB tumor but are still labeled as tumor. Such misannotated data are likely to produce misclassifications. To handle this fact, one of the future works in this field will be to identify which spectral signatures can be found in both tumor and non-tumor images, which may improve the quality of the predictions.

Chapter 5: Deep Learning for the spatial-spectral classification of histological HS data

Among the use of conventional image analysis, HSI technology is presented as an interesting alternative to RGB analysis due to its capability to differentiate between different materials by exploiting both morphological and spectral features. The use of this technology is motivated by the fact that spectral information may detect subtle molecular differences between biological samples [8]. This technology is used together with advanced machine learning algorithms to retrieve useful information about the materials within an HS image. In the previous chapter, we successfully employed FL methods for the diagnosis of histopathological samples using HS information. However, the performance of these approaches may be improved by using DL schemes. Recent studies have proven the advantages of using deep learning approaches for HSI classification [101], which are able to exploit simultaneously both the spatial and the spectral features of HSI.

DL approaches automatically learn from the data which features are optimal for classification, potentially outperforming handcrafted features [347]. In the case of HS images, both the spatial and spectral features are exploited simultaneously. In the recent years, only a few researchers have employed DL for the classification of HS images for histopathological applications.

In this chapter, we explore the use of DL techniques for the classification of two types of specimens. First, we apply DL techniques to the HS human brain dataset which has been described in the previous chapter. Then, we create a novel dataset for discriminating between normal and tumor breast cancer cells using DL.

5.1 Brain cancer approach

In this section, we propose the use of CNNs for the classification of H&E stained brain tumor samples. Specifically, the main goal of this work is to differentiate between high-grade gliomas (i.e. GB) and non-tumor tissue. In the previous chapter, we presented a feature learning approach for this type of disease. Although such research was shown as a useful proof-of-concept on the possibilities of HS for histopathological analysis of GB,

it presented some limitations, such as the exclusive usage of the spectral information for the classification.

5.1.1 Dataset description

The HS dataset used in for this study was described in the previous chapter. In this research, we used a CNN to perform the classification of the samples. Due to the nature of the data for this study, the ground truth assignment into tumor or non-tumor is shared across each selected ROI, and thus each HS image is assigned within a certain class. For this reason, it was decided to perform the classification in a patch-based approach because a fully-convolutional design was not feasible. There are two motivations on the selection of the patch size. Firstly, the patch should be large enough to contain more than one cell, but if the patch is too large, then the CNN could learn that the tumor is located only in dense cell patches. Secondly, the smaller the patches, the higher the quantity of patches will be extracted from a single HS image, so the number of samples to train the CNN will be increased. Finally, we choose a patch size of 87 × 87 pixels. In principle, from a spectral cube of size 800 × 1004, 99 patches can be extracted. However, there are some situations where most parts of the patches consisted only of a blank space of light. For this reason, we decided to reject patches that were composed by more than 50% of light, i.e. half of the patch is empty.

The method to reject the patches which presented high amount of light is as follows. Firstly, the RGB image is extracted from the HS cube and is transformed to the hue-saturation-value color representation. Then, the hue value of each image is extracted and binarized using a threshold empirically configured to separate the pixels belonging to the specimen and the pixels containing background light. The generation of the patches can be observed in Figure 5-1, where the last row of the patches (in Figure 5-1.c) represents patches that have been rejected in the database due to high content of background light pixels.

The database used in this work consists of 527 HS images, where 337 are non-tumor brain samples and 190 were diagnosed as GB. It should be highlighted that only the biopsies from 8 patients presented both non-tumor and tumor samples, the other 5 patients only presented tumor samples. The summary of the employed dataset is detailed in Table 5-1. After extracting the patches that were valid to be processed, we had a total of 32,878 patches from non-tumor tissue and 16,687 from tumor tissue.

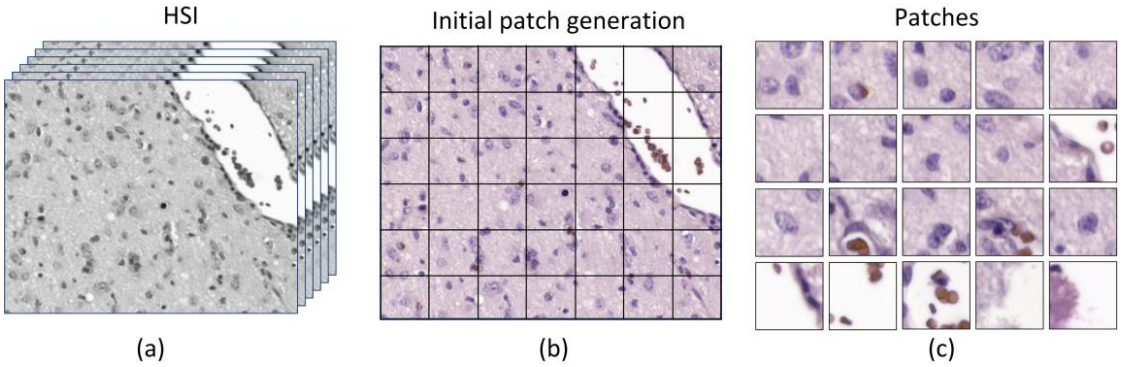

Figure 5-1: Generation of patches. (a) Original HS image. (b) Grid of patches within the HS image (c) Patches of size 87x87 used in the classification. The last row contained patches that were rejected for the dataset for having more than 50% of empty pixels.

Table 5-1: HS histopathological dataset summary.

Patient ID	#Images		#Patches	
	Non-tumor	Tumor	Non-tumor	Tumor
P1	48	12	4,595	1,090
P2	36	12	3,563	1,188
P3	31	12	3,058	1,178
P4	40	12	3,779	1,158
P5	66	12	5,675	1,165
P6	48	12	4,586	1,188
P7	44	12	4,289	1,184
P8	24	36	3,333	2,260
P9	0	22	0	1,695
P10	0	12	0	1,094
P11	0	12	0	1,169
P12	0	12	0	1,137
P13	0	12	0	1,181
Total	337	190	32,878	16,687

5.1.2 Data partition strategy

The data partition strategy is the same used in the previous chapter. In other words, it consists of dividing data in four different folds, each one built with patient-independent train, validation, and test sets (Figure 5-2). A brief summary of the dataset partition into folds is as follows: 1) data from a single patient is located in training, testing, or validation; 2) validation patients should have both types of annotations (non-tumor and tumor); and 3) all patients have to be included in a test set eventually. The limited total number of patients available leads to a limited number of patients used for validation in each fold. Therefore, it is possible to have overfitting of the models to validation patients.

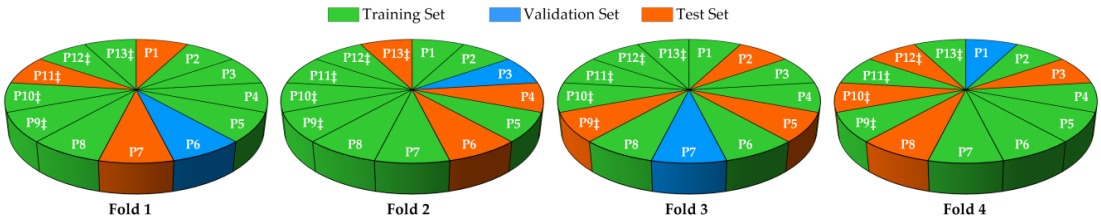

Figure 5-2: Data partition among the different folds (patients with only tumor samples are marked with ‡).

5.1.3 Processing framework

The processing framework applied to each HS cube is composed by the following steps. First, a standard flat field correction is applied to the images. To this end, the images are transformed from radiance to normalized transmittance by using a reference image that is captured from a blank area of the pathological slide [36]. Then, due to the high correlation of spectral information between adjacent spectral bands, a reduced-band HS image is generated by averaging the neighbors' spectral bands, reducing the number of spectral bands from 826 bands to 275 and slightly reducing the white Gaussian noise. This band reduction is also beneficial for alleviating computational cost in the subsequent image processing. Finally, each image is divided into patches, which will train the CNN. In this section, we will detail the architecture of the proposed neural network, the metrics that are used for performance evaluation, and the proposed data partition scheme.

5.1.3.1 Convolutional Neural Network

We employed a custom 2D-CNN for the automatic detection of non-tumor and tumor patches. As mentioned previously, these types of networks are able to exploit together the spatial and spectral features of the sample. The performance of DL approaches for the classification of HS data has been proven both for medical and for non-medical applications [101]. We used the TensorFlow implementation of the Keras Deep Learning API [342], [343] for the development of this network. This selection was made because it allows effective development of CNN architectures, training paradigms, and efficient deployment between the Python programming language and GPU deployment of training/testing. The architecture of this CNN is mainly composed by 2D convolutional layers. We detail the description of the network in Table 5-2, where the input size of each layer is shown in each row, and the output size is the input size of the subsequent layer. All convolutions and the dense layer were performed with ReLU activation functions with a 10% dropout. The optimizer used was stochastic gradient descend with a learning rate of 10^{-3}.

Table 5-2: Schematic of the proposed CNN.

Layer	Kernel size	Input Size
Conv2D	3×3	87×87×275
Conv2D	3×3	85×85×256
Conv2D	3×3	83×83×256
Conv2D	3×3	81×81×512
Conv2D	3×3	79×79×512
Conv2D	3×3	77×77×1024
Conv2D	3×3	75×75×1024
Conv2D	3×3	73×73×1024
Global Avg. Pool	25x25	73×73×1024
Dense	256 neurons	1x1024
Dense	Logits	1×256
Softmax	Classifier	1×2

5.1.3.2 Evaluation metrics

The metrics for measuring the classification performance of the proposed CNN were overall accuracy, sensitivity and specificity. Additionally, we used the area under the curve (AUC) of the receiver operating curve (ROC) of the classifier as an evaluation metric. The AUC has been proven to be more robust compared to overall accuracy. AUC is decision threshold independent, shows a decreasing standard error when the number of test samples increases, and is more sensitive to Analysis of Variance (ANOVA) test [348].

5.1.4 Experimental results

5.1.4.1 Validation results

We trained different CNNs using the data from each fold, and using the validation data, we selected the aforementioned CNN architecture (Table 5-2) as the best candidate for the classification of the samples. As can be observed in Table 5-1, the data between tumor and non-tumor classes are not balanced: the number of non-tumor samples is twice the number of tumor samples. For this reason, we performed data augmentation on the tumor data to balance the data during training, creating twice the number of tumor patches to train the CNN than cited in Table 5-1. Such data augmentation consisted in a single spatial rotation of tumor patches.

At the beginning of the validation phase, some of the folds presented problems when they were trained, showing poor performance metrics in the validation set. For this reason, we carefully examined the tumor HS images from each patient, and we detected that accidentally some necrosis areas were included in the dataset as tumor samples. These necrosis areas (found in P8) were excluded from the dataset. After excluding the necrosis areas, we got competitive results for all the folds in the validation set. These results are shown in Table 5-3. The models for each fold were selected because they all presented high AUC, higher than 0.92, and the results in terms of accuracy, sensitivity and specificity were balanced, indicating that the models identified correctly both non-tumor and tumor tissue.

In order to provide a comparison of performance between HSI and RGB imagery, we performed the classification of synthetic RGB images using the same CNN. Such RGB images were extracted from the HS data, where each color channel was generated equalizing the spectral information to match the spectral response of the human eye [95]. After separately training the CNN with RGB patches, the models selected after the validation were found to be competitive. Nevertheless, the validation performance when using HSI data was more accurate in each fold and presented more balanced sensitivity and specificity values (Table 5-3).

Table 5-3: Classification results on the validation dataset, across all four folds (F).

	HSI				**RGB**			
Partition	**AUC**	**ACC (%)**	**Sensitivity (%)**	**Specificity (%)**	**AUC**	**ACC (%)**	**Sensitivity (%)**	**Specificity (%)**
F1	**0.92**	**84**	**84**	**85**	0.88	77	71	88
F2	**0.97**	**93**	**91**	**94**	0.95	87	83	93
F3	**0.95**	**88**	90	**88**	0.93	87	**91**	79
F4	**0.95**	89	87	**91**	0.92	**92**	**93**	89
Avg.	***0.95***	***88***	***88***	***89***	*0.92*	*86*	*84*	*87*
Std.	***0.02***	***3.70***	***3.16***	***3.87***	*0.03*	*6.29*	*9.98*	*5.91*

5.1.4.2 Test results

After the model selection in the validation phase, we applied them to independent patients for the test set. These results are shown in Table 5-4. Some results show good discrimination between non-tumor and tumor tissues, i.e. patients P1, P3, and P8. For these patients, the AUC, sensitivity and specificity are comparable to the values obtained during validation. The tumor detection in patients P9 to P13 was also highly accurate. However, there are some patients where the classification performance was poor. Although the sensitivity is high in patients P2 and P5, the specificity is low, which indicates there may be an issue classifying non-tumor patches. There are also some patients with poor accuracy, namely patients P4 and P7, which have results slightly better than random guessing. Finally, the results obtained for patient P6 are suspicious, being substantially worse than random guessing.

The selection of the models in the validation phase was performed using independent patients for validation, for this reason such inaccuracies on test data was unexpected. To determine the reasons for the misclassifications, we used the CNN models to generate heat maps for all the patients, and we carefully examined them. After this analysis, we found that some HS images presented problems, and hence the results were worsened for these reasons. As mentioned before, we performed a careful inspection of tumor HS images in the validation set. However, upon inspection after the test outcomes, we discovered there were also problems in non-tumor samples. There were four main

sources of errors in the images: 1) some HS images were contaminated with the ink used by pathologists to delimitate the diagnosed regions ($n = 15$); 2) some images were unfocused ($n = 13$); 3) some samples presented artifacts from histopathological processing ($n = 2$); and 4) other images were composed mainly by red blood cells ($n = 2$). Examples of these images can be observed in Figure 5-3.

Table 5-4: Initial classification results on the test dataset.

	HSI				RGB			
Patient ID	**AUC**	**ACC (%)**	**Sensitivity (%)**	**Specificity (%)**	**AUC**	**ACC (%)**	**Sensitivity (%)**	**Specificity (%)**
P1	**0.97**	**92**	90	**94**	0.92	90	**97**	61
P2	0.75	77	99	69	**0.98**	**85**	**99**	**80**
P3	0.95	85	91	**80**	**0.96**	**92**	**97**	78
P4	0.62	57	57	**58**	**0.69**	**77**	**98**	7
P5	**0.81**	**69**	**81**	**64**	0.66	59	59	60
P6	**0.35**	37	38	**36**	0.21	**67**	**81**	7
P7	**0.64**	**59**	**64**	57	0.51	45	36	**76**
P8	0.98	96	96	96	**0.99**	**97**	**97**	**97**
P9	*N.A.*	**99**	**99**	*N.A.*	*N.A.*	*89*	*89*	*N.A.*
P10	*N.A.*	**89**	**89**	*N.A.*	*N.A.*	*43*	*43*	*N.A.*
P11	*N.A.*	92	92	*N.A.*	*N.A.*	**98**	**98**	*N.A.*
P12	*N.A.*	**92**	**92**	*N.A.*	*N.A.*	*84*	*84*	*N.A.*
P13	*N.A.*	**99**	**99**	*N.A.*	*N.A.*	*88*	*88*	*N.A.*
Avg.	***0.76***	***80***	***84***	***69***	*0.74*	*78*	*82*	*58*
Std.	***0.22***	***19***	***19***	***20***	*0.28*	***19***	*22*	*34*

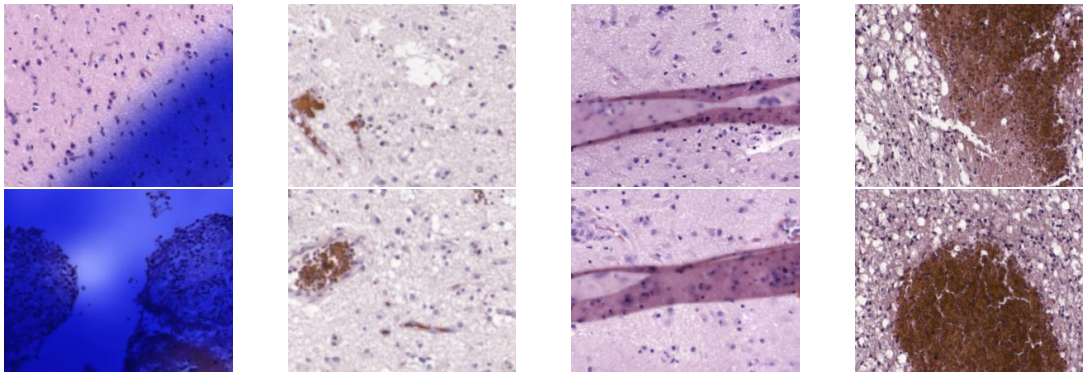

(a) (b) (c) (d)

Figure 5-3: Example of image defects detected in the test dataset. (a) Ink contamination. (b) Unfocused images. (c) Artifacts in the specimens. (d) Samples mainly composed of red blood cells.

Furthermore, due to the suspicious results obtained on patient P6, the specimen was examined again by a pathologist for reassessing the initial diagnosis. After this examination, the pathologist realized a problem with the selection of ROIs in the HS acquisition for the non-tumor areas. In Figure 5-4, we show the initial evaluation of the sample, where the tumor area was annotated by using a red marker contour, and the rest of the sample was considered as non-tumor. Figure 5-4.b corresponds to the second evaluation of the sample. The original annotation of tumor was technically correct, but the yellow markers indicate the location of the highly invasive malignant tumor, i.e. GB. Although the other tumor areas correspond to tumor, their cells are atypical and cannot be considered a high-grade GB. In both Figure 5-4.a and Figure 5-4.b, the ROIs selected for HS acquisitions are highlighted with squared boxes, where red and blue boxes indicate tumor and non-tumor ROIs, respectively. As can be observed in Figure 5-4.b, the non-tumor areas selected for our experiments were located too close to areas where

the infiltrating GB was identified, and thus they contain extensive lymphocytic infiltration and cannot be considered strictly non-tumor samples. Furthermore, it was found that the GB of this patient was not typical, presenting low cellular density in the tumor areas. Finally, the ROI selected from the tumor area was located where the diagnosis is tumor, but cannot be considered a high-grade glioma, i.e. GB. These reasons explain the seemingly inaccurate results obtained in the classification. Nevertheless, such bad results helped us to find an abnormality in the sample.

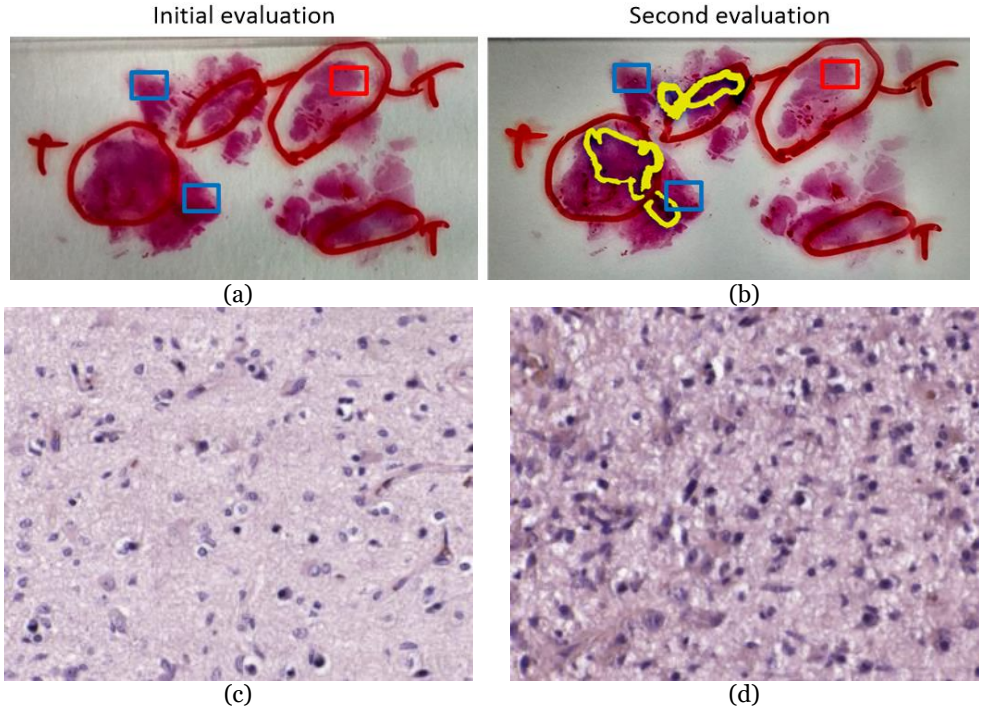

Figure 5-4: Evaluation assessment for the samples of Patient P6. Red pen markers indicate the initial evaluation of tumor regions. Regions without pen contour were considered as non-tumor. Red squares indicate the ROIs of tumor samples. Blue squares indicate the ROIs of non-tumor samples. (a) Initial evaluation of the sample. (b) Second evaluation of the sample, where a yellow marker is used for the updated tumor areas. (c) Example of HSI from tumor ROI. (d) Example of HSI from non-tumor ROI.

In order to quantify the influence of the inclusion of incorrect HS images in the classification, we evaluated again the classifiers when the corrupted HS images were excluded from the dataset. These HS images were only removed from the test. The CNN was not trained again to avoid introducing bias in our experiments. These results are shown in Table 5-5. Patients where data exclusion was performed are indicated with an asterisk (*), and the results of patient P6 were removed due to the diagnosis reasons explained before. The results of the classification after data exclusion improved significantly for patients P2 and P7, while the results of other patients keep constant after the exclusion of some HS images. This data removal also boosts the overall metrics across the patients, due to the improvement in the classification in some patients and because of the removal of patient P6 due to justifiable clinical reasons.

Table 5-5: Final classification results on the test set after excluding incorrect HS images.

	HSI				RGB			
Patient	**AUC**	**ACC (%)**	**Sensitivity (%)**	**Specificity (%)**	**AUC**	**ACC (%)**	**Sensitivity (%)**	**Specificity (%)**
P1*	**0.98**	**93**	91	**96**	0.93	90	**97**	61
P2*	**0.99**	**89**	**99**	83	**0.99**	87	79	**99**
P3*	0.95	85	91	**80**	**0.96**	**92**	**97**	**78**
P4	0.62	57	57	**58**	**0.69**	**77**	**98**	7
P5*	**0.81**	**69**	**81**	**64**	0.66	58	57	60
P6†	-	-	-	-	-	-	-	-
P7*	**0.74**	**66**	**71**	63	0.68	58	50	**77**
P8	0.98	96	96	96	**0.99**	**97**	**97**	**97**
P9	*N.A.*	**99**	**99**	*N.A.*	*N.A.*	*89*	*89*	*N.A.*
P10	*N.A.*	**89**	**89**	*N.A.*	*N.A.*	*43*	*43*	*N.A.*
P11	*N.A.*	92	92	*N.A.*	*N.A.*	***98***	***98***	*N.A.*
P12	*N.A.*	**92**	**92**	*N.A.*	*N.A.*	*84*	*84*	*N.A.*
P13	*N.A.*	**99**	**99**	*N.A.*	*N.A.*	*88*	*88*	*N.A.*
Avg.	***0.87***	***85***	***88***	*77*	*0.84*	*80*	*81*	*68*
Std.	***0.15***	***14***	***13***	***16***	*0.16*	*18*	*20*	*31*

** Data exclusion † Data removed*

Regarding the classification performance of HSI compared to RGB, the results suggest the superiority of HSI (see Table 5-4 and Table 5-5). The average metrics on the whole datasets are worse for RGB images, especially in terms of specificity and sensitivity. We consider good performance in classification when all the metrics are high, with balanced specificity and sensitivity. For example, P4 presents a better AUC for RGB, but really poor specificity (7%). For this reason, the HSI classification for such patient presents a better performance. Only for P2, P3 and P8, the performance of RGB is approximately equivalent to HSI. P11 is the only patient where RGB substantially outperforms HSI. For patients where the performance is the most promising (e.g. P1, P2, P3, and P8), RGB classification is also accurate. However, the sensitivity and specificity are not as balanced compared to HSI. Furthermore, the standard deviation in specificity and sensitivity are higher for RGB classification, which show a wider spread of the classification results compared to HSI. The decrease of performance of RGB images compared to HSI is more evident in patients with only tumor samples, where HSI classification was shown to be really accurate (e.g. P9, P10, P12, and P13). Finally, in patients where the classification of HSI was found poor (e.g. P4, P5, and P7), HSI performance is still shown to be more competitive than the RGB counterpart. On average, the accuracy of the classification is improved 5% when using HSI instead of RGB imaging, and particularly, the specificity and specificity are increased achieving 7% and 9% of improvement, respectively (Table 5-5).

5.1.4.3 Heat map results

Beyond the results obtained for the analysis of the patches, we also qualitatively evaluated the outcomes of the classification by generating classification heat maps from the HS images. In these maps, the probability of each pixel to be classified as tumor is represented, where red values indicate high probability and blue values indicate low probability. The inputs of our CNN are patches of 87×87 pixels, for this reason the resolution of the heat maps cannot contain pixel-level details. To provide them with resolution enough for a useful interpretation, we generated classification results for a 23-pixels sliding window length. We show two different types of heat maps in Figure 5-5 and Figure 5-6.

On the one hand, in Figure 5-5 we illustrate the different types of results that are obtained in patients where the models were proven to classify accurately the samples. Figure 5-5.a and Figure 5-5.c show examples of non-tumor and tumor images that were classified correctly, with no presence of neither false positives nor false negatives, respectively. In Figure 5-5.b we can see the presence of some false positives in a non-tumor tissue image, but such false positives are located in an area where there is a cluster of cells, indicating that it is a suspicious region. Finally, Figure 5-5.d shows a tumor image where there are some regions classified as non-tumor tissue. Nevertheless, such false negatives are located in areas where there are no cells. The FP in Figure 5-5.b suggests the CNN perceives areas with high cell density as tumor. The FN shown in Figure 5-5.d has a clinical interpretation, but it is computed as a bad result in the quantitative evaluation of the classification. Furthermore, a more detailed ground truth scheme for classification may improve the classification performance, e.g. the inclusion of brain background tissue, blood vessels, or blood cells.

On the other hand, we show in Figure 5-6 the heat maps from patients that present the worst performance in the quantitative evaluation of the results. Firstly, Figure 5-6.a and Figure 5-6.b show the results for Patient P4. It can be observed that the heat maps for each kind of tissue are similar, presenting false positives for the non-tumor image and false negatives for the tumor image. For this patient, the heat maps and the quantitative results are coherent, showing that the CNN is not able to accurately classify the samples from this patient. Secondly, Figure 5-6.c and Figure 5-6.d show the heat maps for Patient P6. As mentioned before, the non-tumor tissue of this patient was proven to be adjacent to the tumor area, and hence cannot be considered as non-tumor tissue. In this case, Figure 5-6.c shows that the non-tumor area has been classified as tumor, which is in fact correct. Finally, it was also discussed that Patient P6 presented a non-typical GB with low cellularity. A heat map from a tumor image from this patient (Figure 5-6.d) shows that tumor cells are highlighted as tumor, but the areas with low cellular presence are diagnosed as non-tumor.

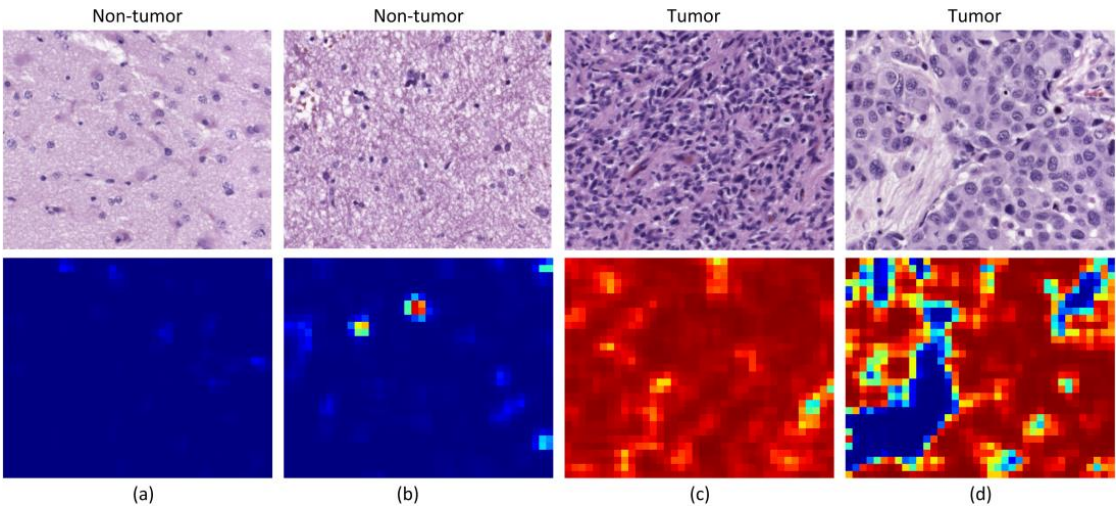

Figure 5-5: Heat maps from good performance patients. (a) Non-tumor tissue with no false positive. (b) Non-tumor tissue with some false positives. (c) Tumor tissue with no false negative. (d) Tumor tissue with some false negatives.

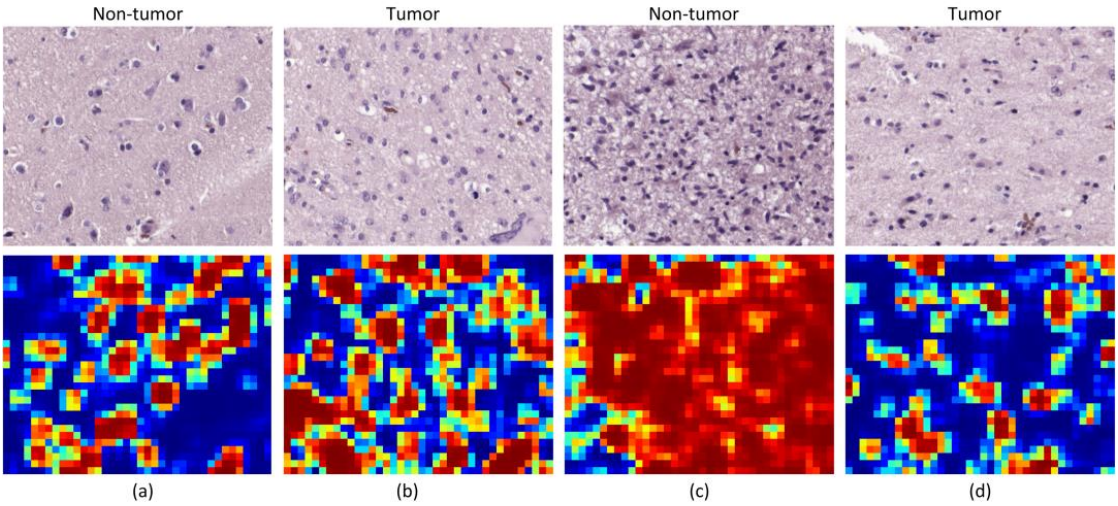

Figure 5-6: Heat maps from bad performing patients. (a) and (b) Non-tumor and tumor maps from Patient P4. (c) and (d) Non-tumor and tumor maps from Patient P6.

5.1.4.4 Comparative between SLIC and CNN

Table 5-6 shows the results of the proposed superpixel approach (reporting both the results at image and superpixel level) and the results from the CNN approach (reporting the results at patch level). As shown in Table 5-6, data from P6 are missing from the CNN experiments. In the CNN approach, we found a pathology error in the annotations of P6, and this patient was removed from the dataset. For the superpixel approach, we corrected the annotation errors of this patient. However, to provide a fair comparison between the two different processing approaches, P6 patient has not been included in the computation of the mean metrics. The average ACC results obtained with the proposed approach (considering the results at image level) is 3% below the CNN-based approach. However, the average sensitivity obtained with the superpixel-based approach is higher than the CNN results, 91% and 88%, respectively. Moreover, the average specificity is slightly improved using the proposed approach (78%) respect to the CNN-based approach (77%). Considering the fact that the superpixel approach only exploits spectral information, the results achieved in this preliminary study are competitive with respect to the CNN approach, which uses both spatial and spectral properties. Moreover, it is worth noticing that the amount of data generated with the patch-based CNN approach is extremely large (49,565 image patches of 87 × 87 pixels with 275 bands, i.e. approx. 768 Gigabytes) compared to the data generated for the superpixel-based approach (426,260 superpixels with 275 bands, i.e. approx. 0.87 Gigabytes). Hence, the CNN approach requires substantial memory and computational requirements to perform the classification of the data, while the superpixel-based approach alleviates these requirements. This is especially important when targeting real-time aid visualization tools for histological screening process during clinical routine practice with the goal of assisting pathologist during diagnostic procedures.

Table 5-6: Results comparison between the proposed superpixel-based approach and a previous work using a CNN-based approach [93].

	Proposed superpixel-based approach (results at image level)			**Proposed superpixel-based approach (results at superpixel level)**			**Previous CNN-based approach** [93] **(results at patch level)**		
Partition	**ACC**	**Sensitivity**	**Specificity**	**ACC**	**Sensitivity**	**Specificity**	**ACC**	**Sensitivity**	**Specificity**
P1	**1.00**	**1.00**	**1.00**	0.91	0.91	0.90	0.93	0.91	0.96
P2	**0.94**	0.83	**1.00**	0.79	0.50	0.97	0.89	**0.99**	0.83
P3	**1.00**	**1.00**	**1.00**	0.90	0.88	0.92	0.85	0.91	0.8
P4	**0.79**	**1.00**	0.73	0.78	**0.87**	0.75	0.57	0.57	0.58
P5	0.68	**1.00**	0.63	0.54	0.67	0.51	**0.69**	0.81	**0.64**
P6*	**0.90**	**0.50**	**1.00**	0.85	0.35	0.98	-	-	-
P7	0.35	**1.00**	0.10	0.53	0.95	0.30	**0.66**	0.71	**0.63**
P8	**0.96**	**0.83**	1.00	0.89	0.75	0.93	**0.96**	**0.96**	0.96
P9	0.95	0.95	-	0.92	0.92	-	**0.99**	**0.99**	-
P10	0.25	0.25	-	0.41	0.41	-	**0.89**	**0.89**	-
P11	**1.00**	**1.00**	-	0.98	0.98	-	0.92	0.92	-
P12	**1.00**	**1.00**	-	0.83	0.83	-	0.92	0.92	-
P13	**1.00**	**1.00**	-	0.97	0.97	-	0.99	0.99	-
Avg.	*0.83*	***0.91***	***0.78***	*0.79*	*0.80*	*0.76*	***0.86***	*0.88*	*0.77*
Std.	*0.27*	*0.22*	*0.34*	*0.19*	*0.19*	*0.26*	***0.14***	***0.13***	***0.16***

* Data not available for CNN-based approach and excluded for the computation of the average (Avg.) and standard deviation (Std.) values.

5.1.5 Discussion

In this research work, we have presented a deep learning approach for the classification of hyperspectral images of H&E pathological slides of brain tissue samples of human patients diagnosed with GB. The dataset employed in this work was described in the previous chapter (Section 4.3.1).

Such dataset was then used to train a CNN and to perform the classification between non-tumor and tumor tissues. Due to the limited number of patients involved in this study and with the aim to provide a data partition scheme with minimum bias, we decided to split the dataset in four different folds where the training, validation and testing data belonged to different patients. Each fold was trained with 9 patients, where only 5 of them presented both types of samples, i.e. tumor and non-tumor tissue.

After selecting models with high AUC and balanced accuracy, sensitivity and specificity in the validation phase, some results on the test set were not accurate at all. For this reason, we carefully inspected the heat maps generated by the classifiers for each patient in order to find a rationale about the inaccurate results. After this, we detected four types of problems in the images that could worsened the results, namely the presence of ink and/or artifacts in the images, unfocused images or excess of red blood cells. We reported both results, before and after cleaning wrong HS images, for a fair experimental design. We consider that the test results after removing such defective HS images are not biased because the rationale of removing the images from the test set is justifiable and transparent. These corrupted images were part of the train set, but it is unknown if the training process of the CNN was affected.

We also found a patient, P6, where the results were really inaccurate. For this reason, the regions of interest that were analyzed by HS were re-examined by the pathologists. After examining the sample, an atypical subtype of GB was found, and examination revealed that the ROIs selected as normal samples were close to the tumor area, which cannot be considered as non-tumor. Although the classification results were not valid for this patient, by using the outcomes of the CNN, we were able to identify a problem with the prior examination and ROI selection within the sample. Additionally, although this

patient was used both as part of the training and as a patient used for validation, the results are not significantly affected by this fact. These results highlight the robustness of the CNN for tumor classification. Firstly, although the validation results of fold 1 were good when evaluating patient P6, the model from this fold was also capable of accurately classifying patients P1 and P11. Secondly, although patient P6 was used as training data for fold 3 and fold 4, the outcomes of these models were not proven to be significantly affected by contaminated training data.

Although the results are not accurate in every patient, after excluding incorrectly labelled and contaminated HS images, nine patients showed accurate classification results (P1 to P3 and P8 to P13). Two patients provided acceptable results (P5 and P7), and only a single patient presented results that were slightly better than random guessing (P4). Nevertheless, these results can be considered promising for two main reasons. First, a limited number of samples were used for training, especially for the non-tumor class, which was limited to only five training patients for each CNN. Second, the high inter-patient variability shows significant differences between tumor samples among the different patients. As can be observed in the analysis of heat maps (Figure 5-5 and Figure 5-6), there is a significant heterogeneity in cellular morphology in different patients' specimens, which makes GB detection an especially challenging application. To handle these challenges, in future works the number of patients should be increased, and to deal with the high inter-patient variability, HS data from more than a single patient should be used to validate the models.

Finally, we found that HSI data perform slightly better than RGB images for the classification. Such improvement is more evident when the classification is performed on challenging patients (e.g. P5 or P7), or in patients with only tumor samples. Furthermore, the classification results of HSI are shown to provide more balanced sensitivity and specificity, which is the goal for clinical applications, improving the average sensitivity and specificity by 7% and 9% with respect to the RGB imaging results, respectively. Nevertheless, more research should be performed to definitively demonstrate the superiority of HSI over conventional RGB imagery.

5.2 Breast cancer approach

In this section, we investigate the use of HSI to differentiate between normal and tumor cells from breast histological samples. The images were acquired using a high spectral resolution system which provided 826 spectral bands from 400 nm to 1000 nm, beyond the visible limitations of naked eye. First, cell-level annotations were performed by a skilled pathologist in digitized whole-slides. Then, HS images from the annotated areas were captured. We applied an image registration method to translate the annotations from the whole-slide RGB image to the HS domain, thus extracting an annotated HS dataset from breast cancer cells. Finally, we used a CNN to automatically discriminate between tumor and normal breast cells.

5.2.1 Biological sample description

In this research work, the samples consisted of pathological slides diagnosed with breast tumor. In this study, two different pathological slides from different patients were analyzed. The tissue samples were processed using a conventional histological process,

including paraffin embedding, tissue sectioning, and staining using H&E. Then, the whole-slides were digitized using a Pannoramic SCAN digital scanner (3D Histech Ltd., Budapest, Hungary).

The samples were examined, and some parts of the digitalize slides were carefully annotated by pathologists using the Pannoramic Viewer software (3D Histech Ltd., Budapest, Hungary). The annotations were performed at cell-level, and different types of cells were annotated: tumor cells, mitotic cells, lymphocytes and normal cells. Different colors markers were used to highlight different types of cells: red for tumor cells, green for mitotic cells, yellow from lymphocytes, and blue for normal cells. We show an example of the whole digitalize slide with and without annotations in Figure 5-7.a and b, respectively. In Figure 5-7.c, a detail from an annotated region of the slide is presented.

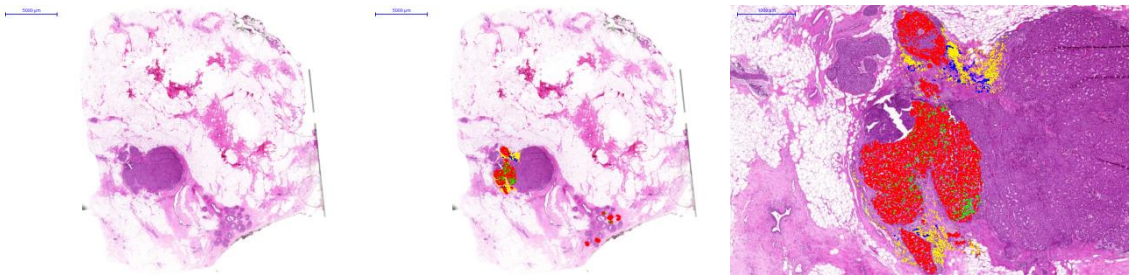

(a) (b) (c)

Figure 5-7: Histological samples used in this study. a) Digitized whole-slide image. b) Digitized whole-slide image including annotations. c) Details of an annotated area in the slide. Different types of cells were annotated by using different colors: tumor cells (red) mitotic cells (green), lymphocytes (yellow) and normal cells (blue).

5.2.2 Dataset description

The instrumentation employed is the System-III, described previously in this document. Using the aforementioned instrumentation, most of the areas annotated by the pathologist were captured. We used a 20× magnification for image acquisition, producing a HSI image size of 375 × 299 μm (1004 × 800 pixels). We imaged a total of 112 HS images, 65 from patient 1 and 47 from patient 2. Flat-field correction and reduction of the spectral bands by averaging contiguous spectral channels were applied to the HS images. The final goal of this study is to establish a relationship between the outcomes of the HS image processing and the diagnosis provided by the pathologists. For this reason, after capturing each HS cube, the consequent annotations from each area were extracted using the Pannoramic Viewer software. Figure 5-8 show an example of several HS images and their corresponding digitized counterparts. The annotations for each image are also shown.

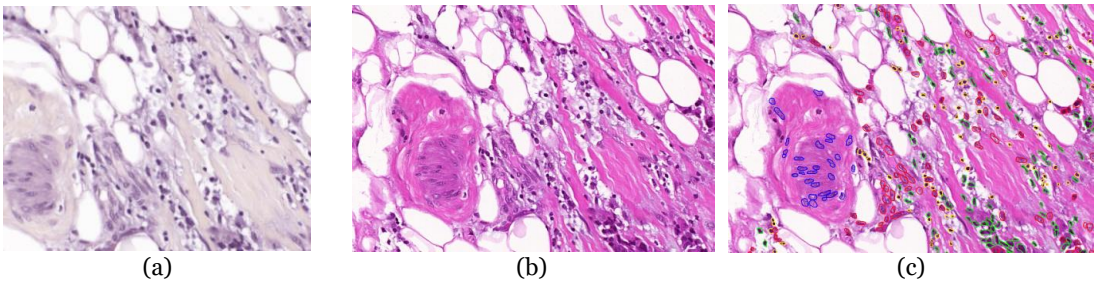

(a) (b) (c)

Figure 5-8: Example of some of the HS images acquired for this study (a), and the same area extracted from the digitized slide (b) and its corresponding annotations (c).

5.2.2.1 Hyperspectral dataset generation

In this study, we processed HS data from different types of cells within a breast cancer histological sample. We extracted the information from the areas that had been previously annotated by the pathologist. We had two different types of images: the annotated regions from digitized RGB slides and the corresponding HS images from the same regions. The size and the orientation of both types of images were different. For this reason, in order to identify the annotated cells in the HS images, an image registration between the HS images and the digitized slides was necessary. Our approach for the image registration consisted of searching for a geometric transformation that matched the information from the annotations to our HS images. To this end, we performed an image registration between the digitized RGB slide and a RGB synthetic image extracted from the HS cube.

The steps of our approach for the image registration are the following. First, the Speeded-Up Robust Features (SURF) algorithm is applied to both images. The output of the SURF algorithm is a set of relevant points of an image that can be used in subsequent image matching tasks. After applying SURF, feature descriptors of relevant points are extracted. Then, feature matching is applied to the feature descriptors retrieved for each image. This feature matching is based on a nearest neighbors search, using the pixel-wise distance between the different feature descriptors of each image. Finally, using the relevant points of both images that present similar features, we search for an appropriate geometric transformation. This computation was performed using the MATLAB Computer Vision Toolbox (MathWorks Inc., Natick, MA, USA).

Figure 5-9 shows a flowchart of the workflow for this task, where the inputs of our image registration approach are the digitized slide and an RGB synthetic image extracted from the HS cube. After obtaining the appropriate geometric transformation to map the digitized slides to the HS domain, we apply this geometric transformation exclusively to the annotations. The annotation image is calculated as the subtraction of the digitized image from the pathological slide and its annotated counterpart. As a result, we retrieve the information about the annotations in the HS domain.

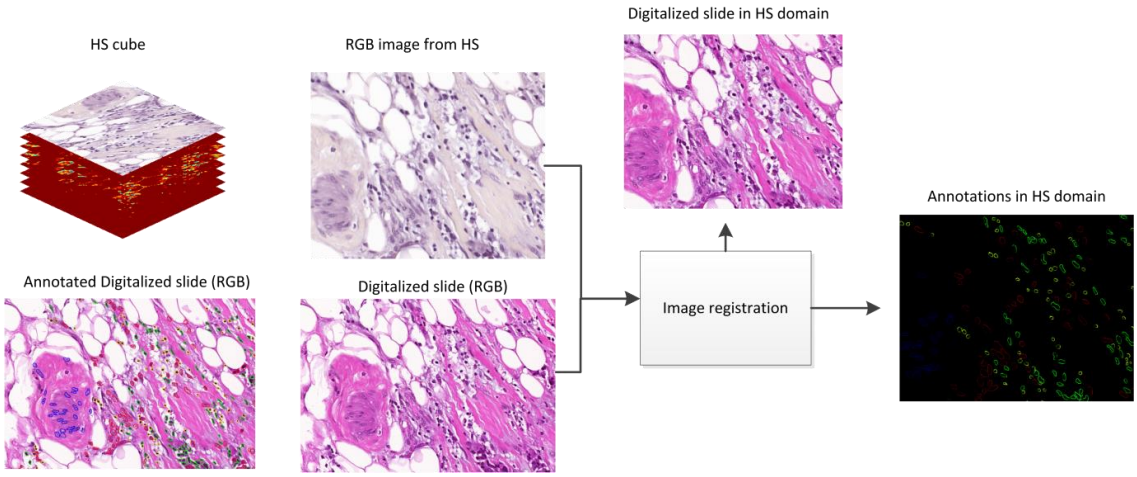

Figure 5-9: Framework for image registration between the digitized slides and the HS images.

After the image registration process, the annotations are geometrically aligned with the HS image. In order to extract the spectral information of each cell, we perform some image processing over the annotated image. First, taking into account that each color used for the cell annotation procedure contains information about a particular cell type,

we separate the different colors (red, green, yellow and blue) for subsequent analysis. These images consist of binary maps containing the contour of the annotations for each cell type. To generate a binary map where the whole cells are identified, we apply morphological operations to retrieve a map containing the location of each cell. Finally, we search for the centroids of each cell. Using this information, we can extract the information about the annotated cells within our HS data, generating HS image-patches of 39 × 39 spatial pixels and 159 spectral channels. This procedure is shown in Figure 5-10.

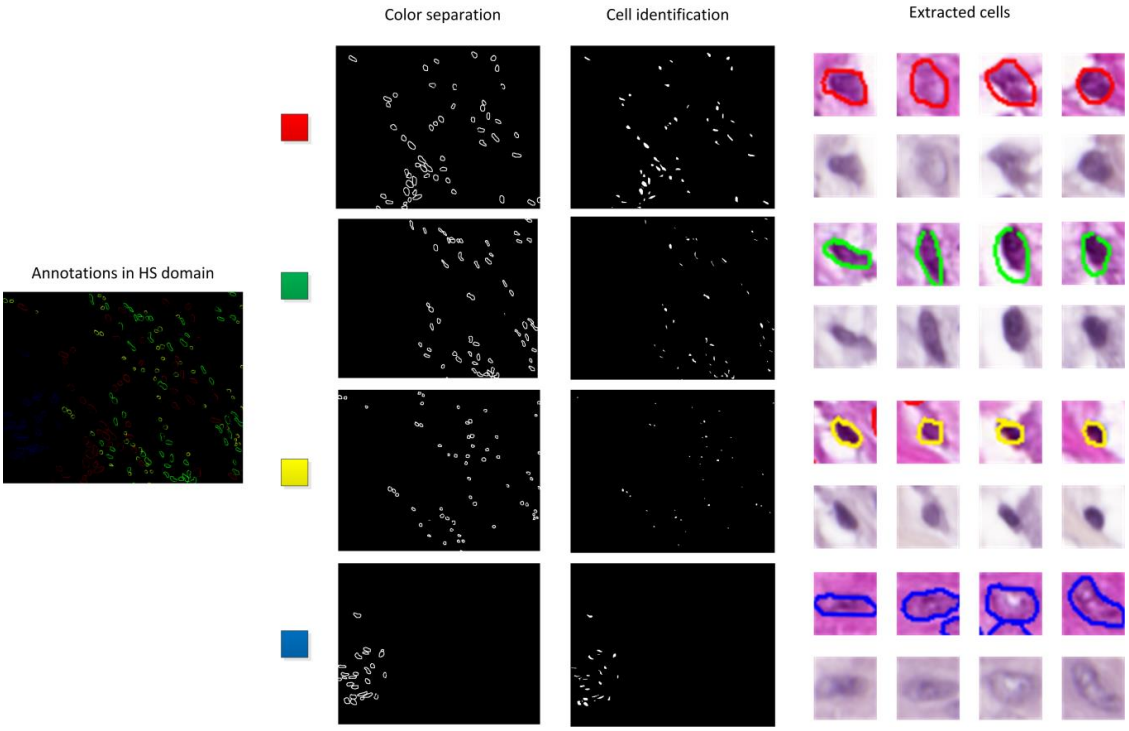

Figure 5-10. Detection of cells within the spectral image.

Table 5-7 shows a summary of our annotated dataset of 112 HS images, and Figure 5-11 shows the average spectral signature for each patient and each cell type. In the experiments presented in this work, we employed only normal and tumor cells to demonstrate the feasibility of the proposed method.

Table 5-7: Number of HS image-patches in the dataset.

Class	Patient 1 (65 images)	Patient 2 (47 images)
Tumor cells	12505	7607
Mitotic cells	576	1082
Lymphocytes	2238	563
Normal cells	300	365

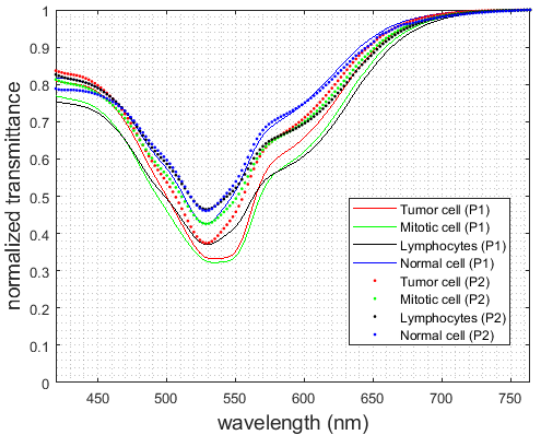

Figure 5-11: Mean spectral signatures found from normal cells (blue), tumor cells (red), mitotic cells (green) and lymphocytes (black), for each patient.

5.2.3 Data partition strategy

Due to the limited number of patients available for this study, we decided to train the network using the data from a single patient and using the data from the remaining patient for both validation (25%) and test (75%). A schematic of the data partition is shown in Figure 5-12. We refer to *Experiment 1* and *Experiment 2* for the situations where the data from patient 1 and patient 2 are used for training, respectively. This preliminary data partition was motivated by the limitation on the number of patients involved in this preliminary study. However, this situation is not realistic for biomedical applications. For this reason, we proposed two additional experiments (namely *Experiment 3* and *Experiment 4*), where the models were trained and validated using the data from one patient, and the test was performed in an independent patient. Additionally, because of the imbalance between classes, we performed data augmentation for the normal cells for training the CNN. This data augmentation consisted of spatial flip and rotation of the patches corresponding to normal cells.

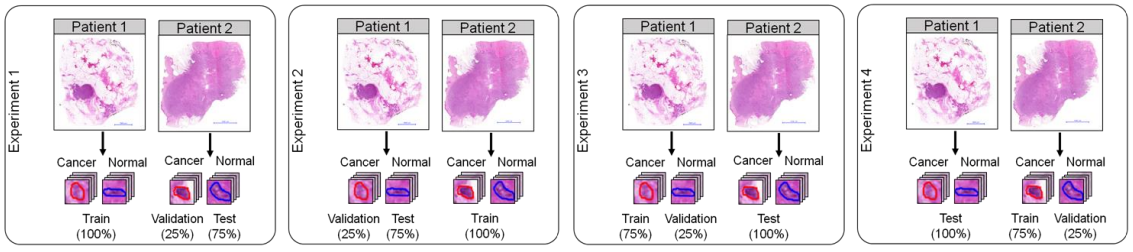

Figure 5-12: Data partition used for the classification experiments and testing.

5.2.4 Processing framework

We employed a custom 2D-CNN for the automatic differentiation between normal and tumor cells. The network was developed using the TensorFlow implementation of the Keras Deep Learning API [342], [343]. This network is mainly composed by 2D convolutional layers. We detail the description of the network in Table 5-8, where the input size of each layer is shown in each row, and the output size is the input size of the consequent layer. All convolutions and the dense layer were performed with ReLU activation functions with a 10% dropout. The optimizer used was stochastic gradient descend with a learning rate of 10^{-4}.

Table 5-8. Schematic of the proposed CNN.

Layer	Kernel size	Input Size
Conv2D	3×3	39×39×159
Conv2D	3×3	37×37×256
Conv2D	3×3	35×35×256
Conv2D	3×3	33×33×512
Conv2D	3×3	33×33×512
Conv2D	3×3	31×31×1024
Conv2D	3×3	29×29×1024
Conv2D	3×3	27×27×1024
Global Avg. Pool	25×25	25×25×1024
Dense	256 neurons	1×1024
Dense	Logits	1×256
Softmax	Classifier	1×2

5.2.5 Experimental results

In order to measure the performance of the classifier in discriminating between normal and tumor cells, we made use of the receiver operating characteristic (ROC) curve on both the validation and test sets. To generate these results, we used different thresholds for each experiment. These thresholds were selected using the validation data, and then were applied to the final classifiers. In Table 5-9, we show the values for AUC, overall accuracy, sensitivity and specificity extracted for both the validation and the test datasets. Additionally, due to the low number of normal tissues in the test and validation sets, we studied the variations of the classifier performance using bootstrapping, and we reported the 95% confidence intervals for such metrics.

Table 5-9: Results on the classification of normal and tumor cells for Experiment 1 and Experiment 2, which performs validation and testing on the same patient (inter-patient validation).

Group	Experiment	AUC	ACC (%)	Sensitivity (%)	Specificity (%)
Validation	*Patient 1*	0.88 (0.83, 0.93)	80 (74, 85)	80 (73, 86)	80 (73, 87)
	Patient 2	0.91 (0.86, 0.95)	82 (76, 88)	85 (77, 91)	80 (73, 87)
	Average	0.89 (0.85, 0.94)	81 (75,87)	82 (75, 89)	80 (73,87)
Test	*Patient 1*	0.87 (0.84, 0.90)	80 (77, 83)	80 (76, 84)	80 (76, 84)
	Patient 2	0.94 (0.91, 0.96)	87 (84, 90)	86 (82, 90)	89 (85, 93)
	Average	0.90 (0.88, 0.93)	84 (80, 87)	83 (78, 87)	85 (81, 89)

The results of experiments 1 and 2 are competitive in terms of AUC, reaching an average AUC of 0.89 and 0.90 for both validation and test. The values of accuracy, sensitivity and specificity are greater than 80% in all the experiments, with narrow confidence intervals. Furthermore, specificity and sensitivity are balanced, showing a competitive detection of both normal and tumor cells. The selected threshold values were 50% for *Experiment 1*, and 10% for *Experiment 2*.

The results for experiments 3 and 4 are shown in Table 5-10. The threshold values were selected during the validation as 25% for both *Experiment 3* and *Experiment 4*. For these experiments, the validation values of all the metrics are high. This is because the data from the same patient was used for training and validation. Nevertheless, the results on an independent patient show competitive results in terms of AUC, with an average of 0.9. In the case of *Experiment 4*, the accuracy is not worsened significantly compared to *Experiment 2*. Unlike *Experiment 2*, however, the specificity and sensitivity values are not as balanced.

Table 5-10: Results on the classification of normal and tumor cells for Experiment 3 and Experiment 4, which performs training and validation on the same patient (intra-patient validation).

Group	Experiment	AUC	ACC (%)	Sensitivity (%)	Specificity (%)
Validation	*Patient 1*	0.97 (0.96, 0.98)	90 (88,91)	99 (98,100)	83 (81, 85)
	Patient 2	0.94 (0.93, 0.95)	87 (85,89)	84 (82,86)	90 (88,92)
	Average	0.95 (0.94, 0.96)	88 (87, 90)	92 (91, 93)	87 (85, 89)
Test	*Patient 1*	0.88 (0.86, 0.90)	78 (75, 81)	70 (68, 72)	97 (95, 99)
	Patient 2	0.91 (0.89, 0.93)	79 (76, 82)	96 (93, 98)	71 (68, 74)
	Average	0.90 (0.87, 0.92)	79 (76, 81)	83 (80, 86)	84 (82, 87)

In Figure 5-13 we present the ROC curves associated with the intra-patient validation experiments for both patients. The AUCs are similar for both patients. Additionally, the ROC curves suggest the classification for Patient 1 is more specialized in correctly detecting tumor cells (low false positive rate), while the classification for Patient 2 is more accurate in detecting normal cells (high true positive rate).

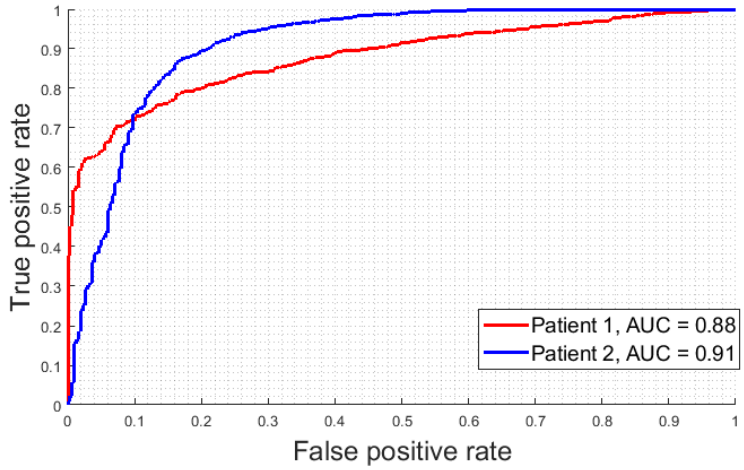

Figure 5-13: ROC curves from Experiment 3 and Experiment 4.

5.2.6 RGB comparison

Finally, in order to investigate if the classification results using HSI boost the classification performance of standard RGB digitized images, in this section we perform a comparison between both types of images. To this end, we generated synthetic RGB images from the HS cubes by using a combination of wavelengths simulating the human eye response. Then, we generated the patches for only Experiment 3 and Experiment 4 and performed the classification using the same CNN described in Section 2.4. After validation, we selected the best performing models, and we summarized the results in Table 5-11. As can observed in the Table, although the validation results suggested models with competitive AUC values where the specificity and sensitivity values were also high, the results on the test show unbalanced results, suggesting an specialization of the CNN on the prediction of a single class, what worsen the overall performance of the classifier for the other one. This fact is more evident in Experiment 3, where the specificity is highly worsened while the sensitivity is high.

Table 5-11: Comparison between HSI and RGB for Experiment 3 and Experiment 4, which performs training and validation on the same patient (intra-patient validation).

Group	Experiment	Technology	AUC	ACC (%)	Sensitivity (%)	Specificity (%)
Validation	*Patient 1*	HSI	**0.97** (0.96, 0.98)	**90** (88, 91)	**99** (98, 100)	**83** (81, 85)
		RGB	0.94 (0.93, 0.96)	85 (83, 86)	97 (96, 99)	77 (75, 79)
	Patient 2	HSI	**0.94** (0.93, 0.95)	**87** (85,89)	84 (82,86)	**90** (88,92)
		RGB	0.88 (0.86, 0.90)	76 (74, 79)	**86** (83. 89)	71 (69, 73)
	Average	HSI	**0.95** (0.94, 0.96)	**88** (87, 90)	**92** (91, 93)	**87** (85, 89)
		RGB	0.91 (0.89, 0.93)	80 (78, 82)	91 (89, 94)	74 (72, 76)
Test	*Patient 1*	HSI	0.88 (0.86, 0.90)	**78** (75, 81)	70 (68, 72)	**97** (95, 99)
		RGB	**0.94** (0.93, 0.95)	66 (64, 68)	**99** (98, 100)	60 (59, 61)
	Patient 2	HSI	**0.91** (0.89, 0.93)	**79** (76, 82)	**96** (93, 98)	71 (68, 74)
		RGB	0.83 (0.81, 0.86)	77 (75, 79)	70 (68, 73)	**89** (86, 92)
	Average	HSI	**0.90** (0.87, 0.92)	**79** (76, 81)	83 (80, 86)	**84** (82, 87)
		RGB	0.88 (0.87, 0.90)	71 (69, 73)	**84** (83, 86)	74 (72, 76)

5.2.7 Discussion

The use of machine learning techniques for assisting pathologists in routine examination of samples is an emerging trend. These computer-assisted tools are devoted to provide a quantitative diagnosis of different diseases, and also to decrease the current inter-observer variability in diagnosis. Although most of the approaches are based on conventional RGB image analysis, HSI is presented as a suitable technology that can boost the outcomes of conventional imagery due to its capability of differentiating between materials that present subtle molecular differences.

This work is novel due to the use of an annotated cell-level dataset using a digitized slide, and the translation of such annotations to the HS domain using image registration techniques. After a cell-based dataset was generated, we used a 2D-CNN for the automatic differentiation of tumor and normal cells. The CNN was trained by using the data from one patient, and the performance of the classifier was measured using data from a different patient. After creating an HSI cell-level annotated dataset from the information of an annotated digitized slide, HSI data was classified by using a 2D-CNN. The AUC for all our experiments were above 0.89, and the sensitivity and specificity values were approximately equivalent for experiments 1, 2 and 3. In the case of experiment 4, sensitivity and specificity values of each patient were not as balanced as in the other experiments. These metrics strongly depend on the threshold selected for the final models. Nevertheless, due to the competitive AUC, there is room for improvement for specificity and sensitivity if the threshold is selected using data from an independent patient. Two main challenges have to be addressed in the future to improve the performance of the CNN in this application. The number of patients should be increased, and more annotated cells from the normal class should be included in the dataset in order to balance the classes for the classification problem.

Finally, we included a comparative between the classification of HSI and conventional RGB. Previous study has proven the feasibility of RGB image analysis for breast cancer applications [349], [350]. Our experiments suggest the outperformance of HSI analysis over RGB images. Nevertheless, further investigations should be performed to prove the boost of HSI performance over RGB analysis for this application.

Although the results of this study are promising, the study is limited by the sample size of the current dataset. Future work involves the inclusion of data from additional

patients, and also the study of the classification of the other types of cells present in the pathological slides, i.e. mitotic and lymphocyte cells. In conclusion, this preliminary investigation demonstrates the potential of semi-automated HS histological imaging.

5.3 Conclusions

In this work, we have presented the use of hyperspectral imaging and deep learning for automatic classification of normal and tumor cells in histological samples. The biological samples used in this study are different since the annotations provided by the pathologist are different. On the one hand, in the case of the brain cancer detection, the annotations are provided at area-level. This causes that each HS cube has a single annotation (i.e. tumor or non-tumor). In order to process such area-based annotated data, the images have been cut in different patches, which are subsequently processed by the CNN. On the other hand, the breast cancer samples were annotated at cell-level. This fact implies a higher workload in the pathologist side, who have to manually annotate the different cells in a digitized slide. Besides, additional image processing techniques are necessary to retrieve the information of the annotations in the HS images. Finally, the patches used for the CNN approach correspond to the different cells. Further investigation should be carried out in order to determine which type of annotations is more convenient from a Machine Learning perspective.

One of the principal shortcomings of this study is the limited number of patients, especially for the breast cancer approach. Although the results of such study are promising, the study is limited by the sample size of the current dataset. Future work should involve the inclusion of data from additional patients, and the study of the classification of the other types of cells present in the pathological slides, i.e. mitotic and lymphocyte cells.

Finally, the architecture used for the classification of samples in both the breast cancer and the brain cancer scenarios consist of 2D-CNNs. However, an exploratory analysis of which Deep Learning architecture is most convenient for the classification of the different types of HS images should be carried out in future works.

Chapter 6: Conclusions & Future Lines

Within this document, the development of this PhD thesis has been presented. In this chapter, we summarize the main contributions of this PhD thesis, as well as we outline the main conclusions depicted from this research work. Then, we present the potential research lines which have arisen from the development of this PhD thesis. Finally, we shown the academic production developed in the context of this PhD.

6.1 Conclusions

In this thesis, we have presented a novel use of HS imaging as an assistant tool for histopathological samples analysis. To this end, first we performed an insight review of the state-of-art about the usage of HS for histological applications. Then, we presented the instrumentation which have been used during this thesis, and we proposed a methodology to acquire high-quality HS images using a push-broom camera and a microscope. Using such instrumentation, we generated several HS datasets of different types of histological samples, corresponding to brain tumor and breast cancer. Finally, we used different Machine Learning algorithms in order to extract information from the HS data, which can be potentially used as a clinical assisting tool, i.e. the discrimination between tumor and non-tumor areas in histological HS images. In this section, we provide a summary of the main contributions of this PhD thesis, as well as we present some concluding remarks regarding the main topics covered in this dissertation.

6.1.1 Context of HSI in computational pathology

One important contribution of this PhD thesis is a detailed overview of the current state of art of HSI for medical applications, especially for computational pathology. First, we outline the most important concepts regarding HSI, with especial emphasis on the instrumentation. Afterwards, in Section 2.1.2, we provided a survey about the most common information extraction techniques applied to medical HS data. There is a wide variety of methods used to extract information from HS data. Furthermore, there is a limited number of publicly available HS datasets. The aforementioned restrictions impose a complication in establishing a fair comparison between the different processing approaches available in the literature.

In Section 2.3 we accomplished a systematic review where the current usage of MSI/HSI for histological applications was analyzed. From such review, the most relevant category refers to the examination of the current usage of HSI/MSI for the analysis of

histological samples targeting clinical applications. According to the analysis presented in Section 2.3.6, we conclude that HSI/MSI is presented in the literature as a useful tool for the identification of diverse diseases and tissues, where cancer detection is the most common application. The two main drawbacks which hinder the standardization of procedures for histological MSI/HSI acquisition and analysis are related to both instrumentation and the image processing approach. On the one hand, the instrumentation strongly varies among different studies. Thus, it is not clear which instrumentation parameters are more appropriate for HSI/MSI histological analysis. On the other hand, there are substantial differences among data analysis methods across the different studies. Most approaches target automated classification of different types of tissues or diseases using machine learning techniques, and others deal with image visualization enhancement of different tissue constituents. In order to reach an agreement on an adequate common framework for HSI/MSI data processing for histopathological applications, there is a need for publicly available datasets, where a fair comparison across different methods could be performed.

Regardless of the high performance shown in the literature for the HS analysis of histological data, there is insufficient evidence to affirm the superiority of this technology over conventional imagery. There are several studies that point out that HSI/MSI are able to outperform standard RGB for disease detection [249], [264], [265], [271], [287], [289]. In order to state if HSI/MSI has a future in computational pathology, more performance comparisons should be carried out to definitively demonstrate the suggested superiority of HSI/MSI over conventional imagery for disease detection. Furthermore, HSI/MSI instrumentation is expensive and not standardized. Therefore, more research should be done to determine the cost-benefit trade-off on the use of HSI/MSI for the diagnosing-aid analysis of histological samples compared to conventional imagery.

Nonetheless, there is room for HSI/MSI technologies to outperform conventional imagery in clinical applications where the identification of diseases using the manual examination of samples is still challenging for pathologists.

6.1.2 Instrumentation

Since the main topic of this PhD is the usage of HSI for histological applications, one of the main achievements is related to the instrumentation. In Chapter 3, we first introduce the background about the most important concepts regarding the HS instrumentation, with a critical perspective on how each element of the instrumentation affects to the overall response of the acquisition system. Second, we presented the instrumentation which has been used to acquire the data in this PhD, which is composed by an optical and a mechanical part. In terms of the optical subsystem, we have shown how the spectral response of the Olympus BX-53 microscope is improved compared to the Olympus BH2-MJLT. While the latter is limited to wavelengths above 750 nm, the former is sensitive throughout the entire VNIR spectral range. Besides, one of the main limitations of the optical system, whatever microscope is used, is the dynamic range. The dynamic range cannot be maximized due to limitations in the light source power and also in the exposure time (which has an upper limit of 40 ms). To improve the dynamic range conditions in this scenario, an external light source could be used. Such maximization of the dynamic range would allow the acquisition of images at higher magnifications. Regarding the mechanical subsystem, we have developed two custom mechanism

devoted to performing the spatial scanning required for push-broom acquisitions. Such mechanical systems can be considered as a suitable low-cost alternative to adapt a microscope to a push-broom HS camera.

Finally, we proposed a methodology for the acquisition of microscopic push-broom HS images. This methodology is an important contribution of this PhD. This methodology is intended to provide a fast and accurate configuration of HS push-broom microscopes, even when certain specifications of the acquisition system are unknown beforehand, e.g. the FOV or the resolution of the mechanical system. It involves the setup of the light conditions, the optical focusing of the system, the camera-microscope alignment and the setup of the optimal scanning speed. In addition, it allows the empirical measurement of both the FOV and the mechanical resolution of the scanning platform, as well as detecting and characterizing the limitations of the acquisition system under analysis.

6.1.3 Datasets

A relevant contribution of this PhD thesis is the creation of novel HS datasets of histological samples. The datasets used in this PhD have been created in close collaboration with two different Pathological Departments from two different hospitals. The creation of the datasets involves a close collaboration with pathologist, who have to prepare the samples and provide them with annotations, i.e. an specification of the location of the different types of tissue within the sample. In this PhD thesis, we analyzed two different types of samples. First, we analyzed brain histological samples diagnosed with GB. Such samples were examined and prepared by pathologists from the Pathology Department from the University Hospital Dr. Negrín at Las Palmas de Gran Canaria. The annotations of such samples were performed macroscopically, where both non-tumor and tumor regions of the sample were highlighted using a pen marker over the pathological slides. Second, we analyzed breast cancer histological samples. Such samples were processed thanks to the collaboration with the Pathology Department of the Hospital de Tortosa Verge de la Cinta. The annotations of such samples were performed at cell level, where different types of cells were highlighted in an RGB digitized slide.

The sample annotation is one of the most important stages within the dataset generation and involves a close multidisciplinary collaboration between engineers and pathologists. Such sample annotations also involve a high workload to pathologists, who have to carefully examined the samples to accurately perform the annotations. The type of annotation scheme has implications in the subsequent research. On the one hand, the macroscopic annotations impose that each HS image has a single annotation, since the images are acquired from areas of the slides annotated with such certain annotation, e.g. tumor or non-tumor. On the other hand, cell level annotations require to use an image processing approach to translate the annotations from an annotated RGB digitized slide to match the acquired HS images. Although both approaches are valid, more research should be performed in order to determine which workflow for sample annotation is more appropriate for the HS analysis of histological samples.

One of the main limitations of this study is the reduced number of patients and the imbalance of the dataset. For example, in the case of brain tumor, only 8 of the 13 patients have annotated data available from the two classes, i.e. tumor and non-tumor. In the case

of breast samples, although a competitive number of annotated cells have been extracted from the slides, the specimens belong only to two patients.

This limited data makes training supervised classification models challenging, especially due to the intra-patient variability of data. For future research in this field, an increased number of patients will be required. More concretely, to obtain statistically significant results, we hypothesize that at least 10 patients are needed with both types of annotations for both validation and test. The rationale of at least 10 patients for each type of annotation is motivated to enable normality assumptions over both test and validation data. Besides, if we would like to train the models with a dataset which is at least twice the data used for validation or test, this would require at least 40 patients (20 for training, 10 for validation, and 10 for test) with both types of annotations to train the classifiers. The main challenges for the acquisition of such a dataset are the large amounts of data generated during image acquisition and the time-consuming manual annotation for the ground-truth.

6.1.4 Algorithms

Besides the characterization of the instrumentation and the generation of datasets, the most important contribution of this PhD is the image processing and machine learning techniques used to retrieve information from the HS cubes. In this PhD, the main goal was the development of algorithms capable to discriminate between non-tumor and tumor in HS histological images.

The types of algorithms that can be used strongly depend on the quality of the available HS data. In our first approach to process HS data (Section 4.2), the HS data presented some restrictions due to limitations of the instrumentation used to capture data (System-I). Namely, the spatial information was not complete due to limitations in the mechanical stage, and the magnification was fixed to 5× due to light source power limitations. For such reason, the classification was performed using three commonly used pixel-wise classifiers: SVM, RF and ANN. In this preliminary approach, we found positive results, which indicate a successful discrimination between normal and tumor tissue by exploiting the spectral information of the samples. However, the results presented in Section 4.2 have room for improvement in several aspects. First, the image quality can be further improved in order to exploit both the spatial and the spectral information of the samples. Second, using a hyperparameter optimization within the classifiers, the classification results can be further improved.

Once the problems related to low image quality were solved, we were able to acquire HS images with full spatial information and high magnifications, thus proposing different strategies to process HS data. Such dataset consists of about 500 HS images from 13 different patients. Furthermore, due to the availability of all the spatial information of the specimens, it was possible to generate heat maps indicating the areas that the algorithms considered affected by tumor.

We followed two different approaches for the processing of this type of data. On the one hand, in Section 4.3 we proposed the use of a spatial-spectral algorithm based on superpixel segmentation followed by a supervised classification of the superpixel spectra. The motivation of the use of a superpixel approach is to summarize the spectral information of a HS cube by searching for spectrally-coherent spatial regions in the HS, and then use such information to train the supervised classifiers. On the other hand, in

Section 5.1 we proposed the use of CNNs for the classification of the brain cancer samples. The main motivation behind the use of CNNs is their theoretical ability to jointly exploit both the spatial and the spectral features of HS data. Both approaches have been demonstrated to be valid for the classification of such samples. These results can be considered positive due to the large heterogeneity of GB tumors, and the limited number of patients available.

One remarkable outcome of this research is shown in Section 5.1.4. After a careful examination of the results of CNNs for a certain patient, whose results were really inaccurate, we asked pathologist to examine the sample again in order to check some abnormality in the sample. With such second analysis, it was determined that the annotated area was incorrectly annotated as normal.

In Section 5.1.4.4 we shown a comparative between the performance of SLIC and CNN methods for brain cancer detection. The performance of both methods was similar in terms of ACC and specificity. However, the average sensitivity obtained with the superpixel-based approach was higher than the CNN results, 91% and 88%, respectively. Considering the fact that the superpixel approach only exploits the spectral information for the classification, the results achieved in the superpixel approach can be considered competitive with respect to the CNN approach, which exploits both spatial and spectral features of HS data.

Finally, we applied the CNN classification to histological breast cancer samples (Section 5.2). The research presented in this context is limited in the number of patients. Although the classification results cannot be considered general due to the limited number of patients, it was possible to correctly classify the different cells (tumor and non-tumor) in a patient-independent data partition. Besides the classification results, an important part of this research was the methodology proposed to retrieve the information about the cell annotation from a conventional digitized slide to the HS domain.

We also performed a comparison between the performance of CNNs in HS and RGB images. Such comparisons are shown on Section 5.1.4 (brain cancer) and Section 5.2.6 (breast cancer). In such comparisons we found a similar average performance within the dataset, where HS classifications is shown to subtly outperform the classification compared to RGB images. However, the performance is shown to be dependent on which patient data are being classified, i.e. there are patients whose RGB classification outperforms the HS classification and vice versa. For such reason, more research should be performed in order to establish a more robust comparative between HSI and RGB in the aforementioned applications.

6.2 Future research lines

In this section, we discuss the more prominent research lines derived from the work presented in this dissertation.

6.2.1 Potential applications

According to our systematic review, we have shown the current status of color correction and digital staining of histological samples using HSI/MSI. First, together

with image analysis techniques, HSI and MSI have demonstrated to be able to correct the variations on the digitized slides among different laboratories. Such differences are mainly caused by differences in the instrumentation and in the histopathological process, *e.g.,* differences in the staining conditions. For these reasons, MSI and HSI are presented as suitable technologies to deal with inter-laboratories variability of digitized slides, which is currently one of the main challenges in computational pathology. Second, HSI/MSI has been also applied to perform digital staining of samples. In this field, one trend consists of applying image processing techniques to standard H&E samples to highlight tissue structures that are barely visualized using such staining. The other trend is to directly use image processing techniques for synthetic staining of unstained samples, avoiding the physical staining. Although the research regarding digital staining is promising, the number of works in this field is still limited and more research should be conducted.

Additionally, one of the most promising fields for future research in HSI/MSI for histopathological applications is the exploitation of unstained samples. The use of unstained samples is mainly motivated by the fact that the stains usually employed for the manual sample examination reduce the spectral range of the samples [316]. In the case of H&E, this staining limits the spectral response of the specimens to the visible spectral range, i.e. wavelengths between 400 and 750 nm. With unstained specimens, there is the possibility to exploit information in a wider spectral range, which may provide more information on some tissue constituents. For example, spectral information about collagen or lipids is more evident beyond 800 nm, and cell fuel sources that are upregulated in certain diseases states, such as FAD and NAD, have spectral responses from 300 to 500 nm [103], [234]. Theoretically, these signals would still be present in stained specimens, but they may have been washed out by the strong visible signals from stains. In this systematic review, we found some successful diagnosis applications using unstained samples [240], [241], [243], [255], [266], [304], [306]–[309]; however, the influence of staining on the spectral response of tissue should be further quantified in the future.

6.2.2 Dataset generation

One of the most evident future lines derived from this PhD is the analysis of a wider variety of histological samples. The most immediate future line would be to improve the research about the breast cancer classification in order to include more patients in the analysis. However, beyond the currently available samples, another important future line is to figure out which type of histological specimens are hardly diagnosed by manual examination of the samples. This type of samples, which are still a challenge for pathologists, would provide information that cannot be observed with conventional imagery.

Regarding the spectral range, attending to the analysis shown in the systematic review (Section 2.3), most of the research performed in the literature is restricted to wavelengths below 1,000 nm. The exception is the research performed by Awan et al., whose results suggest an improvement in performance of the classification of colon cancer tissues when information from NIR bands was also incorporated [284]. Thus, the exploration of the performance of the spectral range beyond 1,000 nm is one of the main challenges in HSI/MSI for histological applications.

Additionally, although in this thesis we focused on fixed magnification experiments, in future studies we will evaluate the influence of the magnification in the classification of histological samples. The main goal of such experimentation is to proof whether the usage of the spectral information would make possible to predict an accurate diagnosis of the samples by using lower magnifications, which would alleviate the acquisition process.

6.2.3 Instrumentation research

Future studies will address some limitations of this work. In this PhD thesis, the images were collected in a laboratory environment under controlled conditions. One of the main challenges associated to medical imaging processing is dealing with noisy images. Although in this work we focused on investigating the potential of HS images for the identification of tumor, in future works we will further analyze the effect of noise-removal strategies in the histological HS images [351]–[353].

Additionally, in this thesis, we have shown how the HS instrumentation strongly varies among different studies. It is not clear which instrumentation parameters are more appropriate for HSI/MSI histological analysis. The most important challenge is to determine which spectral range is more informative. As stated before, the NIR spectral range has been poorly explored for the analysis of histological HS images. The usage of such spectral range also imposes challenges in the instrumentation development. NIR cameras are characterized by a low spatial resolution. For this reason, along with the exploration of the NIR spectral range, techniques devoted to increase the spatial resolution of such images should also be investigated, e.g. superresolution. This challenge is especially important in histology applications, where the morphological features of tissue are important.

Other challenge for the instrumentation is regarding the magnification. As shown in, the light power transmission is inversely proportional to the objective lens magnification. This fact is illustrated in Figure 3-10. For this reason, in order to achieve higher magnifications with an optimal dynamic range, an external light source should be attached to the microscope to increase the light power delivered to the sample.

Finally, in conventional computational pathology, the image acquisition is performed in a Whole Slide Image framework. Such framework includes the acquisition of all the information from a histological slide at the same time. In this thesis, the regions of interest of the samples were manually selected according to the areas which have been previously annotated by the pathologist. The future of the acquisition of HS histological images involves the development of techniques to allow the acquisition of HS-WSI. In order to achieve such goal, further investigation should be performed in, at least, two specific fields. First, since the entire histological slide will require the acquisition of several HS cubes, stitching techniques are necessary to generate seamless spatially coherent HS images from the whole sample. The image stitching of HS samples will impose challenges for both the image acquisition and its subsequent image processing. Second, to ensure the correct focus of the captured image automatically, further investigation should be performed in the automatic analysis of the appropriate focus of the HS cubes. Such analysis may be facilitated by capturing different images with different focusing levels by programming the motorized stage of the System-III microscope.

6.2.4 Algorithm development

As stated in Chapter 2, the methods used to retrieve information from HS images widely vary among different research works. However, the determination of which method is more appropriate for data processing is heavily dependent on the target application. In this dissertation, we have evaluated both classical Machine Learning algorithms and Deep Learning approaches. In our particular case, both types of image processing approaches seem to provide competitive results in the classification of histological samples.

However, one of the most evident future research in this field is to perform a detailed comparison among different image processing approaches in order to quantify which processing approach is more appropriate for the classification of histological HS samples. On the one hand, regarding traditional ML approaches, it would be valuable the evaluation of different techniques such as dimensionality reduction, spectral unmixing, or NDI estimation, among others. On the other hand, regarding the Deep Learning approaches, the main goal is to evaluate which Neural Network architecture is more convenient for this application. In order to reach an agreement about an adequate common framework for HSI/MSI data processing for histopathological applications, there is a need for publicly available datasets, where a fair comparison across different methods could be performed. Additionally to the evaluation of a wide variety of image processing methods, a comparative among the different methods using statistical tools may provide a rationale of which methods are more adequate for this application.

Finally, since the target application of this research work is in the field of medical diagnosis, an interesting research line is in the model interpretability. This means that, together with the classifier predictions, we are able to provide details about the interpretability of the models. In the case of the analysis of histological samples, such study may reveal which spectral regions are more distinctive for a specific disease, or which morphological features are used by the model to generate the predictions.

6.3 Impact of the PhD. Thesis

In this section, all the scientific communications published during the development of the work described in this thesis are detailed. The scientific communications have been divided into conference presentations and journal publications and they have been organized in chronological order. Furthermore, as part of the outcomes achieved during the development of this research project, a patent has been obtained; and a book chapter has been published. The contents are organized in two different sections, differentiating the scientific contributions that are directly related to the contents depicted in this document.

Specifically, 31 journal citation reports (JCR) papers (19 Q1, 7 Q2, 4 Q3 and 1 Q4), 2 non-indexed JCR papers, 24 peer-reviewed conference papers, 1 book chapter, and 1 international patent have been achieved during the course of this thesis. In total, 59 scientific contributions have been accomplished.

6.3.1 Publications and dissemination

6.3.1.1 Directly related to this PhD

6.3.1.1.1 Journal Publications

[J1] **Samuel Ortega**; Himar Fabelo; Martin Halicek; Rafael Camacho; Maria de la Luz Plaza; Gustavo M. Callico; Baowei Fei. Hyperspectral Superpixel-Wise Glioblastoma Tumor Detection in Histological Samples. *Applied Sciences*. **2020**, 10 - 13, pp. 1 - 21. DOI: 10.3390/app10134448 **[IF: 2.474 (2019) – Q2] [Related with Chapter 4]**

[J2] **Samuel Ortega**; Martin Halicek; Himar Fabelo; Gustavo M. Callico; Baowei Fei. Hyperspectral and multispectral imaging in digital and computational pathology: a systematic review [Invited]. *Biomedical Optics Express*. **2020**, 11 - 6, pp. 3195 - 3233. DOI: 10.1364/BOE.386338 **[IF: 3.921 (2019) – Q1] [Related with Chapter 2]**

[J3] **Samuel Ortega**; Martin Halicek; Himar Fabelo; Rafael Camacho; Maria de la Luz Plaza; Fred Godtliebsen; Gustavo M. Callico; Baowei Fei. Hyperspectral Imaging for the Detection of Glioblastoma Tumor Cells in H&E Slides Using Convolutional Neural Networks. *Sensors*. **2020**, 7 - 20, pp. 1 - 16. DOI: 10.3390/s20071911 **[IF: 3.275 (2019) – Q1] [Related with Chapter 5]**

[J4] **Samuel Ortega**; Raul Guerra; Maria Diaz; Himar Fabelo; Sebastian López; Gustavo M. Callicó; Roberto Sarmiento. Hyperspectral Push-Broom Microscope Development and Characterization. *IEEE Access* **2019,** 7, pp. 122473 - 122491. DOI: 10.1109/ACCESS.2019.2937729 **[IF: 3.745 – Q1] [Related with Chapter 3]**

[J5] **Ortega, S.;** Fabelo, H.; Iakovidis, D.; Koulaouzidis, A.; Callico, G.; Ortega, S.; Fabelo, H.; Iakovidis, D. K.; Koulaouzidis, A.; Callico, G. M. Use of Hyperspectral/Multispectral Imaging in Gastroenterology. Shedding Some–Different–Light into the Dark. *J. Clin. Med.* **2019**, *8*, 36, doi:10.3390/jcm8010036. **[IF: 3.303 – Q1] [Related with Chapter 2]**

[J6] **Ortega, S.;** Fabelo, H.; Camacho, R.; Plaza, M. L.; Callicó, G. M.; Sarmiento, R. Detecting brain tumor in pathological slides using hyperspectral imaging. *Biomed. Opt. Express* **2018**, 9, doi:10.1364/BOE.9.000818. **[IF: 3.910 – Q1] [Related with Chapter 4]**

6.3.1.1.2 Book Chapter

[B1] **Samuel Ortega**; Martin Halicek; Himar Fabelo; Eduardo Quevedo; Baowei Fei; Gustavo M. Callico. Information Extraction Techniques in Hyperspectral Imaging Biomedical Applications. *Multimedia Information Retrieval. IntechOpen*, **2020**. DOI: 10.5772/intechopen.93960.

6.3.1.1.3 Conferences

[C1] M. Halicek, **S. Ortega,** H. Fabelo, C. Lopez, M. Lejeune, G. M. Callico, and B. Fei. Conditional generative adversarial network for synthesizing hyperspectral images of breast cancer cells from digitized histology. *Proc. SPIE 11320, Medical Imaging 2020: Digital Pathology*, 113200U (16 March 2020);

[C2] **S. Ortega**, M. Halicek, H. Fabelo, R. Guerra, C. Lopez, M. Lejeune, F. Godtliebsen, G. M. Callico, and B. Fei. Hyperspectral imaging and deep learning for the detection of breast cancer cells in digitized histological images, *Proc. SPIE 11320, Medical Imaging 2020: Digital Pathology*, 113200V (16 March 2020).

[C3] **Samuel Ortega**, Raúl Guerra, Himar Fabelo, María Díaz, Sebastián López, Gustavo M. Callicó, Roberto Sarmiento. Low-Cost Hyperspectral Push-broom Microscope, targeting

Smart Farming Applications. In *2019 34nd Conference on Design of Circuits and Integrated Systems (DCIS)*; Bilbao, 2019.

[C4] **Ortega, S.**; Callico, G. M.; Plaza, M. L.; Camacho, R.; Fabelo, H.; Sarmiento, R. Hyperspectral database of pathological in-vitro human brain samples to detect carcinogenic tissues. In *Proceedings - International Symposium on Biomedical Imaging*; 2016; Vol. 2016–June.

6.3.1.2 Related to the field

6.3.1.2.1 Journal Publications

[J7] Francisco Javier Balea-Fernandez; Beatriz Martinez-Vega; **Samuel Ortega**; Himar Fabelo; Raquel Leon; Gustavo M. Callico; Cristina Bibao-Sieyro. Analysis of Risk Factors in Dementia Through Machine Learning. *Journal of Alzheimer's Disease*. **Preprint (2020)**: 1-17. DOI: 10.3233/JAD-200955 **[IF: 3.909 (2019) – Q2]**

[J8] Francesca Manni; Fons van der Sommen; Himar Fabelo; Svitlana Zinger; Caifeng Shan; Erik Edstrom; Adrian Elmi-Terander; **Samuel Ortega**; Gustavo M. Callico; Peter H. N. de With. Hyperspectral Imaging for Glioblastoma Surgery: Improving Tumor Identification Using a Deep Spectral-Spatial Approach. *Sensors*. **2020**, 20 - 23, pp. 6955. DOI: 10.3390/s20236955 **[IF: 3.275 (2019) – Q1]**

[J9] Emanuele Torti; Raquel Leon; Marco La Salvia; Giordana Florimbi; Beatriz Martinez-Vega; Himar Fabelo; **Samuel Ortega**; Gustavo Marrero Callico; Francesco Leporati. Parallel Classification Pipelines for Skin Cancer Detection Exploiting Hyperspectral Imaging on Hybrid Systems. *Electronics*. **2020**, 9 - 1503, pp. 1 - 21. DOI: 10.3390/electronics9091503 **[IF: 2.412 (2019) – Q2]**

[J10] Alejandro Cruz-Guerrero; Raquel Leon; Daniel Campos-Delgado; Samuel Ortega; Himar Fabelo; Gustavo Marrero Callico. Classification of Hyperspectral in-vivo Brain Tissue Based on Linear Unmixing. *Applied Sciences*. **2020**, 10 - 16, pp. 5686-1 - 5686-20. DOI: 10.3390/app10165686 **[IF: 2.474 (2019) – Q2]**

[J11] Raquel Leon; Beatriz Martinez-Vega; Himar Fabelo; **Samuel Ortega**; Veronica Melian; Irene Castaño; Gregorio Carretero; Pablo Almeida; Aday Garcia; Eduardo Quevedo; Javier A. Hernandez; Bernardino Clavo; Gustavo M. Callico. Non-Invasive Skin Cancer Diagnosis Using Hyperspectral Imaging for In-Situ Clinical Support. *Journal of Clinical Medicine*. **2020**, 9 - 6, pp. 1662. DOI: 10.3390/jcm9061662 **[IF: 3.303 (2019) – Q1]**

[J12] Giordana Florimbi; Himar Fabelo; Emanuele Torti; **Samuel Ortega**; Margarita Marrero-Martin; Gustavo. M. Callico; Giovanni Danese; Francesco Leporati. Towards Real-Time Computing of Intraoperative Hyperspectral Imaging for Brain Cancer Detection using Multi-GPU Platforms. *IEEE Access*. **2019**, 8, pp. 8485 - 8501. DOI: 10.1109/ACCESS.2020.2963939 **[IF: 3.745 (2019) – Q1]**

[J13] Daniel U. Campos-Delgado; Omar Gutierrez-Navarro; Jose J. Rico-Jimenez; E. Duran; Himar Fabelo; **Samuel Ortega**; Gustavo M. Callico. Extended Blind End-member and Abundance Extraction for Biomedical Imaging Applications. *IEEE Access*. **2019**, 7, pp. 178539 – 178552. DOI: 10.1109/ACCESS.2019.2958985. **[IF: 3.745 – Q1]**

[J14] Beatriz Martinez; Raquel Leon; Himar Fabelo; **Samuel Ortega**; Juan F. Piñeiro; Adam Szolna; Maria Hernandez; Carlos Espino; Aruma J. O'Shanahan; David Carrera; Sara Bisshopp; Coralia Sosa; Mariano Marquez; Rafael Camacho; Maria de la Luz Plaza; Jesus Morera; Gustavo M. Callico. Most Relevant Spectral Bands Identification for Brain Cancer Detection Using Hyperspectral Imaging. *Sensors*. **2019**, 19 - 24, pp. 1 - 28. DOI: 10.3390/s19245481 **[IF: 3.275 – Q1]**

[J15] Abelardo Baez; Himar Fabelo; **Samuel Ortega**; Giordana Florimbi; Emanuele Torti; Abian Hernandez; Francesco Leporati; Giovanni Danese; Gustavo M. Callico; Roberto Sarmiento. High-Level Synthesis of Multiclass SVM Using Code Refactoring to Classify Brain Cancer from Hyperspectral Images. *Electronics*. **2019**. 8 - 12, pp. 1 - 17. DOI: 10.3390/electronics8121494 **[IF: 2.412 – Q2]**

[J16] Raquel Lazcano; Daniel Madroñal; Giordana Florimbi; Jaime Sancho; Sergio Sanchez; Raquel Leon; Himar Fabelo; **Samuel Ortega**; Emanuele Torti; Rubén Salvador; Margarita Marrero-Martin; Francesco Leporati; Eduardo Juárez; Gustavo M. Callicó; César Sanz. Parallel Implementations Assessment of a Spatial-Spectral Classifier for Hyperspectral Clinical Applications. *IEEE Access*. 20n19, 7, pp. 152316 - 152333. DOI: 10.1109/access.2019.2938708 **[IF: 3.745 – Q1]**

[J17] Martin Halicek; Himar Fabelo; **Samuel Ortega**; Gustavo M. Callico; Baowei Fei. In-Vivo and Ex-Vivo Tissue Analysis through Hyperspectral Imaging Techniques: Revealing the Invisible Features of Cancer. *Cancers*. **2019**, 11 - 6, DOI: 10.3390/cancers11060756 **[IF: 6.126 – Q1]**

[J18] Martin Halicek; Himar Fabelo; Samuel Ortega; James V. Little; Xu Wang; Amy Y. Chen; Gustavo Marrero Callico; Larry Myers; Baran D. Sumer; Baowei Fei. Hyperspectral imaging for head and neck cancer detection: specular glare and variance of the tumor margin in surgical specimens. *Journal of Medical Imaging*. **2019**, 6- 03, pp. 1 - 1. DOI: 10.1117/1.JMI.6.3.035004 **[No-JCR]**

[J19] Thomas Haugland Johansen; Kajsa Møllersen; Samuel Ortega; Himar Fabelo; Aday Garcia; Gustavo M. Callico; Fred Godtliebsen. Recent advances in hyperspectral imaging for melanoma detection. *Wiley Interdisciplinary Reviews: Computational Statistics*. **2019**, 12 – 1, pp. e1465 - e1465. DOI: 10.1002/wics.1465 **[No-JCR]**

[J20] Fabelo, H.; **Ortega, S.;** Szolna, A.; Bulters, D.; Pineiro, J. F.; Kabwama, S.; J-O'Shanahan, A.; Bulstrode, H.; Bisshopp, S.; Kiran, B. R.; Ravi, D.; Lazcano, R.; Madronal, D.; Sosa, C.; Espino, C.; Marquez, M.; Plaza, M. de L. L.; Camacho, R.; Carrera, D.; Hernandez, M.; Callico, G. M.; Morera, J.; Stanciulescu, B.; Yang, G.-Z.; Salvador, R.; Juarez, E.; Sanz, C.; Sarmiento, R. *In-Vivo* Hyperspectral Human Brain Image Database for Brain Cancer Detection. *IEEE Access*. **2019**, 1–1, doi:10.1109/ACCESS.2019.2904788. **[IF: 3.745 – Q1]**

[J21] Fabelo, H.; Halicek, M.; **Ortega, S.;** Shahedi, M.; Szolna, A.; Piñeiro, J.; Sosa, C.; O'Shanahan, A.; Bisshopp, S.; Espino, C.; Márquez, M.; Hernández, M.; Carrera, D.; Morera, J.; Callico, G.; Sarmiento, R.; Fei, B.; Deep Learning-Based Framework for In Vivo Identification of Glioblastoma Tumor using Hyperspectral Images of Human Brain. *Sensors* **2019**, *19*, 920, doi:10.3390/s19040920. **[IF: 3.275 – Q1]**

[J22] Fabelo, H.; **Ortega, S.;** Casselden, E.; Loh, J.; Bulstrode, H.; Zolnourian, A.; Grundy, P.; Callico, G. M.; Bulters, D.; Sarmiento, R. SVM Optimization for Brain Tumor Identification Using Infrared Spectroscopic Samples. *Sensors* **2018**, *18*, 4487, doi:10.3390/s18124487. **[IF: 3.275 – Q1]**

[J23] Fabelo, H.; **Ortega, S.;** Ravi, D.; Kiran, B. R.; Sosa, C.; Bulters, D.; Callicó, G. M.; Bulstrode, H.; Szolna, A.; Piñeiro, J. F.; Kabwama, S.; Madroñal, D.; Lazcano, R.; J-O'Shanahan, A.; Bisshopp, S.; Hernández, M.; Báez, A.; Yang, G.-Z.; Stanciulescu, B.; Salvador, R.; Juárez, E.; Sarmiento, R. Spatio-spectral classification of hyperspectral images for brain cancer detection during surgical operations. *PLoS One* **2018**, 13, 1–27, doi:10.1371/journal.pone.0193721. **[IF: 2.776 – Q2]**

[J24] Fabelo, H.; **Ortega, S.;** Lazcano, R.; Madroñal, D.; M. Callicó, G.; Juárez, E.; Salvador, R.; Bulters, D.; Bulstrode, H.; Szolna, A.; Piñeiro, J. F.; Sosa, C.; J. O'Shanahan, A.; Bisshopp, S.; Hernández, M.; Morera, J.; Ravi, D.; Kiran, B. R.; Vega, A.; Báez-Quevedo,

A.; Yang, G.-Z.; Stanciulescu, B.; Sarmiento, R. An intraoperative visualization system using hyperspectral imaging to aid in brain tumor delineation. *Sensors* **2018**, 18, doi:10.3390/s18020430. **[IF: 3.275 – Q1]**

[J25] Florimbi, G.; Fabelo, H.; Torti, E.; Lazcano, R.; Madroñal, D.; **Ortega, S.;** Salvador, R.; Leporati, F.; Danese, G.; Báez-Quevedo, A.; Callicó, G. M.; Juárez, E.; Sanz, C.; Sarmiento, R. Accelerating the K-Nearest Neighbors Filtering Algorithm to Optimize the Real-Time Classification of Human Brain Tumor in Hyperspectral Images. *Sensors*. **2018**, 18, doi:10.3390/s18072314. **[IF: 3.031 – Q1]**

[J26] Torti, E.; Florimbi, G.; Castelli, F.; **Ortega, S.;** Fabelo, H.; Callicó, G.; Marrero-Martin, M.; Leporati, F.; Torti, E.; Florimbi, G.; Castelli, F.; Ortega, S.; Fabelo, H.; Callicó, G. M.; Marrero-Martin, M.; Leporati, F. Parallel K-Means Clustering for Brain Cancer Detection Using Hyperspectral Images. *Electronics* **2018**, *7*, 283, doi:10.3390/electronics7110283. **[IF: 1.764 – Q3]**

[J27] Torti, E.; Fontanella, A.; Florimbi, G.; Leporati, F.; Fabelo, H.; **Ortega, S.;** Callico, G. M. Acceleration of brain cancer detection algorithms during surgery procedures using GPUs. *Microprocess. Microsyst.* **2018**, 61, 171–178, doi:10.1016/j.micpro.2018.06.005. **[IF: 1.04 – Q3]**

[J28] Lazcano, R.; Madroñal, D.; Salvador, R.; Desnos, K.; Pelcat, M.; Guerra, R.; Fabelo, H.; **Ortega, S.;** Lopez, S.; Callico, G. M.; Juarez, E.; Sanz, C. Porting a PCA-based hyperspectral image dimensionality reduction algorithm for brain cancer detection on a manycore architecture. *J. Syst. Archit.* **2017**, 77, 101–111, doi:10.1016/j.sysarc.2017.05.001. **[IF: 0.913 – Q3]**

[J29] Madroñal, D.; Lazcano, R.; Salvador, R.; Fabelo, H.; **Ortega, S.;** Callico, G. M.; Juarez, E.; Sanz, C. SVM-based real-time hyperspectral image classifier on a manycore architecture. *J. Syst. Archit.* **2017**, 80, doi:10.1016/j.sysarc.2017.08.002. **[IF: 0.913 – Q3]**

[J30] **Ortega, S.;** Fabelo, H.; Camacho, R.; Plaza, M. L.; Callico, G. M.; Lazcano, R.; Madroñal, D.; Salvador, R.; Juárez, E.; Sarmiento, R. P03.18 Detection of human brain cancer in pathological slides using hyperspectral images. *Neuro. Oncol.* **2017**, 19, iii37, doi:10.1093/neuonc/nox036.133. **[IF: 9.384 – Q1]**

[J31] Pineiro, J. F.; Bulters, D.; **Ortega, S.;** Fabelo, H.; Kabwama, S.; Sosa, C.; Bishop, S.; Martinez-Gonzalez, A.; Szolna, A.; M. Callico, G. Hyperspectral imaging for brain tumour identification and boundaries delineation in real-time during neurosurgical operations. *Neuro. Oncol.* **2017**, doi:https://doi.org/10.1093/neuonc/nox036.160. **[IF: 9.384 – Q1]**

[J32] Szolna, A.; Morera, J.; Piñeiro, J. F.; Callicó, G. M.; Fabelo, H.; **Ortega, S.** Hyperspectral Imaging as A Novel Instrument for Intraoperative Brain Tumor Detection. *Neurocirugia* **2016**, 27, 166. **[IF: 0.310 – Q4]**

[J33] Kabwama, S.; Bulters, D.; Bulstrode, H.; Fabelo, H.; **Ortega, S.;** Callico, G. M.; Stanciulescu, B.; Kiran, R.; Ravi, D.; Szolna, A.; others Intra-operative hyperspectral imaging for brain tumour detection and delineation: Current progress on the HELICoiD project. *Int. J. Surg.* **2016**, 36, S140. **[IF: 2.693 – Q2]**

6.3.1.2.2 Patents

[P1] Gustavo Marrero Callico; Himar Fabelo Gomez; **Samuel Ortega Sarmiento**; Bogdan Stanciulescu; Ravi Kiran Bangalore, “Method of Non-Invasive Detection of Tumour and/or Healthy Tissue and Hyperspectral Imaging Apparatus”, Universidad de las Palmas de Gran Canaria, PCT/EP2016/078477, Spain, Canary Islands.

6.3.1.2.3 Conferences

[C5] A. Martínez-González, A. D. Valle, H. Fabelo, **S. Ortega** and G. Callicó, Can Hyperspectral Images be used to detect Brain tumor pixels and their malignant phenotypes? 2020 *XXXV Conference on Design of Circuits and Integrated Systems (DCIS)*, Segovia, Spain, 2020, pp. 1-5.

[C6] H. Fabelo; R. Leon; **S. Ortega**; F. Balea-Fernandez; C. Bilbao; G. M. Callico; A. Wagner. Novel Methodology for Alzheimer's Disease Biomarker Identification in Plasma using Hyperspectral Microscopy. *2020 XXXV Conference on Design of Circuits and Integrated Systems (DCIS)*, Segovia, Spain, 2020, pp. 1-6.

[C7] R. Leon; B. Martinez-Vega; H. Fabelo; **S. Ortega**; G. M. Callicó; F. Balea-Fernández; C. Bilbao Sieyro. Hyperspectral Imaging for Major Neurocognitive Disorder Detection in Plasma Samples. *2020 XXXV Conference on Design of Circuits and Integrated Systems (DCIS)*, Segovia, Spain, 2020, pp. 1-6.

[C8] Martinez-Vega, B., Quevedo, E., Leon, R., Fabelo, H., **Ortega, S.,** Callico, G. M., ... & Godtliebsen, F. Statistics-based Classification Approach for Hyperspectral Dermatologic Data Processing. *2020 XXXV Conference on Design of Circuits and Integrated Systems (DCIS)*, Segovia, Spain, 2020, pp. 1-6.

[C9] J. C. Peña, **S. Ortega**, E. Quevedo, H. Fabelo and G. M. Callico. Modular Battery Management System for Power Electronics Practical Laboratory Lessons. *2020 XIV Technologies Applied to Electronics Teaching Conference (TAEE)*, Porto, Portugal, 2020, pp. 1-6.

[C10] J. C. Peña, N. Falcon, A. Yanez, **S. Ortega**, R. Leon, H. Fabelo and G. M. Callico. Regulated Power Supply with High Power Factor for Hyperspectral Imaging Applications. *2020 XIV Technologies Applied to Electronics Teaching Conference (TAEE)*, Porto, Portugal, 2020, pp. 1-6.

[C11] Fabelo, H.; Halicek, M.; **Ortega, S.;** Szolna, A.; Morera, J.; Sarmiento, R.; Callicó, G. M.; Fei, B. Surgical aid visualization system for glioblastoma tumor identification based on deep learning and in-vivo hyperspectral images of human patients. In *Medical Imaging 2019: Image-Guided Procedures, Robotic Interventions, and Modeling*; Fei, B., Linte, C. A., Eds.; SPIE, 2019; Vol. 10951, p. 35. **[RFW Best Student Paper Award]**

[C12] Halicek, M.; Fabelo, H.; **Ortega, S.;** Little, J. V.; Wang, X.; Chen, A. Y.; Callicó, G. M.; Myers, L.; Sumer, B.; Fei, B. Cancer detection using hyperspectral imaging and evaluation of the superficial tumor margin variance with depth. In *Medical Imaging 2019: Image-Guided Procedures, Robotic Interventions, and Modeling*; Fei, B., Linte, C. A., Eds.; SPIE, 2019; Vol. 10951, p. 45.

[C13] Madroñal, D.; Lazcano, R.; **Ortega, S.;** Fabelo, H.; Salvador, R.; M. Callico, G.; Juarez, E.; Sanz, C. Implementation of a spatial-spectral classification algorithm using medical hyperspectral images. In *2017 32nd Conference on Design of Circuits and Integrated Systems (DCIS)*; Barcelona, 2017.

[C14] Madronal, D.; Lazcano, R.; Fabelo, H.; **Ortega, S.;** Salvador, R.; Callico, G. M.; Juarez, E.; Sanz, C. Energy consumption characterization of a Massively Parallel Processor Array (MPPA) platform running a hyperspectral SVM classifier. In *Conference on Design and Architectures for Signal and Image Processing, DASIP*; 2017; Vol. 2017–Septe.

[C15] Lazcano, R.; Madronal, D.; Fabelo, H.; **Ortega, S.;** Salvador, R.; Callico, G. M.; Juarez, E.; Sanz, C. Parallel implementation of an iterative PCA algorithm for hyperspectral images on a manycore platform. In *Conference on Design and Architectures for Signal and Image Processing, DASIP*; 2017; Vol. 2017–Septe.

[C16] Madroñal, D.; Lazcano, R.; Fabelo, H.; **Ortega, S.;** Callicó, G. M.; Juarez, E.; Sanz, C. Hyperspectral image classification using a parallel implementation of the linear SVM on a Massively Parallel Processor Array (MPPA) platform. In *Conference on Design and Architectures for Signal and Image Processing, DASIP*; 2017.

[C17] Lazcano, R.; Madroñal, D.; Fabelo, H.; **Ortega, S.;** Salvador, R.; Callicó, G. M.; Juárez, E.; Sanz, C. Parallel exploitation of a spatial-spectral classification approach for hyperspectral images on RVC-CAL. In *Proceedings of SPIE - The International Society for Optical Engineering*; 2017; Vol. 10430.

[C18] Salvador, R.; Fabelo, H.; Lazcano, R.; **Ortega, S.;** Madroñal, D.; Callicó, G. M.; Juárez, E.; Sanz, C. Demo: HELICoiD tool demonstrator for real-time brain cancer detection. In *Conference on Design and Architectures for Signal and Image Processing, DASIP*; 2017. **[Best Demo Award]**

[C19] Salvador, R.; **Ortega, S.;** Madroñal, D.; Fabelo, H.; Lazcano, R.; Marrero, G.; Juárez, E.; Sarmiento, R.; Sanz, C. HELICoiD: Interdisciplinary and collaborative project for real-time brain cancer detection. In *ACM International Conference on Computing Frontiers 2017, CF 2017*; 2017.

[C20] Hernandez, A.; Fabelo, H.; **Ortega, S.;** Baez, A.; Callico, G. M.; Sarmiento, R. Random forest training stage acceleration using graphics processing units. In *2017 32nd Conference on Design of Circuits and Integrated Systems (DCIS)*; 2017; pp. 1–6.

[C21] Domingo, R.; Salvador, R.; Fabelo, H.; Madronal, D.; **Ortega, S.;** Lazcano, R.; Juarez, E.; Callico, G. M.; Sanz, C. High-level design using Intel FPGA OpenCL: A hyperspectral imaging spatial-spectral classifier. In *12th International Symposium on Reconfigurable Communication-Centric Systems-on-Chip, ReCoSoC 2017 - Proceedings*; 2017.

[C22] Torti, E.; Cividini, C.; Gatti, A.; Danese, G.; Leporati, F.; Fabelo, H.; **Ortega, S.;** Callicò, G. M. The HELICoiD Project: Parallel SVM for Brain Cancer Classification. In *Proceedings - 20th Euromicro Conference on Digital System Design, DSD 2017*; 2017.

[C23] Fabelo, H.; **Ortega, S.;** Kabwama, S.; Callico, G. M.; Bulters, D.; Szolna, A.; Pineiro, J. F.; Sarmiento, R. HELICoiD project: A new use of hyperspectral imaging for brain cancer detection in real-time during neurosurgical operations. In *Proceedings of SPIE - The International Society for Optical Engineering*; 2016; Vol. 9860.

[C24] Fabelo, H.; **Ortega, S.;** Guerra, R.; Callicó, G.; Szolna, A.; Piñeiro, J. F.; Tejedor, M.; López, S.; Sarmiento, R. A novel use of hyperspectral images for human brain cancer detection using *in-vivo* samples. In *BIOSIGNALS 2016 - 9th International Conference on Bio-Inspired Systems and Signal Processing, Proceedings; Part of 9th International Joint Conference on Biomedical Engineering Systems and Technologies, BIOSTEC 2016*; 2016.

6.3.2 Research projects

6.3.2.1 European projects

[RP1] **Ref. 618080**: *HELICoiD (HypErspectraL Imaging Cancer Detection)*. *European Commission FP7-ICT-2013-C.* PI: Gustavo M. Callico. ULPGC. 01/01/2014-31/12/2016. 1,428,378.00 €.

6.3.2.2 National projects

[RP2] **Ref. TEC2017-86722-C4-1-R**: *PLATINO (Plataforma HW/SW Distribuida para el Procesamiento Inteligente de Información Sensorial Heterogénea en Aplicaciones de Supervisión de Grandes Espacios Naturales)*. MINECO (Spain) Proyectos I+D+i – Retos

Investigación. PIs: Sebastian Lopez and Gustavo M. Callico. ULPGC. 01/01/2018-31/12/2020. 228,690.00 €.

[RP3] **Ref. TEC2014-58036-C4-4-R**: REBECCA (Sistemas electrónicos empotrados confiables para control de ciudades bajo situaciones atípicas). MINECO (Spain) Proyectos I+D+i – Retos Investigación. PIs: Roberto Sarmiento and Ernestina Martel. ULPGC. 01/01/2015-31/12/2017. 201,000.00 €.

6.3.2.3 Regional projects

[RP4] **Ref. ProID2017010164**: *ITHACA (IdenTificacion Hiperespectral de tumores CerebrAles)*. Gobierno de Canarias (Canary Islands) Programa de Apoyo a la Investigación María del Carmen Betancourt y Molina. PI: Gustavo M. Callico. ULPGC. 01/01/2018-30/09/2019. 69,914.45 €.

[RP5] **Ref. 016/2019**: Dolor por neuropatía periférica inducida por quimioterapia: Valor diagnóstico y predictivo de la imagen hiperespectral en pacientes del ensayo clínico "O3NPIQ" [(Clinical Trial: EudraCT 2019-000821-37) - (BF1-19-03) - (PI 19/00458) - (016/2019)]. Fundación DISA (Canary Islands) Premios Fundación DISA 2019 a la Investigación Biomédica. PI: Bernardino Clavo Varas. Hospital Univ. de Gran Canaria Dr. Negrín. 01/01/2020-01/01/2022. 15,600.00 €.

[RP6] **Ref. PIFUN44/17**: *O3Cardio (Effectiveness and cost-effectiveness of Ozone therapy in patients with ischemic heart disease refractory to medical and surgical treatment: Randomized, triple-blind clinical trial [EudraCT 2018-000201-24])*. FUNCANIS (Canary Islands) Ayudas para la financiación de proyectos de investigación, desarrollo e innovación en Biomedicina y Ciencias de la Salud. PI: Bernardino Clavo. Hospital Univ. de Gran Canaria Dr. Negrín. 01/01/2018-31/12/2019. 21,804.00 €.

6.3.3 Grants obtained

[G1] Pre-doctoral grant given by the “Agencia Canaria de Investigacion, Innovacion y Sociedad de la Información (ACIISI)” of the “Conserjería de Economía, Industria, Comercio y Conocimiento” of the “Gobierno de Canarias”, which is part-financed by the European Social Fund (FSE) (POC 2014-2020, Eje 3 Tema Prioritario 74 (85%)).

[G2] Research intership movility grant given by the “Agencia Canaria de Investigacion, Innovacion y Sociedad de la Información (ACIISI)” of the “Conserjería de Economía, Industria, Comercio y Conocimiento” of the “Gobierno de Canarias”, which is part-financed by the European Social Fund (FSE) (POC 2014-2020, Eje 3 Tema Prioritario 74 (85%)).

6.3.4 Other dissemination activities

[D1] **Samuel Ortega Sarmiento**. Histología Hiperespectral: El Futuro de la Histología Digital. *ZTC, revista de la Asociación Canaria de Ingenieros de Telecomunicación (ACIT) y el Colegio de Ingenieros de Telecomunicación en Canarias (COITC)*. **2020**, 37.

[D2] Gustavo Marrero Callicó, **Samuel Ortega Sarmiento**, Eduardo Juárez Martínez. Proyecto HELICoiD: detección de tumores cerebrales mediante imágenes hiperespectrales. *BIT, revista del Colegio Oficial de Ingenieros de Telecomunicación (COIT) y de la Asociación Española de Ingenieros de Telecomunicación (AEIT)*. **2017**, 208, 64–68.

[D3] Gustavo Marrero Callicó, Himar Fabelo Gómez, **Samuel Ortega Sarmiento**. Proyecto de Investigación HELICoiD. *ZTC, revista de la Asociación Canaria de Ingenieros de Telecomunicación (ACIT) y el Colegio de Ingenieros de Telecomunicación en Canarias (COITC)*. **2016**, 21.

6.3.5 Awards received

[A1] **DASIP 2016 Best Demo Award**. R. Salvador, H. Fabelo, R. Lazcano, **S. Ortega**, D. Madroñal, G. M. Callicó, E. Juárez, C. Sanz, "HELICoiD tooldemonstrator for real-time brain cancer detection", in2016 Conference on Designand Architectures for Signal and Image Processing (DASIP), pp. 237–238, IEEE, 2016

[A2] **RFW Best Student Paper Award.** Fabelo, H.; Halicek, M.; **Ortega, S**.; Szolna, A.; Morera, J.; Sarmiento, R.; Callicó, G. M.; Fei, B. Surgical aid visualization system for glioblastoma tumor identification based on deep learning and in-vivo hyperspectral images of human patients. In Medical Imaging 2019: Image-Guided Procedures, Robotic Interventions, and Modeling; Fei, B., Linte, C. A., Eds.; SPIE, 2019; Vol. 10951, p. 35.

[A3] **Editor's Choice Article**. Fabelo, H.; Halicek, M.; **Ortega, S.;** Shahedi, M.; Szolna, A.; Piñeiro, J.; Sosa, C.; O'Shanahan, A.; Bisshopp, S.; Espino, C.; Márquez, M.; Hernández, M.; Carrera, D.; Morera, J.; Callico, G.; Sarmiento, R.; Fei, B.; Deep Learning-Based Framework for In Vivo Identification of Glioblastoma Tumor using Hyperspectral Images of Human Brain. *Sensors* **2019**, *19*, 920, doi:10.3390/s19040920. **[IF: 3.275 – Q1]**

Annex A: Sinopsis en español

A.1 Introducción y motivaciones

Las imágenes hiperespectrales son una tecnología que combina dos técnicas que han coexistido independientemente durante décadas: la espectroscopia y la fotografía digital. Por una parte, la espectroscopia estudia la interacción entre la radiación electromagnética y la materia. Dicha interacción es única para cada material. La curva que relaciona la radiación electromagnética con un determinado material se denomina firma espectral, y a través de su análisis es posible discriminar entre distintos materiales. Se trata pues, de una especie de huella digital que identifica cada material. Por otro lado, la fotografía digital permite capturar imágenes de una determinada escena, haciendo posible el análisis de características espaciales de determinados objetos tales como su morfología o su textura.

Las imágenes hiperespectrales han sido empleadas tradicionalmente en *Remote Sensing* para labores de teledetección, incluyendo diversas aplicaciones como podrían ser la agricultura de precisión, la mineralogía o los estudios medioambientales. La potencialidad de esta tecnología para diferenciar entre distintos tipos de materiales ha hecho que se emplee en otros campos muy diversos. Por ejemplo, los restauradores de obras de arte emplean esta tecnología para identificar qué pigmentos son los que han sido empleados en una determinada obra de arte para así mejorar su restauración. En las plantas de reciclaje, esta tecnología se emplea para separar automáticamente los distintos tipos de materiales. En la industria alimentaria, esta tecnología se está usando para la inspección de la calidad de diferentes alimentos, evitando los análisis biológicos invasivos requeridos en las metodologías tradicionales. También en la industria farmacéutica se hace uso de las capacidades de las imágenes hiperespectrales para realizar un análisis químico no invasivo.

En el campo de la medicina, las imágenes hiperespectrales también han despertado el interés de la comunidad científica en los últimos años. Esto se debe a que se ha demostrado que la interacción entre la radiación electromagnética y los tejidos proporciona información útil para el diagnóstico. En los últimos años el uso de esta tecnología ha tenido un gran auge en el campo de la biomedicina, dada su eficacia para detectar enfermedades y su carácter no invasivo. En lo que respecta a la detección de cáncer, las imágenes hiperespectrales se plantean con el fin de proporcionar a los cirujanos una herramienta de ayuda al diagnóstico que permita la resección total del tejido tumoral, así como evitar la resección errónea de tejido sano. Esta tecnología se ha empleado desde hace más de veinte años en diferentes áreas de la medicina, como

pueden ser el análisis de tejidos cancerosos en muestras in-vivo y ex-vivo, en la detección de melanomas, o en diversas afecciones en el campo de la gastroenterología, entre otras.

Esta tesis doctoral se enmarca dentro del empleo de imágenes hiperespectrales en muestras histológicas. El diagnóstico tradicional de las muestras histológicas se basa en el examen visual de las características morfológicas de las muestras por patólogos especializados. En los últimos años, el uso de tecnologías asistidas por computador para mejorar estos procedimientos es una tendencia emergente para reducir la subjetividad del diagnóstico. Esas tecnologías tienen por objeto mejorar el diagnóstico, hacerlo reproducible y cuantitativo, así como ahorrar tiempo en el análisis manual de las muestras. La tecnología de imágenes hiperespectrales se presenta como una alternativa interesante a las imágenes RGB, debido a su capacidad de diferenciar entre diferentes materiales mediante la explotación simultánea de las características morfológicas y espectrales de los tejidos. El uso de esta tecnología está motivado por el hecho de que, haciendo uso de la información espectral es posible detectar sutiles diferencias moleculares entre muestras biológicas. Esta tecnología se utiliza junto con algoritmos avanzados de aprendizaje automático para extraer información útil sobre los materiales de una imagen hiperespectral.

En esta tesis doctoral, se propone el empleo de imágenes hiperespectrales para discriminar entre tejido tumoral y no tumoral en muestras histológicas. Específicamente, se aborda el análisis de cáncer cerebral y de cáncer de mama. El trabajo presentado en esta tesis incluye la preparación de las muestras, su captura usando instrumentación de captura de imágenes hiperespectrales, y el procesado de las imágenes capturadas.

A.2 Contexto

Los contenidos de esta tesis doctoral se engloban dentro de los siguientes proyectos de investigación: el proyecto europeo HELICoiD (618080), financiado por la Comisión Europea Programa de Future and Emerging Technologies (FET-Open), dentro del 7º Programa Marco de la Unión Europea; el proyecto ITHaCA (ProID2017010164), financiado por la Agencia Canaria de Investigación Innovación y Sociedad de la Información del Gobierno de Canarias, y el proyecto PLATINO (TEC2017-86722-C4-1-R), financiado por el Programa Estatal de I+D+i Orientada a los Retos de la Sociedad del Ministerio de Ciencia e Innovación del Gobierno de España.

Durante esta tesis se ha tenido estrecha colaboración con dos departamentos de Anatomía Patológica de dos hospitales diferentes, gracias a los cuales se ha tenido acceso a las muestras histológicas que se han digitalizado y procesado usando imágenes hiperespectrales, así como al análisis de los resultados que se han obtenido desde el punto de vista médico. Dichos hospitales son el Hospital Universitario de Gran Canaria Dr. Negrín (Las Palmas de Gran Canaria, España) y el Hospital de Tortosa Verge de la Cinta (Tortosa, España).

Además, en el marco de esta tesis doctoral se ha realizado una estancia de investigación en el Quantitative BioImaging Laboratory, enmarcado en el Departamento de Ingeniería Biomédica de la Universidad de Texas en Dallas (https://fei-lab.org/). Este grupo está liderado por el Prof. Baowei Fei, quien es uno de los pioneros a nivel internacional en el uso de la imagen hiperespectral en medicina y especialmente en la aplicación de esta técnica para el análisis del cáncer.

A.3 Estudio del estado del arte

En esta tesis doctoral se ha realizado una revisión sistemática del estado del arte referente al procesamiento de muestras histológicas usando imágenes hiperespectrales. Para la metodología de dicha revisión sistemática se han empleado las reglas propuestas por PRISMA (http://www.prisma-statement.org) para el desarrollo de revisión sistemática de la literatura. Tras una búsqueda preliminar usando bases de datos extendidas en el ámbito científico (PubMed y Scopus), se han recabado un total de aproximadamente 1600 artículos. Tras la inspección de dichos artículos atendiendo a su resumen, finalmente se han seleccionado 193 artículos para dicha revisión del estado del arte. Realizando un análisis pormenorizado de los 193 artículos, se ha decidido dividir el manuscrito en cuatro secciones principales: autoflorescencia, mejoras del color y tinción digital, análisis inmunohistoquimico de las muestras; y diagnostico rutinario. Dicho artículo, titulado *Hyperspectral and multispectral imaging in digital and computational pathology: a systematic review [Invited]*, ha sido publicado por invitación en la revista Biomedical Optics Express. Con el desarrollo de este artículo se ha conseguido tener una visión general del estado actual y de los futuros retos a los que hay que hacer frente en el uso de imágenes hiperespectrales para el análisis de muestras histológicas.

A.4 Instrumentación y adquisición de imágenes hiperespectrales microscópicas

La captura de imágenes hiperespectrales microscópicas no es algo trivial. En las primeras etapas de esta tesis, se diseñó un sistema de adquisición de imágenes hiperespectrales compuesto por una cámara hiperespectral, un microscopio, y un sistema de posicionamiento para realizar el barrido espacial requerido para obtener dichas imágenes (Figura A-1).

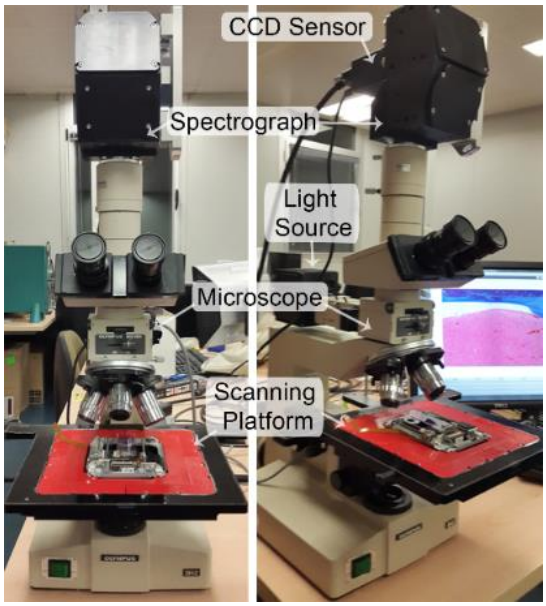

Figura A-1: Sistema de captura preliminar, consistente en una cámara hiperespectral acoplada a un microscopio convencional

El sistema de posicionamiento fue desarrollado en el ámbito de esta tesis, y fue acoplado a un microscopio disponible en el Instituto Universitario de Microelectrónica Aplicada. El microscopio (Olympus BH-2) es estándar, y no está optimizado para las capturas de imágenes hiperespectrales. Esto causa que, aunque las cámaras hiperespectrales usadas en dichos microscopios cubran un rango espectral amplio, el microscopio filtra las longitudes de onda superiores a 700 nm. Esto limita la cantidad de datos que se desean medir. Por este motivo, en el marco del Proyecto PLATINO se adquirió un microscopio que sí tiene capacidad hiperespectral (Olympus BX-53), lo que permite la adquisición de imágenes hiperespectrales microscópicas hasta los 2000 nm (Figura A-2).

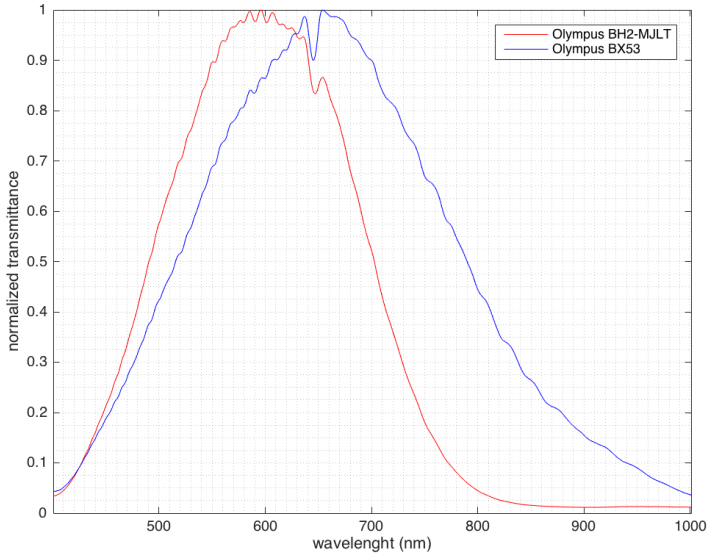

Figura A-2: Rango espectral percibido por un microscopio no optimizado para la captura de imágenes hiperespectrales (azul, Olympus BH-2), y por un microscopio optimizado para la captura de imágenes hiperespectrales (rojo, BX-53)

Al usar dos sistemas de adquisición diferentes, nos hemos percatado de que hay ciertos problemas que siempre aparecen cuando se acopla una cámara de tipo push-broom a un microscopio. Por ese motivo, durante esta tesis se ha propuesto una metodología para la optimización de los parámetros de captura cuando se usa una instrumentación a medida de este tipo. Dicha metodología ha sido presentada en el artículo *Hyperspectral Push-Broom Microscope Development and Characterization*, publicado en la revista IEEE Access.

Dicha metodología consiste en un procedimiento empírico, basado en el procesamiento de imágenes, para optimizar los parámetros de captura de imágenes hiperespectrales de tipo push-broom; especialmente el enfoque, la velocidad de captura y el alineamiento. En la Figura A-3 se puede observar el ejemplo de varias imágenes hipersepectrales de un portaobjetos de calibración, en el que se pueden observar tanto una imagen adquirida en condiciones ideales, así como algunos ejemplos de defectos comunes que aparecen en las imágenes si algunos de los parámetros de captura no son adecuados.

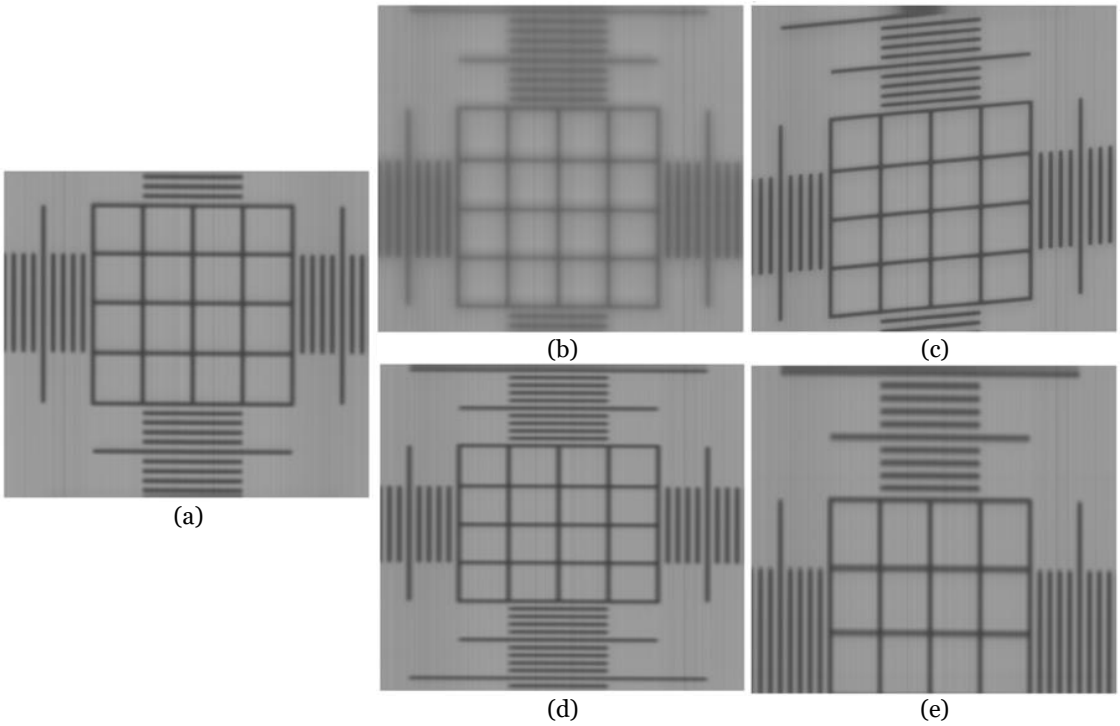

Figura A-3: Imágenes hiperespectrales adquiridas en buenas condiciones (a), o en malas condiciones: imagen desenfocada (b), error de alineamiento entre la cámara y el microscopio (c), imagen adquirida con velocidad superior a la óptima (d), e imagen adquirida con velocidad inferior a la óptima (e).

Usando esta metodología de captura, se han obtenido imágenes hiperespectrales microscópicas de muestras histológicas para su posterior análisis.

A.5 Bases de datos de imágenes hiperespectrales histológicas

Las muestras biológicas empleadas durante esta tesis doctoral consisten en muestras histológicas de dos tipos de tumores: cáncer de mama y tumor cerebral. Un ejemplo de este tipo de muestras se puede observar en la Figura A-4.

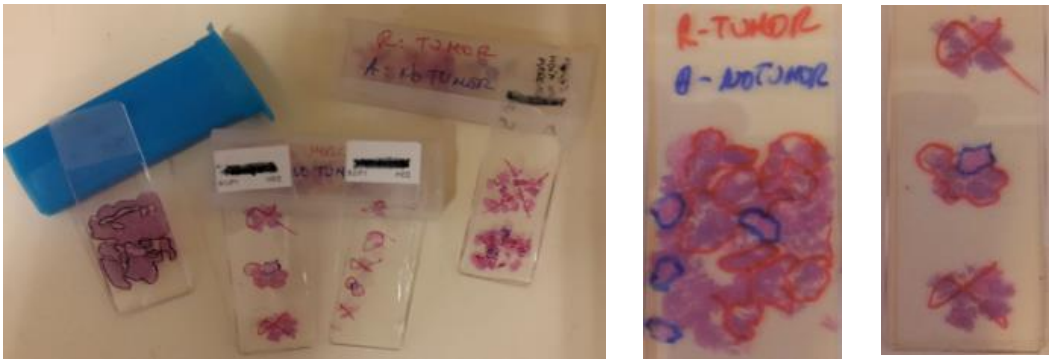

Figura A-4: Ejemplo de muestras histológicas empleadas en esta tesis doctoral.

El objetivo final de este trabajo de investigación es proporcionar una herramienta de ayuda al diagnóstico basada en imágenes hiperespectrales. Sin embargo, de forma previa al desarrollo de algoritmos capaces de realizar un diagnóstico preciso, es necesario elaborar una base de datos etiquetada en la que se tenga un alto número de imágenes hiperespectrales con la correcta identificación de la mayor parte de las zonas de la

imagen. Para esto, los patólogos involucrados en este proyecto han anotado en los portaobjetos las zonas de interés de cada muestra. En la Figura A-5.a se puede observar un ejemplo de una muestra donde se ha indicado el tejido tumoral usando un marcador rojo, y el tejido sano usando un marcador azul. Una vez los patólogos han determinado las zonas de interés, se procede a la captura de las imágenes. En esta tesis doctoral se han usado muestras histológicas correspondientes a tumor cerebral (específicamente de glioblastoma) y a cáncer de mama.

El proceso de captura se puede realizar en diferentes magnificaciones. Usando imágenes con baja magnificación, como 5× (Figura A-5.b) y 10×, es posible determinar si se trata de una zona de tejido tumoral o no (las zonas tumorales presentan alta proliferación celular). Además, en estas imágenes se pueden observar estructuras como vasos sanguíneos, zonas del tejido que presentan hemorragia o núcleos de células. Sin embargo, con estas magnificaciones no es posible observar detalles de las células que permitan a un experto determinar el diagnóstico preciso, siendo necesario utilizar una magnificación mayor, como 20× (Figura A-5.c).

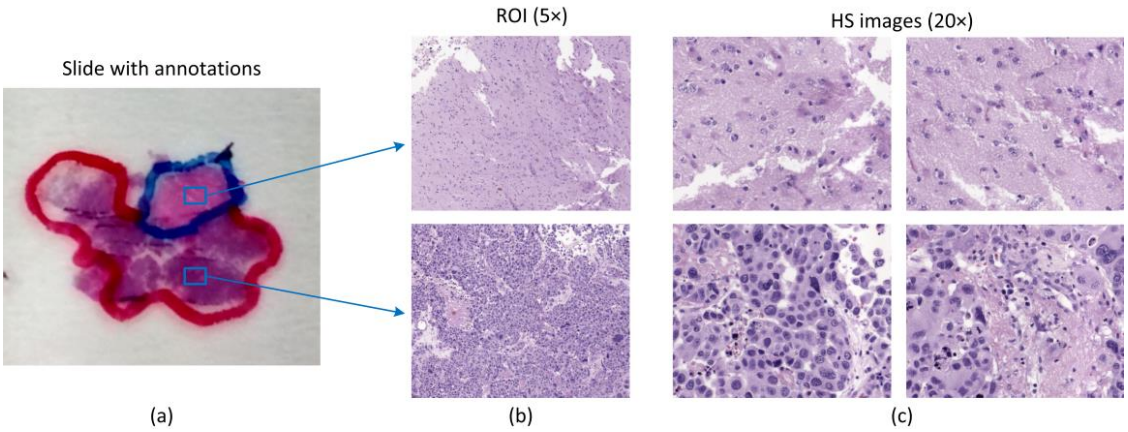

Figura A-5: Ejemplo de muestras histológicas de tumor cerebral. (a) Muestra etiquetada por los patólogos. Las zonas tumorales se han delimitado usando un marcador rojo, y las zonas de tejido sano con marcador azul. (b, c) Imagen hiperespectral a falso color a 5× y 20×, respectivamente

A.6 Procesamiento de las imágenes

Una vez se ha capturado un número significativo de imágenes hiperespectrales, el objetivo es aplicar técnicas de procesado de imágenes para extraer información relevante para el diagnóstico a partir de los datos hiperespectrales.

A.6.1 Tumor cerebral

Empleando las muestras de tumor cerebral capturadas, se ha realizado una clasificación de dichas muestras usando distintas técnicas de procesamiento de imágenes, especialmente *Machine Learning*. Las muestras han sido etiquetadas macroscópicamente en los portaobjetos a nivel de área, indicándose las áreas tumorales y no tumorales (Figura A-5.a). La primera aproximación al procesamiento de este tipo de imágenes se ha realizado con una baja magnificación por restricciones impuestas por el sistema de adquisición. Dichas muestras fueron clasificadas usando clasificadores supervisados a nivel de firma espectral, y los resultados de dicha investigación fueron

publicadas en el artículo *Detecting brain tumor in pathological slides using hyperspectral imaging*, en la revista Biomedical Optics Express.

Sin embargo, esta investigación estaba limitada por la instrumentación, que únicamente permitía la captura de imágenes usando magnificaciones bajas (5×), y con una resolución espacial baja, lo que no permitía explotar las características morfológicas de las muestras. Por ese motivo, tras realizar mejoras en la instrumentación, las muestras fueron digitalizadas de nuevo con una mayor magnificación (20×), y con una calidad de imagen alta. Usando dicha base de datos, se han realizado dos aproximaciones diferentes para el procesamiento de las imágenes hiperespectrales. En primer lugar, se realizó una clasificación de las muestras usando redes neuronales convolucionales. Dicho trabajo fue presentado en el artículo *Hyperspectral Imaging for the Detection of Glioblastoma Tumor Cells in H&E Slides Using Convolutional Neural Networks*, en la revista Sensors. Adicionalmente, también se ha propuesto el uso de una combinación de algoritmos de superpíxel y de clasificación supervisada para esta aplicación. Los resultados de dicha investigación fueron presentados en el artículo *Hyperspectral Superpixel-Wise Glioblastoma Tumor Detection in Histological Samples*, en la revista Applied Sciences.

Los resultados de este estudio han sido prometedores, indicando una buena discriminación entre tejido tumoral y sano. Sin embargo, se ha concluido que, debido a la gran variabilidad de los tumores cerebrales de alto grado, es necesario disponer de un mayor número de pacientes para obtener mejores resultados en la clasificación.

A.6.2 Cáncer de mama

Durante esta tesis doctoral se han procesado también datos hiperespectrales de muestras de cáncer de mama usando técnicas de *Deep Learning*. Concretamente, se ha usado una red neuronal convolucional para realizar el diagnostico a nivel celular de dichas muestras. Los datos de partida consisten en un conjunto de datos hiperespectrales que tienen asociados unas etiquetadas a nivel celular, que han sido anotadas cuidadosamente por patólogos en una muestra digitalizada en RGB (Figura A-6).

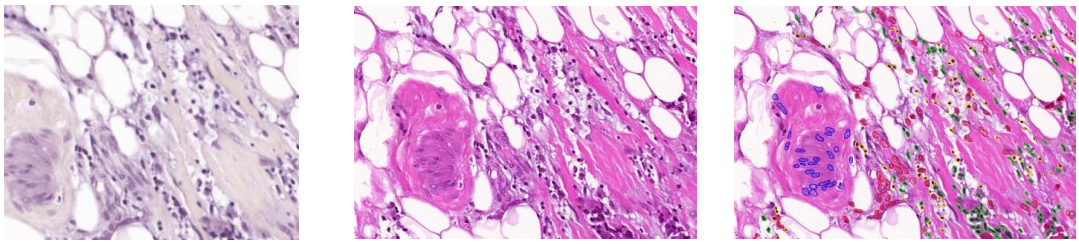

(a) (b) (c)

Figura A-6: Imágenes de cáncer de mama. (a) Imagen hiperespectral adquirida en el IUMA. (b) Imagen RGB digitalizada por los patólogos. (c) Misma imagen que (b) pero con anotaciones sobre los distintos tipos de células: sanas (azul), mitosis (verde), tumorales (rojo), linfocitos (amarillo).

En primer lugar, se ha realizado un procesamiento de las imágenes para extraer automáticamente los distintos tipos de células para una posterior clasificación (Figura A-7). Una vez se han localizado las células indicadas por los patólogos para su clasificación, se ha entrenado una red neuronal convolucional para realizar dicho diagnóstico. Los resultados en la diferenciación entre células tumorales y células no tumorales han aportado resultados prometedores. Los resultados de este estudio se han presentado al congreso SPIE Medical Imaging 2020, con un artículo titulado

Hyperspectral imaging and deep learning for the detection of breast cancer cells in digitized histological images.

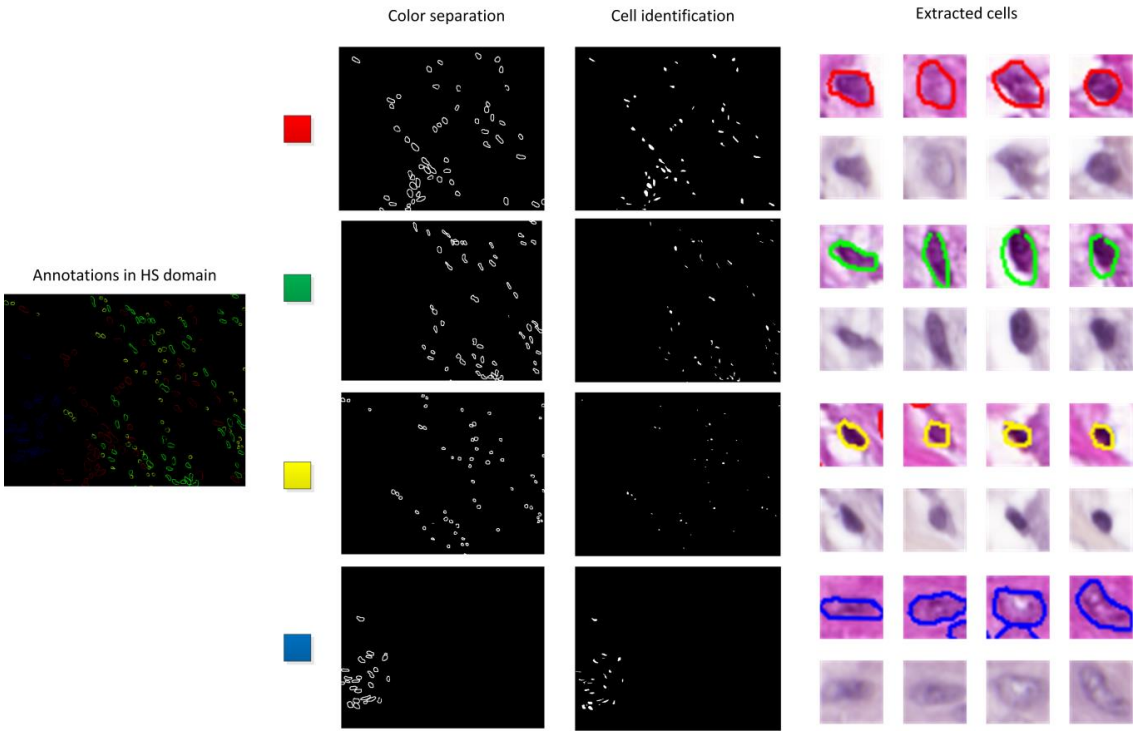

Figura A-7: Extracción de las células indicadas por los patólogos en la imagen hiperespectral.

A.7 Conclusiones

Tras el desarrollo de esta tesis, se concluye que la imagen hiperespectral puede ser una valiosa herramienta de ayuda a la hora de mejorar la precisión del diagnóstico histopatológico, de acelerar los diagnósticos rutinarios más comunes y de objetivar el diagnóstico entre distintos profesionales. Los resultados preliminares son muy alentadores y parecen indicar que la imagen hiperespectral puede ser una disciplina que juegue un importante papel en la anatomía patológica del siglo XXI.

Bibliography

[1] S. Sudharsan, R. Hemalatha, and S. Radha, “A survey on hyperspectral imaging for mineral exploration using machine learning algorithms,” in *2019 International Conference on Wireless Communications, Signal Processing and Networking, WiSPNET 2019*, 2019, pp. 206–212.

[2] T. Lei and D. W. Sun, “Developments of nondestructive techniques for evaluating quality attributes of cheeses: A review,” *Trends in Food Science and Technology*, vol. 88. Elsevier Ltd, pp. 527–542, Jun-2019.

[3] R. Vejarano, R. Siche, and W. Tesfaye, “Evaluation of biological contaminants in foods by hyperspectral imaging: A review,” *Int. J. Food Prop.*, vol. 20, pp. 1–34, Jun. 2017.

[4] M. Shimoni, R. Haelterman, and C. Perneel, “Hypersectral imaging for military and security applications: Combining Myriad processing and sensing techniques,” *IEEE Geosci. Remote Sens. Mag.*, vol. 7, no. 2, pp. 101–117, Jun. 2019.

[5] P. Mishra, M. S. M. Asaari, A. Herrero-Langreo, S. Lohumi, B. Diezma, and P. Scheunders, “Close range hyperspectral imaging of plants: A review,” *Biosystems Engineering*, vol. 164. Academic Press, pp. 49–67, Dec-2017.

[6] T. Adão *et al.*, “Hyperspectral imaging: A review on UAV-based sensors, data processing and applications for agriculture and forestry,” *Remote Sens.*, vol. 9, no. 11, 2017.

[7] M. J. Khan, H. S. Khan, A. Yousaf, K. Khurshid, and A. Abbas, “Modern Trends in Hyperspectral Image Analysis: A Review,” *IEEE Access*, vol. 6. Institute of Electrical and Electronics Engineers Inc., pp. 14118–14129, Mar-2018.

[8] G. Lu and B. Fei, “Medical hyperspectral imaging: a review,” *J. Biomed. Opt.*, vol. 19, no. 1, p. 10901, 2014.

[9] R. A. Schultz, T. Nielsen, J. R. Zavaleta, R. Ruch, R. Wyatt, and H. R. Garner, “Hyperspectral imaging: a novel approach for microscopic analysis,” *Cytometry*, vol. 43, no. 4, pp. 239–247, 2001.

[10] E. Pirard, “Multispectral imaging of ore minerals in optical microscopy,” *Mineral. Mag.*, vol. 68, no. 02, pp. 323–333, Apr. 2004.

[11] J. van der Weerd, M. K. van Veen, R. M. A. Heeren, and J. J. Boon, “Identification of pigments in paint cross sections by reflection visible light imaging microspectroscopy,” *Anal. Chem.*, vol. 75, no. 4, pp. 716–722, 2003.

[12] A.-K. Mahlein, “Plant Disease Detection by Imaging Sensors – Parallels and Specific Demands for Precision Agriculture and Plant Phenotyping,” *Plant Dis.*, vol. 100, no. 2, pp. 241–251, Feb. 2016.

[13] M. Leucker, A.-K. Mahlein, U. Steiner, and E.-C. Oerke, “Improvement of Lesion Phenotyping in Cercospora beticola –Sugar Beet Interaction by Hyperspectral Imaging,” *Phytopathology*, vol. 106, no. 2, pp. 177–184, Feb. 2016.

[14] S. L. Van Es, “Digital pathology: semper ad meliora,” *Pathology*, vol. 51, no. 1, pp. 1–10, Jan. 2019.

[15] T. J. Flotte and D. A. Bell, “Anatomical pathology is at a crossroads,” *Pathology*, vol. 50, no. 4, pp. 373–374, Jun. 2018.

[16] A. Madabhushi and G. Lee, “Image analysis and machine learning in digital pathology: Challenges and opportunities,” *Med. Image Anal.*, vol. 33, pp. 170–175, Oct. 2016.

[17] T. J. Fuchs and J. M. Buhmann, “Computational pathology: Challenges and promises for tissue analysis,” *Comput. Med. Imaging Graph.*, vol. 35, no. 7–8, pp. 515–530, Oct. 2011.

[18] D. N. Louis *et al.*, “Computational Pathology: A Path Ahead,” *Arch. Pathol. Lab. Med.*, vol. 140, no. 1, pp. 41–50, Jan. 2016.

[19] H. F. Grahn and P. Geladi, Eds., *Techniques and Applications of Hyperspectral Image Analysis*. Chichester, UK: John Wiley & Sons, Ltd, 2007.

[20] Y.-Z. Feng and D.-W. Sun, “Application of Hyperspectral Imaging in Food Safety Inspection and Control: A Review,” *Crit. Rev. Food Sci. Nutr.*, vol. 52, no. 11, pp. 1039–1058, Nov. 2012.

[21] D. Lorente *et al.*, “Recent Advances and Applications of Hyperspectral Imaging for Fruit and Vegetable Quality Assessment,” *Food Bioprocess Technol.*, vol. 5, no. 4, pp. 1121–1142, Nov. 2011.

[22] P. Tatzer, M. Wolf, and T. Panner, “Industrial application for inline material sorting using hyperspectral imaging in the {NIR} range,” *Real-Time Imaging*, vol. 11, no. 2, pp. 99–107, 2005.

[23] M. Kubik, “Chapter 5 Hyperspectral Imaging: A New Technique for the Non-Invasive Study of Artworks,” in *Physical Techniques in the Study of Art, Archaeology and Cultural Heritage*, Elsevier {BV}, 2007, pp. 199–259.

[24] C. Cucci, J. K. Delaney, and M. Picollo, “Reflectance Hyperspectral Imaging for Investigation of Works of Art: Old Master Paintings and Illuminated Manuscripts,” *Acc. Chem. Res.*, vol. 49, no. 10, pp. 2070–2079, Oct. 2016.

[25] M. Brossard, R. Marion, and V. Carrére, “Deconvolution of {SWIR} reflectance spectra for automatic mineral identification in hyperspectral imaging,” *Remote Sens. Lett.*, vol. 7, no. 6, pp. 581–590, 2016.

[26] E. Ben-Dor, “Quantitative remote sensing of soil properties,” in *Advances in Agronomy*, Elsevier {BV}, 2002, pp. 173–243.

[27] J. Behmann, J. Steinrücken, and L. Plümer, “Detection of early plant stress responses in hyperspectral images,” *{ISPRS} J. Photogramm. Remote Sens.*, vol. 93, pp. 98–111, Jul. 2014.

[28] Q. Li, X. He, Y. Wang, H. Liu, D. Xu, and F. Guo, “Review of spectral imaging technology in biomedical engineering: achievements and challenges,” *J. Biomed. Opt.*, vol. 18, no. 10, p. 100901, Oct. 2013.

[29] E. E. Holt, M. Aikio, and V. teknillinen tutkimuskeskus, *Hyperspectral Prism-grating-prism Imaging Spectrograph*. Technical Research Centre of Finland, 2001.

[30] H. Akbari, Y. Kosugi, K. Kojima, and N. Tanaka, “Blood vessel detection and artery-vein differentiation using hyperspectral imaging.,” *31st Annu. Int. Conf. IEEE Eng. Med. Biol. Soc.*, pp. 1461–1464, 2009.

[31] H. Fabelo *et al.*, “{HELICoiD} project: a new use of hyperspectral imaging for brain cancer detection in real-time during neurosurgical operations,” in *Hyperspectral Imaging Sensors: Innovative Applications and Sensor Standards 2016*, 2016.

[32] S. Ortega, G. M. Callico, M. L. Plaza, R. Camacho, H. Fabelo, and R. Sarmiento, “Hyperspectral database of pathological in-vitro human brain samples to detect carcinogenic tissues,” in *2016 {IEEE} 13th International Symposium on Biomedical Imaging ({ISBI})*, 2016.

[33] N. Gat, “Imaging spectroscopy using tunable filters: a review,” in *Wavelet Applications VII*, 2000.

[34] R. Leitner, M. De Biasio, T. Arnold, C. V. Dinh, M. Loog, and R. P. W. Duin, "Multi-spectral video endoscopy system for the detection of cancerous tissue," *Pattern Recognit. Lett.*, vol. 34, no. 1, pp. 85–93, 2013.

[35] N. Hagen and M. W. Kudenov, "Review of snapshot spectral imaging technologies," *Opt. Eng.*, vol. 52, no. 9, p. 090901, Sep. 2013.

[36] S. Ortega, H. Fabelo, R. Camacho, M. de la Luz Plaza, G. M. Callicó, and R. Sarmiento, "Detecting brain tumor in pathological slides using hyperspectral imaging," *Biomed. Opt. Express*, vol. 9, no. 2, p. 818, Feb. 2018.

[37] G. Chen and S.-E. Qian, "Denoising of Hyperspectral Imagery Using Principal Component Analysis and Wavelet Shrinkage," *{IEEE} Trans. Geosci. Remote Sens.*, vol. 49, no. 3, pp. 973–980, Mar. 2011.

[38] Q. Yuan, L. Zhang, and H. Shen, "Hyperspectral Image Denoising Employing a Spectral-Spatial Adaptive Total Variation Model," *{IEEE} Trans. Geosci. Remote Sens.*, vol. 50, no. 10, pp. 3660–3677, Oct. 2012.

[39] R. T. Kester, N. Bedard, L. Gao, and T. S. Tkaczyk, "Real-time snapshot hyperspectral imaging endoscope," *J. Biomed. Opt.*, vol. 16, no. 5, p. 56005, 2011.

[40] Q. Dai, J.-H. Cheng, D.-W. Sun, and X.-A. Zeng, "Advances in Feature Selection Methods for Hyperspectral Image Processing in Food Industry Applications: A Review," *Crit. Rev. Food Sci. Nutr.*, vol. 55, no. 10, pp. 1368–1382, Aug. 2015.

[41] J. Khodr and R. Younes, "Dimensionality reduction on hyperspectral images: A comparative review based on artificial datas," in *2011 4th International Congress on Image and Signal Processing*, 2011.

[42] *Pattern Recognition*. Elsevier, 2009.

[43] J. M. Bioucas-Dias *et al.*, "Hyperspectral unmixing overview: Geometrical, statistical, and sparse regression-based approaches," *IEEE J. Sel. Top. Appl. Earth Obs. Remote Sens.*, vol. 5, no. 2, pp. 354–379, 2012.

[44] C. G. Turvey and M. K. Mclaurin, "Applicability of the Normalized Difference Vegetation Index (NDVI) in Index-Based Crop Insurance Design," *Weather. Clim. Soc.*, vol. 4, no. 4, pp. 271–284, 2012.

[45] T. Nagaoka, A. Nakamura, H. Okutani, Y. Kiyohara, and T. Sota, "A possible melanoma discrimination index based on hyperspectral data: A pilot study," *Ski. Res. Technol.*, vol. 18, no. 3, pp. 301–310, 2012.

[46] M. Milanic, A. Bjorgan, M. Larsson, T. Strömberg, and L. L. Randeberg, "Detection of hypercholesterolemia using hyperspectral imaging of human skin," in *Clinical and Biomedical Spectroscopy and Imaging {IV}*, 2015.

[47] M. Milanic, L. A. Paluchowski, and L. L. Randeberg, "Hyperspectral imaging for detection of arthritis: feasibility and prospects," *J. Biomed. Opt.*, vol. 20, no. 9, p. 96011, Sep. 2015.

[48] E. Claridge, D. Hidović-Rowe, P. Taniere, and T. Ismail, "Quantifying mucosal blood volume fraction from multispectral images of the colon," in *Medical Imaging 2007: Physiology, Function, and Structure from Medical Images*, 2007.

[49] I. Goodfellow, Y. Bengio, and A. Courville, *Deep Learning*. The MIT Press, 2016.

[50] H. Arimoto and H. Furukawa, "Retinal blood oxygen saturation mapping by multispectral imaging and morphological angiography," in *Annual International Conference of the IEEE Engineering in Medicine and Biology - Proceedings*, 2007, pp. 1627–1630.

[51] H. Fabelo *et al.*, "Spatio-spectral classification of hyperspectral images for brain cancer detection during surgical operations," *PLoS One*, vol. 13, no. 3, pp. 1–27, 2018.

[52] S. Ortega *et al.*, "Hyperspectral Superpixel-Wise Glioblastoma Tumor Detection in Histological Samples," *Appl. Sci.*, vol. 10, no. 13, p. 4448, Jun. 2020.

[53] C. M. Bishop, *Pattern Recognition and Machine Learning (Information Science and Statistics)*, 1st ed. Springer, 2007.

[54] P. Ghamisi, J. Plaza, Y. Chen, J. Li, and A. J. Plaza, "Advanced Spectral Classifiers for Hyperspectral Images: A review," *IEEE Geosci. Remote Sens. Mag.*, vol. 5, no. 1, pp. 8–32, Mar. 2017.

[55] V. Vapnik, "Support vector machine," *Mach. Learn.*, vol. 20, no. 3, pp. 273–297, 1995.

[56] F. Melgani and L. Bruzzone, "Classification of hyperspectral remote sensing images with support vector machines," *IEEE Trans. Geosci. Remote Sens.*, vol. 42, no. 8, pp. 1778–1790, 2004.

[57] L. Breiman, "Random forests," *Mach. Learn.*, vol. 45, no. 1, pp. 5–32, 2001.

[58] E. Raczko and B. Zagajewski, "Comparison of support vector machine, random forest and neural network classifiers for tree species classification on airborne hyperspectral APEX images," *Eur. J. Remote Sens.*, vol. 50, no. 1, pp. 144–154, Jan. 2017.

[59] D. Böhning, "Multinomial logistic regression algorithm," *Ann. Inst. Stat. Math.*, vol. 44, no. 1, pp. 197–200, Mar. 1992.

[60] H. Akbari, Y. Kosugi, K. Kojima, and N. Tanaka, "Detection and Analysis of the Intestinal Ischemia Using Visible and Invisible Hyperspectral Imaging," *{IEEE} Trans. Biomed. Eng.*, vol. 57, no. 8, pp. 2011–2017, 2010.

[61] H. Akbari, K. Uto, Y. Kosugi, K. Kojima, and N. Tanaka, "Cancer detection using infrared hyperspectral imaging," *Cancer Sci.*, vol. 102, no. 4, pp. 852–857, Feb. 2011.

[62] H. Akbari *et al.*, "Hyperspectral imaging and quantitative analysis for prostate cancer detection," *J. Biomed. Opt.*, vol. 17, no. 7, p. 760051, Jul. 2012.

[63] Z. Liu, H. Wang, and Q. Li, "Tongue tumor detection in medical hyperspectral images," *Sensors*, vol. 12, no. 1, pp. 162–174, 2012.

[64] R. Leon *et al.*, "Non-Invasive Skin Cancer Diagnosis Using Hyperspectral Imaging for In-Situ Clinical Support," *J. Clin. Med.*, vol. 9, no. 6, p. 1662, Jun. 2020.

[65] B. Regeling *et al.*, "Development of an image pre-processor for operational hyperspectral laryngeal cancer detection," *J. Biophotonics*, vol. 9, no. 3, pp. 235–245, Mar. 2016.

[66] D. Nakaya *et al.*, "Development of high-performance pathological diagnosis software using a hyperspectral camera," in *2018 IEEE EMBS Conference on Biomedical Engineering and Sciences, IECBES 2018 - Proceedings*, 2019, pp. 217–220.

[67] G. Lu *et al.*, "Detection of head and neck cancer in surgical specimens using quantitative hyperspectral imaging," *Clin. Cancer Res.*, vol. 23, no. 18, pp. 5426–5436, 2017.

[68] L. J. P. Van Der Maaten, E. O. Postma, and H. J. Van Den Herik, "Dimensionality Reduction: A Comparative Review," *J. Mach. Learn. Res.*, vol. 10, pp. 1–41, 2009.

[69] P. J. Francis and B. J. Wills, "Introduction to Principal Components Analysis," *PM R*, vol. 6, no. 3, pp. 275–278, May 1999.

[70] L. M. Bruce, C. H. Koger, and J. Li, "Dimensionality reduction of hyperspectral data using discrete wavelet transform feature extraction," *IEEE Trans. Geosci. Remote Sens.*, vol. 40, no. 10, pp. 2331–2338, Oct. 2002.

[71] L. J. P. Van Der Maaten and G. E. Hinton, "Visualizing high-dimensional data using t-sne," *J. Mach. Learn. Res.*, vol. 9, pp. 2579–2605, 2008.

[72] S. N. Deepa and S. N. Sivanandam, "Introduction to Genetic Algorithms," Berlin, Heidelberg: Springer Berlin Heidelberg, 2008, pp. 15–37.

[73] Eberhart and Yuhui Shi, "Particle swarm optimization: developments, applications and resources," pp. 81–86, 2002.

[74] W. Sun and Q. Du, "Hyperspectral band selection: A review," *IEEE Geoscience and Remote Sensing Magazine*, vol. 7, no. 2. Institute of Electrical and Electronics Engineers Inc., pp. 118–139, Jun-2019.

[75] K. J. Zuzak, S. C. Naik, G. Alexandrakis, D. Hawkins, K. Behbehani, and E. Livingston, "Intraoperative bile duct visualization using near-infrared hyperspectral video imaging,"

Am. J. Surg., vol. 195, no. 4, pp. 491–497, 2008.

[76] J. W. Wilson, F. E. Robles, S. Deb, W. S. Warren, and M. C. Fischer, "Comparison of pump-probe and hyperspectral imaging in unstained histology sections of pigmented lesions," *Biomed. Opt. Express*, vol. 8, no. 8, p. 3882, Aug. 2017.

[77] M. Halicek *et al.*, "Optical biopsy of head and neck cancer using hyperspectral imaging and convolutional neural networks," in *Optical Imaging, Therapeutics, and Advanced Technology in Head and Neck Surgery and Otolaryngology 2018*, 2019, vol. 24, no. 03, p. 33.

[78] N. Zarei, A. Bakhtiari, P. Gallagher, M. Keys, and C. Macaulay, "Automated prostate glandular and nuclei detection using hyperspectral imaging," in *Proceedings - International Symposium on Biomedical Imaging*, 2017, pp. 1028–1031.

[79] Q. Li *et al.*, "Leukocyte cells identification and quantitative morphometry based on molecular hyperspectral imaging technology," *Comput. Med. Imaging Graph.*, vol. 38, no. 3, pp. 171–178, Apr. 2014.

[80] H. Fabelo *et al.*, "An intraoperative visualization system using hyperspectral imaging to aid in brain tumor delineation," *Sensors*, vol. 18, no. 2, 2018.

[81] X. Hadoux *et al.*, "Non-invasive in vivo hyperspectral imaging of the retina for potential biomarker use in Alzheimer's disease," *Nat. Commun.*, vol. 10, no. 1, pp. 1–12, Dec. 2019.

[82] D. Ravi, H. Fabelo, G. M. Callico, G. G.-Z. Yang, G. M. Callic, and G. G.-Z. Yang, "Manifold Embedding and Semantic Segmentation for Intraoperative Guidance with Hyperspectral Brain Imaging," *IEEE Trans. Med. Imaging*, vol. 36, no. 9, 2017.

[83] L. Ma, M. Halicek, and B. Fei, "In vivo cancer detection in animal model using hyperspectral image classification with wavelet feature extraction," in *Medical Imaging 2020: Biomedical Applications in Molecular, Structural, and Functional Imaging*, 2020, vol. 11317, p. 48.

[84] R. Pourreza-Shahri, F. Saki, N. Kehtarnavaz, P. Leboulluec, and H. Liu, "Classification of ex-vivo breast cancer positive margins measured by hyperspectral imaging," in *2013 IEEE International Conference on Image Processing, ICIP 2013 - Proceedings*, 2013, pp. 1408–1412.

[85] A. Goto *et al.*, "Use of hyperspectral imaging technology to develop a diagnostic support system for gastric cancer," *J. Biomed. Opt.*, vol. 20, no. 1, p. 016017, 2015.

[86] G. Lu *et al.*, "Framework for hyperspectral image processing and quantification for cancer detection during animal tumor surgery," *J. Biomed. Opt.*, vol. 20, no. 12, p. 126012, 2015.

[87] B. Martinez *et al.*, "Most Relevant Spectral Bands Identification for Brain Cancer Detection Using Hyperspectral Imaging," *Sensors*, vol. 19, no. 24, p. 5481, Dec. 2019.

[88] L. He, J. Li, C. Liu, and S. Li, "Recent Advances on Spectral-Spatial Hyperspectral Image Classification: An Overview and New Guidelines," *IEEE Trans. Geosci. Remote Sens.*, vol. 56, no. 3, pp. 1579–1597, Mar. 2018.

[89] Q. Wang *et al.*, "Spectral-spatial feature-based neural network method for acute lymphoblastic leukemia cell identification via microscopic hyperspectral imaging technology," *Biomed. Opt. Express*, vol. 8, no. 6, Jun. 2017.

[90] Q. Li, M. Zhou, H. Liu, Y. Wang, and F. Guo, "Red Blood Cell Count Automation Using Microscopic Hyperspectral Imaging Technology," *Appl. Spectrosc.*, vol. 69, no. 12, pp. 1372–1380, Dec. 2015.

[91] L. Lin and S. Zhang, "Superpixel Segmentation of Hyperspectral Images Based on Entropy and Mutual Information," *Appl. Sci.*, vol. 10, no. 4, p. 1261, Feb. 2020.

[92] H. Fabelo *et al.*, "Deep Learning-Based Framework for In Vivo Identification of Glioblastoma Tumor using Hyperspectral Images of Human Brain," *Sensors*, vol. 19, no. 4, p. 920, Feb. 2019.

[93] S. Ortega *et al.*, "Hyperspectral Imaging for the Detection of Glioblastoma Tumor Cells in H&E Slides Using Convolutional Neural Networks," *Sensors*, vol. 20, no. 7, p. 1911,

Mar. 2020.

[94] M. Halicek *et al.*, "Hyperspectral Imaging of Head and Neck Squamous Cell Carcinoma for Cancer Margin Detection in Surgical Specimens from 102 Patients Using Deep Learning," *Cancers (Basel).*, vol. 11, no. 9, p. 1367, Sep. 2019.

[95] M. Halicek, J. Dormer, J. Little, A. Chen, and B. Fei, "Tumor detection of the thyroid and salivary glands using hyperspectral imaging and deep learning," *Biomed. Opt. Express*, Jan. 2020.

[96] M. Halicek *et al.*, "Tumor margin classification of head and neck cancer using hyperspectral imaging and convolutional neural networks," in *Medical Imaging 2018: Image-Guided Procedures, Robotic Interventions, and Modeling*, 2018, p. 4.

[97] S. Trajanovski, C. Shan, P. J. C. Weijtmans, S. G. B. de Koning, and T. J. M. Ruers, "Tumor Semantic Segmentation in Hyperspectral Images using Deep Learning," in *International Conference on Medical Imaging with Deep Learning -- Extended Abstract Track*, 2019.

[98] E. Kho, B. Dashtbozorg, L. L. de Boer, K. K. Van de Vijver, H. J. C. M. Sterenborg, and T. J. M. Ruers, "Broadband hyperspectral imaging for breast tumor detection using spectral and spatial information," *Biomed. Opt. Express*, vol. 10, no. 9, p. 4496, Sep. 2019.

[99] M. Halicek *et al.*, "Conditional generative adversarial network for synthesizing hyperspectral images of breast cancer cells from digitized histology," in *Medical Imaging 2020: Digital Pathology*, 2020, p. 29.

[100] M. Bengs *et al.*, "Spectral-Spatial Recurrent-Convolutional Networks for In-Vivo Hyperspectral Tumor Type Classification," Jul. 2020.

[101] S. Li, W. Song, L. Fang, Y. Chen, P. Ghamisi, and J. A. Benediktsson, "Deep Learning for Hyperspectral Image Classification: An Overview," *IEEE Trans. Geosci. Remote Sens.*, pp. 1–20, 2019.

[102] V. V. Tuchin, *Tissue optics: Light scattering methods and instruments for medical diagnosis: Third edition*. SPIE, 2015.

[103] S. L. Jacques, "Optical properties of biological tissues: a review," *Phys. Med. Biol.*, vol. 58, no. 11, pp. R37--R61, May 2013.

[104] T. Vo-Dinh, *Biomedical Photonics Handbook: Biomedical Diagnostics*. CRC PRESS, 2019.

[105] D. W. Shipp, F. Sinjab, and I. Notingher, "Raman spectroscopy: techniques and applications in the life sciences," *Adv. Opt. Photonics*, vol. 9, no. 2, p. 315, Jun. 2017.

[106] H. J. Butler *et al.*, "Using Raman spectroscopy to characterize biological materials," *Nat. Protoc.*, vol. 11, no. 4, pp. 664–687, Apr. 2016.

[107] A. C. S. Talari, M. A. G. Martinez, Z. Movasaghi, S. Rehman, and I. U. Rehman, "Advances in Fourier transform infrared (FTIR) spectroscopy of biological tissues," *Applied Spectroscopy Reviews*, vol. 52, no. 5. Taylor and Francis Inc., pp. 456–506, May-2017.

[108] S. Gioux, A. Mazhar, and D. J. Cuccia, "Spatial frequency domain imaging in 2019: principles, applications, and perspectives," *J. Biomed. Opt.*, vol. 24, no. 07, p. 1, Jun. 2019.

[109] B. Zhu and E. M. Sevick-Muraca, "A review of performance of near-infrared fluorescence imaging devices used in clinical studies," *Br. J. Radiol.*, vol. 88, no. 1045, p. 20140547, Jan. 2015.

[110] C. Starr, C. Evers, and L. Starr, *Biology: concepts and applications without physiology*. Cengage Learning, 2010.

[111] D. Manolakis and G. Shaw, "Detection algorithms for hyperspectral imaging applications," *IEEE Signal Process. Mag.*, vol. 19, no. 1, pp. 29–43, 2002.

[112] M. Halicek, H. Fabelo, S. Ortega, G. M. Callico, and B. Fei, "In-Vivo and Ex-Vivo Tissue Analysis through Hyperspectral Imaging Techniques: Revealing the Invisible Features of Cancer," *Cancers (Basel).*, vol. 11, no. 6, p. 756, May 2019.

[113] S. Ortega *et al.*, "Use of Hyperspectral/Multispectral Imaging in Gastroenterology.

Shedding Some–Different–Light into the Dark," *J. Clin. Med.*, vol. 8, no. 1, p. 36, Jan. 2019.

[114] D. Moher, A. Liberati, J. Tetzlaff, and D. G. Altman, "Preferred Reporting Items for Systematic Reviews and Meta-Analyses: The PRISMA Statement," *PLoS Med.*, vol. 6, no. 7, p. e1000097, Jul. 2009.

[115] R. M. Levenson, "Spectral imaging perspective on cytomics," *Cytom. Part A*, vol. 69, no. 7, pp. 592–600, 2006.

[116] R. M. Levenson, A. Fornari, and M. Loda, "Multispectral imaging and pathology: seeing and doing more.," *Expert Opin. Med. Diagn.*, vol. 2, no. 9, pp. 1067–1081, Sep. 2008.

[117] R. Levenson, J. Beechem, and G. McNamara, "Spectral imaging in preclinical research and clinical pathology," *Biophotonics Pathol. Pathol. Crossroads*, vol. 35, no. 5–6, pp. 43–75, 2013.

[118] L. Gao and R. T. Smith, "Optical hyperspectral imaging in microscopy and spectroscopy - a review of data acquisition," *J. Biophotonics*, vol. 456, no. 6, pp. 441–456, 2014.

[119] M. Hermes *et al.*, "Mid-IR hyperspectral imaging for label-free histopathology and cytology," *J. Opt. (United Kingdom)*, vol. 20, no. 2, 2018.

[120] J. R. Mansfield, "Multispectral Imaging: A Review of Its Technical Aspects and Applications in Anatomic Pathology," *Vet. Pathol.*, vol. 51, no. 1, pp. 185–210, 2014.

[121] A. Liberati *et al.*, "The PRISMA Statement for Reporting Systematic Reviews and Meta-Analyses of Studies That Evaluate Health Care Interventions: Explanation and Elaboration," *PLoS Med.*, vol. 6, no. 7, p. e1000100, Jul. 2009.

[122] E. Inc., "Scopus." 2004.

[123] U. S. N. C. for Biotechnology Information (NCBI) and N. L. of Medicine (NLM), "PubMed." 1996.

[124] D. G. Manolakis, R. B. Lockwood, and T. W. Cooley, *Hyperspectral imaging remote sensing: physics, sensors, and algorithms*. Cambridge University Press, 2016.

[125] Q. Li, X. He, Y. Wang, H. Liu, D. Xu, and F. Guo, "Review of spectral imaging technology in biomedical engineering: achievements and challenges," *J. Biomed. Opt.*, vol. 18, no. 10, p. 100901, 2013.

[126] C. N. Pannell, J. D. Ward, E. S. Wachman, B. G. Zhang, and M. K. Reed, "A high-performance passband-agile hyperspectral imager using a large aperture acousto-optic tuneable filter," 2015, vol. 9369.

[127] E. S. Wachman *et al.*, "Simultaneous imaging of cellular morphology and multiple biomarkers using an acousto-optic tunable filter-based bright field microscope," *J. Biomed. Opt.*, vol. 19, no. 5, p. 56006, May 2014.

[128] A. Jarman, A. Manickavasagam, N. Hosny, and F. Festy, "Hyperspectral microscopy and cluster analysis for oral cancer diagnosis," in *Proceedings SPIE BiOS*, 2017, vol. 10076, p. 100761I.

[129] L. Gao, R. T. Kester, N. Hagen, and T. S. Tkaczyk, "Snapshot Image Mapping Spectrometer (IMS) with high sampling density for hyperspectral microscopy," *Opt. Express*, vol. 18, no. 14, p. 14330, Jul. 2010.

[130] L. Gao, N. Bedard, N. Hagen, R. T. Kester, and T. S. Tkaczyk, "Depth-resolved image mapping spectrometer (IMS) with structured illumination.," *Opt. Express*, vol. 19, no. 18, pp. 17439–17452, 2011.

[131] P. Favreau *et al.*, "Thin-film tunable filters for hyperspectral fluorescence microscopy.," *J. Biomed. Opt.*, vol. 19, no. 1, p. 11017, 2014.

[132] K. Shinoda *et al.*, "Multispectral filter array and demosaicking for pathological images," in *2015 Asia-Pacific Signal and Information Processing Association Annual Summit and Conference (APSIPA)*, 2015, pp. 697–703.

[133] M. B. Sinclair, J. A. Timlin, D. M. Haaland, and M. Werner-Washburne, "Design,

construction, characterization, and application of a hyperspectral microarray scanner.," *Appl. Opt.*, vol. 43, no. 10, pp. 2079–2088, 2004.

[134] S. Ortega *et al.*, "Hyperspectral Push-Broom Microscope Development and Characterization," *IEEE Access*, vol. 7, pp. 122473–122491, 2019.

[135] J. Liao *et al.*, "Terapixel hyperspectral whole-slide imaging via slit-array detection and projection," *J. Biomed. Opt.*, vol. 23, no. 6, pp. 1–7, Jun. 2018.

[136] W. J. Cukierski, X. Qi, and D. J. Foran, "Moving beyond color: The case for multispectral imaging in brightfield pathology," in *Proceedings. IEEE International Symposium on Biomedical Imaging*, 2009, vol. 5193251, pp. 1111–1114.

[137] W. J. Cukierski and D. J. Foran, "METAMERISM IN MULTISPECTRAL IMAGING OF HISTOPATHOLOGY SPECIMENS.," in *Proceedings. IEEE International Symposium on Biomedical Imaging*, 2010, vol. 2010, pp. 145–148.

[138] T. Abe, M. Yamaguchi, Y. Murakami, N. Ohyama, and Y. Yagi, "Color correction of pathological images for different staining-condition slides," 2004, pp. 218–223.

[139] T. Abe, Y. Murakami, M. Yamaguchi, N. Ohyama, and Y. Yagi, "Color correction of pathological images based on dye amount quantification," *Opt. Rev.*, vol. 12, no. 4, pp. 293–300, 2005.

[140] Y. Yagi, "Color standardization and optimization in Whole Slide Imaging," *Diagn. Pathol.*, vol. 6 Suppl 1, no. SUPPL. 1, p. S15, Mar. 2011.

[141] P. Bautista, N. Hashimoto, and Y. Yagi, "Color standardization in whole slide imaging using a color calibration slide," *J. Pathol. Inform.*, vol. 5, no. 1, p. 4, 2014.

[142] W.-C. Cheng, F. Saleheen, and A. Badano, "Assessing color performance of whole-slide imaging scanners for digital pathology," *Color Res. Appl.*, vol. 44, no. 3, pp. 322–334, 2019.

[143] F. Saleheen, A. Badano, and W.-C. Cheng, "Evaluating color performance of whole-slide imaging devices by multispectral-imaging of biological tissues," in *Proceedings SPIE Medical Imaging 2017: Digital Pathology;*, 2017, vol. 10140, p. 101400R.

[144] P. A. Bautista, T. Abe, M. Yamaguchi, Y. Yagi, and N. Ohyama, "Digital staining of pathological tissue specimens using spectral transmittance," in *Proceedings SPIE Medical Imaging 2005: Image Processing;*, 2005, vol. 5747, no. III, p. 1892.

[145] P. A. Bautista, T. Abe, M. Yamaguchi, Y. Yagi, and N. Ohyama, "Digital staining for multispectral images of pathological tissue specimens based on combined classification of spectral transmittance," *Comput. Med. Imaging Graph.*, vol. 29, no. 8, pp. 649–657, 2005.

[146] P. A. Bautista, T. Abe, M. Yamaguchi, Y. Yagi, and N. Ohyama, "Digital staining of pathological images: dye amount correction for improved classification performance," in *Proceedings SPIE Medical Imaging 2007: Computer-Aided Diagnosis;*, 2007, vol. 6514, no. PART 2, p. 651433.

[147] P. A. Bautista and Y. Yagi, "Multispectral image enhancement by spectral shifting," in *Proceedings SPIE BiOS*, 2012, vol. 8214.

[148] P. A. Bautista and Y. Yagi, "Multispectral enhancement towards digital staining.," *Anal. Cell. Pathol.*, vol. 35, no. 1, pp. 51–55, 2012.

[149] P. A. Bautista and Y. Yagi, "Digital staining for histopathology multispectral images by the combined application of spectral enhancement and spectral transformation," in *Conference proceedings: Annual International Conference of the IEEE Engineering in Medicine and Biology Society. IEEE Engineering in Medicine and Biology Society. Annual Conference*, 2011, vol. 2011, pp. 8013–8016.

[150] P. A. Bautista, T. Abe, M. Yamaguchi, N. Ohyama, and Y. Yagi, "Multispectral image enhancement for H&E stained pathological tissue specimens," in *Proceedings SPIE Medical Imaging 2008*, 2008, p. 691836.

[151] P. A. Bautista and Y. Yagi, "Multispectral enhancement method to increase the visual

differences of tissue structures in stained histopathology images.," *Anal. Cell. Pathol.*, vol. 35, no. 5–6, pp. 407–420, 2012.

[152] P. A. Bautista and Y. Yagi, "Digital simulation of staining in histopathology multispectral images: Enhancement and linear transformation of spectral transmittance," *J. Biomed. Opt.*, vol. 17, no. 5, p. 56013, May 2012.

[153] P. A. Bautista, T. Abe, M. Yamaguchi, Y. Yagi, and N. Ohyama, "Digital Staining of Unstained Pathological Tissue Samples through Spectral Transmittance Classification," *Opt. Rev.*, vol. 12, no. 1, pp. 7–14, Jan. 2005.

[154] N. Bayramoglu, M. Kaakinen, L. Eklund, and J. Heikkila, "Towards Virtual H&E Staining of Hyperspectral Lung Histology Images Using Conditional Generative Adversarial Networks," in *2017 IEEE International Conference on Computer Vision Workshops (ICCVW)*, 2017, pp. 64–71.

[155] G. Campanella *et al.*, "Clinical-grade computational pathology using weakly supervised deep learning on whole slide images," *Nat. Med.*, vol. 25, no. 8, pp. 1301–1309, Aug. 2019.

[156] F. Fereidouni *et al.*, "Dual-mode emission and transmission microscopy for virtual histochemistry using hematoxylin- and eosin-stained tissue sections," *Biomed. Opt. Express*, vol. 10, no. 12, p. 6516, Dec. 2019.

[157] Y. Rivenson, Z. Göröcs, H. Günaydin, Y. Zhang, H. Wang, and A. Ozcan, "Deep learning microscopy," *Optica*, vol. 4, no. 11, p. 1437, Nov. 2017.

[158] L. A. Sordillo *et al.*, "Third therapeutic spectral window for deep tissue imaging," in *Optical Biopsy XII*, 2014, vol. 8940, p. 89400V.

[159] P. K. Dash *et al.*, "Loss of neuronal integrity during progressive HIV-1 infection of humanized mice.," *J. Neurosci.*, vol. 31, no. 9, pp. 3148–3157, Mar. 2011.

[160] Y. Al-Kofahi *et al.*, "Cell-based quantification of molecular biomarkers in histopathology specimens," *Histopathology*, vol. 59, no. 1, pp. 40–54, Jul. 2011.

[161] K. J. Welsh, S.-A. S.-A. Hwang, S. Boyd, M. L. Kruzel, R. L. Hunter, and J. K. Actor, "Influence of oral lactoferrin on Mycobacterium tuberculosis induced immunopathology," *Tuberculosis (Edinb).*, vol. 91 Suppl 1, no. SUPPL. 1, pp. S105--13, 2011.

[162] C. M. van der Loos, O. J. de Boer, C. Mackaaij, L. T. Hoekstra, T. M. van Gulik, and J. Verheij, "Accurate quantitation of Ki67-positive proliferating hepatocytes in rabbit liver by a multicolor immunohistochemical (IHC) approach analyzed with automated tissue and cell segmentation software.," *J. Histochem. Cytochem.*, vol. 61, no. 1, pp. 11–18, 2013.

[163] J. M. Kruger *et al.*, "Detection of truncated HER2 forms in formalin-fixed, paraffin-embedded breast cancer tissue captures heterogeneity and is not affected by HER2-targeted therapy.," *Am. J. Pathol.*, vol. 183, no. 2, pp. 336–343, 2013.

[164] R. M. Abraham *et al.*, "Lymphatic invasion predicts aggressive behavior in melanocytic tumors of uncertain malignant potential (MELTUMP)," *Am. J. Surg. Pathol.*, vol. 37, no. 5, pp. 669–675, May 2013.

[165] C. H. Ussakli *et al.*, "Mitochondria and tumor progression in ulcerative colitis.," *J. Natl. Cancer Inst.*, vol. 105, no. 16, pp. 1239–1248, 2013.

[166] Y. Cao *et al.*, "Pericyte coverage of differentiated vessels inside tumor vasculature is an independent unfavorable prognostic factor for patients with clear cell renal cell carcinoma," *Cancer*, vol. 119, no. 2, pp. 313–334, 2013.

[167] E. L. Spaeth, C. M. Booth, and F. C. Marini, "Quantitative multispectral analysis following fluorescent tissue transplant for visualization of cell origins, types, and interactions.," *J. Vis. Exp.*, no. 79, p. e50385, Sep. 2013.

[168] K. A. Salva, D. Bennett, J. Longley, J. Guitart, and G. S. Wood, "Multispectral imaging approach to the diagnosis of a CD20+ cutaneous T-cell lymphoproliferative disorder: A case report," *Am. J. Dermatopathol.*, vol. 37, no. 10, pp. e116--21, Oct. 2015.

[169] H. Yoshimura, Y. Matsuda, A. Matsushita, Y. Nakamura, E. Uchida, and T. Ishiwata, "Multispectral imaging of pancreatic mixed acinar-neuroendocrine-ductal carcinoma with

triple-immunoenzyme staining," *J. Nippon Med. Sch.*, vol. 82, no. 3, pp. 122–123, 2015.

[170] B. T. Velayudhan *et al.*, "Ovariectomy in young prepubertal dairy heifers causes complete suppression of mammary progesterone receptors.," *Domest. Anim. Endocrinol.*, vol. 51, pp. 8–18, 2015.

[171] K. A. Salva, M. J. Reeder, R. Lloyd, and G. S. Wood, "c-CBL E3 Ubiquitin Ligase Expression Increases Across the Spectrum of Benign and Malignant T-Cell Skin Diseases.," *Am. J. Dermatopathol.*, vol. 39, no. 10, pp. 731–737, Oct. 2017.

[172] M. J. Campbell *et al.*, "Characterizing the immune microenvironment in high-risk ductal carcinoma in situ of the breast," *Breast Cancer Res. Treat.*, vol. 161, no. 1, pp. 17–28, Jan. 2017.

[173] L. Guo *et al.*, "Quantification of Tyrosine Hydroxylase and ErbB4 in the Locus Coeruleus of Mood Disorder Patients Using a Multispectral Method to Prevent Interference with Immunocytochemical Signals by Neuromelanin.," *Neurosci. Bull.*, vol. 35, no. 2, pp. 205–215, 2019.

[174] R. K. O'Donnell, M. Feldman, R. Mick, and R. J. Muschel, "Immunohistochemical method identifies lymphovascular invasion in a majority of oral squamous cell carcinomas and discriminates between blood and lymphatic vessel invasion.," *J. Histochem. Cytochem.*, vol. 56, no. 9, pp. 803–810, Sep. 2008.

[175] C. M. Gilbert and A. Parwani, "The use of multispectral imaging to distinguish reactive urothelium from neoplastic urothelium.," *J. Pathol. Inform.*, vol. 1, p. 23, Oct. 2010.

[176] S. Safayi *et al.*, "Myoepithelial cell differentiation markers in prepubertal bovine mammary gland: effect of ovariectomy.," *J. Dairy Sci.*, vol. 95, no. 6, pp. 2965–2976, Jun. 2012.

[177] C. Fiore *et al.*, "Utility of multispectral imaging in automated quantitative scoring of immunohistochemistry.," *J. Clin. Pathol.*, vol. 65, no. 6, pp. 496–502, Jun. 2012.

[178] T. M. Bauman *et al.*, "Finasteride treatment alters tissue specific androgen receptor expression in prostate tissues.," *Prostate*, vol. 74, no. 9, pp. 923–932, Jun. 2014.

[179] W. Liu *et al.*, "A Comparative Performance Analysis of Multispectral and RGB Imaging on HER2 Status Evaluation for the Prediction of Breast Cancer Prognosis.," *Transl. Oncol.*, vol. 9, no. 6, pp. 521–530, 2016.

[180] W.-L. Liu *et al.*, "Application of multispectral imaging in quantitative immunohistochemistry study of breast cancer: a comparative study," *Tumour Biol.*, vol. 37, no. 4, pp. 5013–5024, 2016.

[181] D. H. Hepp *et al.*, "Distribution and load of amyloid-b pathology in Parkinson disease and dementia with lewy bodies," *J. Neuropathol. Exp. Neurol.*, vol. 75, no. 10, pp. 936–945, 2016.

[182] H. L. M. Tucker, C. L. M. Parsons, S. Ellis, M. L. Rhoads, and R. M. Akers, "Tamoxifen impairs prepubertal mammary development and alters expression of estrogen receptor alpha (ESR1) and progesterone receptors (PGR).," *Domest. Anim. Endocrinol.*, vol. 54, pp. 95–105, 2016.

[183] C. Jiang *et al.*, "Perivascular cell coverage of intratumoral vasculature is a predictor for bevacizumab efficacy in metastatic colorectal cancer," *Cancer Manag. Res.*, vol. Volume 10, pp. 3589–3597, Sep. 2018.

[184] M. Fang *et al.*, "The heterogenic tumor microenvironment of hepatocellular carcinoma and prognostic analysis based on tumor neo-vessels, macrophages and α-SMA," *Oncol. Lett.*, vol. 15, no. 4, pp. 4805–4812, 2018.

[185] W. Huang, K. Hennrick, and S. Drew, "A colorful future of quantitative pathology: Validation of Vectra technology using chromogenic multiplexed immunohistochemistry and prostate tissue microarrays," *Hum. Pathol.*, vol. 44, no. 1, pp. 29–38, 2013.

[186] T. M. Nicholson, P. D. Sehgal, S. A. Drew, W. Huang, and W. A. Ricke, "Sex steroid receptor expression and localization in benign prostatic hyperplasia varies with tissue

compartment.," *Differentiation.*, vol. 85, no. 4–5, pp. 140–149, 2013.

[187] L. S. Nelson *et al.*, "Automated prognostic pattern detection shows favourable diffuse pattern of FOXP3(+) Tregs in follicular lymphoma.," *Br. J. Cancer*, vol. 113, no. 8, pp. 1197–1205, Oct. 2015.

[188] E. Ansong *et al.*, "Evidence that selenium binding protein 1 is a tumor suppressor in prostate cancer.," *PLoS One*, vol. 10, no. 5, p. e0127295, 2015.

[189] C. M. de Winde, M. Zuidscherwoude, A. Vasaturo, A. van der Schaaf, C. G. Figdor, and A. B. van Spriel, "Multispectral imaging reveals the tissue distribution of tetraspanins in human lymphoid organs.," *Histochem. Cell Biol.*, vol. 144, no. 2, pp. 133–146, 2015.

[190] T. M. Bauman, A. J. Becka, P. D. Sehgal, W. Huang, and W. A. Ricke, "SIGIRR/TIR8, an important regulator of TLR4 and IL-1R-mediated NF-κB activation, predicts biochemical recurrence after prostatectomy in low-grade prostate carcinomas," *Hum. Pathol.*, vol. 46, no. 11, pp. 1744–1751, Nov. 2015.

[191] K. Oguejiofor *et al.*, "Stromal infiltration of CD8 T cells is associated with improved clinical outcome in HPV-positive oropharyngeal squamous carcinoma.," *Br. J. Cancer*, vol. 113, no. 6, pp. 886–893, Sep. 2015.

[192] A. M. Mahmoud *et al.*, "BRCA1 protein expression and subcellular localization in primary breast cancer: Automated digital microscopy analysis of tissue microarrays.," *PLoS One*, vol. 12, no. 9, p. e0184385, 2017.

[193] Z. Feng *et al.*, "Multiparametric immune profiling in HPV- oral squamous cell cancer.," *JCI insight*, vol. 2, no. 14, Jul. 2017.

[194] A. Vasaturo *et al.*, "Multispectral imaging for highly accurate analysis of tumour-infiltrating lymphocytes in primary melanoma," *Histopathology*, vol. 70, no. 4, pp. 643–649, Mar. 2017.

[195] I. J. Park *et al.*, "Prediction of radio-responsiveness with immune-profiling in patients with rectal cancer.," *Oncotarget*, vol. 8, no. 45, pp. 79793–79802, Oct. 2017.

[196] E. R. Parra *et al.*, "Validation of multiplex immunofluorescence panels using multispectral microscopy for immune-profiling of formalin-fixed and paraffin-embedded human tumor tissues.," *Sci. Rep.*, vol. 7, no. 1, p. 13380, Oct. 2017.

[197] M. Surace *et al.*, "Automated Multiplex Immunofluorescence Panel for Immuno-oncology Studies on Formalin-fixed Carcinoma Tissue Specimens.," *J. Vis. Exp.*, no. 143, 2019.

[198] M. E. Ijsselsteijn *et al.*, "Cancer immunophenotyping by seven-colour multispectral imaging without tyramide signal amplification.," *J. Pathol. Clin. Res.*, vol. 5, no. 1, pp. 3–11, 2019.

[199] C. Mascaux *et al.*, "Immune evasion before tumour invasion in early lung squamous carcinogenesis.," *Nature*, vol. 571, no. 7766, pp. 570–575, Jul. 2019.

[200] J. S. Soh *et al.*, "Immunoprofiling of Colitis-associated and Sporadic Colorectal Cancer and its Clinical Significance.," *Sci. Rep.*, vol. 9, no. 1, p. 6833, May 2019.

[201] G. Hong *et al.*, "Multiplexed fluorescent immunohistochemical staining, imaging, and analysis in histological samples of lymphoma," *J. Vis. Exp.*, vol. 2019, no. 143, 2019.

[202] P. D. Sehgal *et al.*, "Tissue-specific quantification and localization of androgen and estrogen receptors in prostate cancer.," *Hum. Pathol.*, vol. 89, pp. 99–108, Jul. 2019.

[203] T. M. Bauman, C. M. Vezina, W. Huang, P. C. Marker, R. E. Peterson, and W. A. Ricke, "Beta-catenin is elevated in human benign prostatic hyperplasia specimens compared to histologically normal prostate tissue.," *Am. J. Clin. Exp. Urol.*, vol. 2, no. 4, pp. 313–322, 2014.

[204] J. Rosenbaum, S. Drew, and W. Huang, "Significantly higher expression levels of androgen receptor are associated with erythroblastosis virus E26 oncogene related gene positive prostate cancer.," *Am. J. Clin. Exp. Urol.*, vol. 2, no. 3, pp. 249–257, 2014.

[205] T. M. Bauman *et al.*, "Expression and colocalization of beta-catenin and lymphoid

enhancing factor-1 in prostate cancer progression.," *Hum. Pathol.*, vol. 51, pp. 124–133, May 2016.

[206] J. Kim *et al.*, "Heterogeneous perivascular cell coverage affects breast cancer metastasis and response to chemotherapy.," *JCI insight*, vol. 1, no. 21, p. e90733, 2016.

[207] T. M. Bauman, W. Huang, M. H. Lee, and E. J. Abel, "Neovascularity as a prognostic marker in renal cell carcinoma.," *Hum. Pathol.*, vol. 57, pp. 98–105, Nov. 2016.

[208] T. M. Bauman, E. A. Ricke, S. A. Drew, W. Huang, and W. A. Ricke, "Quantitation of Protein expression and Co-localization using multiplexed Immuno-Histochemical staining and multispectral imaging," *J. Vis. Exp.*, vol. 2016, no. 110, 2016.

[209] M. A. J. Gorris *et al.*, "Eight-Color Multiplex Immunohistochemistry for Simultaneous Detection of Multiple Immune Checkpoint Molecules within the Tumor Microenvironment.," *J. Immunol.*, vol. 200, no. 1, pp. 347–354, 2018.

[210] K. Silina *et al.*, "Germinal Centers Determine the Prognostic Relevance of Tertiary Lymphoid Structures and Are Impaired by Corticosteroids in Lung Squamous Cell Carcinoma.," *Cancer Res.*, vol. 78, no. 5, pp. 1308–1320, Mar. 2018.

[211] A. Mezheyeuski *et al.*, "Multispectral imaging for quantitative and compartment-specific immune infiltrates reveals distinct immune profiles that classify lung cancer patients," *J. Pathol.*, vol. 244, no. 4, pp. 421–431, 2018.

[212] C. J. Cho *et al.*, "Poor prognosis in Epstein-Barr virus-negative gastric cancer with lymphoid stroma is associated with immune phenotype.," *Gastric Cancer*, vol. 21, no. 6, pp. 925–935, Nov. 2018.

[213] D. Takahashi *et al.*, "Profiling the Tumour Immune Microenvironment in Pancreatic Neuroendocrine Neoplasms with Multispectral Imaging Indicates Distinct Subpopulation Characteristics Concordant with WHO 2017 Classification.," *Sci. Rep.*, vol. 8, no. 1, p. 13166, Sep. 2018.

[214] M. Dobosz, U. Haupt, and W. Scheuer, "Improved decision making for prioritizing tumor targeting antibodies in human xenografts: Utility of fluorescence imaging to verify tumor target expression, antibody binding and optimization of dosage and application schedule.," *MAbs*, vol. 9, no. 1, pp. 140–153, 2017.

[215] B. Solomon *et al.*, "Identification of an excellent prognosis subset of human papillomavirus associated oropharyngeal cancer patients by quantification of intratumoral CD103+ immune cell abundance.," *Ann. Oncol. Off. J. Eur. Soc. Med. Oncol.*, 2019.

[216] R. Scott, F. M. Khan, J. Zeineh, M. Donovan, and G. Fernandez, "Gland ring morphometry for prostate cancer prognosis in multispectral immunofluorescence images.," *Med. Image Comput. Comput. Assist. Interv.*, vol. 17, no. PART 1, pp. 585–592, 2014.

[217] K. S. S. Enfield *et al.*, "Hyperspectral cell sociology reveals spatial tumor-immune cell interactions associated with lung cancer recurrence.," *J. Immunother. cancer*, vol. 7, no. 1, p. 13, 2019.

[218] L. Ying *et al.*, "Understanding immune phenotypes in human gastric disease tissues by multiplexed immunohistochemistry," *J. Transl. Med.*, vol. 15, no. 1, 2017.

[219] S. W. Kim, J. Roh, and C. S. Park, "Immunohistochemistry for pathologists: Protocols, pitfalls, and tips," *Journal of Pathology and Translational Medicine*, vol. 50, no. 6. Seoul National University, pp. 411–418, Oct-2016.

[220] D. Pantalone *et al.*, "Multispectral Imaging Autofluorescence Microscopy in Colonic and Gastric Cancer Metastatic Lymph Nodes," *Clin. Gastroenterol. Hepatol.*, vol. 5, no. 2, pp. 230–236, 2007.

[221] P. Constantinou, R. S. Dacosta, and B. C. Wilson, "Extending immunofluorescence detection limits in whole paraffin-embedded formalin fixed tissues using hyperspectral confocal fluorescence imaging.," *J. Microsc.*, vol. 234, no. 2, pp. 137–146, May 2009.

[222] P. Constantinou, B. C. Wilson, and S. Damaskinos, "Hyperspectral unmixing for removing

autofluorescence from paraffin-embedded, formalin-fixed tissue sections," 2005, vol. 5969.

[223] P. Constantinou, T. Nicklee, D. W. Hedley, S. Damaskinos, and B. C. Wilson, "A high-resolution MACROscope with differential phase contrast, transmitted light, confocal fluorescence, and hyperspectral capabilities for large-area tissue imaging," *IEEE J. Sel. Top. Quantum Electron.*, vol. 11, no. 4, pp. 766–777, 2005.

[224] H. Duong and M. Han, "A multispectral LED array for the reduction of background autofluorescence in brain tissue.," *J. Neurosci. Methods*, vol. 220, no. 1, pp. 46–54, Oct. 2013.

[225] P. G. Ellingsen, N. K. Reitan, B. D. Pedersen, and M. Lindgren, "Hyperspectral analysis using the correlation between image and reference.," *J. Biomed. Opt.*, vol. 18, no. 2, p. 20501, Feb. 2013.

[226] P. G. Ellingsen *et al.*, "Spectral correlation analysis of amyloid beta plaque inhomogeneity from double staining experiments.," *J. Biomed. Opt.*, vol. 18, no. 10, p. 101313, Oct. 2013.

[227] S. J. Leavesley, B. Sweat, C. Abbott, P. F. Favreau, N. S. Annamdevula, and T. C. Rich, "Comparing methods for analysis of biomedical hyperspectral image data," in *Proceedings SPIE BiOS*, 2017, vol. 10068, p. 100680S.

[228] S. J. Leavesley *et al.*, "Hyperspectral imaging microscopy for identification and quantitative analysis of fluorescently-labeled cells in highly autofluorescent tissue," *J. Biophotonics*, vol. 5, no. 1, pp. 67–84, Jan. 2012.

[229] N. G. Dolloff, X. Ma, D. T. Dicker, R. C. Humphreys, L. Z. Li, and W. S. El-Deiry, "Spectral imaging-based methods for quantifying autophagy and apoptosis.," *Cancer Biol. Ther.*, vol. 12, no. 4, pp. 349–356, 2011.

[230] P. F. Favreau, J. A. Deal, D. S. Weber, T. C. Rich, and S. J. Leavesley, "Feasibility for detection of autofluorescent signatures in rat organs using a novel excitation-scanning hyperspectral imaging system," in *Proceedings Volume 9711, Imaging, Manipulation, and Analysis of Biomolecules, Cells, and Tissues IX; 971113*, 2016, vol. 9711, p. 971113.

[231] S. J. Leavesley *et al.*, "Hyperspectral imaging fluorescence excitation scanning for colon cancer detection," *J. Biomed. Opt.*, vol. 21, no. 10, p. 104003, Oct. 2016.

[232] S. J. Leavesley *et al.*, "Hyperspectral imaging fluorescence excitation scanning for detecting colorectal cancer: pilot study," in *Proceedings SPIE BiOS*, 2016, vol. 9703, p. 970315.

[233] J. Deal *et al.*, "Demystifying autofluorescence with excitation scanning hyperspectral imaging," in *Imaging, Manipulation, and Analysis of Biomolecules, Cells, and Tissues XVI*, 2018, p. 40.

[234] J. Deal *et al.*, "Identifying molecular contributors to autofluorescence of neoplastic and normal colon sections using excitation-scanning hyperspectral imaging," *J. Biomed. Opt.*, vol. 24, no. 2, pp. 1–11, 2019.

[235] N. Dey *et al.*, "Tensor decomposition of hyperspectral images to study autofluorescence in age-related macular degeneration," *Med. Image Anal.*, vol. 56, pp. 96–109, 2019.

[236] N. Dey *et al.*, "Multi-modal image fusion for multispectral super-resolution in microscopy," in *Medical Imaging 2019: Image Processing*, 2019, vol. 10949, p. 12.

[237] A. Habibalahi, C. Bala, A. Allende, A. G. Anwer, and E. M. Goldys, "Novel automated non invasive detection of ocular surface squamous neoplasia using multispectral autofluorescence imaging.," *Ocul. Surf.*, Mar. 2019.

[238] J.-R. Duann *et al.*, "Separating spectral mixtures in hyperspectral image data using independent component analysis: validation with oral cancer tissue sections," *J. Biomed. Opt.*, vol. 18, no. 12, p. 126005, 2013.

[239] M. Bouzid, A. Khalfallah, A. Bouchot, M. S. Bouhlel, and F. S. Marzani, "Automatic cell nuclei detection: A protocol to acquire multispectral images and to compare results between color and multispectral images," 2013, vol. 8587.

[240] Q. Li, Z. Chen, X. He, Y. Wang, H. Liu, and Q. Xu, "Automatic identification and quantitative morphometry of unstained spinal nerve using molecular hyperspectral imaging technology," *Neurochem. Int.*, vol. 61, no. 8, pp. 1375–1384, Dec. 2012.

[241] Q. Li *et al.*, "AOTF based molecular hyperspectral imaging system and its applications on nerve morphometry," *Appl. Opt.*, vol. 52, no. 17, p. 3891, Jun. 2013.

[242] E. Vazgiouraki *et al.*, "Application of multispectral imaging detects areas with neuronal myelin loss, without tissue labelling.," *Reprod. Syst. Sex. Disord.*, vol. 65, no. 2, pp. 109–118, 2015.

[243] I. Kopriva *et al.*, "Rational variety mapping for contrast-enhanced nonlinear unsupervised segmentation of multispectral images of unstained specimen," *Am. J. Pathol.*, vol. 179, no. 2, pp. 547–554, 2011.

[244] S. S. More and R. Vince, "Hyperspectral imaging signatures detect amyloidopathy in Alzheimer's mouse retina well before onset of cognitive decline.," *ACS Chem. Neurosci.*, vol. 6, no. 2, pp. 306–315, Feb. 2015.

[245] Q. Li, Y. Xue, J. Zhang, and G. Xiao, "Microscopic hyperspectral imaging studies of normal and diabetic retina of rats.," *Sci. China. Ser. C, Life Sci.*, vol. 51, no. 9, pp. 789–794, Sep. 2008.

[246] Q. Li, J. Zhang, Y. Wang, and G. Xu, "Molecular Spectral Imaging System for Quantitative Immunohistochemical Analysis of Early Diabetic Retinopathy," *Appl. Spectrosc.*, vol. 63, no. 12, pp. 1336–1342, 2009.

[247] Q. Li, Y. Xue, G. Xiao, and J. Zhang, "New microscopic pushbroom hyperspectral imaging system for application in diabetic retinopathy research.," *J. Biomed. Opt.*, vol. 12, no. 6, p. 64011, 2007.

[248] Qingli Li, Yiting Wang, Jingfa Zhang, Guotong Xu, and Yongqi Xue, "Quantitative Analysis of Protective Effect of Erythropoietin on Diabetic Retinal Cells Using Molecular Hyperspectral Imaging Technology," *IEEE Trans. Biomed. Eng.*, vol. 57, no. 7, pp. 1699–1706, Jul. 2010.

[249] S. Abeysekera, M. P.-L. Ooi, Y. C. Kuang, C. P. Tan, and S. S. Hassan, "Detecting spongiosis in stained histopathological specimen using multispectral imaging and machine learning," in *2014 IEEE Sensors Applications Symposium (SAS)*, 2014, pp. 195–200.

[250] N. Vigneswaran and M. D. Williams, "Epidemiologic Trends in Head and Neck Cancer and Aids in Diagnosis," *Oral Maxillofac. Surg. Clin. North Am.*, vol. 26, no. 2, pp. 123–141, May 2014.

[251] M. Ou-Yang, Y.-F. Hsieh, and C.-C. Lee, "Biopsy diagnosis of oral carcinoma by the combination of morphological and spectral methods based on embedded relay lens microscopic hyperspectral imaging system," *J. Med. Biol. Eng.*, vol. 35, no. 4, pp. 437–447, 2015.

[252] H. Akbari, L. V Halig, H. Zhang, D. Wang, Z. G. Chen, and B. Fei, "Detection of Cancer Metastasis Using a Novel Macroscopic Hyperspectral Method.," *Proc. SPIE*, vol. 8317, p. 831711, 2012.

[253] I. Mansoor, C. Zalles, F. Zahid, K. Gossage, R. M. Levenson, and D. L. Rimm, "Fine-needle aspiration of follicular adenoma versus parathyroid adenoma: the utility of multispectral imaging in differentiating lesions with subtle cytomorphologic differences.," *Cancer*, vol. 114, no. 1, pp. 22–26, Feb. 2008.

[254] L. D. Hahn, C. Hoyt, D. L. Rimm, and C. Theoharis, "Spatial spectral imaging as an adjunct to the Bethesda classification of thyroid fine-needle aspiration specimens.," *Cancer Cytopathol.*, vol. 121, no. 3, pp. 162–167, Mar. 2013.

[255] C. He *et al.*, "Characterizing microstructures of cancerous tissues using multispectral transformed Mueller matrix polarization parameters," *Biomed. Opt. Express*, vol. 6, no. 8, pp. 2934–2945, 2015.

[256] X. Wu, J. Thigpen, and S. K. Shah, "Multispectral microscopy and cell segmentation for analysis of thyroid fine needle aspiration cytology smears.," *Conf. Proc. Annu. Int. Conf.*

IEEE Eng. Med. Biol. Soc. IEEE Eng. Med. Biol. Soc. Annu. Conf., vol. 2009, pp. 5645–5648, 2009.

[257] X. Wu and S. K. Shah, "A fast band selection method to increase image contrast for multispectral image segmentation," in *2009 IEEE International Symposium on Biomedical Imaging: From Nano to Macro*, 2009, pp. 1123–1126.

[258] E. Gabriel, V. Venkatesan, and S. Shah, "Towards high performance cell segmentation in multispectral fine needle aspiration cytology of thyroid lesions.," *Comput. Methods Programs Biomed.*, vol. 98, no. 3, pp. 231–240, Jun. 2010.

[259] X. Wu and S. K. Shah, "Random field model for cell segmentation in transmission mode multispectral microscopy images," in *2009 Conference Record of the Forty-Third Asilomar Conference on Signals, Systems and Computers*, 2009, pp. 795–798.

[260] X. Wu, M. Amrikachi, and S. K. Shah, "Embedding topic discovery in conditional random fields model for segmenting nuclei using multispectral data.," *IEEE Trans. Biomed. Eng.*, vol. 59, no. 6, pp. 1539–1549, Jun. 2012.

[261] X. Wu and S. K. Shah, "A bottom-up and top-down model for cell segmentation using multispectral data," in *2010 IEEE International Symposium on Biomedical Imaging: From Nano to Macro*, 2010, pp. 592–595.

[262] Xuqing Wu and Shishir Shah, "Comparative analysis of cell segmentation using absorption and color images in fine needle aspiration cytology," in *2008 IEEE International Conference on Systems, Man and Cybernetics*, 2008, pp. 271–276.

[263] L. E. Boucheron, Z. Bi, N. R. Harvey, B. S. Manjunath, and D. L. Rimm, "Utility of multispectral imaging for nuclear classification of routine clinical histopathology imagery," *BMC Cell Biol.*, vol. 8 Suppl 1, no. SUPPL. 1, p. S8, Jul. 2007.

[264] X. Qi, W. Cukierski, and D. J. Foran, "A comparative performance study characterizing breast tissue microarrays using standard RGB and multispectral imaging," in *Proceedings SPIE Multimodal Biomedical Imaging V;*, 2010, p. 75570Z.

[265] X. Qi, F. Xing, D. J. Foran, and L. Yang, "Comparative performance analysis of stained histopathology specimens using RGB and multispectral imaging," in *Proceedings SPIE Medical Imaging 2011: Computer-Aided Diagnosis*, 2011, vol. 7963, p. 79633B.

[266] Y. Khouj, J. Dawson, J. Coad, and L. Vona-Davis, "Hyperspectral Imaging and K-Means Classification for Histologic Evaluation of Ductal Carcinoma In Situ," *Front. Oncol.*, vol. 8, Feb. 2018.

[267] L. Roux *et al.*, "Mitosis detection in breast cancer histological images An ICPR 2012 contest.," *J. Pathol. Inform.*, vol. 4, p. 8, 2013.

[268] C. Malon and E. Cosatto, "Classification of mitotic figures with convolutional neural networks and seeded blob features," *J. Pathol. Inform.*, vol. 4, no. 1, p. 9, 2013.

[269] H. Irshad, A. Gouaillard, L. Roux, and D. Racoceanu, "Multispectral band selection and spatial characterization: Application to mitosis detection in breast cancer histopathology.," *Comput. Med. Imaging Graph.*, vol. 38, no. 5, pp. 390–402, Jul. 2014.

[270] H. Irshad, A. Gouaillard, L. Roux, and D. Racoceanu, "Spectral band selection for mitosis detection in histopathology," in *2014 IEEE 11th International Symposium on Biomedical Imaging (ISBI)*, 2014, pp. 1279–1282.

[271] Cheng Lu and M. Mandal, "Toward Automatic Mitotic Cell Detection and Segmentation in Multispectral Histopathological Images," *IEEE J. Biomed. Heal. Informatics*, vol. 18, no. 2, pp. 594–605, Mar. 2014.

[272] K. Masood and N. M. Rajpoot, "Texture based classification of hyperspectral colon biopsy samples using CLBP," *IEEE Int. Symp. Biomed. Imaging From Nano to Macro, 2009. ISBI '09*, pp. 1011–1014, Jun. 2009.

[273] M. Maggioni *et al.*, "Hyperspectral microscopic analysis of normal, benign and carcinoma microarray tissue sections," 2006, p. 60910I.

[274] K. Rajpoot and N. Rajpoot, "{SVM} Optimization for Hyperspectral Colon Tissue Cell

Classification," in *Medical Image Computing and Computer-Assisted Intervention {\textendash} {MICCAI} 2004*, Springer Nature, 2004, pp. 829–837.

[275] K. Masood, N. Rajpoot, K. Rajpoot, and H. Qureshi, "Hyperspectral Colon Tissue Classification using Morphological Analysis," in *2006 International Conference on Emerging Technologies*, 2006.

[276] A. Chaddad, C. Tanougast, A. Dandache, A. Al Houseini, and A. Bouridane, "Improving of colon cancer cells detection based on Haralick's features on segmented histopathological images," in *ICCAIE 2011 - 2011 IEEE Conference on Computer Applications and Industrial Electronics*, 2011, pp. 87–90.

[277] A. Chaddad, C. Tanougast, A. Dandache, and A. Bouridane, "Extracted haralick's texture features and morphological parameters from segmented multispectrale texture bio-images for classification of colon cancer cells," *WSEAS Trans. Biol. Biomed.*, vol. 8, pp. 39–50, Apr. 2011.

[278] A. Chaddad, P. Daniel, and T. Niazi, "Radiomics Evaluation of Histological Heterogeneity Using Multiscale Textures Derived From 3D Wavelet Transformation of Multispectral Images.," *Front. Oncol.*, vol. 8, no. APR, p. 96, 2018.

[279] R. Peyret, A. Bouridane, S. A. Al-Maadeed, S. Kunhoth, and F. Khelifi, "Texture analysis for colorectal tumour biopsies using multispectral imagery," in *Conference proceedings: Annual International Conference of the IEEE Engineering in Medicine and Biology Society. IEEE Engineering in Medicine and Biology Society. Annual Conference*, 2015, vol. 2015, pp. 7218–7221.

[280] R. Peyret, A. Bouridane, F. Khelifi, M. A. Tahir, and S. Al-Maadeed, "Automatic classification of colorectal and prostatic histologic tumor images using multiscale multispectral local binary pattern texture features and stacked generalization," *Neurocomputing*, vol. 275, pp. 83–93, 2018.

[281] I. W. Lao, F. Cui, and H. Zhu, "Quantitation of microRNA-92a in colorectal adenocarcinoma and its precancerous lesions: Co-utilization of in situ hybridization and spectral imaging.," *Oncol. Lett.*, vol. 9, no. 3, pp. 1109–1115, Mar. 2015.

[282] A. Chaddad, C. Desrosiers, A. Bouridane, M. Toews, L. Hassan, and C. Tanougast, "Multi texture analysis of colorectal cancer continuum using multispectral imagery," *PLoS One*, vol. 11, no. 2, p. e0149893, 2016.

[283] H. Haj-Hassan, A. Chaddad, Y. Harkouss, C. Desrosiers, M. Toews, and C. Tanougast, "Classifications of multispectral colorectal cancer tissues using convolution neural network," *J. Pathol. Inform.*, vol. 8, no. 1, p. 1, 2017.

[284] R. Awan, S. Al-Maadeed, and R. Al-Saady, "Using spectral imaging for the analysis of abnormalities for colorectal cancer: When is it helpful?," *PLoS One*, vol. 13, no. 6, p. e0197431, Jun. 2018.

[285] I. Kopriva, G. Aralica, M. Popovic Hadzija, M. Hadzija, L.-I. Dion-Bertrand, and X. Chen, "Hyperspectral imaging for intraoperative diagnosis of colon cancer metastasis in a liver," in *Medical Imaging 2019: Digital Pathology*, 2019, vol. 10956, p. 26.

[286] L. Septiana *et al.*, "Elastic and collagen fibers discriminant analysis using H&E stained hyperspectral images," *Opt. Rev.*, vol. 26, no. 4, pp. 369–379, 2019.

[287] E. Hashimoto *et al.*, "Tissue classification of liver pathological tissue specimens image using spectral features," in *Proceedings SPIE Medical Imaging 2017: Digital Pathology;*, 2017, vol. 10140, p. 101400Z.

[288] J. Wang and Q. Li, "Quantitative analysis of liver tumors at different stages using microscopic hyperspectral imaging technology," *J. Biomed. Opt.*, vol. 23, no. 10, p. 1, Oct. 2018.

[289] P. A. Bautista and Y. Yagi, "Localization of eosinophilic esophagitis from H&E stained images using multispectral imaging.," *Diagn. Pathol.*, vol. 6 Suppl 1, p. S2, Mar. 2011.

[290] American Cancer Society, "Cancer Facts & Figures 2019," 2019. .

[291] H. Zhang *et al.*, "An automatic segmentation method for multispectral microscopic cervical cell images," in *Proceedings SPIE Medical Imaging 2006: Image Processing;*, 2006, vol. 6144 II, p. 61443E.

[292] F. Cao, S. Chen, and L. Zeng, "New abnormal cervical cell detection method of multi-spectral pap smears," *Wuhan Univ. J. Nat. Sci.*, vol. 12, no. 3, pp. 476–480, May 2007.

[293] T. Zhao, E. S. Wachman, S. J. Geyer, and D. L. Farkas, "A recursive spectral selection scheme for unsupervised segmentation of multispectral Pap smear image sets," in *Proceedings SPIE Imaging, Manipulation, and Analysis of Biomolecules, Cells, and Tissues II*, 2004, vol. 5322, p. 175.

[294] A. M. Siddiqi *et al.*, "Use of hyperspectral imaging to distinguish normal, precancerous, and cancerous cells.," *Cancer*, vol. 114, no. 1, pp. 13–21, Feb. 2008.

[295] M. A. Tahir and A. Bouridane, "Novel round-robin tabu search algorithm for prostate cancer classification and diagnosis using multispectral imagery," *IEEE Trans. Inf. Technol. Biomed.*, vol. 10, no. 4, pp. 782–793, Oct. 2006.

[296] M. A. Tahir, A. Bouridane, F. Kurugollu, and A. Amira, "Feature selection using tabu search for improving the classification rate of prostate needle biopsies," 2004, vol. 2, pp. 335–338.

[297] M. A. Tahir, A. Bouridane, and M. A. Roula, "Prostate cancer classification using multispectral imagery and metaheuristics," in *Computational Intelligence in Medical Imaging: Techniques and Applications*, Faculty of CEMS, University of the West of England, Bristol, United Kingdom: CRC Press, 2009, pp. 139–166.

[298] R. Khelifi, M. Adel, and S. Bourennane, "Multispectral texture characterization: application to computer aided diagnosis on prostatic tissue images," *EURASIP J. Adv. Signal Process.*, vol. 2012, no. 1, p. 118, 2012.

[299] C. Angeletti, N. R. Harvey, V. Khomitch, A. H. Fischer, R. M. Levenson, and D. L. Rimm, "Detection of malignancy in cytology specimens using spectral-spatial analysis.," *Lab. Invest.*, vol. 85, no. 12, pp. 1555–1564, 2005.

[300] J. Lou, M. Zhou, Q. Li, C. Yuan, and H. Liu, "An automatic red blood cell counting method based on spectral images," in *2016 9th International Congress on Image and Signal Processing, BioMedical Engineering and Informatics (CISP-BMEI)*, 2016, pp. 1391–1396.

[301] N. Guo, L. Zeng, and Q. Wu, "A method based on multispectral imaging technique for White Blood Cell segmentation," *Comput. Biol. Med.*, vol. 37, no. 1, pp. 70–76, Jan. 2007.

[302] Y. Guan, "Pathological leucocyte segmentation algorithm based on hyperspectral imaging technique," *Opt. Eng.*, vol. 51, no. 5, p. 53202, May 2012.

[303] Q. Wu, L. Zeng, H. Ke, W. Xie, H. Zheng, and Y. Zhang, "Analysis of blood and bone marrow smears using multispectral imaging analysis techniques," 2005, p. 1872.

[304] G. S. Verebes, M. Melchiorre, A. Garcia-Leis, C. Ferreri, C. Marzetti, and A. Torreggiani, "Hyperspectral enhanced dark field microscopy for imaging blood cells," *J. Biophotonics*, vol. 6, no. 11–12, pp. 960–967, Dec. 2013.

[305] Q. Li, C. Dai, H. Liu, and J. Liu, "Leukemic cells segmentation algorithm based on molecular spectral imaging technology," in *International Symposium on Photoelectronic Detection and Imaging 2009: Advances in Infrared Imaging and Applications*, 2009, p. 73830V.

[306] D. L. Omucheni, K. A. Kaduki, W. D. Bulimo, and H. K. Angeyo, "Application of principal component analysis to multispectral-multimodal optical image analysis for malaria diagnostics," *Malar. J.*, vol. 13, no. 1, p. 485, Dec. 2014.

[307] A. Merdasa, M. Brydegaard, S. Svanberg, and J. T. Zoueu, "Staining-free malaria diagnostics by multispectral and multimodality light-emitting-diode microscopy," *J. Biomed. Opt.*, vol. 18, no. 3, p. 36002, Mar. 2013.

[308] S. DABO-NIANG and J. T. ZOUEU, "Combining kriging, multispectral and multimodal microscopy to resolve malaria-infected erythrocyte contents," *J. Microsc.*, vol. 247, no. 3,

pp. 240–251, Sep. 2012.

[309] J. T. Zoueu, S. Ouattara, A. Toure, S. Safi, and S. T. Zan, “Spectroscopic approach of multispectral imaging of plasmodium falciparum - infected human erythrocytes,” in *2009 3rd ICTON Mediterranean Winter Conference (ICTON-MW)*, 2009, pp. 1–7.

[310] Y. Qian, Q. Li, H. Liu, Y. Wang, and J. Zhu, “A preprocessing algorithm for hyperspectral images of vessels,” in *2014 7th International Conference on Biomedical Engineering and Informatics*, 2014, pp. 19–23.

[311] Q. Li, Z. Sun, Y. Wang, H. Liu, F. Guo, and J. Zhu, “Histological skin morphology enhancement base on molecular hyperspectral imaging technology,” *Ski. Res. Technol.*, vol. 20, no. 3, pp. 332–340, 2014.

[312] K. Kalleberg, J. Nip, and K. Gossage, “Multispectral imaging as a tool for melanin detection,” *J. Histotechnol.*, vol. 38, no. 1, pp. 14–21, 2015.

[313] S. Gaudi *et al.*, “Hyperspectral Imaging of Melanocytic Lesions,” *Am. J. Dermatopathol.*, vol. 36, no. 2, pp. 131–136, 2014.

[314] D. T. Dicker *et al.*, “Differentiation of normal skin and melanoma using high resolution hyperspectral imaging,” *Cancer Biol. Ther.*, vol. 5, no. 8, pp. 1033–1038, 2006.

[315] Q. Wang, Q. Li, M. Zhou, L. Sun, S. Qiu, and Y. Wang, “Melanoma and Melanocyte Identification from Hyperspectral Pathology Images Using Object-Based Multiscale Analysis,” *Appl. Spectrosc.*, p. 000370281878135, Jun. 2018.

[316] P. Haub and T. Meckel, “A Model based Survey of Colour Deconvolution in Diagnostic Brightfield Microscopy: Error Estimation and Spectral Consideration,” *Sci. Rep.*, vol. 5, no. 1, p. 12096, Dec. 2015.

[317] L. Jiang, G. Cui, and T. Xu, “Effect of Lens on Spectral Characteristics of Imaging System,” 2019, pp. 170–177.

[318] R. W. G. Hunt and M. R. Pointer, *Measuring Colour*. Chichester, UK: John Wiley & Sons, Ltd, 2011.

[319] Kularatna, *Digital and Analogue Instrumentation: Testing and measurement*. Institution of Engineering and Technology, 2003.

[320] L. Gómez-Chova, L. Alonso, L. Guanter, G. Camps-Valls, J. Calpe, and J. Moreno, “Correction of systematic spatial noise in push-broom hyperspectral sensors: application to CHRIS/PROBA images.,” *Appl. Opt.*, vol. 47, no. 28, pp. F46--60, Oct. 2008.

[321] X. Zhao, F. Wang, T. Huang, M. K. Ng, and R. J. Plemmons, “Deblurring and Sparse Unmixing for Hyperspectral Images,” *IEEE Trans. Geosci. Remote Sens.*, vol. 51, no. 7, pp. 4045–4058, Jul. 2013.

[322] D. N. Louis *et al.*, *The 2016 World Health Organization Classification of Tumors of the Central Nervous System: a summary*, vol. 131, no. 6. Springer Berlin Heidelberg, 2016, pp. 803–820.

[323] S. Ortega *et al.*, “P03.18 Detection of human brain cancer in pathological slides using hyperspectral images,” *Neuro. Oncol.*, vol. 19, no. suppl_3, p. iii37, 2017.

[324] A. Plaza *et al.*, “Remote Sensing of Environment Recent advances in techniques for hyperspectral image processing,” *Remote Sens. Environ.*, vol. 113, pp. S110–S122, 2009.

[325] J. A. Richards, *Remote Sensing Digital Image Analysis*. Springer Berlin Heidelberg, 2012.

[326] R. Gillies, J. E. Freeman, L. C. Cancio, D. Brand, M. Hopmeier, and J. R. Mansfield, “Systemic Effects of Shock and Resuscitation Monitored by Visible Hyperspectral Imaging,” *Diabetes Technol. Ther.*, vol. 5, no. 5, pp. 847–855, 2003.

[327] S. Lopez, “A Novel Use of Hyperspectral Images for Human Brain Cancer Detection using in-Vivo A Novel Use of Hyperspectral Images for Human Brain Cancer,” no. January, 2016.

[328] J. Burger and A. Gowen, “Data handling in hyperspectral image analysis,” *Chemom. Intell. Lab. Syst.*, vol. 108, no. 1, pp. 13–22, 2011.

[329] G. Camps-Valls and L. Bruzzone, “Kernel-based methods for hyperspectral image classification,” *{IEEE} Trans. Geosci. Remote Sens.*, vol. 43, no. 6, pp. 1351–1362, Jun. 2005.

[330] H. W. Brown and J. Roberts, “Exploring the factors contributing to sibling correlations in BMI: A study using the panel study of income dynamics,” *Obesity*, vol. 20, no. 5, pp. 978–984, 2012.

[331] J. A. Benediktsson, J. A. Palmason, and J. R. Sveinsson, “Classification of hyperspectral data from urban areas based on extended morphological profiles,” *{IEEE} Trans. Geosci. Remote Sens.*, vol. 43, no. 3, pp. 480–491, Mar. 2005.

[332] H. Akbari, Y. Kosugi, K. Kojima, and N. Tanaka, “Wavelet-Based Compression and Segmentation of Hyperspectral Images in Surgery,” in *Lecture Notes in Computer Science*, Springer Nature, pp. 142–149.

[333] F. Blanco, M. López-Mesas, S. Serranti, G. Bonifazi, J. Havel, and M. Valiente, “Hyperspectral imaging based method for fast characterization of kidney stone types,” *J. Biomed. Opt.*, vol. 17, no. 7, p. 760271, Jul. 2012.

[334] T. G. Dietterich, “Ensemble Methods in Machine Learning,” in *Multiple Classifier Systems*, Springer Nature, 2000, pp. 1–15.

[335] G. Lu, L. Halig, D. Wang, Z. G. Chen, and B. Fei, “Spectral-Spatial Classification Using Tensor Modeling for Cancer Detection with Hyperspectral Imaging.,” *Proc. SPIE-the Int. Soc. Opt. Eng.*, vol. 9034, p. 903413, 2014.

[336] R. Pike, G. Lu, D. Wang, Z. G. Chen, and B. Fei, “A Minimum Spanning Forest-Based Method for Noninvasive Cancer Detection With Hyperspectral Imaging,” *IEEE Trans. Biomed. Eng.*, vol. 63, no. 3, pp. 653–663, 2016.

[337] R. Achanta, A. Shaji, K. Smith, A. Lucchi, P. Fua, and S. Süsstrunk, “SLIC Superpixels Compared to State-of-the-Art Superpixel Methods,” *IEEE Trans. Pattern Anal. Mach. Intell.*, vol. 34, no. 11, pp. 2274–2282, Nov. 2012.

[338] E. C. Carter *et al.*, “CIE 015:2018 Colorimetry, 4th Edition,” Vienna, Oct. 2018.

[339] F. van der Meer, “The effectiveness of spectral similarity measures for the analysis of hyperspectral imagery,” *Int. J. Appl. Earth Obs. Geoinf.*, vol. 8, no. 1, pp. 3–17, Jan. 2006.

[340] G. Mercier and M. Lennon, “Support Vector Machines for Hyperspectral Image Classification with Spectral-based kernels,” in *International Geoscience and Remote Sensing Symposium (IGARSS)*, 2003, vol. 1, pp. 288–290.

[341] C. Chang and C. Lin, “LIBSVM : A Library for Support Vector Machines,” *ACM Trans. Intell. Syst. Technol.*, vol. 2, pp. 1–39, 2013.

[342] M. Abadi *et al.*, “TensorFlow: Large-Scale Machine Learning on Heterogeneous Distributed Systems,” Mar. 2016.

[343] F. Chollet, “Keras,” *GitHub repository*. GitHub, 2015.

[344] J. Snoek, H. Larochelle, and R. P. Adams, “Practical Bayesian Optimization of Machine Learning Algorithms,” Jun. 2012.

[345] W. Zhao and S. Du, “Spectral-Spatial Feature Extraction for Hyperspectral Image Classification: A Dimension Reduction and Deep Learning Approach,” *IEEE Trans. Geosci. Remote Sens.*, 2016.

[346] C. Patil and I. Baidari, “Estimating the Optimal Number of Clusters k in a Dataset Using Data Depth,” *Data Sci. Eng.*, vol. 4, no. 2, pp. 132–140, Jun. 2019.

[347] G. Litjens *et al.*, “A survey on deep learning in medical image analysis,” *Med. Image Anal.*, vol. 42, pp. 60–88, Dec. 2017.

[348] A. P. Bradley, “The use of the area under the ROC curve in the evaluation of machine learning algorithms,” *Pattern Recognit.*, vol. 30, no. 7, pp. 1145–1159, Jul. 1997.

[349] B. Ehteshami Bejnordi *et al.*, “Diagnostic Assessment of Deep Learning Algorithms for Detection of Lymph Node Metastases in Women With Breast Cancer,” *JAMA*, vol. 318, no.

22, p. 2199, Dec. 2017.

[350] Z. Pei, S. Cao, L. Lu, and W. Chen, "Direct Cellularity Estimation on Breast Cancer Histopathology Images Using Transfer Learning," *Comput. Math. Methods Med.*, vol. 2019, pp. 1–13, Jun. 2019.

[351] N. Saulig, J. Lerga, Z. Milanovic, and C. Ioana, "Extraction of Useful Information Content From Noisy Signals Based on Structural Affinity of Clustered TFDs' Coefficients," *IEEE Trans. Signal Process.*, vol. 67, no. 12, pp. 3154–3167, Jun. 2019.

[352] F. Hržić, I. Štajduhar, S. Tschauner, E. Sorantin, and J. Lerga, "Local-Entropy Based Approach for X-Ray Image Segmentation and Fracture Detection," *Entropy*, vol. 21, no. 4, p. 338, Mar. 2019.

[353] I. Mandić, H. Peić, J. Lerga, and I. Štajduhar, "Denoising of X-ray Images Using the Adaptive Algorithm Based on the LPA-RICI Algorithm," *J. Imaging*, vol. 4, no. 2, p. 34, Feb. 2018.